USGS
science for a changing world

A Product of the Water Availability and Use Science Program

Prepared in cooperation with the Department of Geological Sciences at the University of Texas at San Antonio and hosted by the Student Geological Society and student chapters of the Association of Petroleum Geologists and the Association of Engineering Geologists

U.S. Geological Survey Karst Interest Group Proceedings, San Antonio, Texas, May 16–18, 2017

Edited By Eve L. Kuniansky and Lawrence E. Spangler

Scientific Investigations Report 2017–5023

U.S. Department of the Interior
U.S. Geological Survey

U.S. Department of the Interior
RYAN ZINKE, Secretary

U.S. Geological Survey
William Werkheiser, Acting Director

U.S. Geological Survey, Reston, Virginia: 2017

Suggested citation:
Kuniansky, E.L., and Spangler, L.E., eds., 2017, U.S. Geological Survey Karst Interest Group Proceedings, San Antonio, Texas, May 16–18, 2017: U.S. Geological Survey Scientific Investigations Report 2017–5023, 245 p., https://doi.org/10.3133/sir20175023.

ISSN 2328-0328 (online)

Contents

Introduction and Acknowledgments

Karst aquifer systems are present throughout parts of the United States and some of its territories, and have developed in carbonate rocks (primarily limestone and dolomite) and evaporites (gypsum, anhydrite, and halite) that span an interval of time encompassing more than 550 million years. The depositional environments, diagenetic processes, post-depositional tectonic events, and geochemical weathering processes that form karst aquifers are varied and complex. These factors involve biological, chemical, and physical changes that when combined with the diverse climatic regimes in which karst development has taken place, result in the unique dual- or triple-porosity nature of karst aquifers. These complex hydrogeologic systems typically represent challenging and unique conditions to scientists attempting to study groundwater flow and contaminant transport in these terrains.

The dissolution of carbonate rocks and the subsequent development of distinct and beautiful landscapes, caverns, and springs have resulted in the most exceptional karst areas being designated as national or state parks. Tens of thousands of similar areas in the United States have been developed into commercial caverns and known privately owned caves. Both public and private properties provide access for scientists to study the flow of groundwater *in situ*. Likewise, the range and complexity of landforms and groundwater flow systems associated with karst terrains are enormous, perhaps more than for any other aquifer type. Karst aquifers and landscapes that form in tropical areas, such as the cockpit karst along the north coast of Puerto Rico, differ greatly from karst landforms in more arid climates, such as the Edwards Plateau in west-central Texas or the Guadalupe Mountains near Carlsbad, New Mexico, where hypogenic processes have played a major role in speleogenesis. Many of these public and private lands also contain unique flora and fauna associated with these karst hydrogeologic systems. As a result, numerous federal, state, and local agencies have a strong interest in the study of karst terrains.

Many of the major springs and aquifers in the United States have developed in carbonate rocks, such as the Floridan aquifer system in Florida and parts of Alabama, Georgia, and South Carolina; the Ozark Plateaus aquifer system in parts of Arkansas, Kansas, Missouri, and Oklahoma; and the Edwards-Trinity aquifer system in west-central Texas. These aquifers, and the springs that discharge from them, serve as major water-supply sources and form unique ecological habitats. Competition for the water resources of karst aquifers is common, and urban development and the lack of attenuation of contaminants in karst areas due to dissolution features that form direct pathways into karst aquifers can impact the ecosystem and water quality associated with these aquifers.

The concept for developing a platform for interaction among scientists within the U.S. Geological Survey (USGS) working on karst-related studies evolved from the November 1999 National Groundwater Meeting of the USGS. As a result, the Karst Interest Group (KIG) was formed in 2000. The KIG is a loose-knit, grass-roots organization of USGS and non-USGS scientists and researchers devoted to fostering better communication among scientists working on, or interested in, karst science. The primary mission of the KIG is to encourage and support interdisciplinary collaboration and technology transfer among scientists working in karst areas. Additionally, the KIG encourages collaborative studies between the different mission areas of the USGS as well as with other federal and state agencies, and with researchers from academia and institutes.

To accomplish its mission, the KIG has organized a series of workshops that have been held near nationally important karst areas. To date (2017) seven KIG workshops, including the workshop documented in this report, have been held. The workshops typically include oral and poster sessions on selected karst-related topics and research, as well as field trips to local karst areas. To increase non-

USGS participation an effort was made for the workshops to be held at a university or institute beginning with the fourth workshop. Proceedings of the workshops are published by the USGS and are available online at the USGS publications warehouse https://pubs.er.usgs.gov/ by using the search term "karst interest group."

The first KIG workshop was held in St. Petersburg, Florida, in 2001, in the vicinity of the large springs and other karst features of the Floridan aquifer system. The second KIG workshop was held in 2002, in Shepherdstown, West Virginia, in proximity to the carbonate aquifers of the northern Shenandoah Valley, and highlighted an invited presentation on karst literature by the late Barry F. Beck of P.E. LaMoreaux and Associates. The third KIG workshop was held in 2005, in Rapid City, South Dakota, near evaporite karst features in limestones of the Madison Group in the Black Hills of South Dakota. The Rapid City KIG workshop included field trips to Wind Cave National Park and Jewel Cave National Monument, and featured a presentation by Thomas Casadevall, then USGS Central Region Director, on the status of Earth science at the USGS.

The fourth KIG workshop in 2008 was hosted by the Hoffman Environmental Research Institute and Center for Cave and Karst Studies at Western Kentucky University in Bowling Green, Kentucky, near Mammoth Cave National Park and karst features of the Chester Upland and Pennyroyal Plateau. The workshop featured a late-night field trip into Mammoth Cave led by Rickard Toomey and Rick Olsen, National Park Service. The fifth KIG workshop in 2011 was a joint meeting of the USGS KIG and University of Arkansas HydroDays, hosted by the Department of Geosciences at the University of Arkansas in Fayetteville. The workshop featured an outstanding field trip to the unique karst terrain along the Buffalo National River in the southern Ozarks, and a keynote presentation on paleokarst in the United States was delivered by Art and Peggy Palmer. The sixth KIG workshop was hosted by the National Cave and Karst Research Institute (NCKRI) in 2014, in Carlsbad, New Mexico. George Veni, Director of the NCKRI, served as a co-chair of the workshop with Eve Kuniansky of the USGS. The workshop featured speaker Dr. Penelope Boston, Director of Cave and Karst Studies at New Mexico Tech, Socorro, and Academic Director at the NCKRI, who addressed the future of karst research. The field trip on evaporite karst of the lower Pecos Valley was led by Lewis Land (NCKRI karst hydrologist), and the field trip on the geology of Carlsbad Caverns National Park was led by George Veni.

This current seventh KIG workshop is being held in San Antonio at the University of Texas at San Antonio (UTSA). This 2017 workshop is being hosted by the Department of Geological Sciences' Student Geological Society (SGS), and student chapters of the American Association of Petroleum Geologists (AAPG) and Association of Engineering Geologists (AEG), with support by the UTSA Department of Geological Sciences and Center for Water Research. The UTSA student chapter presidents, Jose Silvestre (SGS), John Cooper (AAPG), and Tyler Mead (AEG) serve as co-chairs of the 2017 workshop with Eve Kuniansky of the USGS. The technical session committee is chaired by Eve Kuniansky, USGS, and includes Michael Bradley, Tom Byl, Rebecca Lambert, John Lane, and James Kaufmann, all USGS, and Patrick Tucci, retired USGS. The logistics committee includes Amy Clark, Yongli Gao, and Lance Lambert (Department Chair), UTSA Department of Geological Sciences; and Ryan Banta and Allan Clark, USGS, San Antonio, Texas. The field trip committee is chaired by Allan Clark and includes Amy Clark, Yongli Gao, and Keith Muehlestein, UTSA; Marcus Gary, Edwards Aquifer Authority and University of Texas at Austin; Ron Green, Southwest Research Institute; Geary Schindel, Edwards Aquifer Authority; and George Veni, NCKRI. Additionally, two organizations have assisted the UTSA student chapters in hosting the meeting by donating funds to the chapters: the Edwards Aquifer Authority, San Antonio, Texas, and the Barton Springs Edwards Aquifer Authority, Austin, Texas. Additionally, Yongli Gao, Center for Water Research and Department of Geological

Sciences, UTSA, helped develop sessions on cave and karst research in China for this workshop. These proceedings could not have been accomplished without the assistance of Lawrence E. Spangler as co-editor who not only has subject matter expertise, but also serves as an editor with the USGS Science Publishing Network. We sincerely hope that this workshop continues to promote future collaboration among scientists of varied and diverse backgrounds, and improves our understanding of karst aquifer systems in the United States and its territories.

The extended abstracts of USGS authors were peer reviewed and approved for publication by the USGS. Articles submitted by university researchers and other federal and state agencies did not go through the formal USGS peer review and approval process, and therefore may not adhere to USGS editorial standards or stratigraphic nomenclature. However, all articles had a minimum of two peer reviews and were edited for consistency of appearance in the proceedings. The use of trade, firm or product names is for descriptive purposes only and does not imply endorsement by the U.S. Government. The USGS Water Availability and Use Science Program funded the publication costs of the proceedings.

Eve L. Kuniansky

USGS Karst Interest Group Coordinator

Agenda U.S. Geological Survey Karst Interest Group Workshop

May16–18, 2017, held at the University of Texas at San Antonio

Hosted by the Student Geological Society and student chapters of the Association of Petroleum Geologists and the Association of Engineering Geologists

		DAY 1 TECHNICAL SESSION	
		Tuesday, May 16, 2017	
7:45	Registration	You may pick up name tags until 4pm	
	Session 1	Eve Kuniansky, USGS, Karst Interest Group Coordinator	Moderator
8:00	Welcome	George Perry, Professor and Dean, UTSA College of Sciences	
8:30	George Veni	Status of Karst Science Nationally and Internationally, National Cave and Karst Research Institute Perspective	Day 1 Keynote
9:00	Dale Pate	A Multi-Disciplined Approach to Understanding and Managing Shared Karst Landscapes	Karst Management/National Program
9:20	Timothy P. Sullivan	Methodology for Calculating Probability, Protection, and Precipitation Factors of P3 Method for Karst Aquifer Vulnerability	Karst Vulnerability to Contaminants/Edwards Aquifer
9:40	Stephen Opsahl	Combining Continuous Nitrate Monitoring and Discrete Chemical Analyses to Understand Nitrate Dynamics in Karst	Water Quality/Nitrates
10:00		BREAK	
10:40	Timothy P. Sullivan	Methodology for Calculating Karst Watershed Nitrogen Inputs and Developing a SWAT Model	Contaminants in Karst/Edwards/Nitrate
11:00	Tom Byl	Attenuation of Acid Rock Drainage with a Sequential Injection of Compounds to Reverse Biologically Mediated Pyrite Oxidation	Geochemistry/Microbiology/Acid Rock Drainage
11:20	Yongli Gao	Hydrological and Environmental Reconstruction Based on Speleothem Ages in Southeastern North America	North America Climate Change/Caves
11:40		LUNCH ON YOUR OWN	
	Session 2	Jose Silvestre, UTSA Student Geological Society	Moderator
13:00	Dan Doctor	A GIS-Based Compilation of Spring Locations and Geochemical Parameters in the Appalachian Landscape Conservation Cooperative (LCC) Region	Geochemistry
13:20	John Lane	Surface and Borehole Geophysical Applications for Karst Investigations	Geophysical Methods
13:40	Kevin W. Blackwood	Hydrogeophysical Investigations in the Upper Arbuckle Group on the Tishomingo Anticline in the Central Arbuckle Mountains of Southern Oklahoma	Geophysical Methods
14:00	Charles Taylor	Investigation of Karst Aquifer Characteristics in a Public-Supply Well Field in the Elizabethtown, Kentucky Area	Aquifer Characteristics
14:20		BREAK	

		Featured Session China Caves and Karst	
14:40	Junbing Pu	A Review of Recent Karst Research in the China Geological Survey	China Caves and Karst
15:00	Binggui Cai	Intra-Annual Variations of Soil CO_2 and Drip-Water Chemistry in Shihua Cave, Beijing China and Implications for the Formation of Annual Laminae in Stalagmites	China Caves and Karst
15:20	Hong Liu	Hydrochemical Characteristics of Heilongtan Springs, Kunming, China	China Caves and Karst
15:40	Xiaozhen Jiang	Formation Mechanisms of Extremely Large Sinkhole Collapses in Laibin, Guangxi, China	China Caves and Karst
16:00	See end for list	POSTER SESSION TUESDAY 4 to 6 pm	
		DAY 2 TECHNICAL SESSION	
		Wednesday, May 17, 2017	
	Session 3	John Cooper, UTSA Student Chapter AAPG	Moderator
8:00	Geary Schindel	Edwards Aquifer Region and the Status of Research at the Edwards Aquifer Authority	Day 2 Keynote
8:30	Barbara Mahler	A Tale of Three Aquifers – Setting, Science, and Policy of the Three Segments of the Edwards Aquifer	Edwards Aquifer
8:50	Marylynn Musgrove	Timescales of Groundwater Quality Change in Karst Groundwater: Edwards Aquifer, South-Central Texas	Edwards Aquifer
9:10	Ross Kushnereit	Estimating Recharge to the Edwards Aquifer, South-Central, Texas—Current (2017) Methods and Introduction of an Automated Method Using the Python Scripting Language	Edwards Aquifer
9:30	Allan Clark	Geologic Framework and Hydrostratigraphy of the Edwards and Trinity Aquifers Within Northern Bexar and Comal Counties, Texas	Edwards Aquifer
9:50		BREAK	
10:20	Tom Byl	Aromatic-Ring Biodegradation in Soils From a Crude Oil Spill on Clear Creek, Obed Wild and Scenic River National Park, Tennessee	Geomicrobiology
10:40	Victor Roland	Investigating Microbial Response to Fertilizer Application From Concentrated Animal Feeding Operations Located on Karst Aquifers in Northern Arkansas	Geomicrobiology
11:00	Kevin DeFosset	Evidence for Karst-Influenced Cross-Formational Fluid Bypass of a Dolomite Unit at the Top of the Oldsmar Formation in the Lower Floridan Aquifer, Southeast Florida	Geologic Framework/Floridan Aquifer
11:20	Paul L. Broughton	Collapse of the Devonian Prairie Evaporite Karst in the Western Canada Sedimentary Basin: Structuration of the Overlying Cretaceous Athabasca Oil Sands and Regional Flow System Reversal by Subglacial Meltwater	Geologic Framework/Canada
11:40		LUNCH ON YOUR OWN	

	Session 4	Tyler Mead, UTSA Student Chapter AEG	Moderator
13:00	Mark Hudson	Tufa and Water Radiogenic Geochemistry and Tufa Ages for Two Karst Aquifers in the Buffalo National River Region, Northern Arkansas	Geologic Framework/Isotopes/Buffalo National River
13:20	James B. Paces	Isotopic Constraints on Middle Pleistocene Cave Evolution, Paleohydrologic Flow, and Environmental Conditions From Fitton Cave Speleothems, Buffalo National River, Arkansas	Geologic Framework/Isotopes/Buffalo National River
13:40	J. Van Brahana	Speleogenetic, Tectonic, and Sedimentologic Controls on Regional Karst Aquifers in the Southern Ozarks of the Midcontinent U.S., and Potential Problems at Site-Specific Scales From Aquifer Lumping	Geologic Framework/Southern Ozarks
14:00	David Weary	Geologic Context of Large Karst Springs and Caves in the Ozark National Scenic Riverways, Missouri	Geologic Framework/Ozark Riverways
14:20		BREAK	
15:00	Carol Bitting/J. Van Brahana	Utilizing Fluorescent Dyes to Identify Meaningful Water-Quality Sampling Locations and Enhance Understanding of Groundwater Flow Near a Hog CAFO on Mantled Karst—Buffalo National River, Southern Ozarks	Tracers/Buffalo National River
15:20	Byl/JeTara Brown	Using Quantitative Tracer Studies to Evaluate the Connection Between the Surface and Subsurface at Mammoth Cave, Kentucky	Tracers/Mammoth Cave
15:40	Larry Spangler	Selected Results of Investigations and Tracer Studies to Better Understand the Hydrologic System to Ashley and Adjacent Springs, Utah	Tracers/Utah
16:00	Amy Clark/Eve Kuniansky	Field Trip Logistics/KIG Business	Logistics
		DAY 3 OPTIONAL FIELD TRIP	
8:00	Caravan from Wyndham hotel	Thursday, May 18, all day	Long day if staying for bat flight
	POSTER PRESENTERS	POSTER SESSION IS TUESDAY EVENING	4 to 6 PM
1	Benjamin Lockwood	Statistical Analysis of Groundwater Geochemistry in Southwest Missouri	Geochemistry
2	Zhiguo Rao presented by Yunxia Li	Stalagmite $\delta^{13}C$ and $\delta^{18}O$ Records for the Past 130,000 Years From the Eastern Edge of the Chinese Loess Plateau (CLP): Responses of the CLP as a Carbon Sink to Climate Change	China Geochemistry/Isotopes/Climate Change
3	Yunxia Li	Hydrogeochemical Characteristics of Precipitation and Cave Drip Water in Zhenzhu Cave, North China	China Geochemistry/Cave
4	Dong Li	High-Resolution Summer Monsoon Intensity Variations in Central China From 26,000 to 11,000 Years Before Present as Revealed by Stalagmite Oxygen Isotope Ratios	China Geochemistry/Isotopes
5	Lijun Tian	Controls on the Oxygen Isotopic Variability of Meteoric Precipitation, Drip Water and Calcite Deposition at Baojinggong Cave and Shihua Cave, China	China Geochemistry/Caves
6	Yongli Gao	Comparative Studies of Extremely Large Sinkholes (Tiankengs) in Southern China and Southeastern North America	China Karst Hazards

7	Kevin W. Blackwood	Characterization of Chert Gravels and Their Hydrogeological, Ecological, and Archaeological Significance in a Karst System in the Arbuckle Mountains, Southern Oklahoma	Sediment Transport/Ecosystems
8	Scott Ikard	Geoelectric Signature of Hyporheic and Ambient Groundwater Exchange Flows Between the Guadalupe River, Floodplain Alluvial Aquifer, and the Carrizo Aquifer Outcrop Near Seguin, Texas	Geophysical Methods
9	Kevin Cunningham	Use of Seismic-Reflection and Multibeam-Bathymetry Data to Investigate the Origin of Seafloor Depressions on the Southeastern Florida Platform	Geophysical Methods
10	Shakira Khan	Characterization of Microkarst Capping Lower Eocene High-Frequency Carbonate Cycles, Southeast Florida	Karst Aquifers/Florida
11	Kuniansky and Bellino	Overview of the Revised Hydrogeologic Framework for the Floridan Aquifer System, Florida and Parts of Alabama, Georgia, and South Carolina	Karst Aquifers/Geologic Framework/Floridan Aquifer
12	Bellino and Fine	Comparability of Groundwater Recharge Estimates From the Soil-Water-Balance Code in the Southeastern United States, 1995–2010	Karst Aquifers/Floridan Aquifer
13	Roger B. Pacheco Castro	Numerical Simulations of Groundwater Flow Exchange in Karst	Karst Modeling
14	Rebecca B. Lambert	Hydrograph Recession Curve Analysis to Identify Flow Regimes in Karst Systems	TX Karst Hydrology/Edwards Aquifer
15	Dianne Pavlicek-Mesa	The Edwards Aquifer Protection Program at the Texas Commission on Environmental Quality	TX Karst Management/Edwards Aquifer
16	Christopher Ray	Surface Water and Groundwater Interactions in the Upper Cibolo Creek Watershed, Kendall County, Texas	TX GW/SW Interactions/Karst
17	John Cooper	An Integrated Outcrop and Subsurface Study of the Austin Chalk Stratigraphy in Bexar County, Texas	TX Austin Chalk/Mapping
18	Marylynn Musgrove	Microbial Indicators and Aerobic Endospores in the Edwards Aquifer, South-Central Texas	TX Edwards Aquifer
19	Alexis Godet	Onset, Development, and Demise of a Rudist Patch Reef in the Albian Glen Rose Formation of Central Texas	TX Glen Rose Formation
20	Alexis Godet	Environmental Reconstruction of an Albian Dinosaurs Track-Bearing Interval in Central Texas	TX Glen Rose Formation
21	Chris Thibidaux	Cave and Karst Resource Management by the Air Force at Camp Bullis, Texas	TX Caves/Management

Karst Science: A National and International Review and Status Report

By George Veni

National Cave and Karst Research Institute, 400-1 Cascades Avenue, Carlsbad, NM 88220

Abstract

When I was a graduate student, my advisor Will White told me about the days when submitting a paper to a journal with the four-letter word "cave" in the title was a near-guarantee of an automatic rejection. "Karst" was another forbidden word, which is why the term "carbonate aquifer" was frequently used in the hydrogeologic literature well into the 1980s. Times have changed, and for the better.

Karst science is flourishing. When I entered graduate school in 1983 there were only a handful of US universities with professors specializing in some aspect of cave or karst science. Now I can count nearly 60. At the same time, I recall only two consulting companies that specialized in karst. Many are now spread across the country. More importantly, cave and karst experts were rare in public service, mostly a token few working at caves in the National Park Service. Now I know of about 40 municipal, regional, state, and federal agencies that employee at least one cave or karst expert and specifically for that expertise.

Three major strides in US karst science late in the last century were:

1. Barry Beck establishing the Multidisciplinary Conference on Sinkholes and the Engineering and Environmental Impacts of Karst in 1984, which brought geologists and engineers together to benefit from each other's experience and make major strides in environmental karst research, protection, and remediation. This conference series, which is growing with the next one scheduled for 2018, was instrumental in starting to legitimize "cave" and "karst" in scientific circles.
2. The Federal Cave Resources Protection Act of 1988, the first legislation to recognize the national importance of caves.
3. The creation of the National Cave and Karst Research Institute (NCKRI) in 1998 to conduct, support, facilitate, and promote cave and karst research, education, management, collection and archiving of data, and collaborations to support all of the above on a national and international level.

While these events stand out in my mind, the cumulative effects of many other events were even more influential in bringing karst into the main stream. Four examples include the establishment of the Field Studies at Mammoth Cave program by Western Kentucky University in 1979; creation of the U.S. Geological Survey's Karst Interest Group in 2000 and its conference series in 2001; the Edwards Aquifer Authority's Distinguished Lecture Series, which since 2006 recruits international experts focused on karst hydrogeology; and the Geological Society of America, which formed a Karst Division in 2014 to recognize karst as a major and important discipline in the geosciences.

These advances are certainly noteworthy and all were a struggle to establish and maintain. NCKRI is a prime example. Following 8 years as a federal institute within the National Park Service, it reorganized as a federal and state-supported nonprofit administered by the New Mexico Institute of Mining and Technology starting in 2006. When I was brought on as NCKRI's Executive Director in 2007 to lead it in its new guise, I had high hopes and looked to increase the level of federal support from the seed-money appropriation received annually since 1998. Instead, the global economy collapsed in

2008, and cuts were made in NCKRI's seed money to help balance state and federal budgets. Nonetheless, NCKRI continued to advance, albeit slowly, and now with the economy in better shape NCKRI is enjoying additional funds through contracts, grants, donations, and other sources, and has high hopes to boost its federal funding over the next few years.

NCKRI's story is a microcosm of recent karst programs in the US and internationally. During the economic recession there was less funding for students, basic research, applied contracting research, and management and education programs. Positions vacated by retiring cave and karst experts in all areas of employment were often not backfilled; some were laid off. But economic recovery is seeing restoration and even growth in all sectors.

Other parts of the world have seen similar advances, falls, and recoveries. Some places like China and Europe, where karst is more prevalent, have had a longer and better appreciation of caves and karst. The world's first national karst institute was created in Romania in 1920. But like the US, cave and karst research did not begin to flourish until the late 20th and early 21st centuries, as exemplified by the creation of the International Union of Speleology (UIS) in 1965 and national institutes in China (1976), Switzerland (2000), Ukraine (2006), and Brazil (2007). Unfortunately, the Ukrainian institute has apparently been closed since the 2014 Russian take-over of Crimea where its headquarters was located.

Within the past 20 years, karst knowledge and study have spread widely into developing countries. The annual international karst training program of China's International Research Center on Karst particularly stands out. Since 2008 it has hosted experts from around the world to teach students and professionals from developing countries that include Brazil, Cambodia, Ethiopia, Indonesia, Iran, Malawi, Malaysia, Mexico, Romania, Serbia, Slovenia, Thailand, and Uganda, among others, and covered all of their expenses to attend. As in the US, these attendees conduct their karst work in many sectors of society.

In the US, groundwater quality remains a vital topic of practical concern. While not ignored, it is less important in other countries where alternative water sources and treatment of poor quality water is already established. In contrast, engineering projects such as tunnels and dams are more common in many non-US countries. One major concern for most karst countries is the proliferation of cover-collapse sinkholes, including those in urban non-karst areas where karst-like features can result from infrastructure failures, such as broken water lines.

The lines between basic and applied research are blurring. Speleothem dating and paleoclimate studies are conducted internationally, no longer for purely academic purposes but to advance models of modern climate in the fight against climate change. China has taken a special interest in the karst carbon cycle to identify carbon sinks.

The US currently leads the way in geomicrobiological cave research, with other important work in this field occurring primarily in Europe. Funding for many of these investigations is often tied to the development of new medicines, materials, and industrial processes. This exciting field has amazing implications for karst science and despite rapid advances, is certainly in its infancy. The US also leads in the field of extraterrestrial cave research, but has close partnerships with researchers primarily in Europe and Japan. With hundreds of apparent cave entrances identified on the Moon and Mars, and karst-like features found on Titan and other planetary bodies in absolutely non-karst environments, the definition of karst may be stretched, at least for beyond-Earth applications, to move away from the solution of bedrock to the physics of mobilizing material for subsurface transport.

As excited as I am by the wonders we will see and learn underground in the coming years, I'm even more excited by the human dimension that will make that possible. I come from the generation where your typical karst scientist began as a caver—where physical exploration of the unknown whetted our appetites to solve all cavernous mysteries. My generation also saw the conflicts between traditional scientists and caver scientists, often with neither side appreciating the perspectives and data of the other.

The modern karst generation is wonderfully integrated. It includes caver scientists and scientists who developed their interest in caves and karst in other diverse ways. I'm thrilled to see the blending of "cave-truthed" information with techniques and perspectives from fields once considered unrelated. With this new foundation being poured into a new mold for karst science, rather than end this status report with a projection of the future, I would prefer to sit back quietly and enjoy the future as it unfolds. But first there may be one more major task for the current generation of karst scientists, managers, educators, and explorers to accomplish.

The UIS has developed a proposal for the United Nations Educational, Scientific and Cultural Organization (UNESCO) to recognize 2021 as the International Year of Caves and Karst. This event will promote the need for proper cave and karst research and management through public education programs and coordination with governmental bodies. At the time of this writing, organizations in over 30 countries have agreed to participate, and at least 5 countries will formally carry this proposal to UNESCO, which will vote on it in October 2017. Assuming UNESCO approves, I encourage you to work with me to support this unprecedented opportunity to make "cave" and "karst" words that are known, appreciated, and properly acted upon around the world.

A Multi-Disciplined Approach to Understanding and Managing Shared Karst Landscapes

By Dale L. Pate

National Park Service, Geologic Resources Division, P.O. Box 25287, Denver, CO 80225-0287

Introduction

The National Park Service (NPS) manages significant karst landscapes that are found in about 50 NPS park units. The term "significant" is used to denote karst landscapes that are the dominant land-forming processes within at least a portion of a park unit. Karst landscapes are important for various reasons, including the large amounts of fresh water they provide. NPS park units, in general, only contain portions of larger karst landscapes. Even large parks, such as Grand Canyon National Park at 1.2 million acres in size, only contain a portion of a much larger karst landscape. In order to effectively manage and protect these landscapes, NPS managers must have a clear understanding of the entire karst system and processes at work within and outside of park boundaries. By understanding entire karst systems, managers can work with adjacent landowners to ensure the long-term viability of the NPS portions of these shared karst landscapes.

Management Needs

For many karst landscapes in the United States, and throughout the world, there is limited knowledge about groundwater basins. This includes basic information such as the bedrock geology, location of the total surface recharge area, where recharge into the ground takes place, the flow paths groundwater takes in the subsurface, and where those waters flow back to the surface as a spring. In many cases, the NPS does not have a basic understanding of how these shared karst landscapes operate or of the ecosystems they may contain. Karst landscapes can be complex with changing groundwater conditions based on low- or high-flow conditions. In high-flow conditions water from one groundwater basin can easily flow into one or more other groundwater basins. Highways, buildings, sewer lines, oil and gas drilling rigs, pipelines, concentrated animal feed operations (CAFOs), and other infrastructure create numerous opportunities for contamination to these valuable resources. The complexity of karst systems allows contamination to appear in unexpected places with often devastating consequences.

A report series–Shared Karst Landscapes–has been initiated within the NPS Geologic Resources Division (GRD) to address these basic information needs for park units that contain significant karst landscapes. In order to provide a park manager a more holistic understanding of entire karst systems, the goals of these reports are to (1) provide an overview of available scientific information, (2) identify essential missing information, (3) recommend future research, (4) identify current and (or) potential vulnerabilities from anthropogenic activities within and adjacent to the park unit, and (5) provide documentation for planning efforts for the long-term protection and viability of significant karst landscapes. The first report in this series addresses the shared karst landscape found within Cedar Breaks National Monument and Dixie National Forest in southwestern Utah. For park units that contain karst landscapes, the major landowners adjacent to NPS properties tend to be the U.S. Forest Service, the Bureau of Land Management, other state and local agencies, and some private landowners.

Shared Karst Landscape Studies at Mammoth Cave

Mammoth Cave National Park in Kentucky is a prime example of the NPS successfully managing a portion of a much larger karst landscape based on extensive groundwater studies and ecosystem dynamics. Mammoth Cave was created as a national park in 1941 when little was known of the geology, hydrology, biology, or the extent of the cave. Even less was known of the karst landscape and its many complexities that reached far beyond park boundaries. From the 1940s to the present, members of the National Speleological Society (NSS) and the Cave Research Foundation (CRF) were attracted to the vast cave systems found in the area. Explorations and cave surveys completed by these organizations linked the adjacent Flint Ridge Cave System to Mammoth Cave in 1971 to form the longest known cave in the world at just over 232 kilometers (144 miles). Since then, these surveys have increased the known length of Mammoth Cave to over 652 kilometers (405 miles) and the cave still remains the longest known in the world. These explorations along with studies from other university scientists and students, a number of private, state, and federal agencies, and the efforts of NPS research geologist Dr. James Quinlan, began documentation of the groundwater basin complexities found within this immense karst landscape that included Mammoth Cave (Alexander, 1993).

Dr. Quinlan's work along with numerous other scientists and cavers used the results of more than 400 dye traces to delineate 27 groundwater basins within a huge area south of the Green River. This work showed conclusively that water within groundwater basins originating outside Mammoth Cave National Park boundaries flows directly into the park through various passages within Mammoth Cave. It also showed major contamination issues for Mammoth Cave from the towns of Horse Cave and Park City, Kentucky, and nearby rural areas (Alexander, 1993). Scientific studies have continued to help augment this initial work. The overall basic scientific information gained from this research has provided the park with the ability to better manage its karst resources and has set an example of what is needed for the many other significant karst landscapes managed within the NPS.

Conclusions

There has been some work done in other NPS park units with significant karst landscapes to proactively understand groundwater dynamics, potential contamination issues, and associated cave and karst ecosystems. Several studies have occurred only after actual or potential contamination issues were identified. These include potential lead mining in Mark Twain National Forest that threaten some of the largest springs in the country within Ozark National Scenic Riverways in Missouri, and a large hog CAFO on private property within a major karst landscape that includes portions of Buffalo National River. Because of the extensive karstification of the area, this CAFO potentially threatens the integrity of Buffalo National River. At the present time, both the north and south rims of Grand Canyon National Park get all their water from a cave spring located deep within the canyon below the north rim. The park has recently initiated a series of studies to understand the dynamics of karst groundwater basins in the park in anticipation of a complete replacement of their public water system.

Within the NPS, much work remains for even a basic understanding of karst landscapes. The benefits of the GRD Shared Karst Landscapes report series is to help park managers quickly ascertain what information is available and what information is needed to help them better understand these vital resources. With better understanding and thorough planning efforts, park managers will have the ability to work intelligently with adjacent land managing agencies and other neighbors to provide long-term preservation for these important resources.

Selected References

Alexander, E.C., 1993, The evolving relationship between Mammoth Cave National Park and its hydrogeologic symbionts, *in* Foster, D.L., and others, eds., 1991 National Cave Management Symposium Proceedings, Bowling Green, Kentucky, October 23–26, 1991: American Cave Conservation Association, Inc., p. 11–56.

Pate, D.L., 2008, Overview of National Park Service policies for cave and karst management, *in* Kuniansky, E.L., U.S. Geological Survey Karst Interest Group Proceedings, Bowling Green, Kentucky, May 27–29, 2008: U.S. Geological Survey Scientific Investigations Report 2008-5023, p. 8–11.

Methodology for Calculating Probability, Protection, and Precipitation Factors of the P3 Method for Karst Aquifer Vulnerability

By Timothy P. Sullivan and Yongli Gao

Department of Geological Sciences, Center for Water Research, University of Texas at San Antonio, One UTSA Circle, San Antonio, TX 78249

Abstract

Vulnerability maps are valuable tools used by water resource managers to protect aquifers from contamination. However, in karst aquifers the development of vulnerability maps is subject to explorational bias due to the impracticality of identifying all karst features within watersheds. The P3 method (Probability, Protection, and Precipitation) minimizes this explorational bias by using the probability of encountering karst features in addition to the location of known karst features to assign a probability score. The protection factor accounts for the soil and bedrock layers overlying the aquifer of interest while the precipitation factor accounts for how precipitation affects the infiltration of contaminants. The methodologies for calculating the probability, protection, and precipitation factors for the Edwards aquifer in the Cibolo and Dry Comal Creek basins in south-central Texas are presented in detail to assist in the development of vulnerability maps using the P3 method in other regions. Similarly, a discussion on appropriate methods for validating the resulting vulnerability maps is included to ensure the P3 method has been appropriately applied.

Introduction

There are several methodologies for assessing the intrinsic vulnerability of karst aquifers such as the COP (Vías and others, 2006) and PI (Goldscheider and others, 2000) methods. Both COP and PI consider the protection provided by layers overlying the aquifer (the O-factor in COP and P-factor in PI) and the reduction in protection due to infiltration conditions (the C-factor in COP and I-factor in PI) (Zwahlen, 2004). However, the C-factor in the COP method and I-factor in the PI method suffer from explorational bias in that their results are heavily dependent on knowing the location of all karst features. As an alternative, the P3 method (Probability, Protection, and Precipitation) minimizes explorational bias by using the probability of encountering karst features in addition to the location of known karst features. This methodology allows researchers to assess the vulnerability of karst aquifers by conducting thorough investigations of smaller areas and applying the results to larger study areas. The P3 method was first used to assess the vulnerability of the Edwards aquifer in the Cibolo and Dry Comal Creek basins in south-central Texas, USA (fig. 1) (Sullivan and Gao, 2017). The methodologies for calculating the three factors used in the P3 method are presented here to assist researchers wishing to apply the method to other aquifers.

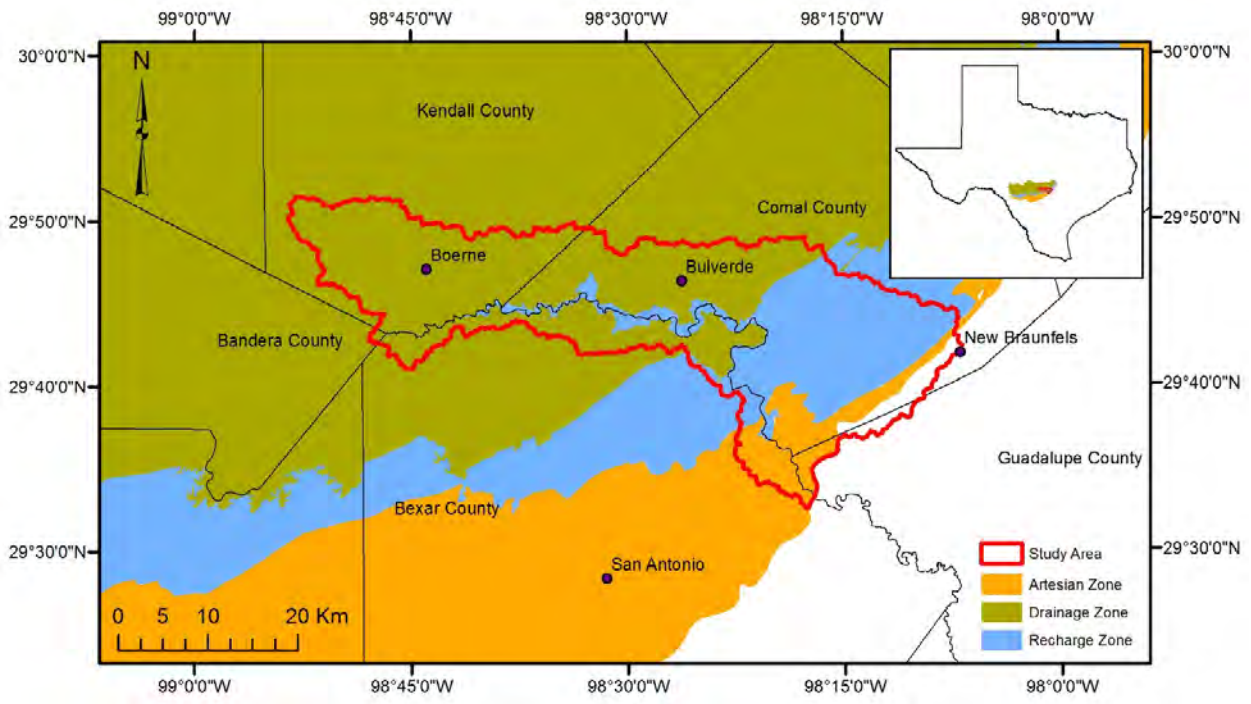

Figure 1. Study area (aquifer zones from Edwards Aquifer Authority, 2004).

Materials and Methods

Probability Factor

The probability factor assigns vulnerability values to areas within map units based on the probability of it containing a karst feature (for example, cave, sinkhole, spring). Based on prior studies, the factors used to assess probability within the study area were distance to streams, distance to faults, lithology, and Distance to Nearest Neighbor (DNN) (Veni, 2003; Hovorka and others, 2004; Lindgren and others, 2004; Gao and Alexander, 2008; Shah and others, 2008; Doctor and Doctor, 2012; Ramanathan and others, 2015). In other locations, additional factors such as distance to ponds, quarries, and sinkholes were used to assess karst feature probability (Doctor and Doctor, 2012). When applying the P3 method to other aquifers, researchers should evaluate the factors likely to influence karst feature probability to determine which to use in their analysis.

The primary data used to calculate the probability factor are the locations of karst features, based on the premise that karst development indicates preferential flow paths for aquifer recharge. The Texas Speleological Survey (TSS) provided GIS data specifying the locations of 2,275 known karst features in Bexar, Comal, and Kendall Counties (TSS, 2016). The locations of an additional 1,124 karst features were taken from detailed karst investigations at the Camp Bullis (Texas) Training Site (Zara Environmental and George Veni and Associates, 2009).

Two initial screenings were conducted to assign probability factor scores. First, areas within 10 meters of a stream and (or) 500 meters of a karst feature were assigned a probability factor score of 0, indicating a very high probability of contaminants infiltrating the aquifer. In this study, probability scores ranged from 0, very high, to 0.9, very low. Second, lithologies within the Edwards aquifer artesian zone and the Fort Terrett Formation were assigned probability factor scores of 0.7, indicating low probability. The lithologies within the artesian zone were assigned low probability scores because the confining

conditions lower the probability of contaminants infiltrating the aquifer in this region. The Fort Terrett Formation was assigned a low probability because only nine karst features were documented in this lithology in the study area counties.

Areas not assigned a probability factor score during the initial screening were analyzed based on distance from streams, distance from faults, and DNN. At the end of the analysis, the lowest of the three probability scores, which equates to the highest vulnerability, was assigned. For example, a region earning a probability score of 0.7 based on distance from a stream and a probability score of 0.1 based on DNN would be assigned a probability score of 0.1.

Distance from streams and faults were both analyzed using the following procedure:

1. Karst point features were created for each lithology (table 1). For lithologies present within the Camp Bullis Training Site, only the Camp Bullis data were used in the analysis because the area was subject to documented, thorough karst investigations. The Person Formation is not present within the Camp Bullis Training Site, so TSS data were used for its analysis.
2. Distance from each karst feature to its nearest stream/fault was calculated by using the NEAR tool in ArcGIS 10.2.2 (all mentions of tools within the manuscript refer to ArcGIS 10.2.2 tools).
3. The distribution type was determined by comparing the actual Cumulative Distribution Function (CDF) against the expected CDF for normal and log-normal distributions.

During this analysis, distance from faults and distance from streams were both found to have normal distributions. Probability factor scores were then assigned to areas based on standard deviation (σ) intervals from the mean distance ($\bar{x}$) (table 2).

Table 1. Predominant lithologies present in the study area.

Map label	Lithology
Kau	Austin Chalk
Kbu	Buda Limestone
Kdr	Del Rio Clay
Kef	Eagle Ford Group
Kft	Fort Terrett Formation
Kgrl	Lower Glen Rose
Kgru	Upper Glen Rose
Kgt	Georgetown Formation
Kk	Kainer Formation
Kp	Person Formation
Kw	Washita Group
Q	Quaternary deposits

Table 2. Assigned probability factor scores[1].
[m, meters; DNN, Distance to Nearest Neighbor; N/A, not applicable]

Initial screening		Additional analysis		
Distance from stream (m)	Distance from karst feature (m)	Distance from stream/fault (m)	DNN (m)	Score
≤10	≤500	N/A	N/A	0 (very high)
		$< \bar{x} + \sigma$	$< \bar{x} + \sigma$	0.1 (very high)
		$< \bar{x} + 2\sigma$	$< \bar{x} + 2\sigma$	0.5 (moderate)
		$< \bar{x} + 3\sigma$	$< \bar{x} + 3\sigma$	0.7 (low)
		$\geq \bar{x} + 3\sigma$	$\geq \bar{x} + 3\sigma$	0.9 (very low)

[1]Areas not assigned a probability factor score of 0 during initial screening were subject to additional analysis. The lowest of the three probability scores, which equates to the highest vulnerability, was assigned.

The DNN was assessed based on the results of Nearest Neighbor Analysis (NNA) (Clark and Evans, 1954), which is used to measure how a population deviates from a random distribution. The key parameters are the Clark-Evans index (*R*), which measures a distribution's deviation from randomness and the standard variate of the normal curve (*c*), which measures whether a distribution is clustered, random, or dispersed. NNA was conducted using the following procedure:

1. The analysis was again restricted to Camp Bullis Training Site data with the exception of the Person Formation.
2. In order to minimize edge effects, karst features closer to the lithological boundary than their nearest neighbor were not used in the analysis. After eliminating these karst features, only the following map units had enough remaining karst features to conduct NNA: Krgl, Kgru, Kk, and Kp (see table 1).
3. The POINT DISTANCE tool was used to identify the DNN for each karst feature.
4. The AVERAGE NEAREST NEIGHBOR tool was used to calculate nearest neighbor statistics.
5. The distribution type was determined by comparing the actual CDF against the expected CDF for normal and log-normal distributions.

In this case, the DNN were found to fit a log-normal distribution so the mean distance and standard deviation of the log-transformed data were used to assign probability factor scores using table 2. Additionally, the use of NNA for sinkholes is most appropriate for *R* values below 0.55 (Galve and others, 2009). Within the study area, all *R* values were below 0.55 (table 3) except for the Kainer Formation (Kk). However, the negative *c* value for the Kainer Formation demonstrates strong clustering, indicating the use of NNA is appropriate.

Table 3. Nearest neighbor statistics by lithology.

Map unit	*c*	*R*
Kgrl	-16.5	0.22
Kgru	-28.0	0.19
Kk	-11.7	0.57
Kp	-25.0	0.16

Protection Factor

The protection factor measures the degree of protection afforded by soil and lithological layers overlying the aquifer under study. The protection factor is identical to the O-factor in the COP method, but calculating the soil protection factor (O_S) and lithological protection factor (O_L) bear some description. The O_S is assigned using the soil descriptions and depth to bedrock from the Soil SURvey GeOgraphic (SSURGO) database (Natural Resources Conservation Service, 2013) and the criteria in table 4.

Table 4. Soil protection factor (O_s)[1] (from Vías and others, 2006).

Thickness (meters)	>30% Clay	>70% Silt	Sand >70% and Clay ≤15%	Loam (all others)
>1.0	5	4	2	3
0.5–1	4	3	1	2
<0.5	3	2	0	1

[1]O_s is 0 when no soil is present.

The criteria for assigning the O_L factor are from Vías and others (2006). The O_L factor was calculated separately for the Edwards aquifer drainage, recharge, and artesian zones (fig. 1). Within the drainage zone, the study area is underlain by the Trinity aquifer whose top elevation was taken as the interface between the upper and lower members of the Glen Rose Formation (map units Kgru and Kgrl, respectively). Within the recharge zone and artesian zones, the study area is underlain by the Edwards aquifer and the aquifer top elevation was set equal to the values used for the Edwards aquifer Groundwater Availability Model (GAM) (Lindgren and others, 2004). Within each area, the geologic map database of Texas (Stoeser and others, 2005) was used to determine the uppermost member.

The thickness of each member (excluding alluvial deposits described below) was determined in ArcGIS by using the following procedure iteratively until the aquifer top was reached:

1. Convert watershed Digital Elevation Model (DEM) to a point feature using RASTER TO POINT.
2. Select point features along the interface of the lithological layer and layer immediately beneath it.
3. Convert points selected in step 2 to a DEM using TOPO TO RASTER. This creates a raster representing the elevation of the interface between the two lithologies.
4. Determine thickness using RASTER CALCULATOR to subtract the DEM created in step 3 from the watershed DEM during the first iteration. During subsequent iterations, the thicknesses of all overlying lithologies must also be subtracted from the watershed DEM:

$$T_{n-1} = \text{DEM} - T_1 - T_2 \ldots - T_n, \quad (1)$$

where T_{n-1} is the thickness of the lithology being calculated

T_n is the thickness of overlying lithologies

DEM is the elevation value from the surface for the watershed being studied.

The above procedure was modified to identify the elevation of the Kgru-Kgrl interface in the eastern portion of the drainage area. Because the interface is not exposed in that area, the raster created in step 3 did not extend to the

eastern portion of the drainage area. This was overcome by assigning the reported average thickness to Kgru in the eastern portion of the drainage area. The resulting estimated interface points were used in step 3 above to create a raster representing the elevation of the Kgru-Kgrl interface.

The thicknesses of alluvial deposits required a different procedure because they occupy areas removed by erosional processes rather than forming a lithological interface. For these areas, the following procedure was used:

1. Create DEM of riverbed with EXTRACT BY MASK from the watershed DEM with the river polyline as the mask.
2. Convert riverbed DEM to point feature using RASTER TO POINT.
3. Convert point feature to DEM using TOPO TO RASTER. This creates a DEM extending the plane of the riverbed elevation underneath the alluvial deposits.
4. Depending on the meander of the river, the riverbed DEM may not extend fully beneath the alluvial deposits. This can be overcome by using FOCAL STATISTICS and selecting the "Ignore NoData in calculations" option. When this option is selected, NoData values (i.e., gaps in the riverbed DEM) will be assigned values by the FOCAL STATISTICS tool. By selecting the MEAN option for statistics type, FOCAL STATISTICS will assign NoData cells values equal to the average values of surrounding cells from the riverbed DEM.
5. Merge DEMs from steps 3 and 4 with RASTER CALCULATOR and the following expression: CON(ISNULL(DEM_step3.tif), DEM_step4.tif, DEM_step3.tif). In the preceding expression DEM_step3.tif and DEM_step4.tif are the DEMs created in steps 3 and 4, respectively.
6. Determine thickness with RASTER CALCULATOR by subtracting DEM created in step 5 from watershed DEM.

This procedure assumes the streambed is free of alluvial deposits and that the stream has not incised the bedrock below the interface between the alluvial deposits and bedrock. The stream network in much of the study area consists of bedrock, making these assumptions appropriate. In areas where these assumptions do not hold, the resulting error will likely be small because the probability factor discussed below assigns areas within 10 meters of streams a probability factor of 0, indicating very high vulnerability.

The resulting lithological thicknesses were then used to calculate the layer index for each region within the study area using equation 2 (from Vías and others, 2006).

$$\text{Layer index} = (\sum(ly)(m))cn, \qquad (2)$$

where ly lithology and fracturation value (see Vías and others, 2006 for values)
m thickness of each layer
cn confined conditions (1 for non-confined; 1.5 for semi-confined; 2 for confined)

The value of O_L was assigned based on the layer index values in table 5. O_L and O_S were then summed to assign the protection factor value.

Table 5. Overlying layer protection factor (O_L) (from Vías and others, 2006).

Layer index	Value
0–250	1
>250–1,000	2
>1,000–2,500	3
>2,500–10,000	4
>10,000	5

Precipitation Factor

The precipitation factor accounts for the impact of typical annual precipitation values as well as the number of intense rainfall events. The factor considers that vulnerability increases with precipitation until dilution of contamination becomes more important than increasing recharge. The effective infiltration curve of Civita and De Maio (2004) was used to define the value intervals for the precipitation quantity sub-factor (P_Q) shown in table 6. The intervals were developed to correspond to precipitation index ratings on the infiltration curve below 6, between 6 and 9, and above 9. There are two recharge estimates for the study area. Ockerman (2007) estimated the recharge rate for the Upper Cibolo Creek basin to be 15 percent whereas the SWAT model developed by Sullivan and Gao (2016) estimated recharge for the entire study area to be 14 percent (Note SWAT model recharge estimate not published in Sullivan and Gao, 2016). The effective infiltration rate for the study area was determined by multiplying the average annual rainfall by 1.15 to account for wet years, then by the recharge rate of 15 percent. For other study areas, the ranges in table 6 must be adjusted based on the corresponding estimated recharge rate. The precipitation intensity sub-factor (P_I) is assigned by first calculating the precipitation intensity, which equals the average annual precipitation (mm yr^{-1}) divided by the number of rainy days. The P_I sub-factor is then assigned using the ranges in table 6. The final precipitation factor is the sum of the P_Q and P_I sub-factors.

Vulnerability Map Development

Vulnerability maps for the P3 method were generated by multiplying the probability, protection, and precipitation values together to obtain a vulnerability score. The resulting scores are rated from very low to very high vulnerability using the criteria in table 7.

Table 6. Precipitation quantity (P_Q) and precipitation intensity (P_I) sub-factor values (P_I values from Vías and others, 2006).
[mm, millimeters; mm d^{-1}, millimeters per day]

Annual precipitation (mm)	P_Q value	Precipitation intensity (mm d^{-1})	P_I value
0–800	0.4	≤10	0.6
>800–1,350	0.3	10–20	0.4
>1,350–1,800	0.2	>20	0.2
>1,800–2,300	0.3		
>2,300	0.4		

Table 7. P3 method vulnerability classification (from Vías and others, 2006).

P3 value	Vulnerability score
0–0.5	Very high
≥0.5–1	High
≥1–2	Moderate
≥2–4	Low
≥4 – 15	Very low

Validation

Assessing the validity of vulnerability maps requires using such tools as spring hydrograph analyses and tracer tests (Zwahlen, 2004). Unlike validation of numerical models, validation of vulnerability maps is a qualitative comparison of the vulnerability map with the expected vulnerability. Spring hydrographs demonstrate how rapidly the aquifer responds to

rainfall, thereby giving an assessment of how quickly contaminants can enter the aquifer. Recharge areas for rapid response springs are associated with very high aquifer vulnerability. Similarly, tracer tests provide an estimated travel time from source input to output as well as indications of contaminant attenuation time along the flow path from source input to output. In this case, tracer velocities of 43 meters/hour are associated with areas of very high aquifer vulnerability (Vías and others, 2010). In addition to these methods, nitrate sample results were also used in the validation process. Once nitrate enters the Edwards aquifer, it is expected to be diluted until it reaches the typical nitrate level for the aquifer of 1.85 milligrams per liter as N (mg-N L^{-1}) (Musgrove and others, 2010). The Edwards Aquifer Authority (EAA) defines nitrate levels above 5 mg-N L^{-1} as elevated (Tremallo and others, 2015). Based on these factors, portions of the aquifer where nitrate concentrations exceeded 5 mg-N L^{-1} were considered areas of very high or high vulnerability. This methodology was used to qualitatively assess accuracy of the P3 vulnerability map.

Conversely, if the P3 vulnerability map does not accurately identify areas of expected very high or high vulnerability there is likely an error in the vulnerability map. This would most likely be caused by karst feature data gaps, because although the P3 method seeks to minimize explorational bias, it does not eliminate it. Were this to occur, additional field studies of the affected areas would be warranted to identify additional karst features and adjust the P3 vulnerability map accordingly.

Summary

The protection of karst aquifers from contamination is of vital importance because they make up a large portion of available worldwide groundwater resources. A key method for aquifer managers to protect karst aquifers is through the development of vulnerability maps. While several methods exist, they suffer from explorational bias because they rely heavily on knowledge of specific locations of karst features. The P3 method was developed to minimize explorational bias by producing vulnerability maps that rely on the probability of encountering karst features as well as the locations of known karst features. The P3 method was first used and successfully validated in the Cibolo and Dry Comal Creek watersheds of south-central Texas, USA. The methodologies for calculating the probability, protection, and precipitation factors were presented as well as how to validate the resulting vulnerability map to allow researchers to utilize the P3 method to assess aquifer vulnerability in other karst regions.

Acknowledgments

The authors would like to thank Mr. David Weary and Dr. Daniel Doctor of the U.S. Geological Survey for their thoughtful reviews of this manuscript. The authors would also like to thank the Texas Speleological Survey for providing access to their database and to Dr. George Veni for his insights on the Edwards aquifer. Mr. Sullivan would like to personally thank Dr. Dutton, Dr. Giacomoni, Dr. Montoya, and Dr. Sharif for their assistance as members of his doctoral committee. This work was supported in part by the Office of Research Support of the University of Texas at San Antonio, the Cibolo Preserve Trustee, and the National Natural Science Foundation of China, grant 41428202.

References Cited

Civita, M., and DeMaio, M., 2004, Assessing and mapping groundwater vulnerability to contamination—The Italian "combined" approach: Geofísica Internacional, v. 43, no. 4, p. 513–532.

Clark, P.J., and Evans, F.C., 1954, Distance to nearest neighbor as a measure of spatial relationships in populations: Ecology, v. 35, no. 4, p. 445–453, accessed February 9, 2016, at http://doi.org/10.2307/1931034.

Doctor, D.H., and Doctor, K.Z., 2012, Spatial analysis of geologic and hydrologic features relating to sinkhole occurrence in Jefferson County, West Virginia: Carbonates and Evaporites, v. 27, no. 2, p. 143–152, accessed May 3, 2016, at http://doi.org/10.1007/s13146-012-0098-1.

Edwards Aquifer Authority, 2004, Zone (shapefile): San Antonio, TX, Edwards Aquifer Authority, accessed August 4, 2013, at http://www.edwardsaquifer.org/scientific-research-and-data/aquifer-data-and-maps/maps/shapefiles.

Galve, J.P., Gutiérrez, F., Remondo, J., Bonachea, J., Lucha, P., and Cendrero, A., 2009, Evaluating and comparing methods of sinkhole susceptibility mapping in the Ebro Valley evaporite karst (NE Spain): Geomorphology, v. 111, no. 3–4, p. 160–172, accessed May 30, 2016, at http://dx.doi.org/10.1016/j.geomorph.2009.04.017 .

Gao, Y., and Alexander, E.C., 2008, Sinkhole hazard assessment in Minnesota using a decision tree model: Environmental Geology, v. 54, no. 5, p. 945–956, accessed May 30, 2016, at http://doi.org/10.1007/s00254-007-0897-1.

Goldscheider, N., Klute, M., Sturm, S., and Hötzl, H., 2000, The PI method—A GIS-based approach to mapping groundwater vulnerability with special consideration of karst aquifers: Zeitschrift für angewandte Geologie, v. 46, no. 3, p. 157–166.

Hovorka, S., Phu, T., Nicot, J.P., and Lindley, A., 2004, Refining the conceptual model for flow in the Edwards aquifer—Characterizing the role of fractures and conduits in the Balcones Fault Zone segment: Austin, TX, Bureau of Economic Geology, 58 p., accessed March 27, 2014, at http://www.edwardsaquifer.org/documents/2004_Hovorka-etal_RefiningConceptualModel.pdf.

Lindgren, R.J., Dutton, A.R., Hovorka, S., Worthington, S.R.H., and Painter, S., 2004, Conceptualization and simulation of the Edwards aquifer, San Antonio region, Texas: U.S. Geological Survey Scientific Investigations Report 2004-5277, 154 p., accessed November 23, 2013, at https://pubs.er.usgs.gov/publication/sir20045277.

Musgrove, M., Fahlquist, L., Houston, N.A., Lindgren, R.J., and Ging, P.B., 2010, Geochemical evolution processes and water-quality observations based on results of the National Water-Quality Assessment Program in the San Antonio segment of the Edwards aquifer, 1996–2006: U.S. Geological Survey Scientific Investigations Report 2010–5129, 93 p., accessed December 8, 2015, at https://pubs.er.usgs.gov/publication/sir20105129.

Natural Resources Conservation Service, 2013, Soil Survey Geographic (SSURGO) database: Fort Worth, TX, U.S. Department of Agriculture, accessed April 13, 2016, at http://websoilsurvey.nrcs.usda.gov.

Ockerman, D.J., 2007, Simulation of streamflow and estimation of ground-water recharge in the upper Cibolo Creek watershed, south-central Texas, 1992–2004: U.S. Geological Survey Scientific Investigations Report 2007–5202, 35 p., accessed January 23, 2015, at https://pubs.er.usgs.gov/publication/sir20075202.

Ramanathan, R., Gao, Y., Demirkan, M.M., Hatipoglu, B., Adib, M., Rosenmeier, M., Gutierrez, J., and El Ganainy, H., 2015, Evaluation of cavity distribution using point-pattern analysis, *in* Doctor, D.H., Land, Lewis, and Stephenson, J.B., eds., 14th Multidisciplinary Conference on Sinkholes and the Engineering and Environmental Impacts of Karst: Rochester, MN, The National Cave and Karst Research Institute (NCKRI), p. 289–298, accessed January 17, 2016, at http://dx.doi.org/10.5038/9780991000951.

Shah, S.D., Smith, B.D., Clark, A.K., and Payne, J.D., 2008, An integrated hydrogeologic and geophysical investigation to characterize the hydrostratigraphy of the Edwards aquifer in an area of northeastern Bexar County, Texas: U.S. Geological Survey Scientific Investigations Report 2008-5181, accessed April 25, 2016, at https://pubs.er.usgs.gov/publication/sir20085181.

Stoeser, D.B., Shock, N., Green, G.N., Dumonceaux, G.M., and Heran, W.D., 2005, Geologic database of Texas: U.S. Geological Survey Data Series 170, scale 1:24,000, accessed April 30, 2016, at https://pubs.usgs.gov/ds/2005/170/.

Sullivan, T.P., and Gao, Y., 2016, Assessment of nitrogen inputs and yields in the Cibolo and Dry Comal Creek watersheds using the SWAT model, Texas, USA 1996–2010: Environmental Earth Sciences, v. 75, no. 9, p. 1–20, accessed April 26, 2016, at http://doi.org/10.1007/s12665-016-5546-0.

Sullivan, T.P., and Gao, Y., 2017, Development of a new P3 (Probability, Protection, and Precipitation) method for vulnerability, hazard, and risk intensity index assessments in karst watersheds: Journal of Hydrology, v. 549, p. 428–451, accessed April 14, 2017, at http://doi.org/10.1016/j.jhydrol.2017.04.007.

Texas Speleological Survey, 2016, Karst feature database (shapefile), Austin, TX: Texas Speleological Survey.

Tremallo, R.L., Johnson, S., Hamilton, J.M., Winterle, J., Eason, S., and Hernandez, J.C., 2015, Edwards Aquifer Authority hydrologic data report for 2014: San Antonio, TX, Edwards Aquifer Authority, 86 p., accessed October 24, 2016, at http://www.edwardsaquifer.org/documents/2015_Tremallo%20(et%20al)_HydroReport2014.pdf.

Veni, G., 2003, GIS applications in managing karst groundwater and biological resources: Ninth Multidisciplinary Conference on Sinkholes and the Engineering and Environmental Impacts of Karst: Huntsville, AL, American Society of Civil Engineers, p. 466–476, accessed January 30, 2016, at http://doi.org/10.1061/40698(2003)42.

Vías, J.M., Andreo, B., Perles, M.J., Carrasco, F., Vadillo, I., and Jiménez, P., 2006, Proposed method for groundwater vulnerability mapping in carbonate (karstic) aquifers—The COP method, Application in two pilot sites in southern Spain: Hydrogeology Journal, v. 14, no. 6, p. 912–925, accessed January 30, 2016, at http://doi.org/10.1007/s10040-006-0023-6.

Vías, J.M., Andreo, B., Ravbar, N., and Hötzl, H., 2010, Mapping the vulnerability of groundwater to the contamination of four carbonate aquifers in Europe: Journal of Environmental Management, v. 91, no. 7, p. 1500–1510, accessed January 30, 2016, at http://dx.doi.org/10.1016/j.jenvman.2010.02.025.

Zara Environmental and George Veni and Associates, 2009, Hydrogeological, biological, archaeological, and paleontological karst investigations, Camp Bullis, Texas, 1993–2009, 2,775 p.

Zwahlen, F., 2004, COST Action 620—Vulnerability and risk mapping for the protection of carbonate (karst) aquifers: Luxembourg, Office for Official Publications of the European Communities, 320 p., accessed November 21, 2015, at http://bookshop.europa.eu/is-bin/INTERSHOP.enfinity/WFS/EU-Bookshop-Site/en_GB/-/EUR/ViewPublication-Start?PublicationKey=KINA20912.

Methodology for Calculating Karst Watershed Nitrogen Inputs and Developing a SWAT Model

By Timothy P. Sullivan and Yongli Gao

Department of Geological Sciences, Center for Water Research, University of Texas at San Antonio, One UTSA Circle, San Antonio, TX 78249

Abstract

Nitrate contamination of drinking-water sources is a worldwide concern due to the negative health effects associated with consumption of water containing elevated levels of nitrate. Estimating the amount of nitrate entering an aquifer is complicated by the numerous nitrogen sources and transformation processes involved. Sullivan and Gao (2016) utilized the Soil & Water Assessment Tool (SWAT) to model these transformation and transport processes in support of ongoing efforts to model nitrate fate and transport within a karst aquifer. The SWAT model includes sources of atmospheric deposition, fertilizer, manure, a wastewater treatment plant, and on-site sewage facilities (OSSFs). The methodologies used to calculate nitrogen inputs and specific techniques used in developing the SWAT model are described herein. This discussion provides modelers with practical advice on data sources and methods as well as pitfalls to avoid when estimating karst watershed nitrogen inputs.

Introduction

The protection of karst aquifers from contamination is of vital importance because they are vulnerable to contamination entering through karst features. Nitrate is a concern because it is associated with methemoglobinemia, or blue-baby syndrome, in which blood loses its oxygen-carrying capacity (Agency for Toxic Substances and Disease Registry, 2015). One method to assess the potential impact of nitrate contamination is to model nitrogen fate and transport on the surface to determine how much nitrogen will be converted to nitrate and transported into the karst aquifer. Sullivan and Gao (2016) estimated nitrate yield in the Cibolo and Dry Comal Creek watersheds in Texas, which overlie the Edwards aquifer (fig. 1), using the Soil & Water Assessment Tool (SWAT) (http://swat.tamu.edu). This effort was complicated by the numerous data sources required to assess nitrogen inputs and the complexity of the SWAT model. The methodology for calculating nitrogen inputs and developing the SWAT model are provided here to document the procedures used and to assist other modelers.

Nitrogen Inputs

Atmospheric Deposition

Wet Deposition

Wet deposition of nitrate and ammonium is measured on a national scale by the National Atmospheric Deposition Program (NADP (NRSP-3), 2015). The data for individual stations are available as total deposition for the winter, spring, summer, and fall seasons. These data were converted to monthly averages using the following procedure:

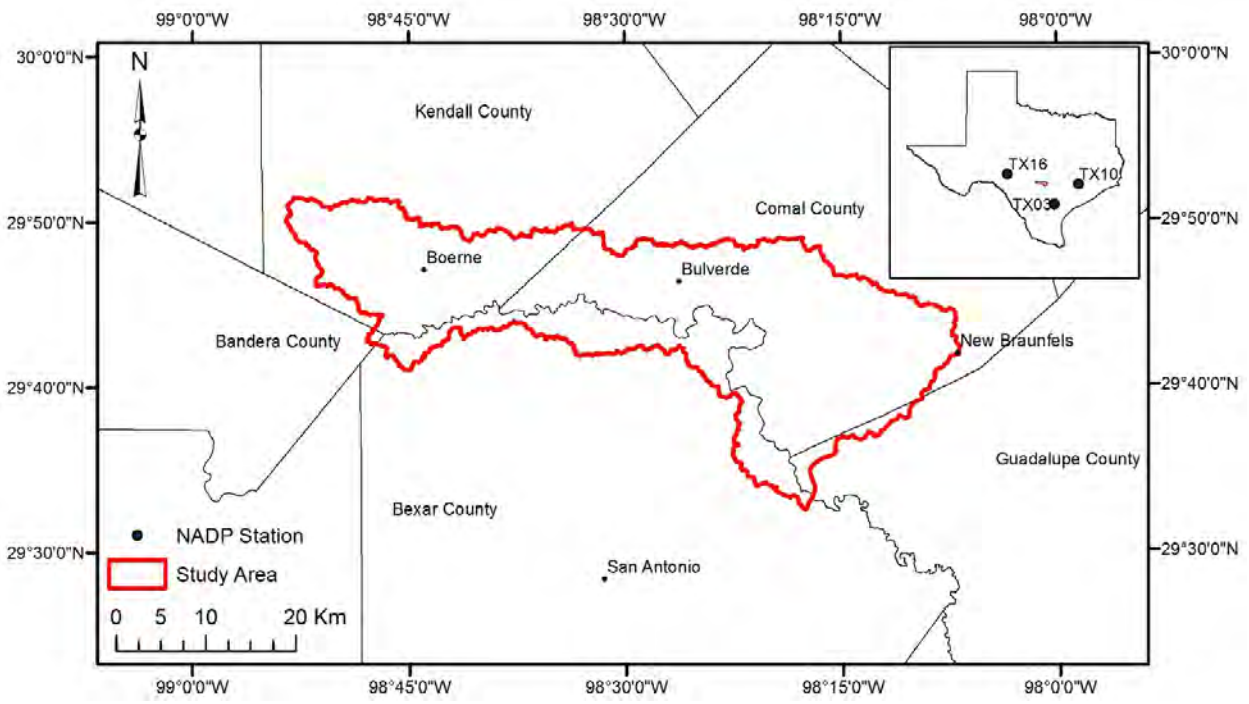

Figure 1. Study area with National Atmospheric Deposition Program (NADP) monitoring site.

1. **Calculate study area annual deposition rate.** The study area annual deposition rate was determined by clipping the national-scale atmospheric wet deposition annual map (2338.383-m resolution) by the study area boundary in ArcGIS 10.2.2. The geometric mean of the resulting raster was multiplied by the area of the study area to determine the annual atmospheric wet deposition of nitrogen.
2. **Calculate weighting factors for monitoring stations to support dividing annual deposition rate into monthly values.** The three closest wet deposition monitoring stations (fig. 1) were given weighting factors based on their distances from the geometric center of the study area:

$$WF_x = \left(1 - \frac{\text{Distance of station } x \text{ from center}}{\sum_{i=1}^{3} \text{Distance of station } i \text{ from center}}\right)/2, \quad (1)$$

where WF_x is the weighting factor for station x

3. **Calculate monthly deposition rates for each monitoring station.** For each season and each monitoring station, the seasonal deposition rates were evenly divided among the season's 3 months.
4. **Calculate distance weighted monthly deposition for study area.** For each month, the corresponding monthly values for the three monitoring stations were multiplied by their weighting factors and the results were summed for each month.
5. **Calculate percent of annual deposition that occurs in each month.** The January through December values calculated in step 4 were summed to determine the annual weighted deposition. The monthly weighted deposition values were then divided by the annual weighted deposition to determine the percentage of annual deposition for each month.

6. **Calculate monthly deposition rates for study area.** The monthly deposition percentages were multiplied by the annual totals calculated in step 1 to determine the nitrogen deposition for each month in kilograms of nitrogen (kg-N). The annual weighted deposition calculated in step 5 is not used in this step because it only uses three monitoring stations and is therefore, less accurate than the value calculated in step 1.

Dry Deposition

Dry deposition is estimated through the Clean Air Status and Trends NETwork (CASTNET), where the calculated weekly flux values for nitric acid, nitrate, and ammonium are used to determine annual aggregate dry deposition values for each constituent (U.S. Environmental Protection Agency [U.S. EPA], 2013). Unlike for NADP, annual national deposition maps are not available from CASTNET. This was overcome by evaluating annual data (U.S. EPA Clean Air Markets Division, 2015) for 12 sites within Texas and surrounding States. The KRIGING tool in ArcGIS was used to interpolate dry deposition rates between the monitoring points. In cases where annual data were missing, the long-term average deposition for that site was used. The mean value of the resulting rasters was then taken from the raster statistics in ArcGIS and multiplied by the land area to calculate the estimated dry deposition within the study area. The annual dry deposition rates were converted to monthly deposition rates by using CASTNET's weekly dry deposition estimates for the three closest monitoring locations to the study area. The methodology used to determine monthly dry deposition rates was identical to that described for wet deposition with the following exception: because weekly data were available, it was not necessary to take averages from seasonal data.

Fertilizer

Non-Farm Fertilizer Use (NFFU)

Gronberg and Spahr (2012) estimated nitrogen inputs from fertilizer use at the county level for 1987–2006 using fertilizer sales data, U.S. Census Bureau population data, and the enhanced national land cover datasets. In this method, annual statewide nitrogen inputs are calculated based on annual sales data from the Association of American Plant Food Control Officials (APFCO) for each State, and the statewide totals are apportioned to the county level based on each county's effective population. For calendar years 2007–2010, APFCO data were not available for analysis, so an alternative method was developed.

First, quarterly non-farm fertilizer total tonnage data were obtained from the Office of the Texas State Chemist (OTSC, 2014). The OTSC reporting periods do not correspond to the calendar year, so converting these values to annual amounts required apportioning the quarterly data to individual months. This conversion was accomplished by using monthly fertilizer sales data from Missouri, which publishes monthly non-farm fertilizer sales information (fig. 2) (Missouri Plant Food Control Service, 2014). The validity of utilizing non-farm fertilizer data from Missouri as a surrogate for Texas was evaluated by comparing the seasonal variations in non-farm fertilizer use against recommended fertilizing practices for turf grass. In Texas, fertilization is recommended approximately 3 weeks after grass turns green in the spring and every 8–10 weeks thereafter (Taylor II and Gray, 1999a, b). Additional fertilization is recommended 4–6 weeks before the anticipated first frost for both Bermuda and St. Augustine grasses as well as in December and February for lawns over-seeded with a winter grass variety (Taylor II and Gray, 1999a, b). The data for Missouri show peaks in March, August, and October, corresponding to the recommended early spring, summer, and fall fertilization times. Slightly higher percentages

in December through February correlate with recommended winter fertilization times for over-seeded turf. The alignment of the monthly Missouri non-farm fertilizer use with recommended fertilization practices for lawns typical of Texas indicates the data from Missouri likely represents non-farm fertilization practices in Texas.

The derived monthly use percentages were then used to determine annual non-farm fertilizer sales from the OTSC data. For calendar years 2007–2010, sales were determined by apportioning quarterly fertilizer sales to individual months based on the use percentages on figure 2. The monthly data were then summed to determine annual fertilizer tonnage use. The resulting values, expressed in tons of product, were converted into kg-N by determining the average nitrogen content of non-farm fertilizer applied in Texas in 2006. This was accomplished by dividing the statewide non-farm nitrogen estimate from Gronberg and Spahr (2012) of 39,445,277 kg-N by 328,341,766 kg-product, the total product reported by the OTSC for 2006 (OTSC, 2014), for a nitrogen content of 12 percent.

Allocating statewide non-farm fertilizer sales to the county level was accomplished by using the method of Gronberg and Spahr (2012). Decennial census population data from 2000 and 2010 were used to determine county population values. Population estimates between years were obtained through linear interpolation. The county NFFU estimates were apportioned to the study area by evaluating the various land uses within each study area county. The percentage of non-farm fertilizer land use (table 1) within the study area at the county level was taken to represent the percentage of each county's NFFU within the study area. The resulting percentages were multiplied by the annual county-level NFFU to determine the estimated NFFU within each study area county. The annual non-farm fertilizer values were then allocated to individual months by multiplying them by the monthly sales percentages from figure 2.

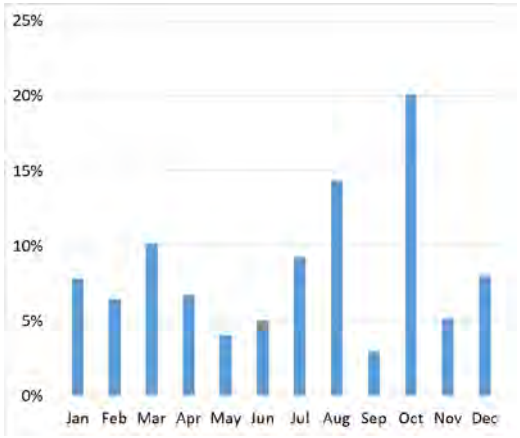

Figure 2. Monthly non-farm fertilizer use in Missouri (from Missouri Plant Food Control Service, 2014).

Farm Fertilizer Use (FFU)

U.S. Department of Agriculture (USDA) National Agricultural Statistics Service (NASS) CropScape geospatial data were used to identify crop areas within the study area (Han and others, 2014). An analysis of these data revealed that corn, oats, sorghum, and winter wheat constitute approximately 94.5 percent of the cropland within the study area. Based on this, these four crops were selected for further analysis. First, the planted area for each crop by county was determined from NASS agricultural surveys (NASS, 2015). Next, CropScape data were used to determine the percentage of each county's crop area located within the study area (for example, 6.55 percent of the corn planted in Bexar County is planted in the study area). The resulting percentages were multiplied by the crop's planted area in each county to determine the total planted area for each crop in the study area. Finally, fertilizer use for each crop was calculated based on application rate data from NASS surveys. Crop area estimates and application rates between survey years were determined through linear interpolation.

Table 1. Land-use classes associated with nitrogen inputs (from Ruddy and others, 2006).

Confined animal operations	Unconfined animal operations	Farm fertilizer use	Non-farm fertilizer use
Pasture/Hay	Pasture/Hay	Pasture/Hay	Low intensity residential
Row crops	Row crops	Row crops	LULC[1] residential
Small grains	Small grains	Small grains	Forested residential
Fallow	Fallow	Fallow	Urban/Recreational grasses
	Grassland/Herbaceous	Orchards/Vineyards/Other	

[1]Land use/Land cover

Determining the month of farm fertilizer application entailed considering crop-specific requirements. The planting and harvest dates for each crop were taken from NASS reported average dates for Texas (NASS, 2010). Corn fertilizer application dates were set to 30 days and 45 days post-emergence according to published guidance (Bean and McFarland, 2008; Bean, 2010). Nitrogen application for oats was set for two equal applications in late September and early March (Twidwell, n.d.). Nitrogen application to sorghum was assumed to occur in the spring prior to planting (Kochenower and others, 2011). Similarly, application to winter wheat was assumed to occur in the fall prior to planting (Sij and others, 2011).

Manure

Farm Animal

Previous research provided estimates of nitrogen inputs from farm animal manure (cattle, domesticated swine, equine, fowl, and sheep) for confined and unconfined animal operations for calendar years 1982–2001 (Ruddy and others, 2006) and for calendar year 2002 (Mueller and Gronberg, 2013). Data for 2003–2012 were calculated using this method and data from the 2007 and 2012 USDA Censuses of Agriculture. For 2007, pullet and broiler poultry data were not available for Guadalupe County, so it was estimated based on the 2012 Census of Agriculture. The statewide percentage change in pullets and broilers from 2007 to 2012 was applied to Guadalupe County's 2012 value to estimate the value for 2007. Manure inputs were apportioned within each of the study area counties based on land uses associated with confined and unconfined animal operations (table 1). Using these land uses, the percentage of confined and unconfined manure inputs within the study area were determined based on the percentage of those land uses within the study area. These percentages were then multiplied by the respective county's confined and unconfined manure loads to determine the nitrogen load from manure within the study area.

Dogs

Dogs have long been considered a potentially significant source of stormwater pollution (Leeming and others, 1996). The American Veterinary Medical Association (AVMA, 2012) identified the percentage of households in Texas owning a dog as 40.9 percent in 1996, 43.8 percent in 2001, 44 percent in 2006, and 39.8 percent in 2011, with the average household owning 1.8 dogs. Dog ownership percentages between AVMA data years were determined by linear interpolation with the exception of 2012, which was set equal to the ownership percentage for 2011. The number of households was determined from

U.S. census data. Data for occupied housing units at the census tract level were converted to housing units within the study area by assuming the housing units were equally distributed throughout the census tract. The percentage of the census tract's area within the study area was then multiplied by the number of homes in the census tract to calculate the number of housing units within the study area. Housing numbers between census dates were interpolated by using OSSF permits issued as a surrogate for houses added to the inventory. With this method, the OSSF permits issued for the respective month were divided by the number of permits issued between census dates to derive a percentage. These percentages were then multiplied by the increase in housing between census dates to determine the number of houses added each month. On average, dogs produce 0.34 kg-manure per day containing 0.7 percent nitrogen (Nemiroff and Patterson, 2007). This manure deposition rate was multiplied by the dog density from the AVMA and the number of occupied housing units to calculate the monthly and annual manure nitrogen inputs from dogs.

Feral Hogs

Estimating the feral hog population requires identifying suitable habitat for feral hogs as well as their population density. Research indicates feral hog habitat includes all areas in the region with the exception of open water, barren ground, and high-intensity development (Timmons and others, 2012). Suitable habitat within the study area was identified from the National Land Cover Dataset (NLCD) for 2001, 2006, and 2011. Suitable habitat in 1992 was determined from the 1992 Retrofit NLCD, which identifies cells that changed between 1992 and 2001 (Fry and others, 2009). For each land class, the percentage of suitable habitat was determined from the average amount of impervious cover within the land class.

The mean statewide feral hog population density in Texas is reported as 7.34×10^{-3} hogs per hectare (Timmons and others, 2012). Available data did not provide density estimates for different years, so the density estimate was held constant. Manure nitrogen output from feral hogs was assumed to equal that of domesticated swine. The methodology of Ruddy and others (2006) was used to determine the daily manure nitrogen output of feral hogs, which was aggregated into monthly and annual values.

Axis and White-Tail Deer

Deer are a potentially significant source of nitrogen loading within the study area because the Edwards Plateau contains the largest percentage of Texas' deer habitat and contains 57.3 percent of the Texas deer herd (Lockwood, 2006). Prior to 2005, the Texas Parks and Wildlife Department conducted deer surveys in each county, but began conducting them based on Resource Management Units (RMU) in 2005 (Lockwood, 2006). Deer density estimates were available for Bandera, Comal, and Kendall Counties for calendar years 1996 through 2003. Area weighted averages of these values were used to determine the average deer density for the study area for years 1996 through 2003. For years 2005 through 2012, deer densities for RMU 7, which encompasses nearly the entire study area, were utilized. Linear interpolation was used between years 2003 and 2005 to estimate the deer density for 2004. Based on data from various studies (Dinerstein and Dublin, 1982; Jenks and others, 1990; Sawyer and others, 1990; Kamler and others, 2003), per capita nitrogen deposition rates are estimated at 0.0125 kg-N per day in the summer and 0.0106 kg-N per day in the winter and spring. In calculating nitrogen loading for the deer herd within the study area, the summer deposition rate was used for the months of June through October and the winter rate for the months of November through May.

Wild Birds

Nitrogen deposition from birds is a concern due to their implication in contaminating water bodies through defecation, with waterfowl being a specific concern (Nadareski, 2000). Bird count data were available for three locations within the study area: approximately 5 kilometers to the northwest of Boerne City Lake in the northwestern part of the study area for 1996–2012 (National Audubon Society, 2012); in the Cibolo Preserve approximately 7 kilometers to the southeast of Boerne City Lake for 2014 (Taylor and Hood, 2014); and in New Braunfels (National Audubon Society, 2012) near the Comal River in the extreme eastern part of the study area for 2001–2012. The bird counts identified 17 waterfowl species in the area requiring analysis. Bird counts in the Cibolo Preserve for 1996–2012 were estimated using population trend analysis data from the North American Breeding Bird Survey for the 11 species with data available for Texas (Sauer and others, 2014). For four species, counts were estimated by assuming the count data varied in the same manner as the data from the Christmas Bird Count in Boerne. Data were not available for the remaining two species, so their counts were held constant at two for the Red-Breasted Merganser and six for the Common Golden-Eye. The same procedure was used to estimate bird counts in New Braunfels for 1996–2000.

Monthly nitrogen deposition values were based on migratory patterns (Poole, 2005) to determine when each species was likely to be present in the study area. The nitrogen deposition rate was then calculated as the sum of the Total Kjeldahl Nitrogen (TKN) deposition rate for ducks and the ammonia nitrogen deposition rate for layers (egg-laying hens) from published data (Arnold and others, 2012). Because ammonia nitrogen deposition data were not available for ducks, data for layers (egg-laying hens) were used because they have a comparable body mass.

Wastewater

Wastewater Treatment Plant (WWTP)

During the period of interest, only one point source of anthropogenic nitrogen was identified in the study area, the City of Boerne's WWTP. As required by permit, the City of Boerne samples the effluent twice weekly for several constituents including ammonia nitrogen (NH_3-N). These values are then submitted to the State of Texas as part of the WWTP's monthly Discharge Monitoring Report (DMR). The DMR includes the daily average NH_3-N value, but does not include any nitrate sampling data. However, regression analysis using estimated nitrate discharges from HDR Engineering, Inc. (2009) indicated that nitrate concentration for this plant's effluent can be estimated as a function of ammonia concentration:

$$[NO_3^-] = 3.318[NH_3]^2 + 3.4114[NH_3] + 0.6441 \; R^2 = 0.98, \quad (2)$$

The ammonia and nitrate concentrations were multiplied by the monthly flow values from the DMR to calculate nitrogen loading from the WWTP.

On-Site Sewage Facilities (OSSFs)

OSSF information was provided in various formats by the respective county engineering offices. Comal County and Bexar County provided GIS files for the entire county containing OSSF information. Kendall County provided a spreadsheet from a legacy database containing OSSF records. Spreadsheet entries were geolocated through either GPS Visualizer (Schneider, 2013) or Google Earth. Records were not available from Guadalupe County, so OSSF information was identified through satellite imagery analysis of the small portion of the study area within the county. The install dates for the OSSFs were assumed to be the date of construction of the home, which was determined from the Guadalupe County Appraisal District's website. Available records did not identify whether 931 OSSFs were aerobic or conventional systems. These systems

were divided between aerobic and conventional systems based on the percentage of each type system installed in the same county in the same year.

The nitrogen inputs from the OSSFs were determined from effluent nitrogen concentrations, per capita effluent values, and population densities. A typical value for total nitrogen in septic system effluent is 70 mg-N per liter (mg-N L^{-1}), whereas the per capita effluent value is 0.227 m^3 per person per day (Arnold and others, 2012). For aerobic systems, total nitrogen is reported as 73 mg-N L^{-1}, comprising 29 mg-N L^{-1} ammonia and 44 mg-N L^{-1} nitrate (McCarthy and others, 2001).

SWAT Model Development

Climatological Data

The Soil & Water Assessment Tool (SWAT) requires the input of multiple weather parameters including temperature, precipitation, relative humidity, wind speed, and solar radiation. The SWAT website (http://globalweather.tamu.edu) provides easy access to climatological data from the Climate Forecast System Reanalysis (CFSR) for 1979–2014. However, use of the CFSR precipitation data is problematic for areas subject to intense rainfall events. CFSR consists of a gridded representation of weather data generated by interpolating between weather stations. This procedure can lead to large differences between observed precipitation values and CFSR values (fig. 3), which in turn negatively impact streamflow calibration efforts. Due to this, National Weather Service (NWS) data from six monitoring stations near the study area were used instead of CFSR data.

Manure

The first step in modeling manure application in SWAT is to determine the average manure application rate in kilograms per hectare per day (kg ha^{-1} d^{-1}) (defined as CFRT_KG in SWAT) for each animal in each Hydrologic Response Unit (HRU). HRUs represent sub-basin areas consisting of the same soil type, land use, and slope. For livestock, the statewide average stocking rates for each animal type were taken from the USDA Census of Agriculture (USDA, 2014). Livestock were then apportioned throughout the study area into HRUs with agricultural land uses. Similarly, dogs were apportioned to HRUs containing urban land classes proportionally to population density. Deer were assumed to be evenly distributed throughout the study area whereas feral hogs were evenly distributed throughout land classes containing suitable habitat. Finally, birds were located in the HRUs associated with the bird count locations identified above.

A second step is necessary because SWAT only reads one manure operation per HRU per year. For HRUs with multiple animal types, this was overcome by combining manure input from multiple animal types into a single CFRT_KG value. Because different animal types have different manure nitrogen characteristics, CFRT_KG values for various animal types could not be simply added together. Rather, the combined CFRT_KG value was based on a continuous fertilizer operation for the animal type with the highest CFRT_KG value in the HRU. The CFRT_KG values for other animals in the HRU were then adjusted based on the ratio of manure nitrogen content for each animal. For example, the CFRT_KG value for deer located in an HRU containing predominantly beef cattle was adjusted using the following formula:

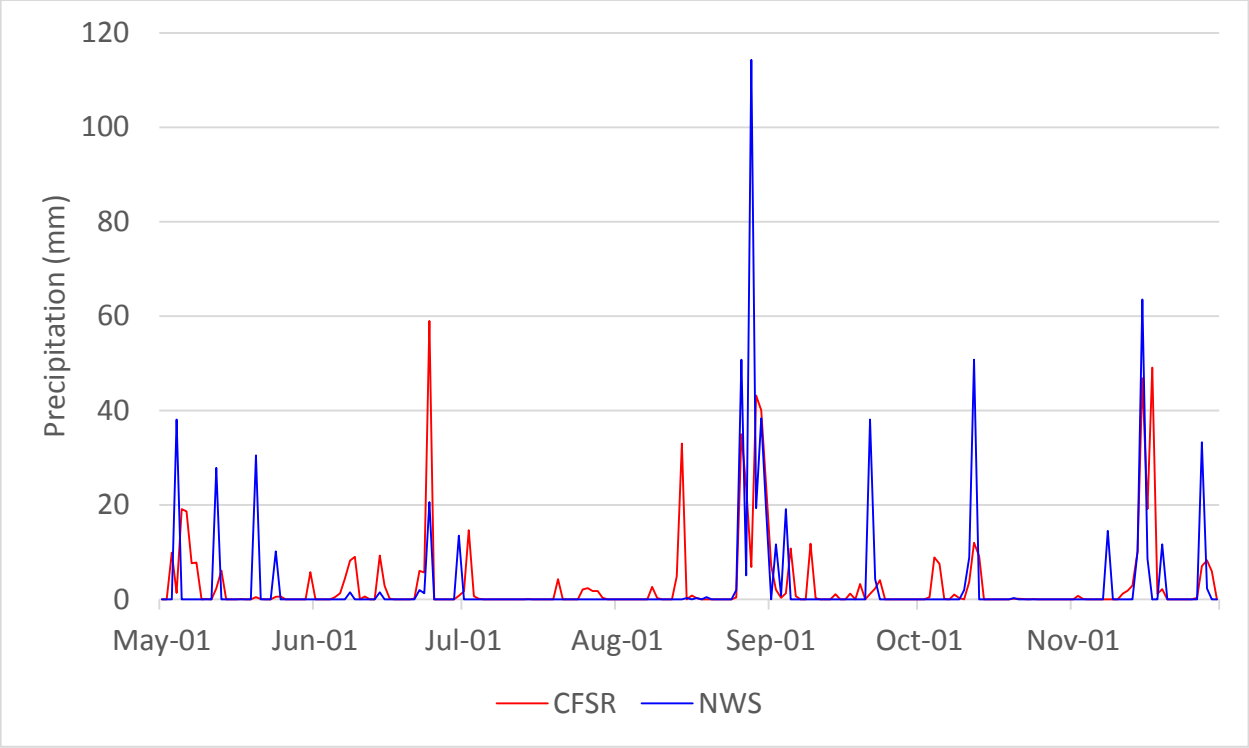

Figure 3. Comparison of National Weather Service (NWS) and Climate Forecast System Reanalysis (CFSR) precipitation data for New Braunfels, Texas (NWS data from Menne and others, 2012; CFSR data from Saha and others, 2010.

$$CFRT\_KG'_{\text{deer}} = \frac{\text{Manure N\%}_{\text{deer}}}{\text{Manure N\%}_{\text{beef cattle}}} CFRT\_KG_{\text{deer}}, \quad (3)$$

where

$CFRT\_KG'_{\text{deer}}$ is the adjusted manure application rate for deer (kg ha^{-1} d^{-1})

$\text{Manure N\%}_{\text{deer}}$ is the manure N percent for deer

$\text{Manure N\%}_{\text{beef cattle}}$ is the manure N percent for beef cattle

$CFRT\_KG_{\text{deer}}$ is the initial manure application rate for deer (kg ha^{-1} d^{-1})

The CFRT_KG' values were then added to the CFRT_KG value for the predominant animal type in the HRU to get the combined CFRT_KG value for use in SWAT.

On-Site Sewage Facilities

There are three broad categories of OSSFs within the study area: traditional septic systems (SEPT), aerobic treatment units with sub-surface drip systems (ATUD), and aerobic treatment units with surface spray application (ATUS). OSSFs have a nominal leach field of 100 m^2 (Arnold and others, 2012), which requires use of a 10 m × 10 m land use map to accurately locate them. The 30 m × 30 m NLCDep306 (Hitt, 2008) was resampled to 10 m × 10 m resolution in ArcGIS. New land use classes were created for each OSSF type (SEPT, ATUD, and ATUS) by using raster calculator to combine the OSSF point feature class with the land use raster.

Because SWAT overlays the land use raster with the Digital Elevation Model (DEM) during HRU processing, the requirement to use a 10-m resolution land use raster also necessitated the use of a 10-m resolution DEM.

A further complication arose due to how the septic system module in SWAT works. In its current form, the septic system module turns all OSSFs within an HRU on at the same time. This is significant because if SWAT agglomerates multiple OSSFs into a single HRU, there is no way to account for OSSFs having different installation dates. This problem was mitigated by exempting the three OSSF land uses from the land use threshold during HRU delineation as well as defining four slope classes (0–2, 2–4, 4–6, and greater than 6 percent) rather than the typical three slope classes.

The septic system module within SWAT is designed to model leachate from traditional septic systems, but is unable to model aerobic treatment unit effluent. ATUDs were modeled by altering the properties of one of the septic system types within SWAT to account for ATUDs different effluent characteristics and shallower effluent discharge. This was accomplished by changing the depth of effluent discharge to 100 mm and the effluent concentrations for total nitrogen to 73 mg-N L^{-1}, ammonia to 29 mg-N L^{-1}, and nitrate to 44 mg-N L^{-1} (McCarthy and others, 2001). The same effluent concentrations were used for ATUS systems, with the difference being that the effluent is surface applied. ATUS discharge was therefore simulated by adding a continuous fertilizer operation with daily application of organic nitrogen for each ATUS HRU. Because there is no continuous irrigation operation in SWAT, the effluent water was added to the soil in monthly irrigation operations using the nominal effluent load of 0.227 m^3 per capita per day (Arnold and others, 2012). With 343 ATUS HRUs, daily irrigation would have resulted in 238,042 irrigation operations, which would exceed the database size limitation.

Summary

The assessment of nitrogen fate and transport in karst watersheds requires gathering and processing significant amounts of data. When conducting surface-water modeling, the SWAT model provides an effective means of modeling nitrogen fate and transport in karst watersheds. However, there are limitations to how SWAT models nitrogen processes that must be considered when developing these models to minimize errors in model output. The methodologies for calculating nitrogen inputs from atmospheric deposition, fertilizer, manure, and wastewater were presented along with specifics on how to develop SWAT models for nitrogen fate and transport. Although the SWAT model only accounts for karst features indirectly at a sub-basin scale through streambed hydraulic-conductivity values, it was able to successfully model streamflow in the karstic Cibolo and Dry Comal Creek watersheds. Watershed modelers will find these methodologies useful when modeling nitrogen fate and transport in other karst watersheds.

Acknowledgments

The authors would like to thank Mr. David Weary and Dr. Daniel Doctor of the U.S. Geological Survey for their thoughtful reviews of this manuscript. The authors would also like to thank Dr. Jaehak Jeong from the Texas AgriLife Blackland Research Center for assistance with the septic module in SWAT. Mr. Sullivan would also like to personally thank Dr. Dutton, Dr. Giacomoni, Dr. Montoya, and Dr. Sharif for their assistance as members of his doctoral committee. This work was supported in part by the Office of Research Support of the University of Texas at San Antonio, the Cibolo Preserve Trustee, and the National Natural Science Foundation of China, grant 41428202.

References Cited

Agency for Toxic Substances and Disease Registry, 2015, ToxFAQ—Nitrates and nitrites, 2 p.: accessed August 15, 2013, at https://www.atsdr.cdc.gov/toxfaqs/tfacts204.pdf.

American Veterinary Medical Association, 2012, U.S. pet ownership & demographic sourcebook: Schaumburg, IL, American Veterinary Medical Association, 168 p.

Arnold, J.G., Kiniry, J.R., Srinivasan, R., Williams, J.R., Haney, E.B., and Neitsch, S.L., 2012, Soil & Water Assessment Tool—Input/output documentation: Texas Water Resources Institute Report TR-439, 650 p., accessed March 8, 2014, at http://swat.tamu.edu.

Bean, B., 2010, Corn development and key growth stages: Amarillo, TX, Texas A&M AgriLife Extension Service, 4 p., accessed July 12, 2014, at http://publications.tamu.edu/CORN_SORGHUM/PUB_Corn%20Development%20and%20Key%20Growth%20Stages.pdf.

Bean, B., and McFarland, M., 2008, Getting the most out of your nitrogen fertilization in corn: Amarillo, TX, Texas A&M AgriLife Extension Service, 5 p., accessed July 12, 2014, at http://amarillo.tamu.edu/files/2010/11/NitrogenFertilization.pdf.

Dinerstein, E., and Dublin, H.T., 1982, Daily defecation rate of captive axis deer: The Journal of Wildlife Management, v. 46, no. 3, p. 833–835, accessed April 19, 2014, at https://doi.org/10.2307/3808586.

Fry, J., Coan, M., Homer, C., Meyer, D.K., and Wickham, J., 2009, Completion of the National Land Cover Database (NLCD) 1992–2001 land cover change retrofit product: U.S. Geological Survey Open-File Report 2008–1379, 18 p., accessed September 7, 2014, at http://pubs.er.usgs.gov/publication/ofr20081379.

Gronberg, J.M., and Spahr, N.E., 2012, County-level estimates of nitrogen and phosphorus from commercial fertilizer for the conterminous United States, 1987–2006: U.S. Geological Survey Scientific Investigations Report 2012–5207, 30 p., accessed March 9, 2014, at https://pubs.er.usgs.gov/publication/sir20125207.

Han, W., Yang, Z., Di, L., and Yue, P., 2014, A geospatial web service approach for creating on-demand cropland data layer thematic maps: Transactions of the American Society of Agricultural and Biological Engineers, v. 57, no. 1, p. 239–247, accessed March 5, 2016, at https://doi.org/10.13031/trans.57.10020.

HDR Engineering, Inc., 2009, Cibolo Creek water quality monitoring and modeling—Boerne, TX: City of Boerne, 95 p., accessed January 18, 2015, at http://www.ci.boerne.tx.us/documentcenter/.

Hitt, K.J., 2008, Enhanced National Land Cover Data 1992 revised with 1990 and 2000 population data to indicate urban development between 1992 and 2000 (NLCDep0306) (3rd ed.): U.S. Geological Survey data release, accessed March 9, 2014, at https://water.usgs.gov/lookup/getspatial?nlcdep0306.

Jenks, J.A., Soper, R.B., Lochmiller, R.L., and Leslie, D.M., Jr., 1990, Effect of exposure on nitrogen and fiber characteristics of white-tailed deer feces: The Journal of Wildlife Management, v. 54, no. 3, p. 389–391, accessed April 19, 2014, at https://doi.org/10.2307/3809644.

Kamler, J., Homolka, M., and Kráčmar, S., 2003, Nitrogen characteristics of ungulates faeces—Effect of time of exposure and storage: Folia Zoologica, v. 52, no. 1, p. 31–35.

Kochenower, R., Larson, K., Bean, B., Kenny, N., and Martin, K., 2011, United Sorghum Checkoff Program—High plains production handbook: Lubbock, TX, United Sorghum Checkoff Program, 113 p., accessed July 14, 2014, at http://www.sorghumcheckoff.com/newsroom/2016/03/28/high-plains-production-guide/.

Leeming, R., Ball, A., Ashbolt, N., and Nichols, P., 1996, Using faecal sterols from humans and animals to distinguish faecal pollution in receiving waters: Water Research, v. 30, no. 12, p. 2893–2900, accessed April 19, 2014, at http://dx.doi.org/10.1016/S0043-1354(96)00011-5.

Lockwood, M., 2006, White-tailed deer population trends: Austin, TX, Texas Parks and Wildlife Department, 30 p.

McCarthy, B., Geerts, S.M., Axler, R., and Henneck, J., 2001, Performance of an aerobic treatment unit and drip dispersal system for the treatment of domestic wastewater at the Northeast Regional Correction Center: Natural Resources Research Institute Technical Report NRRI/TR-01/33, 12 p.

Menne, M.J., Durre, I., Vose, R.S., Gleason, B.E., and Houston, T.G., 2012, An overview of the global historical climatology network-daily database: Journal of Atmospheric and Oceanic Technology, v. 29, no. 7, p. 897–910, accessed December 13, 2015, at http://dx.doi.org/10.1175/JTECH-D-11-00103.1.

Missouri Plant Food Control Service, 2014, Monthly fertilizer tonnage report: Columbia, MO, Missouri Agricultural Experiment Station, accessed April 13, 2014, at http://aes.missouri.edu/pfcs/fert/index.stm.

Mueller, D.K., and Gronberg, J.M., 2013, County-level estimates of nitrogen and phosphorus from animal manure for the conterminous United States, 2002: U.S. Geological Survey Open-File Report 2013–1065, accessed March 10, 2014, at https://pubs.er.usgs.gov/publication/ofr20131065.

Nadareski, C.A., 2000, Water Birds, *in* Dissmeyer, G.E., ed., Drinking water from forests and grasslands—A synthesis of the scientific literature: U.S. Forest Service General Technical Report SRS-39, p. 164–168, accessed February 16, 2015, at https://treesearch.fs.fed.us/pubs/1866.

National Agricultural Statistics Service, 2010, Field crops—Usual planting and harvesting dates: National Agricultural Statistics Service Agricultural Handbook Number 628, 51 p., accessed April 21, 2014, at http://usda.mannlib.cornell.edu/usda/current/planting/planting-10-29-2010.pdf.

National Agricultural Statistics Service, 2015, Quick Stats 2.0: U.S. Department of Agriculture, accessed February 15, 2015, at http://quickstats.nass.usda.gov/.

National Atmospheric Deposition Program (NRSP-3), 2015, NADP Program Office, Illinois State Water Survey: University of Illinois (ed.), accessed July 7, 2014, at http://nadp.sws.uiuc.edu/data/ntn/.

National Audubon Society, 2012, The Christmas bird count historical results: New York, NY, National Audubon Society, accessed February 16, 2015, at http://netapp.audubon.org/cbcobservation/?_ga=1.17984633.1565359313.1486919132.

Nemiroff, L., and Patterson, J., 2007, Design, testing and implementation of a large-scale urban dog waste composting program: Compost Science & Utilization, v. 15, no. 4, p. 237–242, accessed May 5, 2016, at http://dx.doi.org/10.1080/1065657X.2007.10702339.

Office of the Texas State Chemist, 2014, Commercial fertilizer annual report: College Station, TX, Office of the Texas State Chemist, accessed April 6, 2014, at http://otscweb.tamu.edu/Reports/Annual.aspx.

Poole, A.E., 2005, The birds of North America: Ithaca, NY, Cornell Laboratory of Ornithology, accessed February 16, 2015, at http://bna.birds.cornell.edu/BNA/.

Ruddy, B.C., Lorenz, D.L., and Mueller, D.K., 2006, County-level estimates of nutrient inputs to the land surface of the conterminous United States, 1982–2001: U.S. Geological Survey Scientific Investigations Report 2006–5012, 23 p., accessed May 16, 2013, at https://pubs.er.usgs.gov/publication/sir20065012.

Saha, S., Moorthi, S., Pan, H.-L., Wu, X., Wang, J., Nadiga, S., Tripp, P., Kistler, R., Woollen, J., Behringer, D., Liu, H., Stokes, D., Grumbine, R., Gayno, G., Wang, J., Hou, Y.-T., Chuang, H.-y., Juang, H.-M.H., Sela, J., Iredell, M., Treadon, R., Kleist, D., Van Delst, P., Keyser, D., Derber, J., Ek, M., Meng, J., Wei, H., Yang, R., Lord, S., van den Dool, H., Kumar, A., Wang, W., Long, C., Chelliah, M., Xue, Y., Huang, B., Schemm, J.-K., Ebisuzaki, W., Lin, R., Xie, P., Chen, M., Zhou, S., Higgins, W., Zou, C.-Z., Liu, Q., Chen, Y., Han, Y., Cucurull, L., Reynolds, R.W., Rutledge, G., and Goldberg, M., 2010, The NCEP climate forecast system reanalysis: Bulletin of the American Meteorological Society, v. 91, no. 8, p. 1015–1057, accessed August 15, 2014, at http://doi.org/10.1175/2010BAMS3001.1.

Sauer, J.R., Hines, J.E., Fallon, J.E., Pardieck, K.L., Ziolkowski Jr., D.J., and Link, W.A., 2014, The North American breeding bird survey, results and analysis 1966–2013: Laurel, MD, U.S. Geological Survey Patuxent Wildlife Research Center, accessed February 16, 2015, at http://www.mbr-pwrc.usgs.gov/bbs/.

Sawyer, T.G., Marchinton, R.L., and Lentz, W.M., 1990, Defecation rates of female white-tailed deer in Georgia: Wildlife Society Bulletin, v. 18, no. 1, p. 16–18, accessed April 20, 2014, at https://www.jstor.org/stable/pdf/3782300.pdf.

Schneider, A., 2013, GPS visualizer's address locator: Portland, OR, Adam Schneider, accessed March 12, 2014, at http://www.gpsvisualizer.com/.

Sij, J., Belew, M., and Pinchak, W., 2011, Nitrogen management in no-till and conventional-till dual-use wheat/stocker systems: Texas Journal of Agriculture and Natural Resources, v. 24, p. 38–49, accessed July 14, 2014, at http://txjanr.agintexas.org/index.php/txjanr/article/view/48.

Sullivan, T.P., and Gao, Y., 2016, Assessment of nitrogen inputs and yields in the Cibolo and Dry Comal Creek watersheds using the SWAT model, Texas, USA 1996–2010: Environmental Earth Sciences, v. 75, no. 9, p. 1–20, accessed April 26, 2015, at http://doi.org/10.1007/s12665-016-5546-0.

Taylor, D., and Hood, R., 2014, Cibolo Preserve waterfowl monitoring: Boerne, TX, Cibolo Nature Center, 9 p.

Taylor II, G.R., and Gray, J., 1999a, Maintaining bermudagrass lawns: College Station, TX, Texas A&M AgriLife Extension Service, 4 p., accessed June 27, 2015, at http://publications.tamu.edu/TURF_LANDSCAPE/PUB_turf_Maintaining%20Bermudagrass%20Lawns.pdf.

Taylor II, G.R., and Gray, J., 1999b, Maintaining St. Augustine lawns: College Station, TX, Texas A&M AgriLife Extension Service, 4 p., accessed June 27, 2015, at http://publications.tamu.edu/TURF_LANDSCAPE/PUB_turf_Maintaining%20St.%20Augustine%20Grass%20Lawns.pdf.

Timmons, J.B., Higginbotham, B., Cathey, J.C., Mellish, J., Griffin, J., Sumrall, A., and Skow, K., 2012, Feral hog population—Growth, density and harvest in Texas: College Station, TX, Texas A&M AgriLIFE Extension, 2 p., accessed March 19, 2014, at http://feralhogs.tamu.edu/files/2011/05/FeralHogFactSheet.pdf.

Twidwell, E., [n.d.], Planting and management practices for wheat and oats: Baton Rouge, LA, Louisiana State University Agricultural Center, 3 p., accessed July 14, 2014, at http://www.lsuagcenter.com/MCMS/RelatedFiles/%7B0217A37E-DDD5-410C-ACCB-9240D96B1EDF%7D/PlantingManagementPractices.pdf.

U.S. Department of Agriculture, 2014, Texas state and county data —Geographic area series: 2012 Census of Agriculture Report Number AC-12-A-43B, vol. 1, part 43B, 623 p., accessed May 2, 2014, at https://www.agcensus.usda.gov/Publications/2012/Full_Report/Volume_1,_Chapter_1_State_Level/Texas/txv1b.pdf.

U.S. Environmental Protection Agency, 2013, Clean Air Status and Trends Network (CASTNET): Washington, D.C., U.S. Environmental Protection Agency Fact Sheet, 4 p., accessed March 14, 2014, at https://java.epa.gov/castnet/documents.do.

U.S. Environmental Protection Agency, 2015, Clean Air Status and Trends Network (CASTNET): Aggregate deposition data—Weekly dry deposition data table, accessed February 15, 2015, at https://java.epa.gov/castnet/clearsession.do.

Attenuation of Acid Rock Drainage with a Sequential Injection of Compounds to Reverse Biologically Mediated Pyrite Oxidation in the Chattanooga Shale in Tennessee

By Thomas D. Byl[1,2], Ronald Oniszczak[2], Diarra Fall[2], Petra K. Byl[3], De'Etra Young[2], and Michael W. Bradley[1]

[1]U.S. Geological Survey, Lower Mississippi-Gulf Water Science Center, 640 Grassmere Park, Suite 100, Nashville, TN 37211

[2]Tennessee State University, Dept. of Agricultural and Environmental Sciences, 3500 John H Merritt Blvd, Nashville, TN 37209

[3]Geophysics Dept., University of Chicago, Chicago, IL 60637

Abstract

Iron sulfide minerals, such as pyrite, are common minerals in distinct geologic formations in the karst regions of middle and east Tennessee. Pyrite, also known as fool's gold, is stable under anaerobic conditions in the Chattanooga Shale, located stratigraphically between the Fort Payne Formation and the Leipers Limestone. However, in the presence of oxygen and water, acid-loving chemolithotrophic bacteria can transform the iron sulfide minerals into a toxic solution of sulfuric acid, dissolved iron, and other trace metals known as acid rock drainage (ARD). The objective of this study was to disrupt chemolithotrophic bacteria responsible for ARD associated with the Chattanooga Shale in Tennessee's karstic central basin using chemical treatments and to foster an environment favorable for competing micro-organisms to attenuate the biologically induced ARD. Chemical treatments were injected into flow-through microcosms consisting of 501 grams of pyrite-rich shale pieces inoculated with ARD bacteria. Treatments included a sodium hydroxide-bleach mix, a sodium lactate solution, a sodium lactate-soy infant formula mix—each treatment with or without phosphate buffer, or injected sequentially with sodium hydroxide. The effectiveness of the treatments was assessed by monitoring pH, dissolved iron, and other geochemical properties in the discharge waters. The optimal treatment was a sequential injection of 1.5 grams sodium hydroxide, followed by 0.75 gram lactate and 1.5 grams soy formula dissolved in 20 milliliters of water. The pH of the discharge water rose to 6.0 within 10 days, dissolved-iron concentrations dropped below 1 milligram per liter, the median alkalinity increased to 98 milligrams per liter as $CaCO_3$, and sulfur-reducing and slime-producing bacteria populations were stimulated and exhibited an increase in the estimated population counts. The ARD attenuating benefits of this treatment were still evident after 33 weeks. Other treatments provided a number of ARD attenuating effects but were tempered by problems such as high phosphate concentrations, short longevity, or other shortcomings.

A GIS-Based Compilation of Spring Locations and Geochemical Parameters in the Appalachian Landscape Conservation Cooperative (LCC) Region

By Daniel H. Doctor[1], Katherine S. Paybins[2], and Mark D. Kozar[2]

[1]U.S. Geological Survey, Eastern Geology and Paleoclimate Science Center, 12201 Sunrise Valley Drive, Reston, VA 20192

[2]U.S. Geological Survey, Virginia and West Virginia Water Science Center, 11 Dunbar Street, Charleston, WV 25301

Abstract

Springs are crucially important for understanding karst aquifer systems, yet information on springs in the eastern United States is generally sparse and incomplete. Here, we present an effort to compile information on locations, flow, and selected geochemical parameters for springs within carbonate karst areas of the Appalachian Landscape Conservation Cooperative (LCC), a region intersecting fifteen States. The publicly available sources queried for this compilation were the National Hydrography Dataset (NHD), the Geographic Names Information System (GNIS), and the Water Quality Portal (WQP). The NHD and GNIS databases provided spring locations only, whereas the WQP provided information on location, flow, and selected geochemical parameters. Karst springs were subsampled from the available population of springs by intersecting their locations with carbonate geologic unit polygons, buffered to 1 kilometer. The resulting springs were categorized according to their location within the general physiographic regions of the Appalachian Valley and Ridge or Appalachian Plateaus, and according to their location by State. Summary statistics of flow and geochemistry within each category are presented. Statistical results show that the median specific conductance and calcium concentration of the Plateau springs were notably greater than those of the Valley and Ridge springs; however, alkalinity and magnesium concentrations were all higher in springs of the Valley and Ridge region than those in the Plateau springs. Median nitrate and chloride concentrations in springs were roughly comparable between the two regions, while total phosphorus concentration in springs was greater in the Plateaus. Median spring water temperature was slightly higher for the Plateau springs than that for the Valley and Ridge springs. Median spring discharge was greater overall in the Valley and Ridge region than in the Plateaus, but the paucity of discharge data precluded any meaningful comparisons of spring discharge among the different States or physiographic regions. In general, this study highlights the need for more work focused on spring inventories and monitoring of springs in the karst regions of the eastern United States.

Introduction

As part of a broader study related to karst ecosystem assessment (Christman and others, 2016), an effort was undertaken in late 2014 to compile spring locations and associated flow and geochemical data for the Appalachian Landscape Conservation Cooperative (LCC) region. Currently available data on spring locations, flow, and selected geochemical parameters were compiled from the National Hydrography Dataset (NHD) (U.S. Geological Survey, 2017a), the Geographic Names Information System (GNIS) (U.S. Geological Survey, 2017b), and the Water Quality Portal (WQP) (U.S. Geological Survey and others, 2017). The WQP is jointly sponsored by the U.S. Geological Survey (USGS), the Environmental Protection Agency (EPA), and the National Water Quality Monitoring Council (NWQMC). The WQP database integrates publicly available water-quality data from the USGS National Water Information System (NWIS), the EPA STOrage and RETrieval (STORET) Data Warehouse, and data from the Agricultural Research Service's (ARS) Sustaining The Earth's Watersheds-Agricultural Research Database System (STEWARDS). These data were entered into a single geodatabase, and an effort was made to achieve consistency among various flow and geochemical measurements that were reported. Here, we present a brief summary of the results of this compilation effort, and some of the challenges encountered along the way.

Within the fifteen States that intersect the Appalachian LCC region, a total of 3,654 springs were in the GNIS database, 7,545 were in the WQP database, and 9,910 point features were in the NHD as "Spring/Seep" (4619) or "Sink/Rise" (5291) feature types. In the NHD, a "Spring/Seep" feature is defined as "a place where water issues from the ground naturally," whereas a "Sink/Rise" feature is defined as "the place at which a stream disappears underground or reappears at the surface in a karst area." Because of this dual definition of a spring, both NHD feature types contain individual unique springs. At present, there is not a specific category for just "Sinks," but that is currently under consideration for inclusion in the NHD as a point feature type, which would allow the "Sink/Rise" feature type to be reserved only for estavelles (Alan Rea, U.S. Geological Survey, oral comm., 2016).

Certain parameters available within the WQP data were selected on the basis of overall spatial coverage and pertinence to karst systems; these included concentrations of calcium, magnesium, nitrate-nitrogen, chloride, total phosphorus and alkalinity, and physical measurements of specific conductance, temperature and flow. After selecting for the occurrence of at least one of these measured parameters for each spring location, the number of springs in the examined dataset was reduced to 6,133. The data were summarized among springs in the folded and faulted rocks of the Appalachian Valley and Ridge province and those in the flat-lying rocks of the Appalachian Plateaus, as described below.

Because of the lack of a unique identifier for each spring that would serve as a common key attribute among these databases, it was unfortunately not possible to accurately identify and account for overlapping entries within the databases. For example, a spatial check using the exact geographic coordinates of each spring yielded only two overlapping entries between the GNIS springs and NHD springs, one overlapping entry between the NHD springs and WQP springs, and no overlapping entries between the WQP springs and GNIS springs; however, applying a buffer distance of 100 feet yielded 1,432 overlapping entries between the GNIS springs and NHD springs, 444 overlapping entries between the NHD and WQP springs, and 1,062 overlapping entries between the WQP springs and GNIS springs. Clearly, overlapping features exist among the three databases, therefore it should be decided by the user of the data on a case by case basis whether

a given spring feature is duplicated, or may represent multiple spring orifices at a single geographic location.

Because many of the NHD springs were originally added from the GNIS database, it was expected that there would be at least as many springs in the NHD database as there are in the GNIS database, but there is notable inconsistency between the two databases. For example, in Georgia the number of springs in the GNIS database is 207, whereas the NHD database only reports 46 "Spring/Seep" or "Sink/Rise" point features. The current categorization of point-feature types in the NHD database may identify springs as either a "Spring/Seep" or as a "Sink/Rise"; however, an effort is currently underway to identify and break out sinks separately within the NHD (Alan Rea, U.S. Geological Survey, oral comm., 2016). Interestingly, the majority of "Spring/Seep" or "Sink/Rise" points in the NHD are located in States west of the Mississippi River (fig. 1). This fact highlights the degree to which the springs in the eastern United States are under-studied, the majority of which are not captured within the queried WQP or GNIS databases.

Results by State

Within the fifteen States that intersect the Appalachian LCC region, the numbers of all known springs from the three databases queried for this study are shown by State on figure 2. Kentucky and Tennessee stand out as having the largest number of spring locations identified. Note, however, that these springs were mostly obtained from the NHD, and many lack a unique name and (or) USGS groundwater identifying number that would facilitate cross-checking against the other databases.

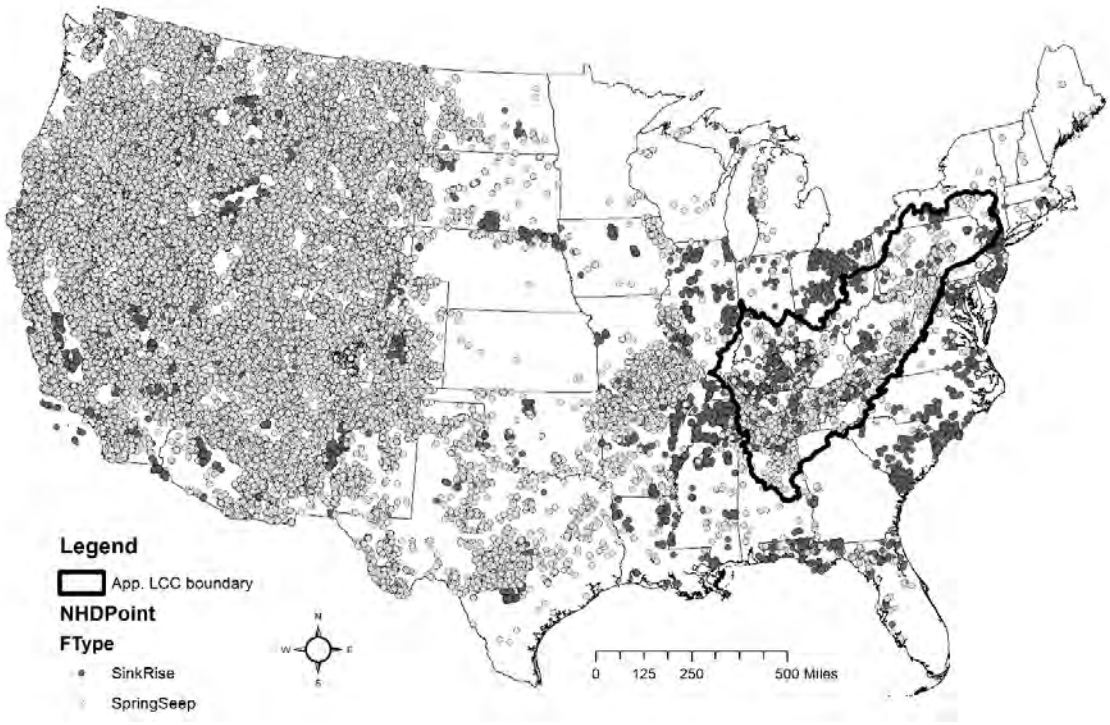

Figure 1. Distribution of Spring/Seep and Sink/Rise feature points across the conterminous United States within the National Hydrography Dataset (NHD). The study area of the Appalachian (App.) LCC region is shown in heavy black line for reference.

The locations of springs that intersect the areas of carbonate bedrock obtained from the national-scale karst map database of Weary and Doctor (2014) and those within a 1-kilometer buffer around carbonate polygons were selected as karst springs. The distribution of these karst springs among the various States (fig. 3) is very similar to that for all springs (fig. 2), indicating that the majority of springs in most of these States are karst springs. This finding is supported by the percentage of karst springs in each State, as shown on figure 4. States having less coverage of karst areas such as North Carolina, Maryland, New Jersey, and New York show the lowest percentages of karst springs.

Within the boundary of the Appalachian LCC region itself, 6,133 springs (irrespective of lithology) were identified that have some associated flow or geochemical data. It is worth noting that of these 6,133 springs, 682 springs (11 percent) had flow or geochemical data that were not collected by the USGS; the majority of these (606, or 89 percent) contained data collected by the National Park Service. Approximately 60 percent of the springs with flow and (or) water-quality data were in regions underlain by carbonate bedrock, and are assumed to be karst springs (n=3,741).

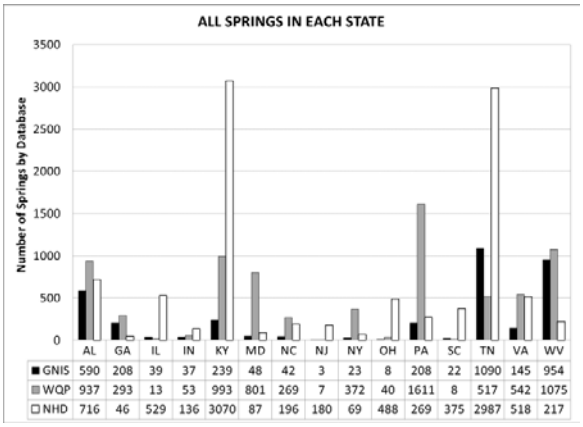

Figure 2. All springs in each State intersected by the Appalachian LCC region in each of the three databases queried.

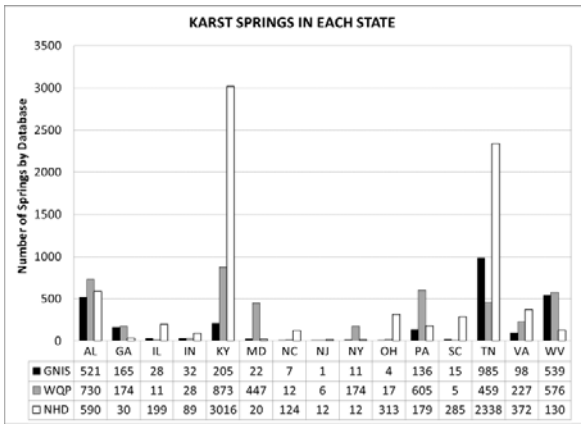

Figure 3. Karst springs in each State intersected by the Appalachian LCC region in each of the three databases queried.

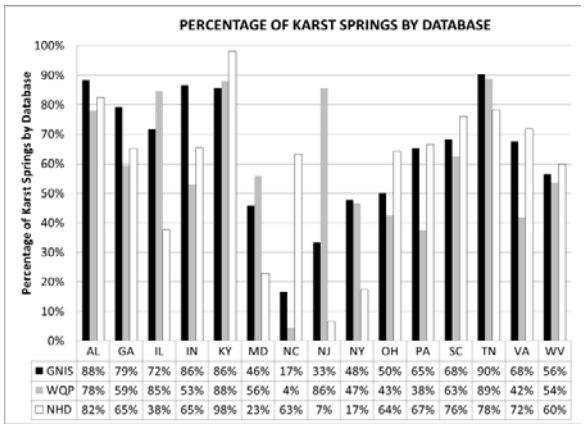

Figure 4. Percentage of karst springs in each State intersected by the Appalachian LCC region in each of the three databases queried.

Karst Springs in the Appalachian LCC Region

Karst springs within the Appalachian LCC region were divided into two broad categories based on general physiography: (1) Valley and Ridge, and (2) Plateaus physiographic regions. The boundaries of these regions were identified using this two-fold categorization applied to 20 kilometer x 20 kilometer grid cells as described in Christman and others (2016). A map illustrating the spatial distribution of the springs in the WQP database that had associated flow and (or) selected geochemical data is shown on figure 5. No karst springs were found to lie within the boundary of

the Appalachian LCC region in the States of Ohio, Illinois, and South Carolina.

Available geochemical and discharge data from the springs were summarized by both State and physiographic region to examine the data for any general trends, and summary statistics were calculated (table 1). The geochemical parameters were chosen on the basis of completeness of the data as well as pertinence to karst systems, but the uneven spatial distribution of the collected geochemical and flow data preclude more than a broad, regional comparison of the data. If a single spring was associated with multiple measurements of any given parameter, the arithmetic mean value for that parameter was calculated and reported for that spring; thus, the values in the compiled dataset represent mean values for each parameter. Table 1 includes the count, median, mean, standard deviation, minimum, and maximum of the mean parameter values for each physiographic region within each State. The distributions of the mean values for nearly all of the geochemical parameters were highly skewed (only water temperature exhibited a normal distribution), therefore, only the median values of the parameters were used for further comparison. Because of the inability to account for overlapping springs among the databases, the distributions of the geochemical parameters are unlikely to be accurate representations of the sample population. A more rigorous statistical characterization can be conducted once overlapping springs are removed from the compilation.

A plot comparing the median values of geochemical parameters between the Valley and Ridge and Plateaus physiographic regions is shown on figure 6, with a multiplicative factor applied to several of the parameter values for ease of illustration. The median specific conductance and calcium concentration of the Plateau springs were notably greater than those of the Valley and Ridge springs. In contrast, alkalinity and magnesium concentrations were higher in springs of the Valley and Ridge region than those in the Plateau springs. Median nitrate and chloride concentrations in springs were roughly comparable between the two regions, while total phosphorus concentration was greater in the Plateau springs. Median spring water temperature was slightly higher for the Plateau springs than for the Valley and Ridge springs, as might be expected due to the higher elevations and thus, cooler temperatures of the Valley and Ridge. Median spring discharge was greater in the Valley and Ridge region than in the Plateaus region overall, but the standard deviation and overall range of discharge values varied greatly among different States (table 1). The paucity of discharge data in general precluded any meaningful comparisons of spring discharge among different States or physiographic regions.

Conclusion

A preliminary assessment of a compilation database of springs within the Appalachian Landscape Conservation Cooperative (LCC) region is presented. We queried and combined data from the National Hydrography Dataset (NHD), the Geographic Names Information System (GNIS), and the Water Quality Portal (WQP) for this compilation. Issues regarding the lack of unique spring identifier codes precluded the evaluation of overlapping features within these databases; this issue deserves additional attention to allow for better comparison and linkage among these datasets. It is evident from this exercise that springs in the eastern United States are under-inventoried and under-studied.

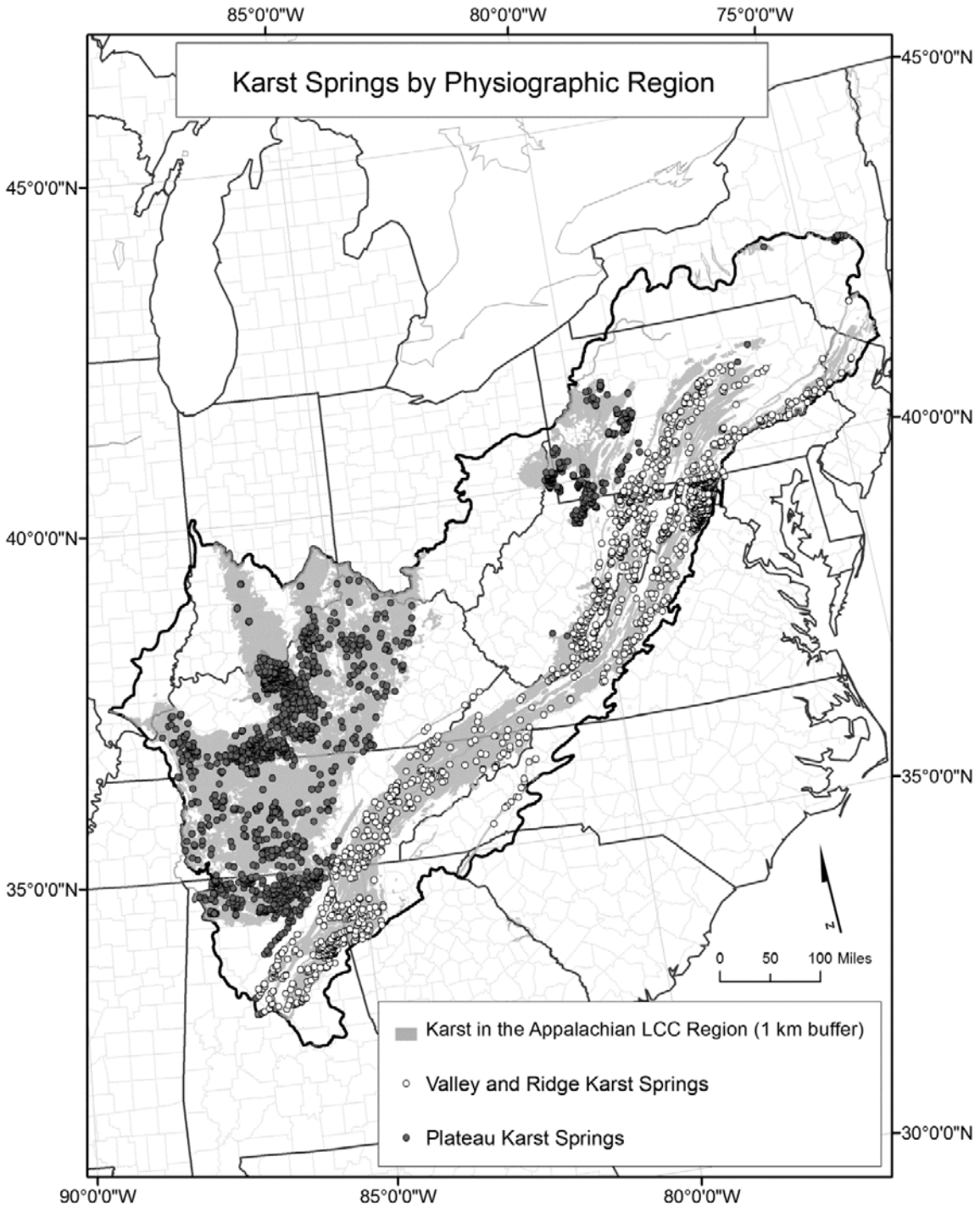

Figure 5. Spatial distribution of springs with associated flow or water-quality parameters between the generalized Valley and Ridge and Plateaus physiographic regions. Karst polygons from Weary and Doctor (2014).

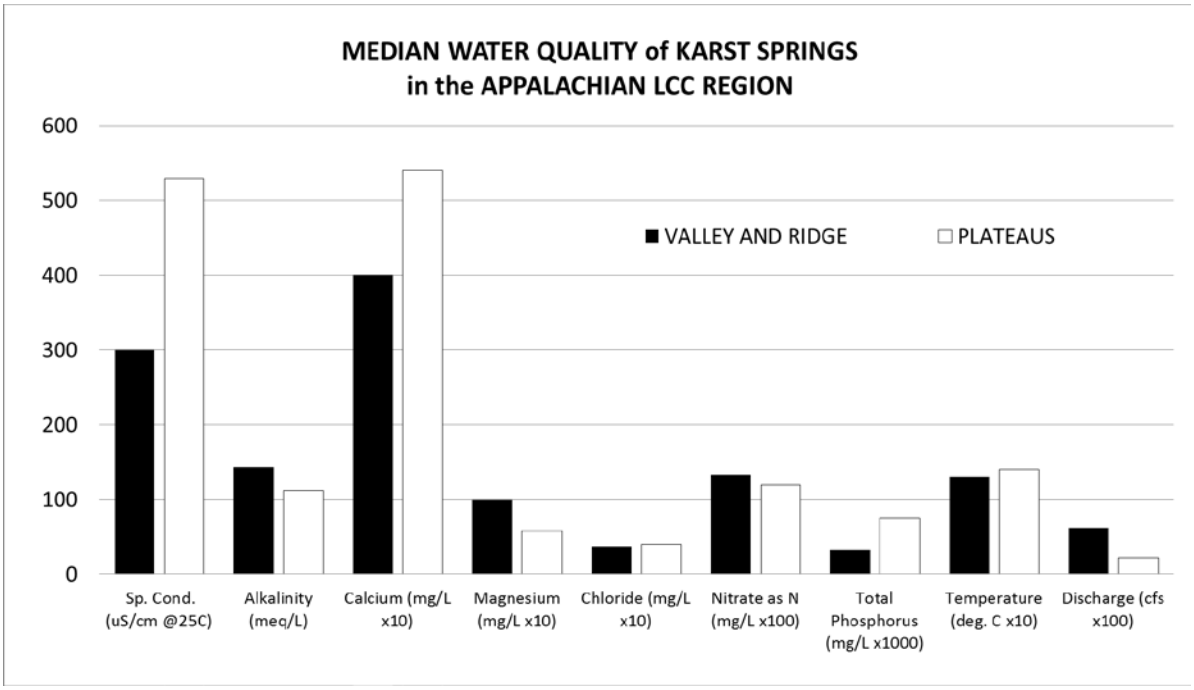

Figure 6. Comparison of the median values of water-quality parameters between the Valley and Ridge and Plateaus physiographic regions.

Table 1. Summary statistics of water-quality data for karst springs in the Appalachian Landscape Conservation Cooperative (LCC) region.

[AL, Alabama; GA, Georgia; IN, Indiana; KY, Kentucky; MD, Maryland; NJ, New Jersey; NY, New York; NC, North Carolina; PA, Pennsylvania; TN, Tennessee; VA, Virginia; WV, West Virginia; V&R, Valley and Ridge; P, Plateaus; µS/cm @ 25, microsiemens per centimeter at 25 degrees Celsius; Std. Dev., standard deviation; Min., minimum; Max., maximum; meq/L ANC, milliequivalents per liter acid neutralizing capacity; mg/L, milligrams per liter; ft^3/s, cubic feet per second; n/a, not available]

State:	AL	AL	GA	IN	KY	KY	MD	NJ	NY	NY	NC	PA	PA	TN	TN	VA	WV	WV
Region:	V&R	P	V&R	P	V&R	P	V&R	V&R	V&R	P	V&R	V&R	P	V&R	P	V&R	V&R	P
Frequency																		
Count:	255	401	90	17	6	865	338	5	7	26	11	273	206	208	248	204	466	115
Specific conductance (µS/cm @ 25 °C)																		
Count:	73	52	29	11	4	398	40	1	6	4	11	123	93	95	156	121	105	7
Median:	222	195	180	647	153	360	340	694	79	316	23	360	195	268	390	366	471	445
Mean:	223	234	291	586	160	1190	330	694	118	279	34	368	556	274	449	370	434	414
Std. Dev.:	56	162	422	270	70	5873	241	n/a	101	180	35	212	1,100	126	460	211	216	220
Min.:	13	73	58	56	91	23	0.4	694	60	49	7	22	30	20	17	5	18	64
Max.:	382	1,100	1,900	999	241	69,800	928	694	321	433	133	849	7,000	797	3,360	1,100	814	632
Alkalinity (meq/L ANC)																		
Count:	50	46	26	0	0	217	39	1	0	4	0	135	86	87	107	23	64	7
Median:	118	83	70	n/a	n/a	140	154	226	n/a	122	n/a	131	16	150	156	125	160	186
Mean:	117	92	81	n/a	n/a	140	134	226	n/a	108	n/a	128	49	152	146	139	169	137
Std. Dev.:	23	41	43	n/a	n/a	92	90	n/a	n/a	80	n/a	89	73	107	71	90	91	105
Min.:	45	33	18	n/a	n/a	0	3	226	n/a	12	n/a	n/a	n/a	3	3	1	2	5
Max.:	175	189	165	n/a	n/a	1,010	273	226	n/a	177	n/a	328	280	874	342	280	299	256
Calcium (mg/L)																		
Count:	46	32	15	9	2	191	34	1	6	4	0	122	74	62	118	38	91	7
Median:	28	29.8	26.0	78.0	30.0	58.0	39	60.5	7.53	50.5	n/a	46.4	23.2	34.3	63.5	50.5	63.0	65.0
Mean:	30.5	34.8	27.4	78.6	30.0	59.0	42.0	60.5	15.6	44.9	n/a	50.5	56.2	41.1	67.5	51.5	63.1	47.3
Std. Dev.:	9.2	19.4	12.7	35.6	17.0	40.3	32.5	n/a	19.1	32.0	n/a	55.1	82.0	23.2	61.8	32.4	34.6	29.4

State:	AL	AL	GA	IN	KY	KY	MD	NJ	NY	NY	NC	PA	PA	TN	TN	VA	WV	WV
Region:	V&R	P	V&R	P	V&R	P	V&R	V&R	V&R	P	V&R	V&R	P	V&R	P	V&R	V&R	P
Min.:	0.2	11.0	9.1	3.0	18.0	2.1	1.1	60.5	5.8	5.2	n/a	1.6	1.9	7.4	1.2	0.9	0.4	5.2
Max.:	55.0	100.0	47.0	120.0	42.0	462.5	122.0	60.5	54.3	73.5	n/a	558.0	390.0	130.0	451.0	142.7	130.0	72.0
Magnesium (mg/L)																		
Count:	46	26	18	9	2	220	34	1	6	4	4	117	86	84	119	72	91	7
Median:	10.9	3.5	7.7	31.0	3.6	6.3	7.0	35.0	1.81	5.3	0.6	11.4	8.0	11.6	5.2	12.4	8.4	12.0
Mean:	10.1	5.3	8.3	30.4	3.6	8.3	12.3	35.0	2.1	5.1	1.1	14.6	901	12.0	13.1	13.1	10.4	12.3
Std. Dev.:	4.7	8.4	4.3	13.4	1.9	15.4	14.8	n/a	1.4	3.8	1.2	16.2	2979	7.0	41.5	9.2	8.3	9.3
Min.:	0.2	n/a	1.8	0.3	2.2	0.6	0.1	35.0	0.9	0.8	0.4	0.5	0.5	1.9	0.5	0.2	0.4	0.3
Max.:	18.9	46.0	14.0	49.0	4.9	216.0	59.0	35.0	4.9	9.2	2.9	146.0	18,930	27.0	328.0	31.2	37.0	25.0
Nitrate as N (mg/L)																		
Count:	17	12	9	0	4	209	24	1	5	2	0	122	63	29	28	29	67	5
Median:	0.59	1.25	0.37	n/a	0.29	1.45	2.73	9.69	0.05	1.61	n/a	2.29	0.53	1.16	0.96	1.17	1.27	0.32
Mean:	0.67	1.36	0.44	n/a	0.31	1.92	3.66	9.69	0.15	1.61	n/a	2.61	1.39	1.07	1.09	2.00	2.45	1.60
Std. Dev.:	0.41	0.73	0.37	n/a	0.18	2.08	3.36	n/a	0.17	1.26	n/a	2.36	2.07	0.66	0.89	2.00	2.39	2.44
Min.:	0.18	0.17	0.02	n/a	0.11	0.00	0.02	9.69	0.02	0.72	n/a	n/a	0.04	0.08	0.02	0.06	0.02	0.29
Max.:	1.52	2.74	1.10	n/a	0.54	16.70	13.00	9.69	0.35	2.50	n/a	9.30	9.50	2.17	3.28	7.37	7.90	5.90
Chloride (mg/L)																		
Count:	54	51	16	9	4	361	37	1	6	4	10	136	82	62	118	79	81	3
Median:	2.4	3.2	5.1	4.1	8.0	4.8	7.5	22.5	27.8	98.8	5.3	4.0	5.0	2.4	2.7	3.7	3.4	7.5
Mean:	4.0	133	8.2	4.0	8.0	389	22.6	22.5	51.2	98.7	6.0	9.3	8.1	4.0	7.0	6.6	5.4	5.8
Std. Dev.:	8.0	439	6.1	1.2	4.8	2,601	34.7	n/a	78.9	1.2	4.0	13.4	7.1	4.1	15.8	11.8	6.6	3.3
Min.:	0.6	0.9	0.3	2.2	3.0	0.0	1.3	22.5	0.9	97.2	1.7	n/a	1.0	0.6	0.5	0.5	0.3	2.0
Max.:	60.0	2,127	19.0	5.3	13.0	32,800	180.0	22.5	210.0	100.0	16.0	77.0	33.0	21.5	141.0	76.4	38.7	8.0

State:	AL	AL	GA	IN	KY	KY	MD	NJ	NY	NY	NC	PA	PA	TN	TN	VA	WV	WV
Region:	V&R	P	V&R	P	V&R	P	V&R	V&R	V&R	P	V&R	V&R	P	V&R	P	V&R	V&R	P
Total phosphorus (mg/L)																		
Count:	7	8	2	8	n/a	93	14	0	6	2	0	98	12	49	40	22	41	0
Median:	0.02	0.039	0.77	0.095	n/a	0.096	0.101	n/a	0.05	0.204	n/a	0.040	0.040	0.037	0.033	0.026	0.021	n/a
Mean:	0.024	0.093	0.765	0.086	n/a	0.200	0.605	n/a	0.051	0.204	n/a	0.132	0.115	0.069	0.133	0.025	0.063	n/a
Std. Dev.:	0.009	0.117	1.068	0.058	n/a	0.234	1.287	n/a	0.019	0.277	n/a	0.305	0.194	0.090	0.266	0.018	0.121	n/a
Min.:	0.015	n/a	0.010	0.010	n/a	0.000	0.010	n/a	0.026	0.008	n/a	n/a	n/a	0.001	0.002	n/a	n/a	n/a
Max.:	0.038	0.280	1.520	0.193	n/a	1.000	4.100	n/a	0.084	0.400	n/a	2.450	0.665	0.452	1.123	0.064	0.670	n/a
Discharge (ft^3/s)																		
Count:	16	6	6	0	0	32	17	0	0	0	0	106	21	5	7	2	3	0
Median:	1.4	3.121	2.26	n/a	n/a	5.176	0.342	n/a	n/a	n/a	n/a	0.506	0.027	0.075	0.060	0.667	5.244	n/a
Mean:	1.785	5.609	1.732	n/a	n/a	28.472	1.503	n/a	n/a	n/a	n/a	2.462	0.107	0.523	0.495	0.667	9.161	n/a
Std. Dev.:	1.582	6.789	1.248	n/a	n/a	58.104	2.623	n/a	n/a	n/a	n/a	4.793	0.147	1.062	0.818	0.942	11.508	n/a
Min.:	0.091	0.176	0.115	n/a	n/a	n/a	0.003	n/a	n/a	n/a	n/a	0.002	0.004	0.001	0.015	0.001	0.123	n/a
Max.:	4.921	18.022	2.860	n/a	n/a	225.05	9.326	n/a	n/a	n/a	n/a	33.745	0.593	2.420	2.083	1.334	22.117	n/a

Acknowledgments

The authors thank Alan Rea, U.S. Geological Survey, for providing access to the full database of National Hydrography Dataset point features. Funding was provided by the Appalachian Landscape Conservation Cooperative and the U.S. Geological Survey National Cooperative Geologic Mapping Program.

References Cited

Christman, M.C., Doctor, D.H., Niemiller, M.L., Weary, D.J., Young, J.A., Zigler, K.S., and Culver, D.C., 2016, Predicting the occurrence of cave-inhabiting fauna based on features of the earth surface environment: PLoS One, v. 11, no. 8, p. e0160408, http://journals.plos.org/plosone/article?id=10.1371/journal.pone.0160408.

U.S. Geological Survey, 2017a, National Hydrography Dataset (NHD) web page, accessed February 7, 2017, at https://nhd.usgs.gov/.

U.S. Geological Survey, 2017b, Geographic Names Information System (GNIS) web page, accessed February 7, 2017, at https://nhd.usgs.gov/gnis.html.

U.S. Geological Survey, Environmental Protection Agency, and the National Water Quality Monitoring Council, 2017, Water Quality Portal (WQP) web page, accessed February 7, 2017, at https://www.waterqualitydata.us/.

Weary, D.J., and Doctor, D.H., 2014, Karst in the United States—A digital map compilation and database: U.S. Geological Survey Open-File Report 2014–1156, 23 p., available online only at http://dx.doi.org/10.3133/ofr20141156.

Hydrogeophysical Investigations in the Upper Arbuckle Group on the Tishomingo Anticline in the Central Arbuckle Mountains of Southern Oklahoma

By Kevin W. Blackwood, Kyle W. Spears, and Todd Halihan

Boone Pickens School of Geology, Oklahoma State University, 103 Noble Research Center, Stillwater, OK 74078

Abstract

The groundwater systems in the Arbuckle Group of the Tishomingo Anticline are largely controlled by karst conduits and caverns. Determining the subsurface extent of these systems and the effects geologic structures may have on their behavior is important for effective management of the karst groundwater and subterranean ecosystems. For this study we use the geophysical application of electrical resistivity imaging to aid cave survey efforts by locating anomalies in the subsurface to help determine the extent and boundaries of this karst system.

Introduction

The Arbuckle Mountains are a complex geologic province, characterized by thick sequences of intensely folded and faulted carbonates, sandstones, and shales that are Late Cambrian through Pennsylvanian in age. Karst features are common within most of the carbonates and cavernous groundwater systems have developed in most of the Early Ordovician carbonates. Delineating the subsurface extent of these cavernous groundwater systems is important for effective management of groundwater resources and for protecting the unique subterranean ecosystem.

Structural Geology

The Arbuckle Mountains form a roughly triangular area of approximately 2,600 square kilometers (km^2). The Tishomingo Anticline is an uplifted lobe of the central Arbuckle Mountains, encompassing an area of nearly 200 km^2. This anticline is bounded to the south by the Washita Valley Fault Zone and Sycamore Creek Anticline, to the north by the Reagan Fault and Mill Creek Syncline, to the east by the Troy Granite, and to the west by the Dougherty Anticline and Washita Valley Syncline (Ham and McKinley, 1954).

The Tishomingo Anticline is non-symmetrical and dips to the west at an average of approximately 12 degrees. The eastern half of this anticline has been entirely eroded down to granite. An axis is apparent in the northwestern exposure trending west-northwest with dips becoming steeper to the northwest at 25 degrees (Ham and McKinley, 1954).

All of the mapped faults associated with the anticline trend roughly northeast and are all pre-Desmoinesian (Early Pennsylvanian) in age. There are no northwest-trending faults (such as the Reagan and Washita Valley Faults) on the anticline, but instead these faults bound the anticline to the north and south, are of Missourian (Late Pennsylvanian) age, and dip to the south. These faults are also quite large and where drilled on the Arbuckle Anticline, vertical displacements of greater than 2,300 meters (m) have been measured (R.W. Allen and R.L. Newman, oral presentation, October 2012; R.W. Allen, Ardmore Sample Cut and Library, oral commun.).

Hydrology

The Arbuckle and Timbered Hills Groups on the Tishomingo Anticline are approximately 1,970 m thick and thicken toward the basin axis (Puckette and others, 2009). To the west of Highway 177 in T2S R3E Sections 11 and 25, deep wells drilled through the Simpson Group penetrated the top of the Arbuckle Group at a depth of –153 m mean sea level (MSL) and produced freshwater at depths of 237 m (36 m MSL) and 492 m (-208 m MSL)

(Puckette and others, 2009). Beneath most outcrops of the Ordovician Upper Arbuckle Group, groundwater can be found in caves at depths of less than 35 m. To the east, grading into outcrops of the Cambrian Middle/Lower Arbuckle Group, groundwater is reported at depths between 64 and 152 m. This change in water table depth without any significant rise in topographic relief could indicate that a hydraulic connection probably does not exist between the Ordovician and Cambrian Arbuckle Group aquifers on the Tishomingo Anticline.

Karst Hydrogeology

A large cave system, known locally as Mystic Cave, dominates much of the hydrogeology of the western/northwestern part of the Tishomingo Anticline. Two lesser known systems are located in the southern (Blue Hole Spring) and southeastern (Dotson Cave) portions of the anticline. In April 1990, a tracer test was performed in the cave using approximately 1 kilogram of sodium fluorescein dye (color index Acid Yellow 73). Twelve activated charcoal dye detectors were deployed in creeks, springs, and caves in the area. Two intriguing positive results were obtained at the overflow spring and at a lower level spring. Results of this tracer test are reported in Thomas (1991). For this investigation we focused on delineating the karst groundwater system associated with the Mystic Cave system in the western portion of the anticline.

Surface Hydrology

The largest fraction of surface water from the Tishomingo Anticline drains to Oil Creek (100 km^2) and Mill Creek (80 km^2), with a smaller fraction draining to Sycamore Creek (12 km^2), and the rest draining to Courtney Creek and Chili Creek. All streamflow is autogenic, with runoff derived directly from precipitation (about 93centimeters/year) or spring discharge. Numerous springs are present and potentially represent three major hydraulically nested systems within the Arbuckle Group, on the basis of spring elevation data. The base-level spring elevations associated with Mystic Cave occur at 271 m, while those associated with the springs in the Sycamore Creek area occur at 283–285 m. Springs draining to Mill Creek in the northeastern portion of the anticline occur near an elevation of 300 m. The lowest known spring on the anticline (Blue Hole) occurs in the southeastern portion of the anticline along the Washita Valley Fault Zone at an elevation of 235 m. According to Thomas (1994), a flowstone bank was discovered during a cave dive of Blue Hole Spring at a "depth of 20 feet." This indicates that the cave may share a hydraulic connection with a lower level spring, which could have lowered the water table in Blue Hole, resulting in the formation of flowstone as the conduit was exposed to the atmosphere, probably during a period of extreme drought.

Stratigraphic Source Material Indicators

Thick sequences of limestone and dolostone compose the greatest fraction of the Arbuckle Group on the Tishomingo Anticline, each with discernible mineralogical characteristics that make their sediments useful as stratigraphic source material indicators in fluvial systems. The most obvious of these mineralogical distinctions is the presence of glauconite and absence of chert in the Cambrian-age Arbuckle formations. The opposite is true for the Ordovician-age Arbuckle formations (Puckette and others, 2009). Certain groupings of these chert types may be used as reliable formation markers (Ham, 1950).

Using glauconite as an indicator of stratigraphic source material for the Arbuckle Group is appropriate because the Cambrian Lower Arbuckle Group is topographically isolated from the Ordovician Upper Arbuckle. As such, surface water flowing from the Cambrian Arbuckle Group does not drain to any of the recharge features known to connect to the cave and therefore, appears to receive no

surface-derived material from the Lower Arbuckle. This would indicate that any glauconite found in the cave would erode into the cave from the subsurface Cambrian strata.

Using glauconite as a stratigraphic source material indicator proves to be difficult, however, as it has very low weathering resistance. Chert on the other hand, is much harder and less soluble than carbonate rock and makes up the overwhelming fraction of mobile sediments within the cave. The chert gravel samples obtained from the cave contained a diverse suite of cryptocrystalline silicate materials, the most common being milky quartz, smoky quartz, and flint. Jasper and agate chalcedony are common as well as siliceous oolites, which are exclusive to the Cool Creek Formation (Decker, 1939). Many of the chert samples had coatings of manganese oxides and are more diverse than what is found in the Upper Arbuckle Group's West Spring Creek and Kindblade Formations, indicating they are most likely derived from the Cool Creek Formation (Decker, 1939). These gravels also range from sub-angular to well rounded, indicating fairly significant movement. Sediments were visually inspected for glauconite, but results were negative. The Cool Creek Formation crops out in an adjacent watershed from the known extent of Mystic Cave and it is this watershed where surface-derived chert gravels are entrained into swallow holes and sinkholes. Because these gravels have not been found to be carried into swallow holes or sinkholes in the Kindblade Formation, we conclude that any surface-derived chert gravel is entering the subsurface from the watershed overlying the outcrop area of the Cool Creek Formation.

Methods and Data Collection

The data collected and discussed in this abstract are the results of Electrical Resistivity Imaging (ERI) surveys and continuous water-level and electrical conductivity data collected with transducers installed in Mystic Cave. The ERI surveys are a surface geophysical method that is used to see changes in electrical resistance in the subsurface and potentially used to find and map conduits. The continuous water-level and electrical conductivity data collected from the cave streams can be used for understanding recharge episodes within Mystic Cave.

Electrical Resistivity Imaging (ERI)

The major contribution of our investigations to the study of Mystic Cave involves the use of ERI. Electrical Resistivity Imaging is an appealing method of unobtrusive subsurface data collection that provides continuous data related to properties of the underlying rock. Locations for the ERI lines are chosen based on the hydrologic, geologic, and structural characteristics of the site. These data help in the interpretation of the location of the water table, presence of void spaces, differentiation of rock units, and detection of structural features. The results of these surveys help to understand the overall hydrogeological context of the cave system. This technique is based on the measurement of electrical resistivity between electrodes. Resistance, in ohms, is a fundamental property of a volume of material defined as the material's opposition to the flow of electrical current (Reynolds, 1997). In a volume of material with length (L) and cross-sectional area (A), the material's resistance will be proportional to the potential drop of an induced electrical current (V/I), where V is the voltage and I is the current. Resistivity, in ohm-meters (ohm-m), is expressed as the resistance through a distance, making it independent of material geometry (Halihan and others, 2009). Advanced Geosciences, Inc. SuperSting 8-channel, a switch box, and 56 electrode surface cables were used to collect data. AGI EarthImager software and proprietary software owned by Oklahoma State University were used for data inversion.

Continuous Water Monitoring

Three transducers were deployed inside Mystic Cave, beginning February 20, 2016, through May 16, 2016. These transducers recorded water-level and electrical conductivity readings every 15 minutes. Data from these transducers provide important information about recharge episodes and how water chemistry changes based on electrical conductance. Several other analyses can be used to learn more about the characteristics of how the cave floods and basin characteristics.

Hydrogeophysical Investigations

During this study, four ERI surveys were conducted within the study area (fig. 1), although only three of these four surveys were processed for this project. Furthermore, only one of the survey image profiles is presented for this paper. The first two surveys were located over a survey gap between the upstream and downstream sections of Mystic Cave. The length to depth ratio of these surveys is 5:1, such that a 550-m survey will result in an image 110 m deep.

Electrical Resistivity Imaging Surveys

Survey ER1-550 (fig. 2) was completed on September 16, 2016, at a length of 550 m with 10-m electrode spacing. This survey was located 80 m south from Sump B with a heading of 152° N. This path was chosen with the objective to image the flooded downstream section and also to inspect a fault that paralleled and intersected sections of the cave.

Survey ER2-330 was completed on December 2, 2016, and was located approximately 80 m east from Sump A with a total length of 330 m and 6-m electrode spacing and a heading of 330° N. This path was chosen to determine if the passage upstream from Sump A might be following a fault or veer off to the south following the strike of the bedding.

Survey ER3-550 was completed on December 17, 2016, and located far to the northeast of the Mystic River passage. This survey was 550 m long with a 10-m electrode spacing at a heading of 330° N. This path was chosen to determine if the upstream sections might extend far to the north and share a relation with any of three faults, one of which hosts Bison Tooth Cave.

Electrical Resistivity Imaging Results

ER1-550—Electrical Resistivity Image 1 spans 550 m over a survey gap between the upstream and downstream sections (fig. 2). The 600–800-ohm-m area near the surface on the southeast end of the image is the result of an epikarst setting where the soil mantle contains a dense network of fractured limestone. On the right side of the image is a large conductive feature, 0–600 ohm-m, with a large “lobe” shaped feature extending to the left and a linear component extending to the bottom of the image. This is interpreted as a potential void. The upper 25 m of this void is expected to be air-filled, but displays a similar conductive signature as the phreatic zone. The reason for the air-filled void space to be more conductive than the surrounding rock matrix is a result of the cave walls being covered in films of mineral-enriched water leaching downward from the surface. Water with high concentrations of dissolved minerals is a good conductor, which would provide a medium for an electrical current to flow through.

The geometry of this feature is not seen in other ERI surveys from the Arbuckle Mountains (Halihan, and others, 2009). However, the profile of this feature shares a close resemblance to an underwater survey sketch of a large chamber by John Brooks during a cave dive in the 1990s.

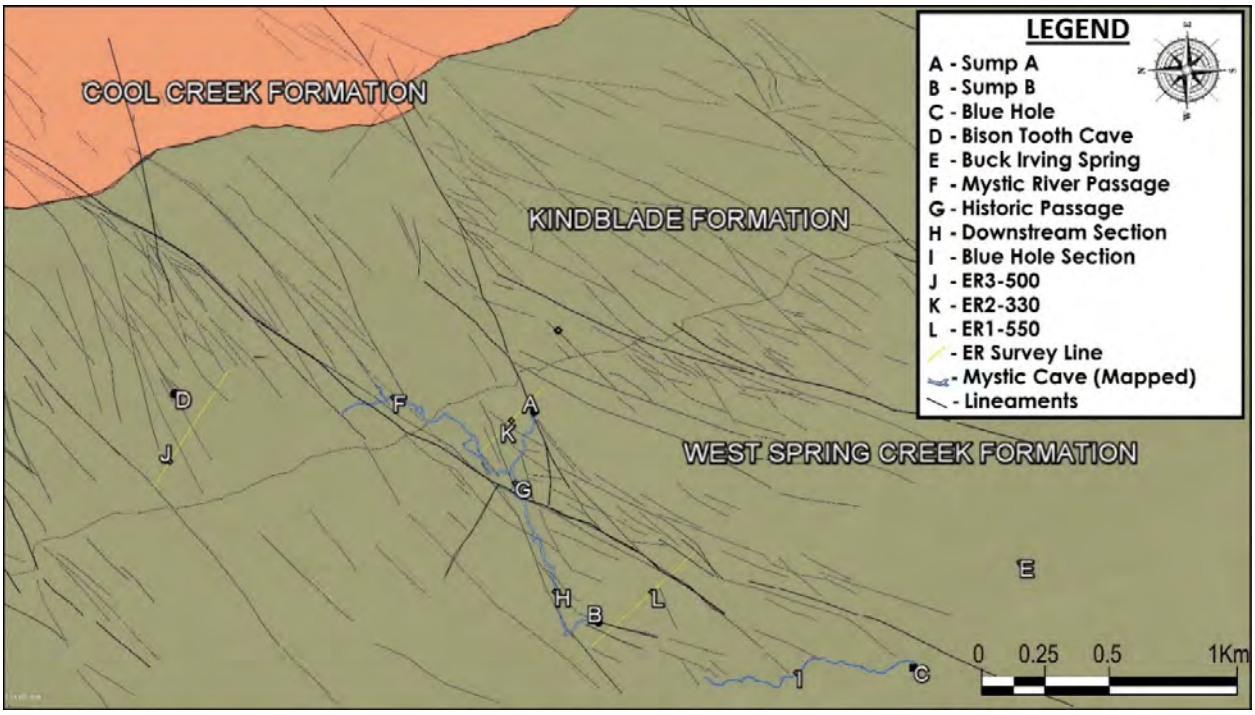

Figure 1. Geology and location of notable features within Mystic Cave and in the study area.

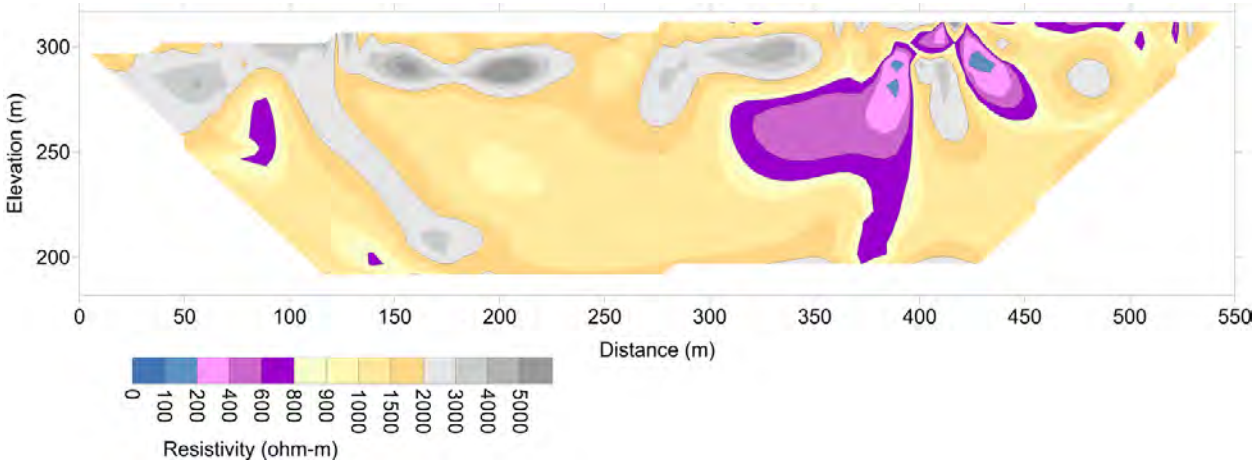

Figure 2. Electrical resistivity image from ER1-550. The image color is based on isolines of electrical resistivity ranging from 0–5,000 ohm-m. Cooler colors represent less resistive material and warmer colors represent more resistive material.

The geometry of this feature is not seen in other ERI surveys from the Arbuckle Mountains (Halihan, and others, 2009). However, the profile of this feature shares a close resemblance to an underwater survey sketch of a large chamber by John Brooks during a cave dive in the 1990s.

The linear feature ranging from 2,000–4,000 ohm-m on the northwest side of the image

starting at the surface and extending over 100 m below the surface is interpreted as a fault, which can be seen as a lineament on satellite imagery. The majority of the image ranges from 900–2,000 ohm-m, which is consistent with values for bedrock surveyed using this same technique near Connerville, OK (Halihan and others, 2009) and other electrical resistivity data collected in the Arbuckle Mountains.

ER2-330—This survey was located east of Sump A near a southeast-trending branch of the main cave passage. The epikarst zone is present across the top of the image; however, it thins in the center of the image and thickens toward the southeast and northwest ends of the survey. Two fractures are apparent at 82 m and 252 m on the image. Both fractures are visible via lineaments on satellite imagery. The cavern profile signatures seen in ER1-550 are not present at the expected depth of the cave, indicating the passage may have veered off to the south following the strike of the bedding.

ER3-550—This survey was located northeast of the Mystic River passage, and the data were acquired just west of Bison Tooth Cave. This image is similar to ER2-330 in that it shows competent bedrock with fractures and an epikarst zone along the top of the image. The resistivity values are lower than ER2-330, likely due to enhanced dissolution of the limestone. The conductive features near the surface occur at surface expressions of bedding planes and fractures, indicating that these areas are where recharge predominantly occurs. The cavern profile signatures seen in ER1-550 are not present at the expected depth of the cave. A resistive feature occurs at the appropriate depth along the Bison Tooth Cave fault, but it is thought that these resistivity values are too consistent with the surrounding bedrock. A conductive feature appears along a fault to the north, but this feature is clipped off from the profile due to the way the data was collected and processed and its significance remains inconclusive.

Continuous Water Monitoring Results

Increases in barometric pressure from the Sulphur Mesonet appear to correspond to water-level increases from transducer data in Mystic Cave. This indicates that atmospheric pressure is being exerted elsewhere, causing the water levels to rise in the cave in order to maintain pressure equilibrium throughout the system.

The transducers recorded a significant recharge event on March 8, 2016. This rain event raised water levels from 3.4 to 16.4 feet inside the cave (fig. 3). Inversely, electrical conductivity dropped from 450 to 320 microsiemens per centimeter. This indicates a major influx of rain water with low electrical-conductivity values.

Groundwater is typically more conductive than meteoric water as a result of dissolved minerals from the host rock. This is due to an increase in ionic strength, which increases electrical conductance. The greater the volume of fresh water entering the system the more the electrical conductance will decrease. As the meteoric water flushes through the system and flow returns to base-level conditions, electrical-conductivity values will begin to increase as they return to "background" levels.

Each rain event that causes an increase in water level also decreases the electrical conductivity, but not proportionally. The inconsistency between the responses in water level and electrical conductivity are likely a result of the way in which recharge enters the karst system.

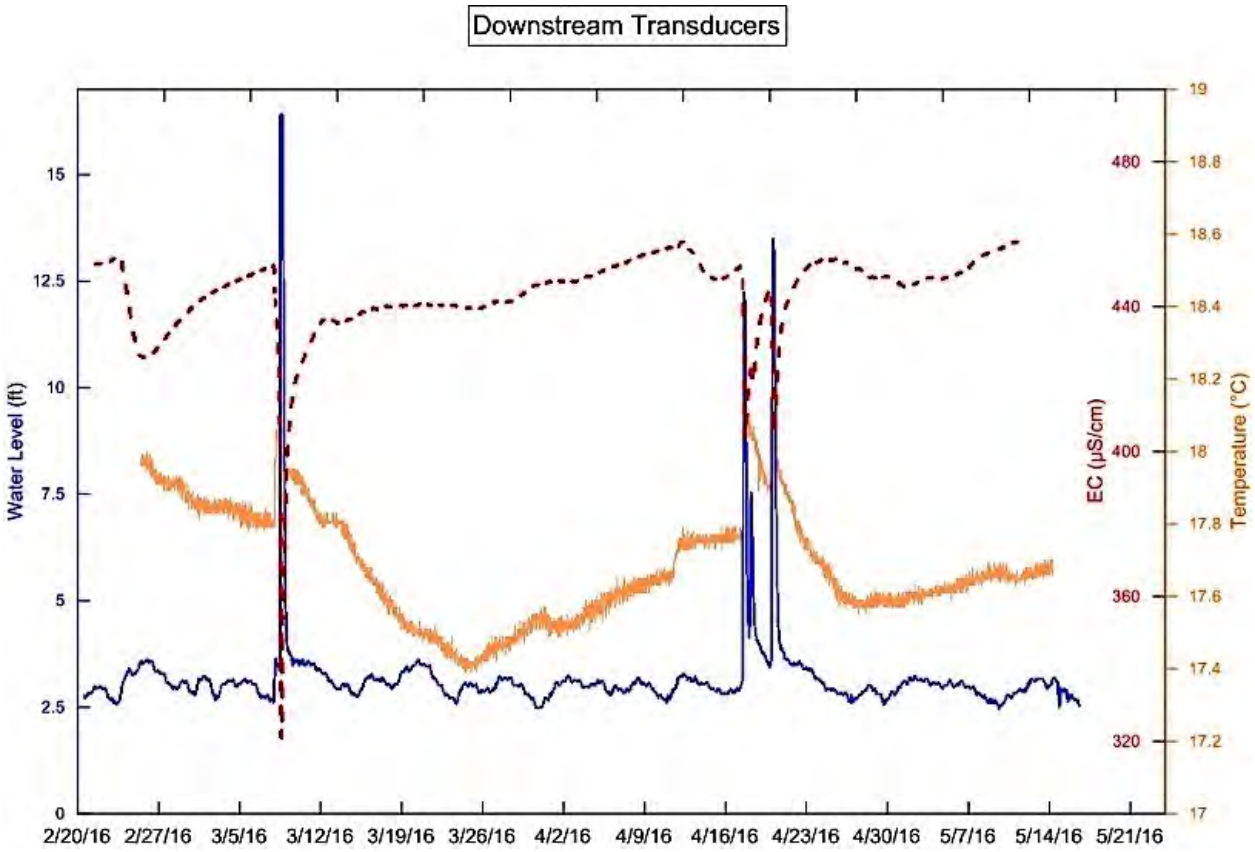

Figure 3. Graph showing water-level recordings from Mystic Cave. Water level is shown as a solid blue line, temperature is shown as a thick orange line, and electrical conductivity (EC) is shown as a red dashed line.

On March 7, 2016, a 2.08-inch rain event was recorded at the Sulphur Mesonet north-northeast station. On March 8, 2016, at approximately 10:00 am, water levels began to rise from 3.39 to 16.4 feet by 12:45 pm, resulting in a total increase of 13.01 feet in less than 3 hours. The water level remained steady at 16.4 feet until 4:30 pm and then began to decrease rapidly until nearly 2:00 am. By this time water levels were near static conditions.

The responses in water level and electrical conductivity from this rain event are substantially different than responses observed from April 17–20, 2016 (fig. 3). During this 4-day period, the Sulphur Mesonet Station recorded a total of 3.81 inches. The majority of the rainfall (2.93 inches) occurred on April 17, which resulted in a water-level increase from 3.02 to 12.25 feet in 4 hours. However, instead of a sudden spike and flat peak, the observed rise was a steep curve followed by another smaller steep curve 7 hours later. This pulse pattern indicates that water is initially entering a reservoir or impoundment before flowing into the cave. This could also explain why some precipitation events do not cause water-level rises and electrical conductivity drops and other precipitation events do. The shape of the water-level graph is also controlled by precipitation type. A sudden input of a large volume of meteoric water at a high flow rate will result in a similar pattern.

Discussion

From geospatial analyses of the geologic map and cave map layers, we could see that the passages of Mystic Cave were heavily controlled by faulting, with a few faults seemingly guiding the passages. We expected to see an influence of faulting in the ERI results,

but the results from ER1-550 were totally unexpected. A large anomaly with a conductive signature was apparent in the data and situated along the fault. The profile and description of this feature appear to be consistent with the 'Optimystic Chamber', a large cavern that was encountered by cave diver John Brooks during the 1990s. The upper reaches of this feature appear to extend very close to the surface with a discernable expression near the fault. Additional high-resolution ERI surveys are currently being planned for a non-invasive investigation.

The second anomaly at the left on figure 2 looks nearly identical in profile to the downstream section of the cave upstream from Sump B. This feature is interpreted as being consistent with the downstream section in expected location, depth, and profile.

The results from ER2-330 were mostly negative, although a shallow epikarst zone is apparent. However, with regard to Mystic Cave, it is thought that the cave beyond Sump A veers off the fault to follow the strike of the bedding to the south.

For ER3-550, we strayed far north of the main fault to survey three additional faults near Bison Tooth Cave to see if anomalies with conductive signatures might extended this far and to investigate the possibility of phreatic conduits associated with these faults. The results from this survey were mostly negative, but a few anomalies may require further investigation.

Comparing transducer water-level data with Mesonet rainfall data, a rain event on February 23 had no effect on water level within the cave. However, every rain event thereafter had a direct effect within the cave.

Upon analyzing these data, we postulated that a farm pond was required to fill before water could overflow the spillway into a sinkhole or swallow hole. However, at least three farm ponds are known on this ranch and each contains a swallow hole immediately below their dam although only one of those ponds was observed to overflow during the time of this investigation. The surface water from the overflowing pond terminates in a large swallow hole, which at the time of this paper, remains unexplored because of difficulty navigating surface debris. The swallow holes below the other two ponds have both been surveyed, but the cave nearest the main fault is currently the longest and most voluminous of all the caves surveyed during this investigation.

The main fault appears to drain a fragmented basin of approximately 2.6 km^2. This basin contains numerous sinkholes and swallow holes that drain areas within the basin ranging from a few square meters to several hundred square meters. We expect this basin to be the primary source of input for Mystic Cave. Several caves have been revealed after removing farm trash that was discarded into these sinkholes throughout the 20^{th} century. These caves are all of considerable length and trending in the direction of Mystic Cave.

Because of the size of the study area, large data gaps currently exist. However, by continuing this study, we plan to fill these gaps through additional ERI surveys, Ground Penetrating Radar (GPR) surveys, tracer tests, and by physically surveying and exploring the subsurface through caves. We expect Mystic Cave to contain many tributaries, which may become more numerous in the farther upstream sections beyond the Mystic River passage; many leads remain unexplored.

Acknowledgments

The authors thank the Boone Pickens School of Geology at Oklahoma State University, and the Chickasaw Nation. John Brooks, Mark Micozzi, Wayne Kellogg, Eddie Easterling, Gary Pratt, Stacy Blackwood, Britney Temple, Brad Woods, Lainee Sanders, John Richins, Randal Ross, Thomas Thompson, Camille Schlegel, Zay Shaeffer, and university students provided valuable assistance and data during the project. The authors are also especially grateful to landowners in the study area for property access.

References

Decker, C.E., 1939, Progress report on the classification of the Timbered Hills and Arbuckle Groups of rocks, Arbuckle and Wichita Mountains, Oklahoma: Oklahoma Geological Survey Circular No. 22, p. 27.

Halihan, Todd, Puckette, Jim, Sample, Michael, and Riley, Matthew, 2009, Electrical resistivity imaging of the Arbuckle-Simpson aquifer: Oklahoma State University, Boone Pickens School of Geology, 152 p.

Ham, W.E., 1950, Geology and petrology of the Arbuckle Limestone in the southern Arbuckle Mountains, Oklahoma: New Haven, Conn., Yale University Ph.D. dissertation, 162 p.

Ham, W.E., and McKinley, M.E., 1954, Geologic map and sections of the Arbuckle Mountains, Oklahoma, *in* Hydrology of the Arbuckle Mountains area, south-central Oklahoma: Oklahoma Geological Survey Circular 91, Norman, Oklahoma, University of Oklahoma, pl. 1 [separate].

Puckette Jim, Halihan, Todd, and Faith, Jason, 2009, Characterization of the Arbuckle-Simpson aquifer: Final report submitted to the Oklahoma Water Resources Board, Stillwater, Oklahoma State University School of Geology, 53 p.

Reynolds, J.M., 1997, An introduction to applied and environmental geophysics: Chichester, New York, John Wiley, 796 p.

Thomas, W.W., 1991, A preliminary investigation of the groundwater flow in the Arbuckle-Simpson aquifer, south central Oklahoma: Unpublished M.S. thesis, Western Kentucky University, p. 1–26.

Thomas, W.W., 1994, The 1992 project update, Murray County, Oklahoma: Central Oklahoma Grotto Newsletter, Oklahoma Underground, v. 17, p. 16–18.

Karst Aquifer Characteristics in a Public-Supply Well Field Near Elizabethtown, Kentucky

By Charles J. Taylor

Kentucky Geological Survey, Water Resources Section, 228 Mining and Mineral Resources Building, University of Kentucky, Lexington, KY 40506-0107

Abstract

Karstified limestones are among the most productive aquifers in the world and are important sources of water to many public-supply wells. However, water well drilling in extremely heterogeneous karst aquifers is typified by unpredictable results, with some wells providing very good water yields and water quality while others, often located only meters away, provide poorer yields and (or) water quality. Local scale (less than 100 meters) hydrogeologic factors that influence the distribution of permeability at, and flow of groundwater to, individual wells, and regional scale (100s to 1,000s of meters) factors that influence groundwater recharge, storage, and flow in karst aquifers contribute to this seemingly erratic variability.

Numerous boreholes and completed water wells have been drilled over the years in a public-supply well field near Elizabethtown, Kentucky, as the demand for public-supplied water has increased. The well field is underlain by karstic Mississippian limestones characterized by very low primary porosity and permeability but extensive fracture and dissolution porosity and permeability. Although four wells are regularly pumped, one primary well (PW1) supplies approximately 57 percent of the total daily average amount of water withdrawn from all wells, and nearly a quarter of the daily average amount of raw water processed by the water treatment plant. Borehole drillers' and caliper logs indicate that fractures and "brecciated" zones are more abundant and developed in the upper 25 meters of bedrock in PW1 than in most of the other wells. The reasons for this are not entirely clear; however, a video camera examination of PW1 confirmed the presence of several prominent solutionally widened bedding-plane partings and highly stratified zones of enhanced vuggy or brecciated porosity in the upper half of the well. Horizontal hydraulic conductivity in the karst aquifer at PW1 was estimated to be about 129 meters per day using pumping test data collected in October 2015 and leaky-confined analytical solution methods. In comparison, a hydraulic-conductivity estimate of about 8 meters per day was reported from results of a prior pumping test of an unused public-supply well (OW4) located approximately 1,000 meters south of PW1. Bedding-plane partings identified on a caliper log of well OW-4 appear to be more dispersed vertically and relatively less widened solutionally.

In spite of the unpredictability in yield among wells, and water-quality issues such as high turbidity and sulfate concentrations in some wells, the Elizabethtown area is considered one of the better locations for karst groundwater development in Kentucky. Local and regional hydrogeologic factors that contribute to this assessment include extensive shallow karst conduit development, solutional enhancement of areally extensive bedding-plane partings, bedrock structure and dip, proximity of mapped faults, and the presence of scattered but relatively thick residual and alluvial deposits of sand and gravel that overlie the karstic limestone in many locations.

A Review of Recent Karst Research in the China Geological Survey

By Junbing Pu, Zhongcheng Jiang, Daoxian Yuan, Cheng Zhang, Jianhua Cao, Riyuan Xia, Weihai Chen, Mingtang Lei, and Fuping Gan

Key Laboratory of Karst Dynamics, Ministry of Land and Resources & Guangxi Zhuang Autonomous Region, Institute of Karst Geology, Chinese Academy of Geological Sciences, Guilin 541004, China (www.karst.ac.cn; www.karst.edu.cn) and International Research Center on Karst under the auspices of UNESCO, Guilin 541004, China (www.irck.edu.cn)

Abstract

Karst covers approximately 344.3×10^4 km^2, nearly one third, of mainland China. It crosses tropical, subtropical, and temperate climate zones from south to north. Karst in China shows the following spectacular four characteristics that result in outstanding conditions for karst research: (1) old, compact, and hard carbonate rock, (2) dramatic uplift since the Cenozoic (Himalayan orogeny), (3) no glacial scouring or denuding, and (4) the heat-moisture combination of the Asian monsoon climate. Over the past 20 years, Chinese karst scientists have striven to better understand and apply these unique conditions to further academic progress through a series of novel scientific researches. Prof. Daoxian Yuan adopted the philosophy of Earth System Science to establish the field of Karst Dynamics, which is the theoretical basis of the UNESCO-based International Research Center on Karst. The China Geological Survey is leading the hydrogeological survey to study China's karst areas. Up to now, hydrogeological maps at 1:250,000 scale cover 78×10^4 km^2 and maps at 1:50,000 scale span 25×10^4 km^2 in the South China Karst. Preliminary data estimate total groundwater storage to be $1{,}620\times10^8$ m^3 in the South China karst area, which have helped to solve drinking- water-shortage problems for more than 22 million people. A new process of CO_2–H_2O–carbonate–aquatic phototrophic interaction has preliminarily estimated the atmospheric CO_2 sink in karst could be as large as 0.477 petagrams of carbon per year (PgC/yr) in the world's continents. The ecological rehabilitation of about 4×10^4 km^2 of karst rocky desertification in China was treated during 2006−2015 under the support of the Chinese central government. The South China Karst was successfully added to the World Natural Heritage List in 2007 and 2014. In addition, numerous caves have been surveyed and mapped in the past 10 years. Many new geophysical methods (e.g. multi-source high-power mise-a-la-masse method, and controlled source audio magnetotellurics) were successfully employed to raise the percentage of well completions and solve water-shortage problems in mountainous karst areas. Based on the results of environmental geological surveys in recent years and historic data, Chinese karst scientists have analyzed the sinkhole risk hazard for the whole country. Some new ideas and techniques were broadly employed to monitor and treat sinkhole hazards. In addition to reviewing the recent advances in karst research in China, this paper shows some opportunities and directions for further international cooperation.

Introduction

Globally, karst covers roughly 2.2×10^7 km^2 or about 10 to 15 percent of the world's continental areas (Ford and Williams, 2007). China has one of the largest karst areas in the world, with more than 344.3×10^4 km^2 of carbonate rock, which covers one-third of the total country (Yuan and others, 1991). The karst in China extends from the reef islands at 3° N in the South China Sea to the Lesser Khingan Mountains at 48° N, and from the Pamirs at 74° E across to Taiwan Island at 121° E (fig. 1). There are two large areas of concentrated karst. One is the karst area in the Shanxi Plateau and adjacent regions, also called the North China Karst, which have a combined area of nearly 47×10^4 km^2 and is a semi-arid to arid karst type. The other is the famous South China Karst with an area of nearly 55×10^4 km^2, mainly lying in Guizhou, Yunnan,

and Guangxi provinces, and also includes parts of Chongqing, Sichuan, Hunan, Hubei, and Guangdong provinces. The South China Karst is famous for its outstanding series of karst landforms such as fenglin (peak forest), fengcong (peak cluster), tiankeng (huge doline), deep karst gorges, caves, and the stone forest, in humid and semi-humid to tropical and subtropical climates. In addition, there is a large karst area on the Tibetan plateau, which is called plateau karst in China, with a total area of 11.5×10^4 km^2.

Karst in mainland China covers a very large area, spanning from south to north and from west to east because of the broad distribution of carbonate rock. As a result of the differences in latitude, altitude, distance from the ocean, and climate, the characteristics of karst development in China, especially karst feature complexity, are quite varied from place to place (Yuan and others, 1991). China karst has an unusual character that arises from both its geological and climatic history. The following four synergistic characteristics of karst in China are distinct from other karst areas in the world (Yuan and others, 1991, 1998). The first is that most of the carbonate rocks in mainland China are pre-Triassic age, compact and hard, especially those of Paleozoic age, the exception being the Tibetan plateau, where the majority of the carbonate rocks are of Jurassic and Cretaceous age. The second is the dramatic Cenozoic uplift of mainland China, especially in western China, which has not only brought about conspicuous karst landforms but has also placed the karst features formed in different geological ages at different altitudes. The third is that most of the karst areas of mainland China escaped scouring and denudation during the last glaciation, which allowed the preservation of a remarkable diversity of karst features developed in rocks of different geological ages. The fourth is that because of the Asian monsoon, the combination of heat and moisture in mainland China provides strong external factors that support karst processes. Thus, many features of the Chinese karst occur only in China and are not truly comparable with landforms of somewhat similar superficial appearance in other parts of the world (Yuan and others, 1998).

Karst environments are quite fragile and have been especially affected by fast economic development and urban expansion since the 1980s, and the frequently extreme climate events under the impact of global warming in mainland China. While people enjoy attractive and beautiful karst landscapes in China, a series of environmental and engineering geological problems in karst areas have risen, including drought, flooding, sinkhole collapse, rocky desertification, water pollution, and cessation of spring flow.

Drought and flooding are usually more extreme in karst areas because of the dual impact on surface and subsurface waters. Liu and others (2014) stated that karst areas in Yunnan, Guangxi, and Guizhou provinces had generally become drier (regional mean annual precipitation decreased by 11.4 mm per decade) and experienced enhanced precipitation extremes between 1951 and 2012.

Sinkhole problems have long plagued China and challenged its geologists and engineers. The total area at high risk for sinkhole collapse is 34.3×10^4 km^2, which is mainly in Guangxi, Yunnan, Guizhou, Hunan, and Hubei provinces. Since the 1950s, 3,315 sinkhole events and at least 40,000 sinkhole pits have been documented, of which more than 70 percent were triggered by human activities, especially groundwater extraction and tunneling, such as mining and railway tunnels. Also, extremely heavy rainfall is another key trigger for some natural sinkholes formed in the recent decade (China Geological Survey, 2016a).

Rocky desertification is a serious ecological disaster in the South China Karst. It refers to the transformation of a karst landscape covered by vegetation and soil into a rocky landscape almost devoid of soil and vegetation in tropical and subtropical karst regions (Yuan, 1997a; Wang and others, 2004; Jiang and others, 2014). The area of rocky desertification in the South China Karst was 9.2×10^4 km^2 in 2015, mainly in Guizhou, Yunnan, and Guangxi provinces (China Geological Survey, 2016b).

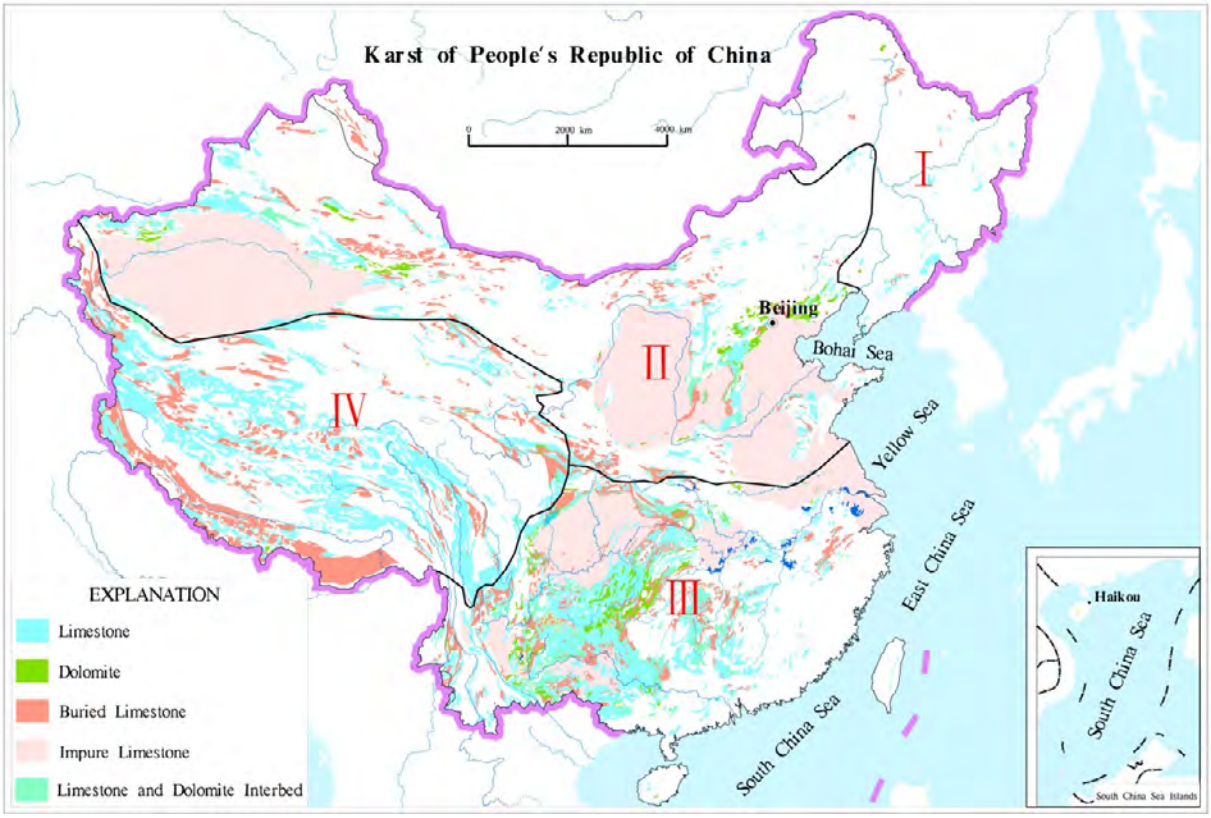

Figure 1. Karst map of People's Republic of China, showing I, Wet temperate zone karst region, II, Semi-arid and arid karst region, III, Tropical and subtropical karst region, and IV, Alpine and cold karst region (modified from Jiang and others, 2011).

Water pollution is also a severe problem in China's karst areas. Guo and others (2010) pointed out that there are four main types of contamination of karst aquifers: (1) rural and agricultural pollution, (2) pollution from urban development and industry, (3) pollution from mining, and (4) accidental groundwater pollution. In addition, organochlorine pesticides (OCPs) and antibiotics have been found in karst waters in recent years (Hu and others, 2011; Ma and others, 2015; Sun and others, 2016).

Cessation of flow from major karst springs and water-bursting during tunneling are often important environment problems. In the North China Karst there are more than 200 karst springs. Tens of them are the main local sources of water, but most of them have gone dry in the past few decades (Yuan and others, 1991). Liang and others (2013) stated that 30 percent of karst springs have dried up, discharge of 80 percent of karst springs has been dramatically reduced, and regional karst groundwater levels have been continuously declining at a rate of 1 to 2 meters in each aquifer over the past 30 years.

Environmental geological problems in karst areas are always related to changes in natural equilibrium of the karst environmental system. Moreover, they are always related to karst processes (Yuan and others, 1991). Facing these problems in China's karst areas, the China Geological Survey has funded a series of scientific investigation projects on karst hydrogeology, sinkhole collapse, rocky desertification treatment, karst processes and the carbon cycle, and karst landform and cave protection, which yielded fruitful achievements and attracted much attention from home and abroad. Chinese karst scientists work hard to solve these complex problems and to contribute to the development of global karst research through academic ideas, new theories, case practices, international cooperation and exchanges, and the sharing of technology and knowledge.

Since 1990, the famous Chinese karst scientist Prof. Daoxian Yuan has successfully proposed and hosted three successive international karst projects of the International Geoscience Programme (formerly International Geological Correlation Programme [IGCP]) of UNESCO:

1. IGCP 299 "Geology, Climate, Hydrology and Karst Formation" (1990−1994),
2. IGCP 379 "Karst Processes and the Global Carbon Cycle" (1995−1999), and
3. IGCP 448 "World Correlation on Karst Geology and its Relevant Ecosystem" (2000−2004).

In addition, he has also taken part in other two successive karst-related IGCP projects as co-leader: IGCP 513 "Global Study of Karst Aquifers and Water Resources" (2005−2009) and IGCP/SIDA598 "Environmental Change and Sustainability in Karst Systems" (2011−2015). These projects not only strongly promote the international development of karst science, but also put forward a new area of study in karst science—Karst Dynamics Theory.

The International Research Center on Karst (IRCK) was established in 2008 as a new international academic research organization on karst under the auspices of UNESCO, under the Institute of Karst Geology, Chinese Geological Academy of Sciences in Guilin, Guangxi, China. Karst Dynamics Theory is the basis for IRCK's programs. For decades, Chinese karst scientists have been working hard to focus on the theoretical connotations of karst dynamics, hydrogeological surveys and groundwater exploration, global changes, rehabilitation of degraded karst ecosystems, karst environmental protection, and the prevention and control of karst geological hazards.

Karst Dynamics Theory

Prof. Daoxian Yuan proposed and created Karst Dynamics Theory in 1997 (Yuan, 1997b), which adopted the philosophy from Earth System Science. Karst dynamics is the discipline that studies the structure, functions, and rules of running and applying a Karst Dynamic System (KDS) (fig. 2) (Yuan, 1997b). A KDS could be defined as the transportation and transferring system of material and energy that controls the formation and evolution of karst, which occurs at the interfaces between the lithosphere, hydrosphere, atmosphere, and biosphere, but is constrained by existing karst features, and dominated by carbon cycling, water cycling, and calcium (magnesium) cycling (Yuan, 1997b) (fig. 2). Carbon dioxide (CO_2) and H_2O are the two main driving forces of the KDS, which interact within the different spheres. Therefore, from the viewpoint of Earth System Science and Karst Dynamics, karst processes involve the dissolution or deposition of carbonate rock in the carbon cycle with its coupled water and calcium (magnesium) cycles. Karst features are the result and evidence of these processes on carbonate rock. An intrinsic feature of the KDS is the sensitivity of its responsiveness to surrounding environmental changes; as a result, karst processes play an important role in the global carbon and water cycles (Yuan, 1997b).

The KDS is an open, tri-phase disequilibrium system, which consists of gaseous, aqueous, and solid phases. The gaseous phase consists of gases involved in karst processes, predominantly CO_2, and is part of the atmosphere. It links with the biosphere through photosynthesis and decomposition, and links to human activities through the making of lime and cement, and the burning of fossil fuel, thus involving them in karst processes. The aqueous phase is the water flow that contains Ca^{2+}, Mg^{2+}, HCO_3^-, CO_3^{2-}, H^+, and dissolved CO_2 as its major constituents. It is a part of the global hydrosphere. It is not only the core of the KDS, but also serves as a link between the lithosphere, atmosphere, biosphere, and human activities, and includes them in karst processes, particularly dissolution and deposition. The solid phase is dominated by different types of carbonate rocks and other soluble rocks in the lithosphere, and also linked to the mantle through deep faults and joints, thus gaining additional CO_2 from deeper parts of the Earth.

The four principal functions of the KDS were established by numerous studies (Yuan, 1997b). The first function is to better understand the formation of karst features (or karstification), which cause environmental and geological problems. The second is to regulate the content of greenhouse gases (mainly CO_2) in karstification, and thus help to mitigate environmental acidification. The third is to evaluate the migration, enrichment, and precipitation of certain elements that influence both the formation of mineral deposits and biodiversity in karst areas. The final principal function of the KDS is to record the course of climatic and environmental changes (paleoenvironmental reconstruction or rehabilitation), and thus provide a basis for the study of global change. Thus, comparing traditional karst research from the academic perspectives based on geological-geographical descriptions, Karst Dynamics expand upon research areas and highlight interdisciplinary aspects, which is consistent with the tenets of modern science. In general, an accurate understanding of the structure, functions, and rules of running a KDS is the key to scientifically and reasonably solving resource and environmental problems in karst areas at local to global scales.

Hydrogeological Surveys in China's Karst Areas

As a developing country, China is making a huge effort to create hydrogeological maps of its karst areas at multiple scales. The China Geological Survey is the leading agency on hydrogeological surveys and research in China's karst. Many surveys were finished between 2003 and 2015, at a total expenditure of 480 million renminbi (RMB) ($69.3 million U.S.). Up to now, hydrogeological maps at 1:250,000 scale cover 78×104 km^2 and maps at 1:50,000 scale span 25×104 km^2 in the South China Karst (Xia, 2016). These maps show that total groundwater storage is $1{,}620\times108$ m^3 in the South China Karst and the total sustainable yield is 536.0×108 m^3/yr; presently, only 12.1 percent is utilized. In the North China Karst, the total sustainable yield is 103×108 m^3/yr, 66.0 percent of which is utilized (table 1, fig. 3). These values show that a huge potential reservoir of karst groundwater is available for use.

An outstanding characteristic of karst groundwater systems in the South China Karst is the well-developed cave streams (Yuan and others, 1991). The latest studies show that there are 2,763 subterranean streams with a total groundwater discharge of 470×10^8 m^3/yr during the dry season, which is nearly the volume of the Yellow River. However, only 10 percent of the subterranean streams are sustainably exploited at present (Xia, 2016). In contrast, the outstanding characteristic of karst groundwater systems in the North China Karst is the large karst springs with catchment areas greater than 1,000 km^2. There are 41 karst springs with a discharge of more than 1,000 liters (L)/s in north China and 171 karst springs with a discharge of more than 100 L/s (Liang and others, 2013).

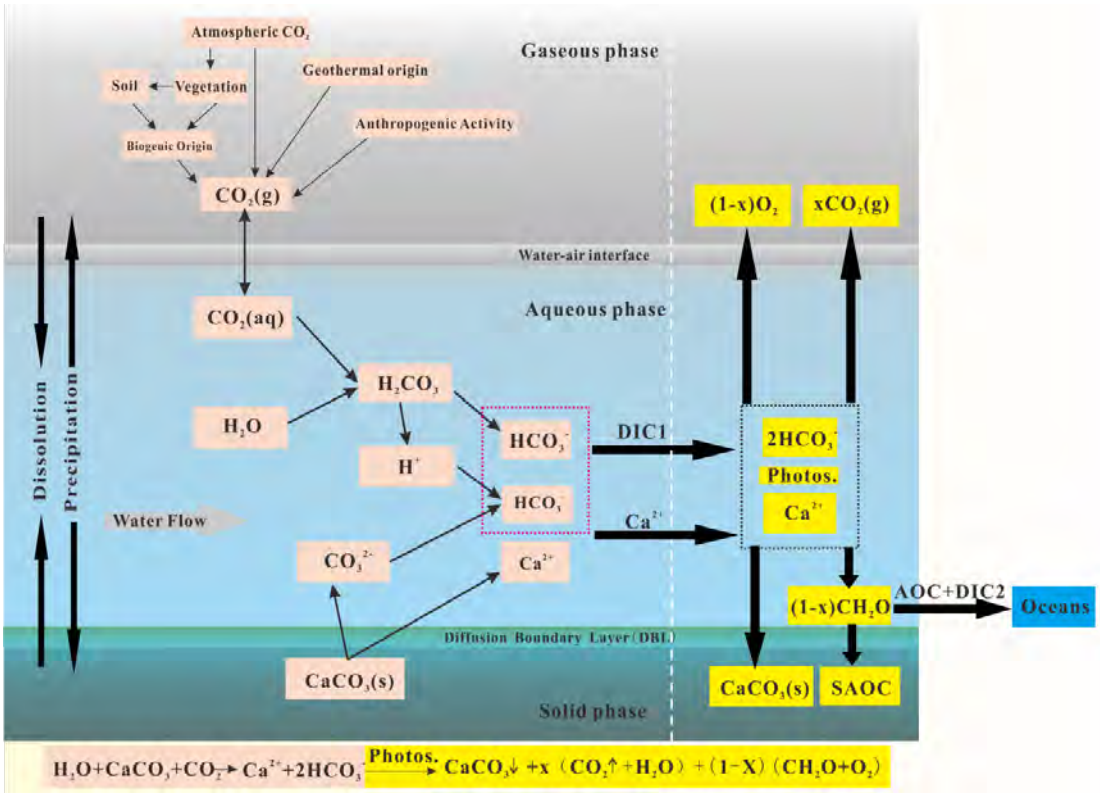

Figure 2. Conceptual model of a Karst Dynamic System (modified after Bögli, 1980; Yuan, 1997b; Liu and Dreybrodt, 2015). The area left of the white dashed line shows the basic framework, rules of material origin, and movement in a Karst Dynamic System. The area to the right of the white dashed line shows the fate of DIC (HCO_3^-) from karst processes, which is utilized by photosynthesis of aquatic phototrophs. The diffusion boundary layer (DBL) and water-air interface are both key boundary layers. Photos: photosynthesis by aquatic phototrophs; AOC: autochthonous organic carbon; SAOC: sedimentary autochthonous organic carbon; DIC1: dissolved inorganic carbon concentration in the groundwater system; DIC2: dissolved inorganic carbon concentration in the surface-water system.

Karst groundwater has been captured for use in four primary ways, depending on local hydrogeology, geology, landforms, and the ecological environment:

1. damming of karst conduits to create underground or surface-underground reservoirs,
2. tank storage of high-elevation epikarst springs in peak-cluster areas where water shortages are severe,
3. pumping of vadose and phreatic zone groundwater in peak-forest areas, and
4. installation of grout curtains in fissured karst aquifers to concentrate groundwater discharge and hydraulic head to fill water-supply tanks.

According to distribution, exposed features, and demands for karst water, the groundwater exploitation and utilization ways mentioned above are widely used in the karst areas of southwest China. After 1999, over 10 large capture and exploitation projects for subterranean stream or karst spring use have been successfully constructed in accordance with the above ways (fig. 4) (Jiang and others, 2006; Wang and others, 2006; Mo and others, 2006). These groundwater capture systems have greatly improved the water-supply capacities and effectively solved the water-shortage problems of 22 million people in the mountainous karst areas

in south China. In addition, scientific studies of the karst water cycle along with modeling simulations and water quality have sharply increased since the 2000s. Some new techniques in karst groundwater studies, such as stable isotopes, non-traditional isotopes, rare earth elements, radioisotopes, persistent organic pollutants, biomarkers, microbiology, antibiotics, and others, have been widely used in karst hydrogeology. New ideas, such as global and extreme climate change, along with ecological water requirements in a karst system, also have been incorporated in new karst water research. In addition, an outstanding benefit of karst hydrogeology in China is that it connects closely with the needs of social and national economic development, and can solve many practical and theoretical problems.

The Carbon Cycle in Karst Systems

The role of karst processes in global climate change has increased scientific interest in the carbon cycle in karst systems for over 20 years. A preliminary conceptual model of the karst carbon cycle is illustrated on figure 2. In the 1990s, IGCP 379 preliminarily estimated that the global quantity of atmospheric CO_2 trapped by "carbon dioxide–water–carbonate (CO_2– H_2O – CO_3)" is roughly 0.61 petagrams of carbon (PgC)/yr (Yuan, 1997; Yuan and Jiang, 2000). However, at that time, the estimate only considered an inorganic process whereby CO_2 is dissolved and consumed by carbonate rocks on continents and transformed to HCO_3^- in water. Curl (2012) suggested that these processes cannot sequester carbon in karst systems. Veni (2013) proposed that most carbon moves rapidly through karst aquifers, but carbon may be stored in sediments and in secondary calcite deposited in caves, with a total stored global organic carbon volume of 2.2×10^2 km^3, and a potentially greater volume in paleokarst hydrocarbon reservoirs.

Liu and others (2010, 2015) described a new model of CO_2–H_2O–carbonate–aquatic phototroph interaction, which suggests that the rapid kinetics of carbonate dissolution, coupled with the aquatic photosynthetic uptake of HCO_3^-, could provide a net carbon sink in karst stream organisms and sediments. Karst groundwater is often rich in dissolved inorganic carbon (DIC) because of carbonate dissolution by carbonic acid generated during the hydration of CO_2. This DIC can be consumed by submerged aquatic phototrophs because the clear water allows light to penetrate stream benthic environments. The consumed DIC could then be sequestered as organic carbon (Jiang and others, 2013; Liu and others, 2015; Liu and Dreybrodt, 2015; Yang and others, 2015; Pu and others, 2017). Thus, the combination of inorganic and organic processes is a potentially bright prospect for sequestering carbon in surface karst systems. A preliminary estimate of the net atmospheric CO_2 sink produced by this new model could be as large as 0.477 PgC/yr on continents (Liu and Dreybrodt, 2015), which accounts for about 17 percent of the terrestrial missing carbon sink and is comparable with the carbon sink in the world's forests (Pan and others, 2011). In addition, catchment-scale estimates of the carbon sink in karst systems has been ongoing since 2013. The Institute of Karst Geology of the Chinese Academy of Geological Sciences is doing such research in the Yangtze River, Yellow River, and Pearl River. Tracing organic carbon sources (autochthonous or allochthonous), defining inorganic carbon-organic carbon mutual transformation, quantifying the impacts of sulfuric acid and nitric acid involvement and their promotion of carbonate dissolution reactions, and determining the regulating potential of carbon sinks with respect to climate and land use, are becoming a new frontier in Chinese karst research.

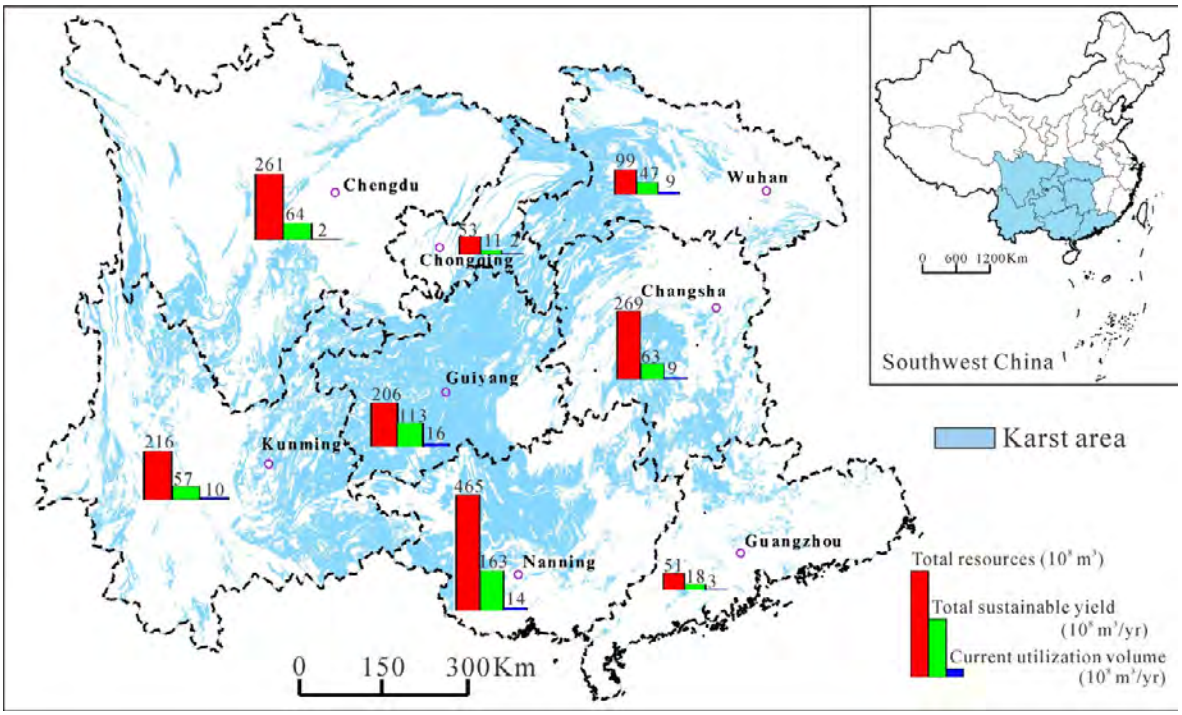

Figure 3. Groundwater resources in the South China Karst (modified from Xia, 2016).

Table 1. Groundwater resources in China's karst areas.

[modified from Yuan and others, 1991; Xia, 2016]

Area	Province (region or municipality)	Total resources (10^8 m^3)	Total sustainable yield (10^8 m^3/yr)	Current utilization volume (10^8 m^3/yr)	Surplus yield (10^8 m^3/yr)
South China Karst	Yunnan	216.0	57.0	10.0	47.0
	Guizhou	206.0	113.0	16.0	97.0
	Guangxi	465.0	163.0	14.0	149.0
	Hunan	269.0	63.0	9.0	54.0
	Hubei	99.0	47.0	9.0	38.0
	Chongqing	53.0	11.0	2.0	9.0
	Sichuan	261.0	64.0	2.0	62.0
	Guangdong	51.0	18.0	3.0	15.0
	Total	**1,620.0**	**536.0**	**65.0**	**471.0**
North China Karst		128.0	103.0	68.0	35.0

Figure 4. Exploitation and utilization of Pijiazhai karst spring (flow of 1.0 to 1.9 m^3/s) for water supply and irrigation in Luxi Basin, Yunnan Province, China. It was exploited and utilized by installation of a grout curtain in order to concentrate groundwater discharge.

Control of Rocky Desertification

Rocky desertification is an extreme degradation of the karst landscape and its surface ecosystem through soil erosion (figs. 5 and 6). To address this problem, the Chinese government has launched a national program of integrating rocky desertification controls in karst areas. The first stage of work occurred during 2006−2015. In this stage, according to the local characteristics of the surface karst ecosystem and rocky desertification processes in the South China Karst, the critical countermeasures can be summarized as follows:

1. effective exploitation and sustainable utilization of water resources,
2. protecting soil cover,
3. recovering native vegetation or developing sustainable economic plant communities, and
4. building win-win relationships between regional surface ecologies and economies, with reducing poverty as the ultimate goal (Jiang and others, 2014).

As of 2015, the Chinese central government had invested 11.9 billion RMB ($1.73 billion U.S.) and received 130 billion RMB ($18.9 billion U.S.) from local governments and societal donations to implement that work. The 4×10^4 km^2 area of rocky desertification had received first time treatment. Their remarkable results included preliminary ecological rehabilitation, reduction of bare rock ratios and rates of soil erosion, and a decrease in local poverty. Although these results are very good, some new problems have emerged:

1. although the trend of rocky desertification was curbed as a whole, rocky desertification in remote mountainous regions remained severe.
2. surface ecosystem functions have not been established in rehabilitation areas after surface revegetation.
3. there are no effective countermeasures to prevent soil piping through fissures, fractures, or conduits into underground spaces or aquifers.
4. water shortages are still severe in mountainous regions, while only 15 percent of the groundwater is utilized.
5. the win-win principle for restoration of the surface ecology lacks sustainable impetus as some cash crops face a series of problems such as continuous cropping of some crops and invasion of exotic species.

In 2016, the Chinese government started the second stage of work, which extends from 2016 to 2020. This work will attempt to solve the above five problems and further focus on surface karst ecosystem stability and function, rational utilization of water and soil resources, and sustainable development by the people and nature in karst areas.

Karst and Cave Heritage in China

Zhang (2010) reported more than 3,000 caves in China, with a combined length of more

than 4,000 km. Nearly all are south of the line from the Qinling Mountains to the Huaihe River, which is the important geographical boundary between the semi-arid temperate zone to the north and the humid-subtropical zone to the south (Zhang, 2010). Among the known caves, 78 are more than 5 km long, including 23 more than 10 km long. The longest cave is Shuanghe Cave, 186 km long, in Suiyang County, Guizhou Province. The deepest cave is Tianxing Cave, 1,020 m deep, in Wulong County, Chongqing municipality. The largest cave room is the Miao Chamber with a volume of $1{,}078\times10^4$ m^3, in Gebihe Cave in Ziyun County, Guizhou Province (Vergano, 2014).

Figure 5. Rocky desertification landscape in Guizhou Province, China. (photograph by Prof. Kangning Xiong).

The attractive karst landscapes in China are the product of a long and complex geological history with a unique natural aesthetic beauty. The global significance of China's karst is recognized by the World Heritage listing of several areas. The Huanglong and Jiuzai karst areas were listed in 1992 for their beautiful travertine landscapes along the east edge of the Tibetan plateau with average elevations of 3,000 m. Parts of the South China Karst were listed as World Heritage sites in 2007 (Wulong, Libo, and Shilin) and 2014 (Guilin, Shibin, Huanjiang, and Jinfo Mountain). Additionally, China has 47 national geoparks that feature karst landscapes as the core or major part of their landscapes, plus 7 global geoparks in karst (West Mountain of Beijing, Zhangjiajie, Yuntaishan, Leye-Fengshan, Xingwen, Shilin, and Zhijin Cave).

Karst Groundwater Exploration

One of the big challenges in karst hydrogeology is understanding the heterogeneity of karst aquifers and raising the percentage of productive water wells. Thus, accurate characterization of karst aquifers is a crucial international need. A series of geophysical methods, such as high-density resistivity and transient electromagnetics, are widely used to explore the characteristics of karst aquifers. In recent years, karst scientists at the Institute of Karst Geology have developed many new geophysical methods to reveal the location, depth, extent, and structure of karst aquifers, including the multi-source high-power mise-a-la-masse technique (Han and others, 2016) and controlled source audio magnetotellurics (CSAMT) (Gan and others, 2017). These methods effectively raised the exploration accuracy for karst groundwater, and the average percentage of well completions has been greatly increased from 30 percent to over 70 percent in the South China Karst.

Severe droughts occurred in southwest China karst areas in 2010 and in north China karst areas in 2011. The China Geological Survey organized more than 2,000 geologists and hydrogeologists to seek karst groundwater in these disaster-stricken areas. The geophysical exploration techniques mentioned above were employed, and successful rates of well completion of 87 percent and 95 percent, respectively, were achieved in those areas to greatly relieve water-shortage problems.

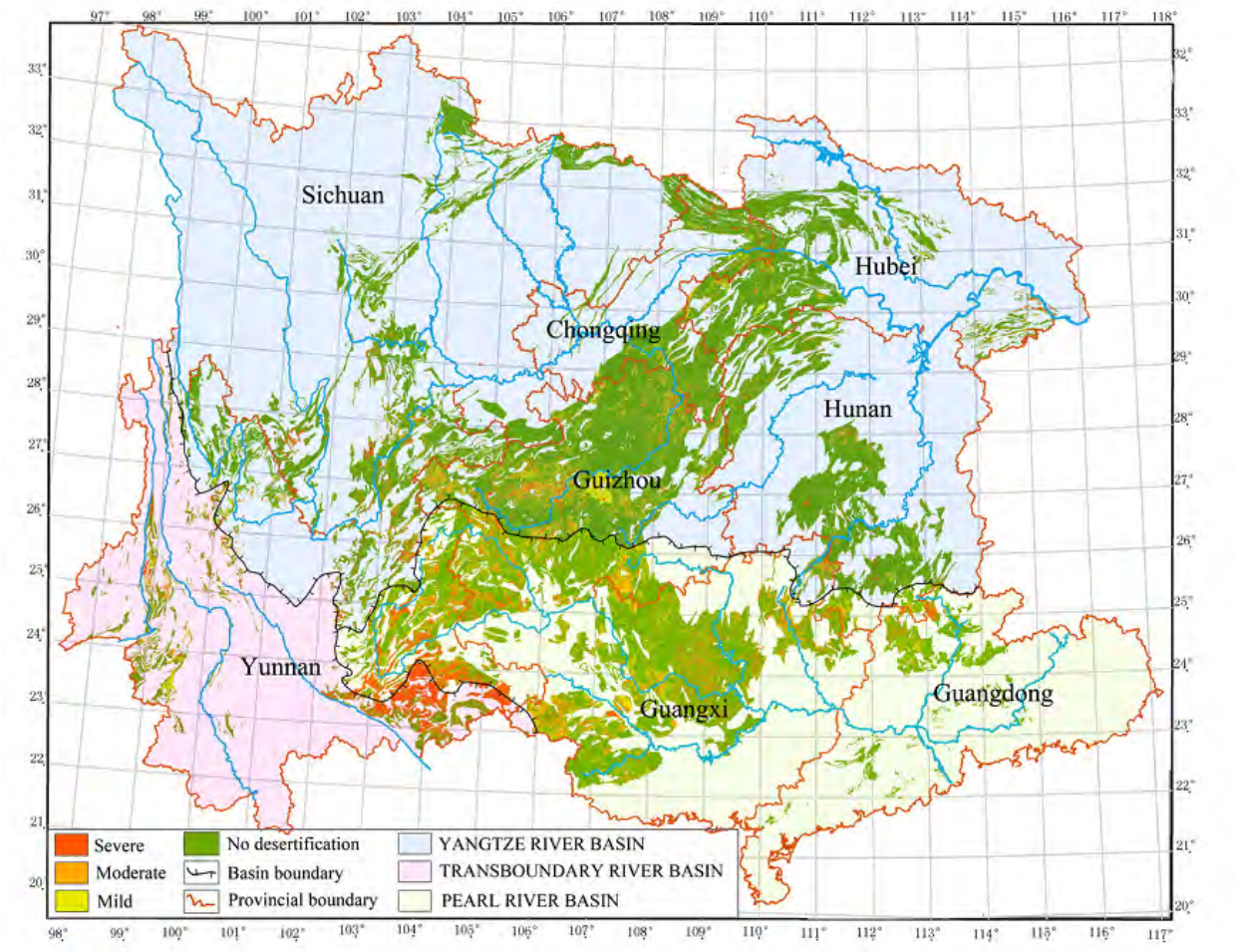

Figure 6. Distribution and classification of rocky desertification areas in southwest China (Jiang and others, 2014).

Sinkhole Collapses

From the 1950s to 2016, 3,315 sinkholes and at least 40,000 sinkhole collapses have been documented in China (China Geological Survey, 2016a), spanning 22 provinces, regions, or municipalities. On the basis of results of environmental geological surveys in recent years and historical data, Chinese karst scientists analyzed the risk hazard for sinkhole collapses and subsidence and classified the risks as high, medium, and low. High-risk areas cover 34.3×10^4 km^2, mainly in Guangxi, Yunnan, Guizhou, Hunan, and Hubei provinces. Historic sinkholes in these areas have been responsible for 43 percent of all sinkhole collapses in China since the 1950s, and the average collapse density is 0.4/100 km^2. The medium-risk areas cover 72.4×10^4 km^2, mainly in Guangxi, Yunnan, Guizhou, and Hunan provinces. Historic sinkholes in these provinces total 28.7 percent of all sinkhole collapses in China, and the average collapse density is 0.13/100 km^2. The low-risk areas cover 238×10^4 km^2, and occur mainly in regions with few carbonate rock outcrops, such as in Xinjiang, Xizang, and Sichuan provinces. In these areas, the average historic collapse density is 0.04/100 km^2 (Lei and others, 2002, 2015; China Geological Survey, 2016a).

Some new techniques that are broadly employed for sinkhole research include modeling, ground-penetrating radar, Brillouin optical time domain reflectometry (BOTDR), and optical time domain reflectometry (OTDR) (Lei and others, 2015). Through these methods, the following

conclusions were established for karst sinkhole collapses in China (Lei and others, 2002, 2015; China Geological Survey, 2016a):

1. occur generally in areas of pure carbonate rock, especially in areas or zones of fault breccia, fold axis fracturing, and contact zones between soluble and non-soluble rocks,
2. distributed generally in areas of substantial surface-water runoff over karst, zones of significant fluctuation in the karst potentiometric surface along riparian zones, and high variation areas of groundwater dynamics,
3. occur generally in areas with soil covers less than 30 m (cover collapse sinkholes of this type account for 96 percent of China's sinkholes),
4. have diameters generally less than 30 m and depths less than 10 m,
5. occur where surface subsidence and soil fractures are common, and
6. the frequency of sinkhole development has increased significantly since 2005 in high-risk areas because of large-scale engineering activities.

The annual rate of sinkhole formation in China has grown from 50 collapses per year before 2005 to the current (2016) rate of 150 collapses per year. The coupling of extreme climate events and karst sinkhole collapse is now a new research frontier in China (Lei and others, 2016).

Conclusions

Numerous investigations projects have been funded by the China Geological Survey since 2000. Under support from the China Geological Survey, the rate of development of karst research and hydrogeological surveys has been rapidly growing in China in recent years, covering nearly the whole discipline of modern karst geoscience. This growth has been aided by frequent international academic exchanges and the big demands of social and national economic development.

The China Geological Survey held a top meeting to propose an international big scientific plan on "Resource and Environmental Effects of Global Karst Dynamic Systems" (also called "Global Karst") on November 14, 2016, in Guilin, China. Fourteen karst scientists from 11 countries jointly signed a support statement on Global Karst at the meeting, meaning that an important and widespread international cooperation opportunity on karst research is coming soon. The China Geological Survey has released the 13th 5-year plan for geological science and technology, which states that the development direction of Karst Dynamics is a priority. Global climate change in karst areas, and the structure, function, and evolution of the karst critical zone, and environmental protection of karst are priority development disciplines. Chinese karst scientists are making huge efforts to promote development of modern karst science at home and abroad.

Acknowledgments

The authors thank Dr. George Veni and Prof. Jonathan B. Martin for their constructive reviews and comments, which greatly improved the manuscript. We also thank Eve L. Kuniansky and Dr. Yongli Gao for their warm invitation and perfect arrangements for this meeting. Financial support for this work was provided by the Key Research & Development Fund of Ministry of Science and Technology of China (No. 2016YFC0502501), the National Natural Science Foundation of China (No. 41572234, No. 41202185), the Special Fund for Basic Scientific Research of the Chinese Academy of Geological Sciences (No. YYWF201636), the Guangxi Natural Science Foundation (2016GXNSFCA380002), the Special Fund for Public Benefit Scientific Research of the Ministry of Land and Resources of China (201311148), and the Geological Survey Project of the China Geological Survey (DD20160305-03).

References Cited

Bögli, A., 1980, Karst hydrology and physical speleology: Springer-Verlag, 284 p.

China Geological Survey, 2016a, Geological Survey report of karst sinkholes of China: China Geological Survey Report P51. [in Chinese], also available at http://www.cgs.gov.cn/ddztt/cgs100/bxcg/fwgj/.

China Geological Survey, 2016b, Geological Survey report of karst rocky desertification of China: China Geological Survey Report P28. [in Chinese], also available at http://www.cgs.gov.cn/ddztt/cgs100/bxcg/fwgj/.

Curl, R.L., 2012, Carbon shifted but not sequestered: Science, v. 335, no. 6069, p. 655.

Ford, D.C., and Williams, P., 2007, Karst hydrogeology and geomorphology: John Wiley and Sons Ltd., 562 p.

Gan, F.P., Han, K., Lan, F.N., Chen, Y.L., and Zhang, W., 2017, Multi-geophysical approaches to detect karst channels underground—A case study in Mengzi of Yunnan Province, China: Journal of Applied Geophysics, v. 136, p. 91–98.

Guo, F., Yuan, D.X., and Qin, Z.J., 2010, Groundwater contamination in karst areas of southwestern China and recommended countermeasures: Acta Carsologica, v. 39, no. 2, p. 389–399.

Han, K., Zhen, Z.J., Gan, F.P., Chen, Y.X., and Chen, Y.L., 2016, Determination of complex karst water channel using multi-source high power mise-a-la-masse method: Journal of Jilin University (Earth Science Edition), v. 46, no. 5, p. 1,501–1,510.

Hu, Y., Qi, S., Zhang, J., Tan, L., Zhang, J., Wang, Y., and Yuan, D.X., 2011, Assessment of organochlorine pesticides contamination in underground rivers in Chongqing, southwest China: Journal of Geochemical Exploration, v. 111, no. 1-2, p. 47–55.

Jiang, Y.J., Hu, Y.J., and Schirmer, M., 2013, Biogeochemical controls on daily cycling of hydrochemistry and $\delta^{13}C$ of dissolved inorganic carbon in a karst spring-fed pool: Journal of Hydrology, v. 478, p. 157–168.

Jiang, Z.C., Lian, Y.Q., and Qin, X.Q., 2014, Rocky desertification in southwest China—Impacts, causes, and restoration: Earth-Science Reviews, v. 132, p. 1–12.

Jiang, Z.C., Qin, X.Q., Cao, J.H., Jiang, X.Z., He, S.Y., and Luo, W.Q., 2011, Calculation of atmospheric CO_2 sink formed in karst processes of the karst divided regions in China: Carsologica Sinica, v. 30, no. 4, p. 363–367. [in Chinese]

Jiang, Z.C., Qin, X.Q., Lao W.K., Tan, J.S., and Deng, Y., 2006, Investigation and exploitation of typical epikarst water in karst areas of southwest China, *in* Yin, Y.P., and others, eds., Karst groundwater exploitation and utilization in southwest China: Geological Publishing House, Beijing, p. 1–10. [in Chinese]

Lei, M.T., Gao, Y.L., and Jiang, X.Z., 2015, Current status and strategic planning of sinkhole collapses in China, *in* Lollino, G., and others, eds., Engineering geology for society and territory–Volume 5: Springer International Publishing, Switzerland, p. 529–533.

Lei, M.T., Gao, Y.L., Jiang, X.Z., and Guan, Z.D, 2016, Mechanism analysis of sinkhole formation at Maohe village, Liuzhou City, Guangxi Province, China: Environmental Earth Sciences, v. 75, no. 7, p. 542.

Lei, M.T., Jiang, X.Z., and Yu, L., 2002, New advances in karst collapse research in China: Environmental Geology, v. 42, no. 5, p. 462–468.

Liang, Y.P., Wang, W.T., Zhao, C.H., Wang, W., and Tang, C.L., 2013, Variations of karst water and environmental problems in north China: Carsologica Sinica, v. 32, no. 1, p. 32–42. [in Chinese with English abstract]

Liu, H., Liu, Z.H., Macpherson, G.L., Yang, R., Chen, B., and Sun, H.L., 2015, Diurnal hydrochemical variations in a karst spring and two ponds, Maolan Karst Experimental Site, China—Biological pump effects: Journal of Hydrology, v. 522, p. 407–417.

Liu, M.X., Xu, X.L., Sun, A.Y., Wang, K.L., Liu, W., and Zhang, X.Y., 2014, Is southwestern China experiencing more frequent precipitation extremes?: Environmental Research Letter, v. 9, no. 6, 064002.

Liu, Z.H., and Dreybrodt, W., 2015, Significance of the carbon sink produced by H_2O–carbonate–CO_2–aquatic phototroph interaction on land: Science Bulletin, v. 60, no. 2, p. 182–191.

Liu, Z.H., Dreybrodt, W., and Wang, H.J., 2010, A new direction in effective accounting for the atmospheric CO_2 budget—Considering the combined action of carbonate dissolution, the global water cycle and photosynthetic uptake of DIC by aquatic organisms: Earth-Science Reviews, v. 99, no. 3-4, p. 162–172.

Ma, Y.P., Li, M., Wu, M.M., Li, Z., and Liu, X., 2015, Occurrences and regional distributions of 20 antibiotics in water bodies during groundwater recharge: Science of the Total Environment, v. 518-519, p. 498–506.

Mo, R.S., and Qiu, S.M., 2006, Groundwater exploitation and utilization in Guangxi, China, *in* Yin, Y.P., and others, eds., Karst groundwater exploitation and utilization in southwest China: Geological Publishing House, Beijing, p. 62–72. [in Chinese]

Pan, Y.D., Birdsey, R.A., Fang J.Y., Houghton, R., Kauppi, P.E., Kurz, W.A., Phillips, O.L., Shvidenko, A., Lewis, S.L., Canadell, J.G., Ciais, P., Jackson, R.B., Pacala, S.W., McGuire, A.D., Piao, S.L., Rautiainen, A., Sitch, S., and Hayes, D., 2011, A large and persistent carbon sink in the world's forests: Science, v. 333, no. 6045, p. 988–993.

Pu, J.B., Li, J.H., Khadka, M.B., Martin, J.B., Zhang, T., and Yu, S., 2017, In-stream metabolism and atmospheric carbon sequestration in a groundwater-fed karst stream: Science of the Total Environment, v. 579, p. 1,343–1,355.

Sun, Y., Liang, Z., Xiang, X., Lan, J., Zhang, Q., and Yuan, D.X., 2016, Simulation of the transfer and fate of γ-HCH in epikarst system: Chemosphere, v. 148, p. 255–262.

Veni, G., 2013, A framework for assessing the role of karst conduit morphology, hydrology, and evolution in the transport and storage of carbon and associated sediments: Acta Carsologica, v. 42, no. 2-3, p. 203–211.

Vergano, D., 2014, China's "supercave" takes title as world's most enormous cavern: National Geographic News, 27 September, http://news.nationalgeographic.com/news/2014/09/140927- largest-cave-china-exploration-science/.

Wang, S.J., Liu, Q.M., and Zhang, D.F., 2004, Karst rocky desertification in southwestern China—Geomorphology, land use, impact and rehabilitation: Land Degradation & Development, v. 15, no. 2, p. 115–121.

Wang, Y., Zhang, G., and Lu, A.H., 2006, Research on exploitation and utilization features and typical projects of subterranean streams in Yunnan Province, China, *in* Yin, Y.P., and others, eds., Karst groundwater exploitation and utilization in southwest China: Geological Publishing House, Beijing, p. 11–34. [in Chinese]

Xia, R.Y., 2016, Groundwater resources in karst area in southern China and sustainable utilization pattern: Journal of Groundwater Science and Engineering, v. 4, no. 4, p. 301–309.

Yang, R., Chen, B., Liu, H., Liu, Z.H., and Yan, H., 2015, Carbon sequestration and decreased CO_2 emission caused by terrestrial aquatic photosynthesis—Insights from diel hydrochemical variations in an epikarst spring and two spring-fed ponds in different seasons: Applied Geochemistry, v. 63, p. 248–260.

Yuan, D.X., 1997a, Rock desertification in the subtropical karst of south China: Zeitschrift fur Geomorphologie, v. 108, no. supple.-Bd, p. 81–90.

Yuan, D.X., 1997b, The carbon cycle in karst: Zeitschrift für Geomorphologie, v. 108, no. supple.-Bd, p. 91–102.

Yuan, D.X., and Jiang, Z.C., 2000, The research progress on IGCP379 "Karst Processes and the Carbon Cycle" in China: Hydrogeology and Engineering Geology, v. 27, no. 2, p. 49–51.

Yuan, D.X., Li, B., and Liu, Z.H., 1998, Karst of China, *in* Yuan, D.X., and Liu, Z.H., eds., Global karst correlation: Science Press and VSP BV, Beijing, China and Utrecht, The Netherlands, p. 167–177.

Yuan, D.X., Zhu, D.H., Weng, J.T., Zhu, X.W., Han, X.R., Wang, X.Y., Cai, G.H., Zhu, Y.F., Cui, G.Z., and Deng, Z.Q., 1991, Karst of China: Geological Publishing House, Beijing.

Zhang, Y.H., 2010, Large caves in China: Cave and Karst Science, v. 37, no. 2, p. 53–58.

Intra-Annual Variations of Soil CO_2 and Drip-Water Chemistry in Shihua Cave, Beijing, China and Their Implications for the Formation of Annual Laminae in Stalagmites

By Binggui Cai[1,2], Fengmei Ban[3], Ming Tan[4], Xiaoguang Qin[4], Jian Zhu[4]

[1]Institute of Geography, Fujian Normal University, Fuzhou 350007, China

[2]State Key Laboratory of Subtropical Mountain Ecology (Funded by Ministry of Science and Technology and Fujian Province), Fujian Normal University, Fuzhou 350007, China

[3]Faculty of Environment Economics, Shanxi University of Finance & Economics, Taiyuan, Shanxi 030006, China

[4]Institute of Geology and Geophysics, Chinese Academy of Sciences, Beijing 100029, China

Abstract

Annually laminated stalagmites from Shihua Cave, Beijing, China, have been identified and successfully used for high-resolution paleoclimate and paleo-environmental reconstruction. However, further paleoclimatic applications of stalagmites require an improved knowledge of stalagmite laminae formation and their relation with climate and (or) environmental changes. To this end, monthly monitoring of (1) in-situ soil moisture, temperature, and CO_2 content of soil air, and (2) chemistry and calcite growth rate from drip water, were carried out in Shihua Cave, Beijing, from January 2004 to February 2008. The goal was to determine their seasonal variability and mechanisms of calcite precipitation forming laminae from the drip water.

It had been observed that seasonal variation of soil CO_2 followed a sinusoidal pattern similar to that of the soil surface temperature, with much higher values in the summer season and lower values in the winter season. In summer, peak values of soil CO_2 were always observed after rainfall events, while low values occurred during dry episodes. These observations indicate that soil moisture is the key controlling factor on soil CO_2 during the summer months when soil temperature is high and relatively stable.

The content of dissolved organic carbon (DOC) in drip waters varies inter- and intra-annually and has a positive correlation with drip water discharge at rapid response sites. The DOC content of drip water increases sharply above a threshold of rainfall intensity (greater than 50 millimeters per day) and shows several pulses corresponding with intense rain events (greater than 25 millimeters per day). The DOC content was lower and less variable during the dry period than during the rainy period.

Calcite growth rates from drip water exhibit significant intra-annual variations, with the lowest rates occurring during the summer monsoonal rainy season (July-August) and the peak rates occurring from autumn to spring. The temporal change in the calcite growth rate is negatively correlated to the drip rate and cave air PCO_2, and positively correlated to the pH of the feeding drip water. The seasonal recharge regime of drip water is likely to be the primary control on the drip water quality and quantity, which, in turn, control the calcite growth rate in Shihua Cave. During the summer rainy season, periodic rainstorm events result in drip water with lower pH, lower calcite saturation indexes, and high DOC content, while at the same time cause an increase in PCO_2 of the cave air, which inhibits calcite growth.

Notably, the annual laminae of some stalagmites in Shihua Cave are characterized by bi-optical variation in transparency and luminescence. Under conventional light transmission microscopy, an annual lamina is identified as a couplet of a thick transparent band and a thin opaque band. The very thin dark layers often, but not always, coincide with an enhanced luminescent band under reflected light microscopy with UV-excitation. The abrupt decrease in growth rate during the rainy season probably results in more defects in the calcite crystals, and forms the thin opaque (luminescent) layer observed in stalagmites. Inclusions (liquid and solid) in the calcite crystals probably incorporate luminescent organic colloids and trace elements.

Acknowledgments

We are grateful to Dr. D.H. Doctor, U.S. Geological Survey, and Dr. Calvin Alexander, University of Minnesota, for their efforts in reading and improving the English. This research was partially supported by the Natural Science Foundation of China (award numbers 41661144021 and 41272197).

The Chemical and Stable Isotopic Characteristics of Heilongtan Springs, Kunming, China

By Liu Hong[1,2], Huang Huacheng[1], Zhang Yinghua[1], Liu Jian[1], and Yang Xiangpeng[1]

[1]School of Resource Environment and Earth Science, Yunnan University, Kunming, Yunnan, 650091, China

[2]International Joint Research Center for Karstology, Yunnan University, Kunming, Yunnan, 650223, China

Abstract

Weak confined springs are the typical springs in a karst faulted basin where karst waters from mountainous recharge areas emerge at the edge of the basin where they contact Quaternary sediments. Heilongtan Springs, typical weak confined karst springs, are springs that respond to precipitation, whereas typical confined karst springs are more or less constant or stable. Heilongtan Springs are located in the foothills of the Wulao Mountains in the northern suburb of Kunming City. The springs comprise the Qingshuitan (QST), Hunshuitan (HST), and Xiaoshuitan (XST) springs. The QST and HST springs yield clear and muddy water respectively, although they share a common outlet at the southern end of the QST spring pool. In order to better understand hydrological processes in such springs, comprehensive hydrochemical samples were collected from 2010 through 2013, and stable isotope studies were carried out on Heilongtan Springs during 2014.

Methods

A Greenspan CTDP300 multi-parameter data logger was installed in the QST spring pool to obtain water temperature, electrical conductivity (EC), pH, and water level, with an interval of 15 minutes, and precipitation data were recorded by an RG2-M rain gauge at Heilongtan Park. Waters from two springs (QST and HST) were sampled weekly from 2010 to 2013 to analyze for concentrations of Ca^{2+}, Mg^{2+}, HCO_3^-, Cl^-, NO_3^-, NH_4^+, and PO_4^{3-}. Water temperature, EC, and pH were measured in the field by a Hach HQ40d meter. Calcium and Mg^{2+} values were determined by ethylenediaminetetraacetic acid (EDTA) titration, and HCO_3^- and Cl^- values by hydrochloric acid and argentum nitricum liquor titration, respectively, in the Karst Lab of the International Joint Research Center for Karstology, Yunnan University. Nitrate, NH_4^+, and PO_4^{3-} were analyzed by a series of Macherey-Nagel visocolor® ECO colorimetric boxes. The stable isotopes of oxygen-18 (^{18}O) and deuterium (^{2}H) samples collected during 2014 from all three springs were analyzed by using Laser Absorption Spectroscopy (LAS) performed on a TIWA-45EP (Los Gatos Research) in the same Karst Lab. The stable isotope composition of water is expressed in terms of δ (del) values (δ^2H, $\delta^{18}O$), in units of per mil (‰), which represent the relative difference between the ratios of less abundant and predominant isotopes in a sample (for example, $^{2}H/^{1}H$ or $^{18}O/^{16}O$ in the sample) to those in an internationally accepted standard ($^{2}H/^{1}H$ or $^{18}O/^{16}O$ in the standard). The measurements were made against three laboratory standards that range from -51‰ to -123.6‰ for δ^2H, and from -7.69‰ to -16.14‰ for $\delta^{18}O$, with precision better than 0.1‰ for oxygen and better than 0.5‰ for hydrogen.

Results

- In contrast to stable EC values of about 305 and 317 microsiemens per centimeter (μS/cm) during the dry season, the EC values of QST and HST springs increased to 330 and 350 μS/cm, respectively, and were more dynamic during the wet season. After heavy rains, the EC values of QST spring initially increased for a few days and then dropped sharply. Although the yearly average temperatures of QST and HST springs are 18.5 and 18.4 degrees Celsius (^{o}C), respectively, the temperature range for QST spring was from 18 to 19.15 ^{o}C and is higher during the dry season. For HST spring, the temperature range was 12.6 to 21.7 ^{o}C, which is mainly influenced by air temperature, due to the larger water- surface area of the spring pool.

- The concentrations of Ca^{2+}, Mg^{2+}, and HCO_3^- of the springs shared the same value ranges and change tendencies, which imply that the water of the springs mainly comes from the same aquifer. The concentrations of Ca^{2+} and HCO_3^- were higher in the dry season and lower in the wet season; in contrast, the concentrations of Mg^{2+} were higher in the wet season and lower in the dry season. Variations in Cl^-,NO_3^-,NH_4^+,and PO_4^{3-} concentrations in both springs were considered to be due to the impacts of other water sources from nearby urbanized areas.

- The isotopic study indicates that precipitation is the main water source to all three springs, especially summer rainfall. The isotopic values for $\delta^{18}O$ and $\delta^{2}H$ of the springs ranged from -12.60‰ to -11.64‰ and -88.54‰ to -85.96‰ (QST); -12.40‰ to -10.81‰ and -90.01‰ to -78.76‰ (HST); and -12.25‰ to -11.27‰ and -88.87 ‰ to -84.08‰ (XST), respectively. In general, the isotopic values in QST spring were slightly lighter (isotopically) than in the other two springs (fig. 1). The stable isotope values of the groundwater from QST and XST springs exhibited a more or less similar behavior, which was more obvious during the dry season but dampened, especially for values of $\delta^{2}H$ during the wet season due to the mixture of the spring waters. The isotopic composition of water from HST spring was different from the other two springs (fig. 1), which indicates that HST spring may have other recharge sources.

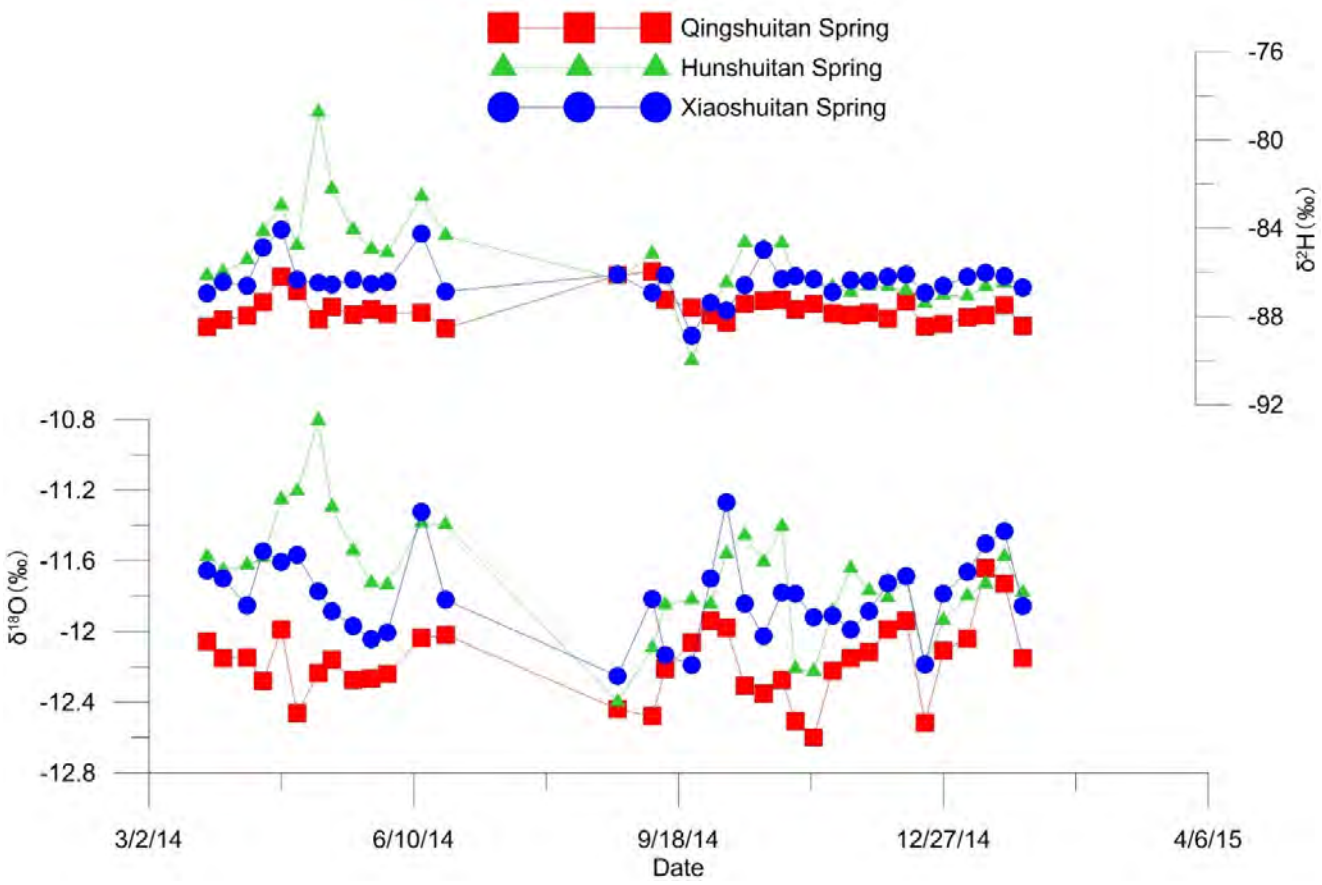

Figure 1. Oxygen-18 and deuterium isotope values for samples collected at springs QST, HST, and XST in 2014.

Formation Mechanisms of Extremely Large Sinkhole Collapses in Laibin, Guangxi, China

By Xiaozhen Jiang[1], Mingtang Lei[1], and Yongli Gao[2]

[1]Institute of Karst Geology, Chinese Academy of Geological Sciences, 50 Qixing Rd., Guilin, Guangxi, China, 541004

[2]Center for Water Research, Department of Geological Sciences, University of Texas at San Antonio, One UTSA Circle, San Antonio TX 78249

Abstract

On June 3rd, 2010, a series of sinkhole collapses occurred in Jili village surrounded by the Gui-Bei highway, Wu-Ping highway, and Nan-Liu High-Speed Railway in Laibin, Guangxi, China. The straight-line distances from an extremely large sinkhole pit, 85 meters (m) in diameter and 38 m in depth, to the highways and railway were 200 m, 600 m, and 500 m, respectively. Several methods including geophysical surveying, borehole and well drilling, groundwater elevation survey, and hydrochemical analysis of groundwater were used to study the formation mechanisms of these sinkholes. The spatial distribution of the Jili subterranean river was consistent with the north-south strike of the contact between the middle Carboniferous limestone bedrock and the overlying Quaternary deposits which control the location of sinkhole formation. In addition, both historical sinkhole events and analysis of data from a groundwater-air pressure monitoring system installed in the underlying karst conduit system indicate that sinkholes in this area are more likely induced by extreme weather conditions within typical karst settings. Extreme weather conditions in the study area before the sinkhole collapses consisted of a year-long drought followed by continuous precipitation, with a daily maximum precipitation of 442 millimeters between May 31 and June 1, 2010. Typical geological conditions include the Jili subterranean river in middle Carboniferous limestone overlain by the Quaternary overburden with thick clayey gravels. In the recharge zone of the subterranean river, a stabilized shallow water table was formed in response to the extreme rainstorm because of the presence of the thick clayey gravels. When the subterranean conduit was flooded through the cave entrance on the surface, air blasting may have caused cave roof collapse followed by the formation of soil cavities and surface collapses. Borehole monitoring results of the groundwater and air pressure monitoring show that potential karst sinkhole collapse can pose threats to Shanbei village, the Nan-Liu High-Speed Railway, and the Wu-Ping highway. Local government and land-use planners need to be aware of any early indicators of this geohazard so that devastating sinkholes can be prevented in the future. Monitoring results also indicate that groundwater and air pressure data collected from both the Quaternary deposits and the bedrock karst system can provide useful indicators for potential sinkhole collapses in similar karst areas.

Timescales of Groundwater Quality Change in Karst Groundwater: Edwards Aquifer, South-Central Texas

By MaryLynn Musgrove

U.S. Geological Survey, Texas Water Science Center, 1505 Ferguson Lane, Austin, TX 78754

Abstract

Understanding the timescales over which groundwater quality changes, and what drives these changes, informs groundwater management, use, and protection. This is especially true in karst aquifers where rapid recharge and groundwater flow rates can quickly affect water levels in wells, spring discharge, and groundwater geochemistry. The Edwards aquifer in south-central Texas is a highly productive fractured karst aquifer that responds rapidly to changes in hydrologic conditions in a region characterized by cyclic periods of drought and wet conditions. To better understand how groundwater quality changes over short (daily to monthly) and long (seasonal to decadal) timescales, the U.S. Geological Survey's National Water-Quality Assessment (NAWQA) Project began a monitoring and sampling effort in 2013 that combines high-frequency water-quality monitoring with discrete sample collection at different timescales. Three water wells in the Edwards aquifer have been instrumented to provide near-continuous (subhourly) water-quality data (temperature, pH, specific conductance, and dissolved oxygen). These data are augmented by the collection of six discrete samples per year for a range of geochemical constituents, including major ions, nitrate, selected isotopes, and age tracers. The wells are near San Antonio, Texas, along an updip-to-downdip aquifer transect, and consist of one monitoring well in the unconfined (recharge) zone and two public-supply wells in the confined zone of the aquifer. Discrete sample results indicate updip-to-downdip trends in groundwater geochemistry with respect to water-rock interaction and groundwater residence time. Drought conditions prevailed during the first year of data collection, providing baseline information for a period when little aquifer recharge occurred. Subsequent wet conditions resulted in extensive recharge and an accompanying regional hydrologic response. Groundwater geochemistry at the updip monitoring well varies rapidly in response to aquifer recharge. In contrast, groundwater geochemistry at the public-supply wells in the confined part of the aquifer is less variable. The combination of high-frequency and discrete data collection provides unique insights into changes in groundwater geochemistry in a dynamic karst aquifer at different temporal scales.

Estimating Recharge to the Edwards Aquifer, South-Central, Texas—Current (2017) Methods and Introduction of an Automated Method Using the Python Scripting Language

Ross K. Kushnereit[1, 2], Yongli Gao[2], and Richard N. Slattery[1]

[1]U.S. Geological Survey, Texas Water Science Center, 5563 De Zavala Rd # 290, San Antonio, TX 78249

[2]Department of Geological Sciences, Center for Water Research, University of Texas San Antonio, 1 UTSA Circle, San Antonio, TX 78249

Abstract

The U.S. Geological Survey (USGS) publishes annual estimates of recharge to the Edwards aquifer by using a mass water-balance method. The current (2017) methodology relies on a hand-drawn base-flow separation technique to obtain components of the stream hydrograph such as base flow and storm runoff. These components are then used in the mass-balance equations for estimating recharge in the study area. However, the current method is labor intensive and is subject to a potential lack of consistency between different hydrographers using the method. In contrast, the new approach for estimating recharge to the Edwards aquifer automates the methodology by using the computational scripting language, Python, to estimate recharge from hydrologic input data such as rainfall and streamflow. The new automated approach increases the transparency and reproducibility for recharge calculations.

Introduction

The Edwards aquifer is one of the most prolific karst aquifers in the United States. It is a major source of water for residents in Bexar, Comal, Hays, Medina, and Uvalde Counties. The Edwards aquifer also supplies large quantities of water to agriculture, business, and industry in the region. The major artesian springs of the Edwards aquifer provide water for recreational activities, businesses, and downstream users, and habitat for several threatened or endangered species (Edwards Aquifer Research and Data Center, 2010).

The Edwards aquifer is primarily recharged by direct infiltration as streams in the catchment area cross the limestone outcrops of the Edwards Group (recharge zone). The catchment area and recharge zone of the Edwards aquifer are depicted on figure 1. As the streams cross the recharge zone, they lose substantial amounts of water as direct infiltration into the highly permeable, faulted and fractured rocks of the outcrop. Direct infiltration of rainfall also occurs in the interstream areas of the recharge zone (Maclay and Small, 1976).

The current (2017) method of estimating recharge to the Edwards aquifer (Puente, 1978) relies on a hand-drawn base-flow separation technique to identify the base-flow and storm runoff components of the streamflow hydrograph. The current method is hereinafter referred to as the "Puente method." The base-flow and storm runoff components are then used in a series of mass-balance equations for estimating the amount of recharge to the Edwards aquifer. The Puente method is labor intensive and is subject to a potential lack of consistency in the results obtained by different hydrographers.

A new approach for estimating recharge to the Edwards aquifer is being developed that automates the methodology by using the computational scripting language, Python, to estimate recharge from hydrologic input data such as rainfall and streamflow. The new automated approach will increase the transparency and reproducibility for recharge calculations.

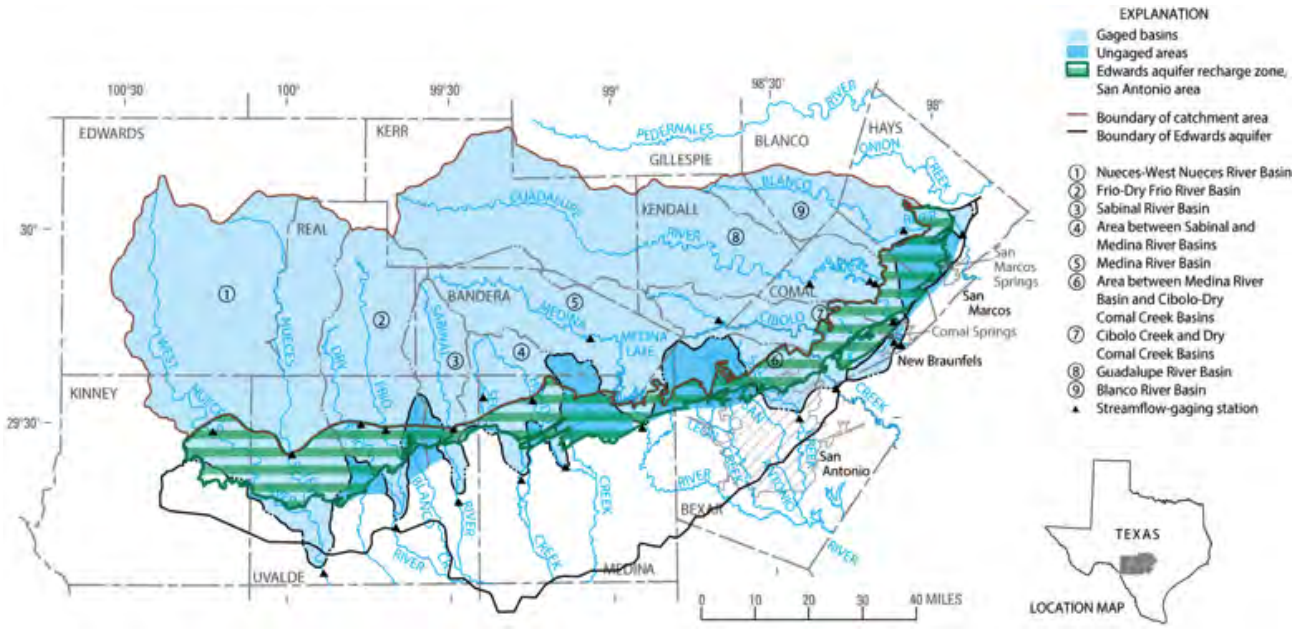

Figure 1. Map of the catchment area and the recharge zone for the Edwards aquifer (modified from Puente, 1978, fig. 1).

Methods

Currently (2017), annual recharge estimates are calculated separately for each of the major basins in the catchment area of the Edwards aquifer, as well as for the ungaged areas between the major basins (fig. 1). The Puente method uses streamflow data collected at USGS streamflow-gaging stations near the upstream and downstream boundaries of the recharge zone (fig. 1), and estimates of the distribution of rainfall. Since 2004, the distribution of rainfall in the catchment area and recharge zone of the Edwards aquifer has been estimated by using calibrated NEXRAD (NEXt-generation weather RADar) data (Edwards Aquifer Authority, written commun., 2016).

The basic equation for computing recharge is as follows (from Puente, 1978):

$$R = (Q_c - Q_r + IA)(1.9835) \quad (1)$$

where

R is the recharge, in acre-feet,

Q_c is the measured annual volume of streamflow at the outlet of the catchment area gage(s), in cubic feet per second-days,

Q_r is the measured volume of flow at the outlet of the recharge zone gage(s), in cubic feet per second-days,

IA is the estimated volume of surface runoff resulting from rainfall in the intervening area, in cubic feet per second-days, and

1.9835 is a conversion factor from cubic feet per second-days to acre-feet.

The volume of flow measured at each outlet gage of the catchment area is the sum of base flow and storm runoff. Base flow is the part of the hydrograph that is sustained by local springs and bank storage of water flowing into the stream. Base flow is generally characterized by a gradual increase or decrease in the hydrograph's discharge, depending on the amount of contribution from groundwater discharge (A and B) (fig. 2) (Puente, 1978). The storm runoff is the part of the hydrograph that results from overland flow generated by a storm event, typically characterized by a sharp increase in discharge from base flow (C) (fig. 2) (Szilagyi and others, 2003).

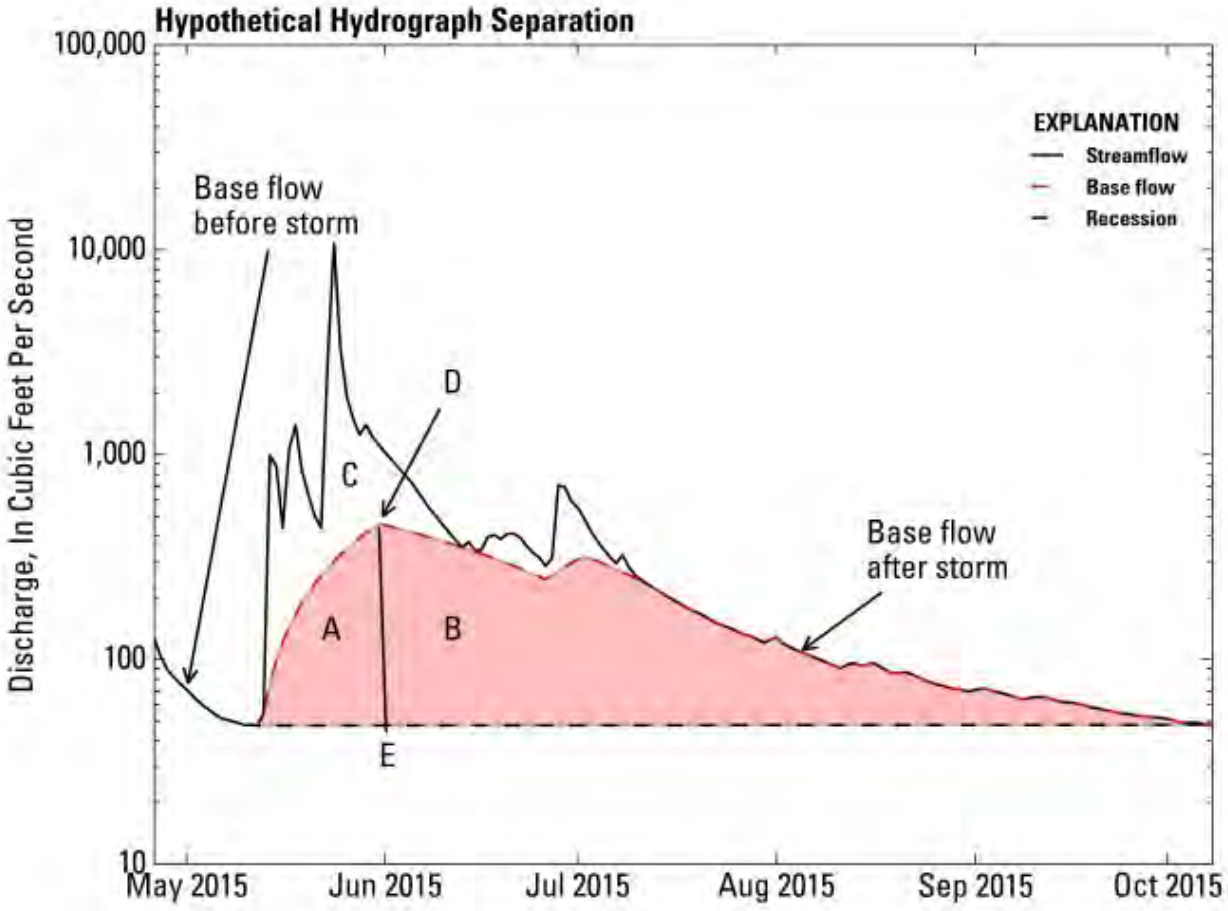

Figure 2. Graphical separation of a hypothetical hydrograph for estimating base flow (parts A and B of the hydrograph) and storm runoff (part C of the hydrograph) (modified from Puente, 1978, fig. 3).

The equation for estimating total runoff from direct rainfall in the areas between the catchment area and recharge zone is as follows (modified from Puente, 1978):

$$IA = \frac{A_r}{A_c} Q_a \text{ x } RF \quad (2)$$

(2)

where

IA is the volume of water (runoff plus infiltration) contributed by rainfall in the intervening drainage area, in cubic feet per second-days,

A_r is the area of the recharge zone for each basin, in square miles,

A_c is the area of the catchment area for each basin, in square miles,

Q_a is the volume of water contributed to direct recharge above the upper gage(s) in the cathment area, in cubic feet per second-days, and

RF is the ratio of average rainfall for the lower basin to the upper basin, in inches.

The Q_a term in equation 2 is derived from a base-flow separation method described by Puente (1978), and is manually drawn by hand. The Q_a is computed from a function of the difference between the peak of the base-flow storm response and the recession curve before the storm (D and E), added to the initial increase in base flow during a flood (A) and the base-flow component after a flood (B) (fig. 2). The difference between components D and E (fig. 2) is then applied to the relation between base-flow discharge in cubic feet per second, and the estimated groundwater storage contribution, in thousand acre-feet per second-days. This relation is represented as a polynomial function that is based on observations of long-term streamflow hydrographs collected during the winter months when evapotranspiration is less and storm events are less common compared to the rest of the year (Puente, 1978). It is assumed that runoff within the recharge zone occurs at a similar rate per unit area as in the catchment area. Similarly, the loss of water in the stream as a result of evapotranspiration is assumed to be proportionately equal for both the catchment and infiltration areas (Puente, 1978).

References Cited

Edwards Aquifer Research & Data Center, 2010, Threatened and endangered species in the Edwards aquifer system: Texas State University College of Science & Engineering, accessed January 29, 2010, at http://www.eardc.txstate.edu/Aquifer-Info/endangered.html.

Maclay, R.W., and Small, T.A., 1976, Progress report on the geology of the Edwards aquifer, San Antonio area, Texas, and preliminary interpretation of borehole geophysical and laboratory data on carbonate rocks: U.S. Geological Survey Open-File Report 76-627, 65 p.

Puente, Celso, 1978, Method of estimating natural recharge to the Edwards aquifer in the San Antonio area, Texas: U.S. Geological Survey Water-Resources Investigations Report 78-10, 34 p.

Szilagyi, J., Harvey, E.F., and Ayers, J.F., 2003, Regional estimation of base recharge to ground water using water balance and a base-flow index: Ground Water, v. 41, no. 4, July-August 2003, p. 504–513.

Geologic Framework and Hydrostratigraphy of the Edwards and Trinity Aquifers Within Northern Bexar and Comal Counties, Texas

By Allan K. Clark[1], James A. Golab[2], and Robert R. Morris[1]

[1]U.S. Geological Survey, Texas Water Science Center, 5563 Dezavala Road, San Antonio, TX 78249

[2]University of Kansas, Department of Geology, 1475 Jayhawk Blvd, Lawrence, KS 66045

Abstract

During 2014–16, the U.S. Geological Survey, in cooperation with the Edwards Aquifer Authority, documented the geologic framework and hydrostratigraphy of the Edwards and Trinity aquifers within northern Bexar and Comal Counties, Texas. The Edwards and Trinity aquifers are major sources of water for agriculture, industry, and urban and rural communities in south-central Texas. Both the Edwards and Trinity are classified as major aquifers by the State of Texas and recognized as carbonate aquifers with karst features. The resulting study produced a detailed 1:24,000-scale hydrostratigraphic map, and names and descriptions of the geologic and hydrostratigraphic units (HSUs) in the study area, and focused on the geologic framework and hydrostratigraphy of the outcrops and hydrostratigraphy of the Edwards and Trinity aquifers within northern Bexar and Comal Counties, Texas. In addition, parts of the adjacent upper confining unit to the Edwards aquifer are included. This abstract is reprinted from Clark and others (2016).

The study area, approximately 866 square miles, is within the outcrop area of the Edwards and Trinity Groups and overlying confining units (Washita, Eagle Ford, Austin, and Taylor Groups) in northern Bexar and Comal Counties. The rocks within the study area are sedimentary and range in age from Early to Late Cretaceous. The Miocene-age Balcones fault zone is the primary structural feature within the study area. The fault zone is an extensional system of faults that generally trend southwest to northeast in south-central Texas. The faults have normal throw, are en echelon, and are mostly downthrown to the southeast.

The Early Cretaceous Edwards Group rocks were deposited in an open marine to supratidal environment during two marine transgressions. The Edwards Group consists of the Kainer and overlying Person Formations. Following tectonic uplift, subaerial exposure, and erosion near the end of Early Cretaceous time, the area of present-day south-central Texas was again submerged during the Late Cretaceous by a marine transgression resulting in deposition of the Georgetown Formation of the Washita Group.

The Edwards Group overlies the Trinity Group and consists of mudstone to boundstone, dolomitic limestone, argillaceous limestone, an evaporite, shale, and chert. The Kainer Formation is subdivided into (from bottom to top) the basal nodular, dolomitic, Kirschberg Evaporite, and grainstone members. The Person Formation is subdivided into (from bottom to top) the regional dense, leached, and collapsed (undivided), and cyclic and marine (undivided) members.

Hydrostratigraphically, the rocks exposed in the study area represent a section of the upper confining unit to the Edwards aquifer, the Edwards aquifer, the upper zone of the Trinity aquifer, and the middle zone of the Trinity aquifer. The Pecan Gap Formation (Taylor Group), Austin Group, Eagle Ford Group, Buda Limestone, and Del Rio Clay are generally considered to be the upper confining unit to the Edwards aquifer.

The Edwards aquifer was subdivided into HSUs I to VIII (Maclay and Small, 1976). The Georgetown Formation of the Washita Group contains HSU I. The Person Formation of the Edwards Group contains HSUs II (cyclic and marine members [Kpcm], undivided), III (leached and collapsed members [Kplc], undivided), and IV (regional dense member [Kprd]). The Kainer Formation of the Edwards Group contains HSUs V (grainstone member [Kkg]), VI (Kirschberg Evaporite Member [Kkke]), VII (dolomitic member [Kkd]), and VIII (basal nodular member [Kkbn]).

The Trinity aquifer is separated into upper, middle, and lower aquifer units (hereafter referred to as "zones") (Ashworth, 1983). The upper zone of the Trinity aquifer is in the upper member of the Glen Rose Limestone. The middle zone of the Trinity aquifer is in the lower member of the Glen Rose Limestone, Hensell Sand, and Cow Creek Limestone. The lower zone of the Trinity aquifer consists of the Sligo and Hosston Formations, which do not crop out in the study area. The regionally extensive Hammett Shale forms a confining unit between the middle and lower zones of the Trinity aquifer.

The upper zone of the Trinity aquifer is subdivided into five informal HSUs (from top to bottom): cavernous, Camp Bullis, upper evaporite, fossiliferous, and lower evaporite (Clark, 2003; Clark and others, 2009). The middle zone of the Trinity aquifer consists of (from top to bottom) the Bulverde, Little Blanco, Twin Sisters, Doeppenschmidt, Rust, Honey Creek, Hensell, and Cow Creek HSUs (Blome and Clark, 2014; Clark and others, 2016). The underlying Hammett HSU is a regional confining unit between the middle and lower zones of the Trinity aquifer. The lower zone of the Trinity aquifer is not exposed in the study area.

Groundwater recharge and flow paths in the study area are influenced not only by the hydrostratigraphic characteristics of the individual HSUs, but also by faults and fractures and geologic structure. Faulting associated with the Balcones fault zone (1) might affect groundwater flow paths by forming a barrier to flow that results in water moving parallel to the fault plane, (2) might affect groundwater flow paths by increasing flow across the fault because of fracturing and juxtaposing porous and permeable units, or (3) might have no effect on groundwater flow paths (Maclay and Small, 1976, 1983).

The hydrologic connection between the Edwards and Trinity aquifers and the various HSUs is complex. The complexity of the aquifer system is a combination of the original depositional history, bioturbation, primary and secondary porosity, diagenesis, and fracturing of the area from faulting. All of these factors have resulted in the development or modification of porosity, permeability, and transmissivity within and between the aquifers. Faulting has produced highly fractured areas that have allowed for rapid infiltration of water and subsequent development of solutionally enhanced fractures, bedding planes, channels, and caves that are highly permeable and transmissive. The juxtaposition resulting from faulting also has resulted in areas of interconnectedness between the Edwards and Trinity aquifers and the various HSUs that compose the aquifers.

References Cited

Ashworth, J.B., 1983, Ground-water availability of the Lower Cretaceous formations in the Hill Country of south-central Texas: Texas Department of Water Resources Report 273, 172 p. [Also available at http://eahcp.org/documents/1983_Ashworth_GroundWaterAvailability.pdf.]

Blome, C.D., and Clark, A.K., 2014, Key subsurface data help to refine Trinity aquifer hydrostratigraphic units, south-central Texas: U.S. Geological Survey Data Series 768, 1 sheet. [Also available at http://dx.doi.org/10.3133/ds768.]

Clark, A.K., 2003, Geologic framework and hydrogeologic features of the Glen Rose Limestone, Camp Bullis Training Site, Bexar County, Texas: U.S. Geological Survey Water-Resources Investigations Report 03–4081, 9 p., 1 pl., scale 1:24,000.

Clark, A.R., Blome, C.D., and Faith, J.R., 2009, Map showing the geology and hydrostratigraphy of the Edwards aquifer catchment area, northern Bexar County, south-central Texas: U.S. Geological Survey Open-File Report 2009–1008, 24 p., 1 pl., scale 1:50,000, http://pubs.usgs.gov/of/2009/1008/.

Clark, A.K., Golab, J.A., and Morris, R.R., 2016, Geologic framework, hydrostratigraphy, and ichnology of the Blanco, Payton, and Rough Hollow 7.5-minute quadrangles, Blanco, Comal, Hays, and Kendall Counties, Texas (ver. 1.1, September 20, 2016): U.S. Geological Survey Scientific Investigations Map 3363, 21 p., 1 sheet, scale 1:24,000. [Also available at http://dx.doi.org/10.3133/sim3363.]

Maclay, R.W., and Small, T.A., 1976, Progress report on geology of the Edwards aquifer, San Antonio area, Texas, and preliminary interpretation of borehole geophysical and laboratory data on carbonate rocks: U.S. Geological Survey Open-File Report 76–627, 65 p.

Maclay, R.W., and Small, T.A., 1983, Hydrostratigraphic subdivisions and fault barriers of the Edwards aquifer, south-central Texas: Journal of Hydrology, v. 61, p. 127–146.

Aromatic-Ring Biodegradation in Soils From a Crude Oil Spill on Clear Creek, Obed Wild and Scenic River National Park, Tennessee

By Thomas D. Byl[1,2] and Michael W. Bradley[1]

[1]U.S. Geological Survey, Lower Mississippi-Gulf Water Science Center, 640 Grassmere Park, Suite 100, Nashville, TN 37211

[2]Tennessee State University, Dept. of Agricultural and Environmental Sciences, 3500 John H Merritt Blvd, Nashville, TN 37209

Abstract

The Obed Wild and Scenic River (WSR) National Park, in north-central Tennessee, is characterized by exceptional biological, scenic, and recreational resources, all dependent on the quality of water in the river. The WSR is located on the Cumberland Plateau, which has a Pennsylvanian-age sandstone cap protecting underlying Mississippian-age limestones from dissolution. However, there are fractures of varying sizes that allow water to percolate through the sandstone cap and recharge the underlying limestone aquifer. Oil and gas production occurs in areas bordering the WSR, and some of these areas are targeted for a significant increase in exploratory drilling. During July 2002, an exploratory drilling operation near the boundary of the WSR encountered a highly pressurized petroleum zone and released an estimated 12,000 barrels of oil in 24 hours. The spilled crude oil flowed down the embankment, and an unknown quantity percolated down into the sandstone cap. After 14 years, oil is still seeping out of the sandstone and into the creek. The objective of this project was to identify contaminated seeps, characterize the microbial community, and measure the rate of natural bioremediation. Several new seeps were identified and located with GPS. Subsurface bacteria from clean and contaminated sites along the creek found Pseudomonads, which are effective at biodegradation. Higher Pseudomonad concentrations were observed in soils with moderate concentrations of oil. Some of the more contaminated soils were dominated by sulfur-reducing bacteria, which are slow at biodegrading petroleum compounds. The more efficient heterotrophic aerobic and iron-reducing bacteria were present, but in smaller proportions. Microcosms were established using 40 cm^3 of sediment collected from contaminated seeps on White Creek. The concentration of aromatic petroleum compounds was measured using a fluorometer. The half-life for aromatic rings in un-amended soils was 583 days. Adding peroxide and vitamin B-12 enhanced the rate of biodegradation and reduced the half-life to 163 days.

Investigating Microbial Response to Fertilizer Application From Concentrated Animal Feeding Operations Located on Karst Aquifers in Northern Arkansas

By Victor L. Roland II

U.S. Geological Survey, 640 Grassmere Park, Suite 100, Nashville, TN 37221

Abstract

The application of dry and liquid fertilizers derived from concentrated animal feeding operations (CAFOs) lagoons impacts groundwater quality by introducing excessive amounts of nutrients (organic matter, nitrate, and ammonia), metals, and antibiotic compounds to underlying aquifers. In northern Arkansas, swine and poultry CAFOs have increased in number in the Buffalo River watershed and neighboring watersheds and could result in increasing nutrient loads to karst groundwater systems underlying the region. In 2014, the U.S. Geological Survey (USGS) conducted a study designed to discover whether increased concentrations of labile dissolved organic carbon (DOC) and nitrate from CAFO-derived fertilizer applications would result in increased microbial activity along groundwater flow paths. Additionally, this study hypothesized that increasing heavy metal and antibiotic concentrations in association with increasing labile DOC concentrations could be detrimental to microbial nutrient cycling processes, with the exception of resistant bacteria species. To test both hypotheses, laboratory microcosm experiments were conducted to characterize the effect of microbial activity on concentrations of dissolved inorganic carbon (DIC) produced and denitrification activity. The microcosms were subjected to different treatment combinations of acetate, nitrate, phosphate, and heavy metals at varying concentrations plus controls. Field studies were used to evaluate laboratory conditions, and to compare biomass production and composition between samples from laboratory microcosms and field samples. Isotopes of DIC (^{13}C-DIC) and nitrate (^{15}N-NO_3), and dissolved oxygen (DO) were used to assess microbial response to increasing DOC concentrations. Fatty acid methyl ester (FAME) analysis was used to characterize biomass produced during the experiments.

Initial results indicate that DOC was converted to DIC, and NO_3 concentrations decreased in microcosms not treated with heavy metals. Microbial activity in the microcosms was greatest when the concentration of NO_3 was 10 times less than the concentration of DOC. Metals generally inhibited microbial activity at concentrations above 10 micrograms per liter. FAME biomarker analysis indicated gram-negative bacteria were present in biomass samples from the spring orifice and metal-treated microcosms, but microcosms amended with only nutrients (NO_3, PO_4, and DOC) contained predominantly gram-positive microbial communities.

Evidence for Karst-Influenced Cross-Formational Fluid Bypass of a Dolomite Unit at the Top of the Oldsmar Formation in the Lower Floridan Aquifer, Southeast Florida

By Kevin L. DeFosset[1] and Kevin J. Cunningham[2]

[1]Nova Southeastern University, 3301 College Avenue, Ft. Lauderdale, FL 33314

[2]U.S. Geological Survey Caribbean-Florida Water Science Center, 3321 College Avenue, Davie, FL 33314

Abstract

In southeastern Florida, a permeable zone in the lower part of the Lower Floridan aquifer has been used for decades to dispose of both treated wastewater effluent and reverse osmosis concentrate. The Boulder Zone, which is the permeable zone that receives the injected effluent, is a thick, fractured and cavernous dolomite in the lower part of the Oldsmar Formation, a shallow marine platform carbonate of early Eocene age. A comparatively thinner dolomite unit occurs at the top of the Oldsmar Formation and the Lower Floridan aquifer. The U.S. Geological Survey has reported that this dolomite unit is part of the uppermost major permeable unit of the Lower Florida aquifer. However, because it has been interpreted as a confining unit in at least one consultancy report, controversy surrounds its hydraulic nature in the south Florida hydrogeologic community.

As use of the Floridan aquifer system in southeast Florida has increased, geologic and hydrogeologic frameworks have been developed and refined to assist water management decisions. Specific attention has been directed toward the dolomite unit due to its perceived potential to serve as an aquiclude to potential upward migrating Boulder Zone injectate. Cross-formational injectate bypass of this dolomite unit would pose a risk to the Underground Source of Drinking Water (USDW) that lies above in the Upper Floridan aquifer. Recent analyses of geologic, borehole geophysical, and seismic-reflection data provide evidence that fracture- and solution-enhanced porosity and permeability are characteristic of the dolomite unit. This may cast doubt on the potential for this dolomite to serve as a confining unit to upward migration of injected effluent.

The lithology of the dolomite unit has been consistently documented across southeast Florida in core and cuttings samples as a dense, crystalline dolomite with a characteristic signature in the data acquired by gamma, resistivity, and sonic borehole geophysical logging. The conceptualization that this unit serves as a confining unit is largely based on the results of hydraulic testing on plugs sampled from whole core, which are representative of comparatively smaller scale matrix porosity. However, indications of enhanced permeability are evident on borehole video imaging as secondary porosity associated with bedding plane and irregular touching vugs, and fractures. Borehole temperature log data from wells at a southeast Florida wellfield indicate tortuous stratiform lateral flow through fractures and vuggy megapores contained in the dolomite unit. Few hydraulic tests have been performed that isolate this unit and allow a quantitative hydraulic characterization at the field scale that takes into account the documented pore system.

The characteristics of the dolomite unit have been generally interpreted from a borehole-scale perspective. However, new seismic-reflection data enable a more regional and continuous perspective on this interval of the Lower Floridan aquifer that is not possible from individual wells. Seismic-reflection profiles image an upper bounding surface to this unit that is a major regional karst unconformity related to subaerial exposure. This exposure would have allowed for the development of dissolution along bedding planes and creation of irregular vugs and sinkholes. Also, numerous columniform seismic-sag structures are identified on the seismic-reflection profiles, and there are some tectonic faults that might provide vertical pathways for cross-formational fluid flow upward through the dolomite unit. Subaerial karst unconformities at the upper surfaces of carbonate depositional cycles at several hierarchical scales and associated secondary porosity have produced stratiform permeable zones that contribute to much of the dissolution-enhanced permeability within the Floridan aquifer and in many large oil and gas fields around the world.

Collapse of the Devonian Prairie Evaporite Karst in the Western Canada Sedimentary Basin: Structuration of the Overlying Cretaceous Athabasca Oil Sands and Regional Flow System Reversal by Subglacial Meltwater

Paul L. Broughton

Broughton and Associates, P.O. Box 6976, Calgary, Alberta T2P 2G2, Canada

Abstract

The Middle Devonian Prairie Evaporite accumulated halite-dominated beds up to 200 meters (m) thick across western Canada, covering large areas of northern Alberta, southern Saskatchewan, southwestern Manitoba, and adjacent eastern Montana and western North Dakota. In the Alberta and Williston constituent sub-basins of the Western Canada Sedimentary Basin, aquifer water migrated to the northeast up-structure along permeable Devonian strata in combination with vertical compaction-driven flows responding to basin loading. Resulting salt removal patterns included a 1,000 kilometer (km)-long and 150 km-wide trend developed along the eastern margin of the salt basin on-lap with the Canadian Shield, and across the southern Saskatchewan area of the northern Williston Basin. Removal of up to 100 m of salt section in northeastern Alberta and up to 200 m of halite-dominated evaporite beds in southern Saskatchewan resulted in the largest known hypogene halite karst collapse and associated configuration of overlying strata. Multi-stage dissolution events in northeastern Alberta were mostly during the Middle Jurassic to Early Cretaceous Columbian orogeny, followed by post-orogenic dissolution and collapse trends during deposition of the McMurray Formation (Aptian) strata. In contrast, dissolution stages across the southern Saskatchewan area of the northern Williston Basin occurred throughout the Paleozoic Antler and Mesozoic Laramide orogenic events. The hypogene karst collapses across southern Saskatchewan resulted in 10s to 100s of km-long subsidence troughs controlling depositional trends in the overlying 2 km-thick stratigraphic column. In contrast, northeastern Alberta was an unusual evaporite karst area because of the very low 1:2 thickness ratio of removed halite beds to overlying limestone strata, resulting in dissolution controlled structuration that impacted the distribution of overlying McMurray Formation (Aptian) fluvial-estuarine point bar sand complexes. This Athabasca Oil Sands deposit was emplaced above a 300-km-long segment of the halite dissolution trend that extended along the eastern margin of the Prairie Evaporite salt basin, only 200 m below. These sand reservoirs trapped Laramide oil migrations into the area that were subsequently biodegraded into commercially attractive bituminous sand deposits. During the Pleistocene, the hydraulic head resulting from Laurentide ice sheet loading resulted in pressured subglacial meltwater movement into the subsurface along permeable Devonian strata. The meltwater to the southwest mixed with regional basin aquifer water flows up-structure to the northeast, temporarily reversing the direction of regional flows. Subglacial meltwaters coming into contact with shallowly buried salt beds during glacial loading and unloading reactivated older 10s to 100s of km² collapse structures in southern Saskatchewan. Sinkholes aligned along lineaments on the subglacial topography in northeastern Alberta.

Introduction

The impact of salt dissolution trends in the Middle Devonian Prairie Evaporite, Elk Point Group, on the overlying strata across southern and central Saskatchewan has been documented by numerous researchers (DeMille and others, 1964; Holter, 1969; Broughton, 1977, 1985; McTavish and Vigrass, 1987), and across northern Alberta (Ford, 1997; Grobe, 2000; Broughton, 2013, 2015; Hein and others, 2013). Dissolution stages since the Late Devonian removed up to 200 meters (m) of halite-dominated evaporite beds across southern Saskatchewan. At least a 100–150-m interval of salt was removed in northeastern Alberta since the Middle Jurassic.

The strata above areas of salt removal in the subsurface of southern Saskatchewan were as much as 1–2 kilometers (km) thick (Broughton, 1977), but only a 200–400-m section in northeastern Alberta. As a result, the northern part of the Athabasca deposit had an unusually low 1:2 thickness ratio of removed salt beds (100 m) with overlying strata (200 m), resulting in 10s of km-long collapse trends in the halite karst with structural controls on the overlying depositional surface unlike anywhere else (Broughton, 2015, 2016).

It is generally accepted that the dissolution stages resulted from subsurface water moving upward into the Prairie Evaporite Formation salt beds. There were multiple regional and local post-burial water flow systems that variously impacted the salt removal patterns.

The hydraulic head resulting from the newly formed Rocky Mountain uplands to the west along with tectonic compression impacted deep basin aquifer water flows to the northeast and controlled regional salt removal patterns within the halite-dominated beds of the Prairie Evaporite basin (fig. 1). The drive was enhanced by movement of water from mountainous areas northeastward into areas with lower topographic relief (Garven, 1989). Flows variously mixed with influxes of surface-charged groundwater. These flows combined with compaction-driven vertical flows of Devonian formation waters mostly from the Keg River Formation moved into the overlying Prairie Evaporite salt beds as responses to sedimentary basin loading.

It is uncertain if aquifer flows up-structure to the northeast were largely basin-wide for 10s to 100s of km distances, or as lesser incremental flows that did not flush the entire system. Alternative models suggest that most salt dissolution patterns resulted only from compaction driven vertical water movements within the Devonian strata during sediment loading (Bachu and Underschultz, 1993; Bachu, 1995, 1999). All of these hypogene salt karstification processes may have contributed to the widespread dissolution patterns in the halite salt basin, but the relative contribution by each remains uncertain.

Tectonism and Evaporite Dissolution Trends

Continental-scale tectonism exerted major regional controls on the evolution of the Western Canada Sedimentary Basin (WCSB). The deepening Alberta foreland and Williston constituent basins of the WCSB resulted in aquifer water flows up-structure to the northeast. These basin deformations are interpreted to have significantly impacted the removal of salt beds across extensive areas of the Middle Devonian Prairie Evaporite basin, and resulted in hypogene salt karst collapse trends that structurally configured the overlying strata.

The continental-scale tectonics are attributed to the creation of the Pangea supercontinent and subsequent fragmentation as North and Central America separated from Europe and western Africa. The tectonism broadly segmented the Paleozoic succession, including the Middle Devonian Prairie Evaporite salt basin extending across western Canada, into regional basins northeastward of the Rocky Mountain uplands. The foreland Alberta Basin and the Williston Basin across southern Saskatchewan, north of the central Montana Uplift and Black Hills, were draped by multi-kilometer thick Cretaceous strata as the overarching WCSB.

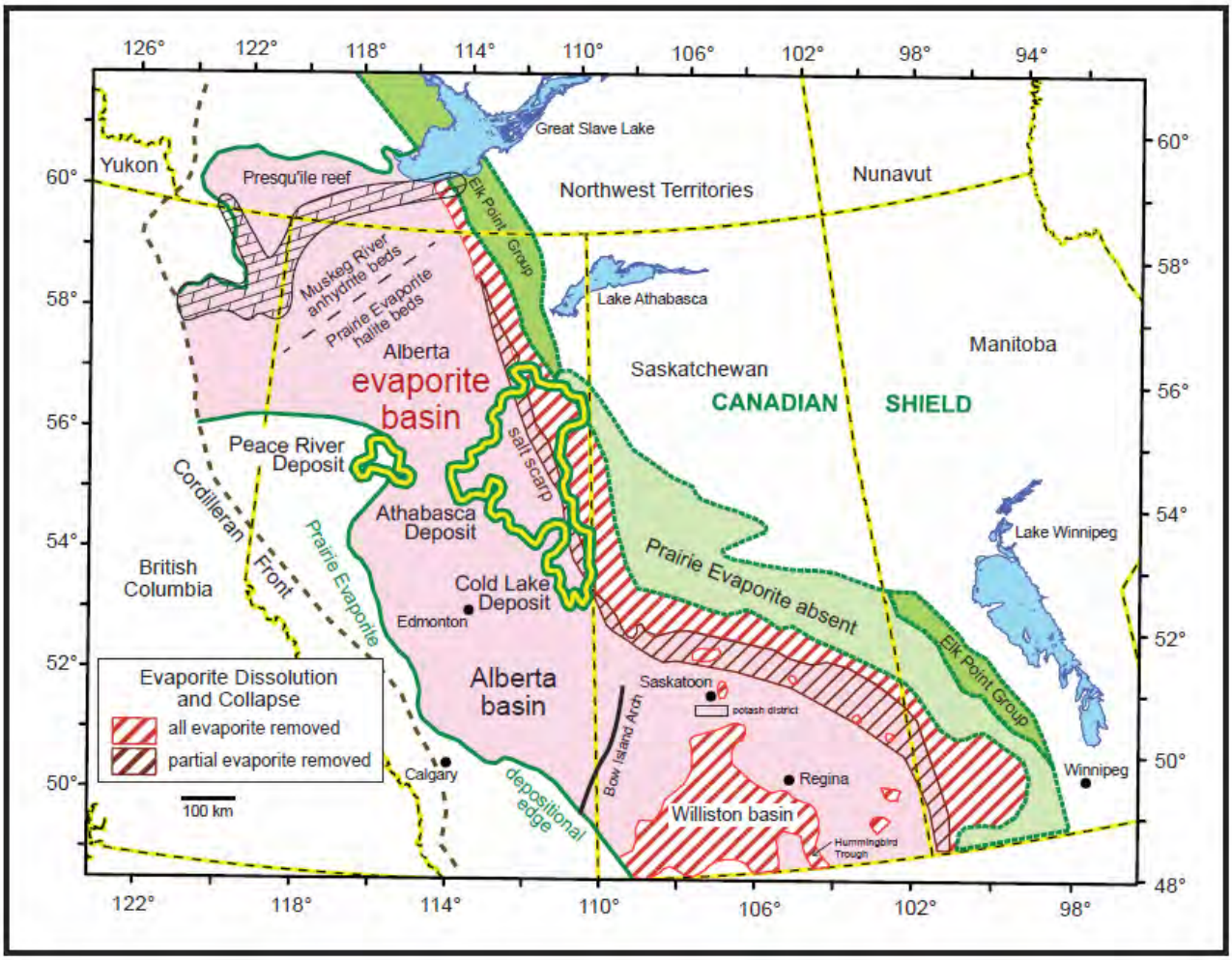

Figure 1. The Prairie Evaporite Formation salt basin across western Canada, illustrating the 1,000-km long and 150-km wide dissolution trend along the eastern basin margin, and across the southern Saskatchewan area of the northern Williston Basin. The northern area of the Athabasca Oil Sands deposit overlies a 300-km-long segment of this regional dissolution trend. Modified from Broughton (2013, 2015).

Early stage dissolution resulted from aquifer water flows that responded to hydraulic heads associated with burial-uplift cycles during the Late Devonian to Carboniferous tectonism of the Antler orogeny in southern Saskatchewan. Dissolution events related to such tectonism during the Paleozoic were mostly absent across northeastern Alberta. An exception to this occurred with the development of dissolution trends along the Presqu'ile carbonate barrier reef during the Middle-Late Devonian at the northern seaward end of the Elk Point evaporite basin. This barred basin permitted sustained evaporation of the inland sea that extended into the interior of the Laurentia paleocontinent from present-day Alberta to western North Dakota, resulting in the Prairie Evaporite salt basin. Early stage shallow karstification events during the Devonian resulted in 10s of km-long dissolution channels within the Presqu'ile carbonate reef. Late Antler tectonism by the end of the Carboniferous resulted in deeper burial and massive dolomitization of the barrier reef as the Presqu'ile Dolomite. Metalliferous hydrothermal brines flowed into the eastern end of this dolomitized barrier reef, resulting in the Mississippi Valley-type lead-zinc sulphide deposit at Pine Point (Rhodes and others, 1984). Alternative models interpret the deep burial and

hydrothermal karstification occurred during Late Cretaceous Laramide tectonism (Qing and Mountjoy, 1992).

Extensive dissolution stages occurred during the Middle-Late Jurassic to Early Cretaceous Columbian orogeny in the Alberta foreland basin, continuing as post-orogenic dissolution events during the Aptian accumulation of McMurray Formation strata. In Alberta, the Cordilleran fold and thrust fault belt developed as the deformation front advanced eastward, and northeastern Alberta was uplifted by Middle-Late Jurassic Columbian tectonism, concurrent with the buckling deformation of the craton underlying the foreland. The Lower Cretaceous Athabasca Oil Sands and the Cold Lake deposit to the south, accumulated along a broad paleovalley trunk segment of a continental-scale drainage that flowed north to the Boreal Sea (Benyon and others, 2014). Cretaceous dissolution patterns also occurred across extensive areas of southern Saskatchewan as the intracratonic Williston Basin subsidence continued.

Three areas were selected to illustrate the structural styles of the hypogene Prairie Evaporite karst collapse across western Canada.

Area 1. Eastern Basin Margin from NE Alberta to SE Saskatchewan and SW Manitoba

Regional groundwater flow within permeable Devonian strata was mostly directed up-structure to the northeast, concurrent with deepening of the foreland Alberta Basin and intracratonic Williston Basin. These flows resulted in a 1,000-km long and 100–150-km-wide dissolution trend along the eastern margin of the Prairie Evaporite Formation salt basin. The dissolution trend extends from northeastern Alberta to southeastern Saskatchewan and into southwestern Manitoba (fig. 1). A 300-km-long segment of the 10–20-km-wide dissolution front in the northeastern Alberta Basin, known as the salt scarp, underlies the Lower Cretaceous Athabasca Oil Sands.

Multiple dissolution stages removed halite-anhydrite beds in the strata below the Athabasca deposit as a result of the Middle Jurassic to Early Cretaceous Columbian orogeny, and post-orogenic salt removal stages concurrent with the Aptian accumulation of the McMurray Formation. These sand deposits unconformably covered the Devonian karstic limestone terrain, a mosaic of differentially subsided Middle-Upper Devonian fault blocks overlying the dissected salt scarp and salt removal areas to the east (Bachu, 1995, 1999; Anfort and others, 2001; Hein and others, 2013; Schneider and Grobe, 2013; Broughton, 2013, 2015).

Area 2. Roncott Platform-Hummingbird Trough in Southern Saskatchewan

Multi-stage salt dissolution events occurred throughout the post-burial subsidence history of the Prairie Evaporite basin, impacting overlying strata across most of southern Saskatchewan. The earliest dissolution events occurred during the Late Devonian, probably as meteorically charged groundwater came into contact with shallowly buried salt beds. Late Paleozoic Antler tectonism, particularly during the Carboniferous, resulted in formation waters that flowed northward up-structure from ancestral tectonic structures in northeastern Montana and western North Dakota, toward the northeastern rim of the Williston Basin in southeastern Saskatchewan and southwestern Manitoba (figs. 2 and 3).

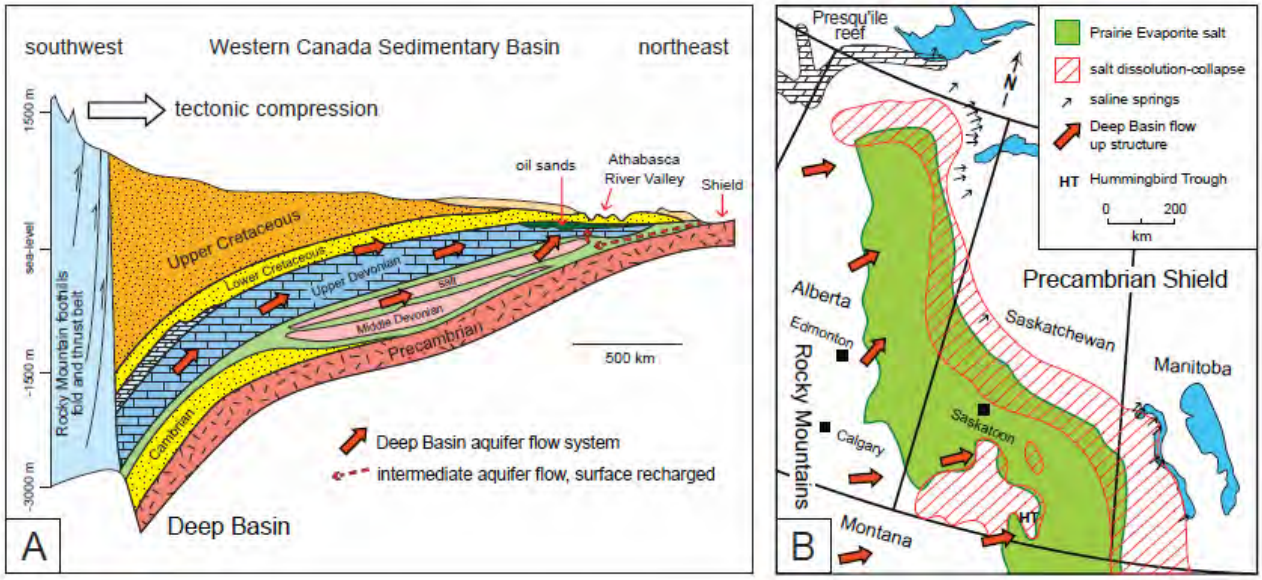

Figure 2. Tectonic compression and hydraulic head resulted in deep basin aquifer water flows to the northeast along Devonian strata, combined with compaction driven vertical flows into the overlying salt beds of the Middle Devonian Prairie Evaporite. A, Schematic profile of the Alberta foreland basin, and B, Dissolution trends developed along the eastern up-dip salt basin margin of the Western Canada Sedimentary Basin and across the southern Saskatchewan part of the northern Williston Basin. Numerous brine seeps and saline springs at the surface are distributed along river valleys and topographic lowlands near the exposed Canadian Shield. Modified from Garven (1989).

The Roncott Platform in southern Saskatchewan, consisting of undisturbed salt beds, was bounded on the east by the multi-stage collapse of the 150-km-long Hummingbird Trough (Holter, 1969). Dissolution events along the western and eastern margins of the Roncott Platform commenced during the Late Devonian, and were the earliest known dissolution stages impacting the Prairie Evaporite halite beds. Extensive areas of salt removal during the Mississippian to Jurassic resulted in further definition of the Roncott Platform margins. Deepening of the Hummingbird Trough (fig. 4) resulted in salt collapse-induced closures that trapped oil migrations into the area. Extensive post-Jurassic salt removal stages subsequently impacted most of south-central Saskatchewan beyond the area of the Roncott Platform. More subdued collapse-subsidence trends developed during the Maastrichtian and into the Early Paleogene, controlling deposition patterns along the margins of the Roncott Platform. Lignite coal basins of the Ravenscrag Formation (Paleocene) developed within the Hummingbird Trough along the eastern margin and the Coronach Trough along the western margin of the Roncott Platform (Broughton, 1977, 1985). Overall, up to 200 m of halite and halite-anhydrite beds were removed across most of southern Saskatchewan (fig. 1).

Area 3. Pleistocene Collapse Structures in Southern Saskatchewan

Pleistocene subglacial and proglacial meltwater into the subsurface mixed with the regional aquifer water flows, resulting in salt dissolution collapse structures distributed across southern and central Saskatchewan. These were usually rejuvenated older collapse sites. For example, the Saskatoon Low south of the city is a 40-km-long and 25-km-wide depression with 200 m of closure on the Cretaceous structure (Christiansen, 1967). It resulted from a large salt dissolution collapse that was propagated into the overlying 1,350-m-thick strata. Superimposed on

this pre-glacial structure was a 16-km-long and 8-km-wide Pleistocene (Wisconsinan) collapse structure with 70 m of closure. Another site with significant Pleistocene salt collapse is the 360-km² Rosetown Low located near the city of Saskatoon with 110 m of closure. The Regina Low near the Roncott Platform resulted from a collapse structure with 175 m of closure (Christiansen and Sauer, 2002). Not all salt dissolution events resulted in only collapse-subsidence structures. For example, the Howe Lake site in southeastern Saskatchewan was a salt collapse structure, but extreme pressure built up from invasion by glacial meltwaters, resulted in a blowout crater (Christiansen, 1971; Christiansen and others, 1982).

Subglacial Meltwaters

Geochemical studies of total dissolved solids (TDS) and stable isotopes such as $\delta^{18}O$ (H_2O) in aquifer waters and saline surface seeps indicate that Pleistocene glacial meltwaters mixed with regional aquifer water. This resulted in undersaturated waters in contact with the salt scarp trend, rejuvenating dissolution of Middle Devonian salt beds across large areas of the Alberta and Williston basins of the WCSB (Grasby and Chen, 2005; Gue, 2012; Cowie and others, 2014a, 2014b, 2015).

Strongly pressured subglacial meltwaters were driven into the subsurface by the hydraulic head of the 1.5–2-km-thick ice sheet during the Laurentide glacial maximum (about 25–40 thousand years [ka]) and recession (about 8–12 ka) (Dyke and others, 2002). These influxes of glacial meltwaters into the regional aquifer extended along the length of the 1,000-km-long salt dissolution trend following the eastern margin of the Prairie Evaporite basin (fig. 1). The hydraulic head of the glacial meltwater flows was sufficient to reverse the regional aquifer water flows in the subsurface for up to 200–300 km southwest of the WCSB margin.

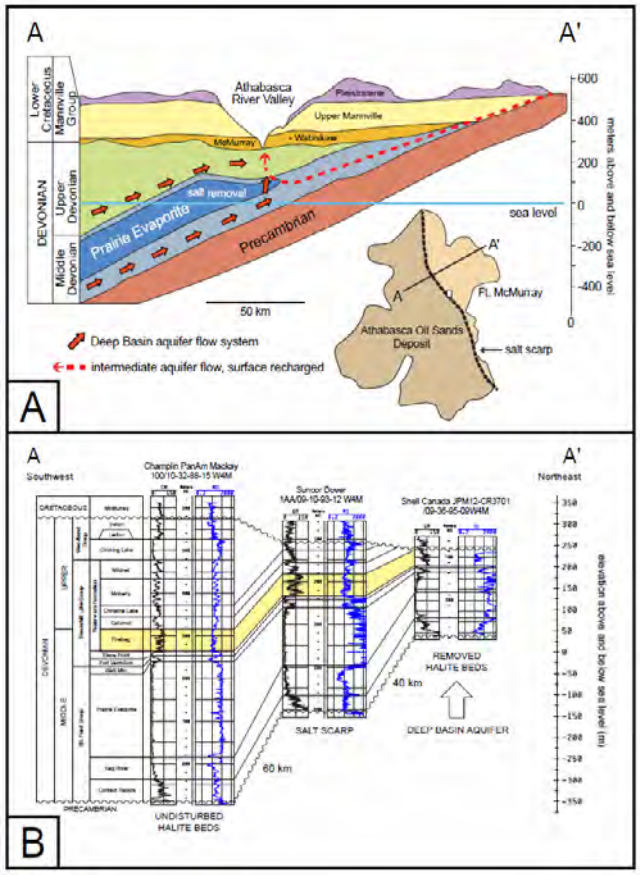

Figure 3. Profiles of the Athabasca Oil Sands illustrating thinned Paleozoic strata resulting from surface erosion during the Middle Jurassic to Early Cretaceous Columbian orogeny. A, Schematic profile illustrating Cretaceous strata on the Devonian unconformity surface. As much as 1.5 kilometers of Paleozoic strata may have been eroded across northeastern Alberta as the foreland basin deepened and northeastern Alberta was uplifted, resulting in strata tilted to the southwest. B, Concurrent salt removal patterns resulted from aquifer water flows up-structure to the northeast combined with compaction driven vertical flows from the Keg River Formation into the overlying Prairie Evaporite salt beds. The surface and subsurface erosion resulted in a thinned Paleozoic interval underlying the Athabasca Oil Sands. These flows to the northeast up-structure were reversed during the Pleistocene by glacial meltwaters that flowed into the subsurface. The meltwaters came in contact with shallowly buried salt beds, rejuvenating dissolution. Modified from Broughton (2013, 2015).

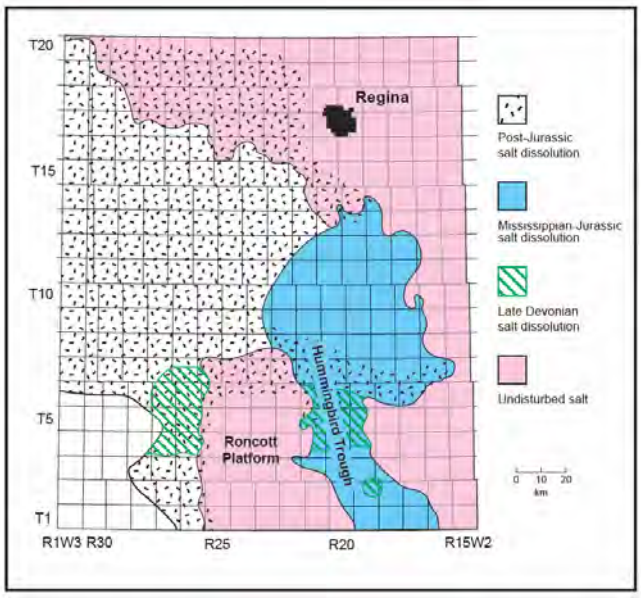

Figure 4. Paleozoic and Mesozoic salt dissolution patterns across southern Saskatchewan included the multi-stage collapse of the Hummingbird Trough along the eastern margin of the Roncott Platform. Modified from Holter (1969).

Alberta Basin

The geochemistry of these regional aquifer flows along permeable Devonian strata to the northeast up-structure indicate mixture with subglacial meltwaters that invaded and reversed the regional flow during glacial loading. These subglacial meltwaters flowed down structure to the southwest into the shallow Cretaceous and Devonian aquifers, encountering the regional flow to the northeast in areas such as below the proto-Athabasca River Valley, which dissected the northern Athabasca Oil Sands (fig. 5A).

The geochemical evidence indicates TDS in McMurray Formation pore waters vary widely from freshwater (240 milligrams per liter [mg/L]) to hypersaline brines as high as 280,000 mg/L (Cowie, 2013; Cowie and others, 2014a, 2014b, 2015). Elevated salinity values for formation water samples, collected from McMurray Formation strata, are observed along an approximately linear trend from Township (Twp.) 78, Range (Rge.) 4, to the northwest into Twp. 100, Rge. 10, W4M (fig. 5B). This near linear trend of elevated salinity values (greater than 25,000 mg/L) coincides with the underlying trend of the Prairie Evaporite salt scarp, only 200 m below.

Stable isotopes, mostly $\delta^{18}O$ (H_2O), observed in saline spring and brine seeps at the surface along the Athabasca and Clearwater river valleys, which dissected the Athabasca Oil Sands deposit, indicate chemical compositions consistent with waters derived from glacial meltwaters mixed with Devonian aquifer waters, but also incorporating dissolved solids from evaporite beds within the Middle Devonian substrate (Grasby and Chen, 2005; Gue, 2012). Gue and others (2015) measured spring waters with $\delta^{18}O$ (H_2O) values as low as -23.5‰ (permil). The proportion of glacial meltwater in these spring water samples ranged from 39 percent to as much as 75 percent. The geochemistry, such as isotope ratios and total dissolved solids for these mixed glacial, Devonian aquifer, and dissolved Prairie Evaporite beds, is similar to other geochemical measurements of water salinity in the Devonian substrate, such as below the bitumen mine floors.

Broughton (2013) and Cowie (2013) interpreted that karstic collapse features, such as breccia pipe-sinkhole complexes and salt collapse-related faults within the Middle-Upper Devonian and Lower Cretaceous strata, served as vertical pathways for saline water migrations upward into overlying the McMurray beds. The saline waters were eventually discharged as saline seeps and springs at the surface (Gibson and others, 2013). These trends may have been accelerated during glacial loading and unloading (Grasby and Chen, 2005). Karst conduits were more highly developed and effective in the areas overlying the salt scarp and eastward across salt removal areas, providing connectivity between the Devonian aquifer and overlying McMurray hydraulic systems. These areas overlying the salt scarp contrast with areas to the west where the evaporite beds were not extensively impacted by dissolution. Nevertheless, extensive areas of the Middle Devonian salt beds sourced dissolved solids in the formation waters west of the salt scarp, particularly within strata underlying northeast-trending paleovalleys (fig. 6).

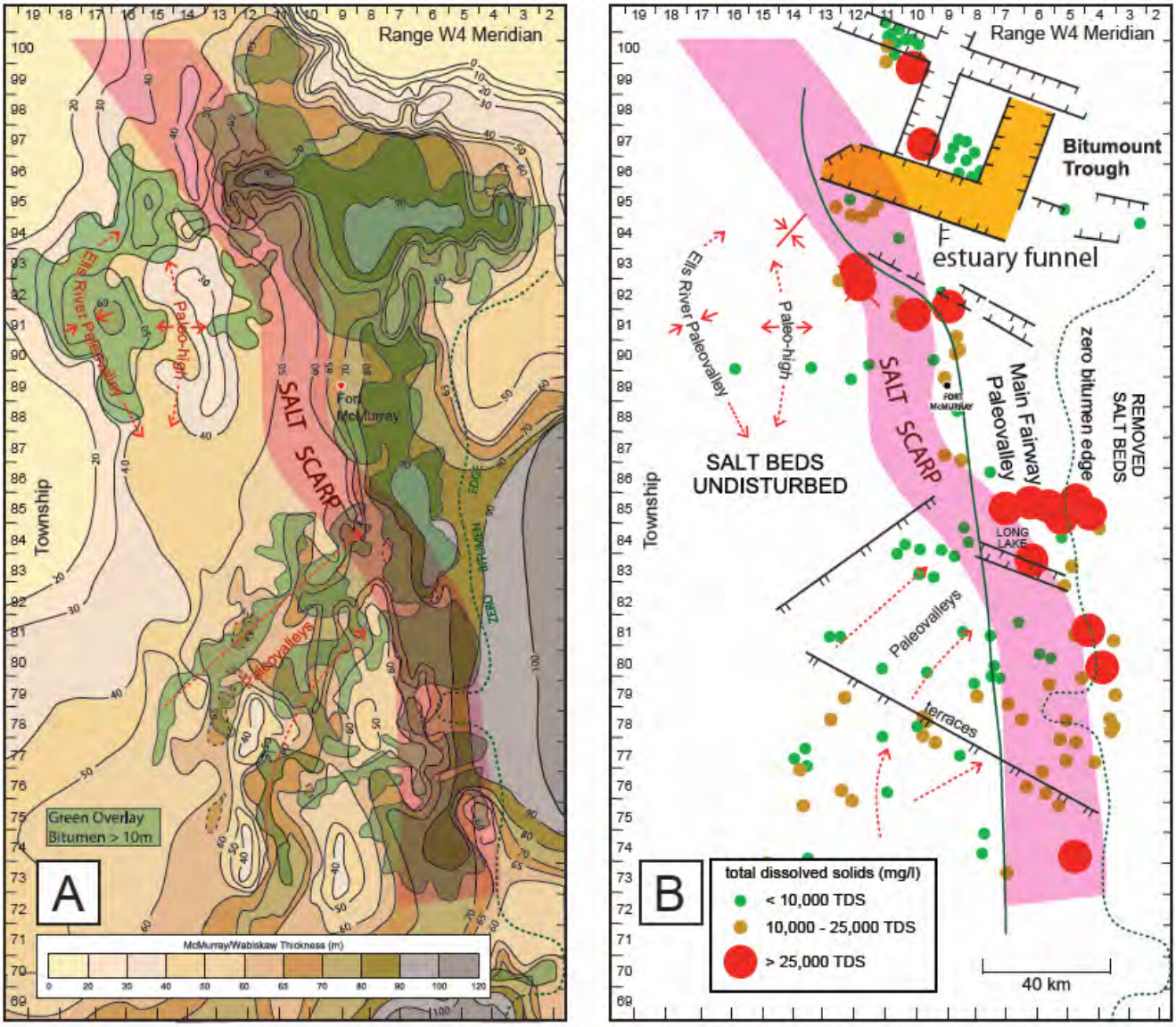

Figure 5. The Athabasca Oil Sands deposit in northeastern Alberta. A, Thickness of the McMurray Formation (Aptian) and overlying Wabiskaw Member, Clearwater Formation (Albian) strata. Overlay of bitumen sand bed distribution (BWB >8%; >10 m thick), and the Prairie Evaporite salt scarp (pink), 200 m below. B, Interpretation of structural trends on the sub-Cretaceous unconformity surface, consisting of karstic limestone terrain flooring deposits of the McMurray Formation. Overlay of McMurray Formation water geochemistry illustrates the trend of elevated total dissolved solids, which follows the underlying salt scarp. Modified from Broughton (2013, 2015) and Cowie (2013).

Williston Basin

Recharge areas for the Williston Basin in the Montana Uplift and the Black Hills resulted in north-northeast aquifer water flows up-structure toward topographically lower areas in southern Saskatchewan and southwestern Manitoba (Grasby and Chen, 2005). There is a broad range of salinity values in the carbonate strata of the basin, ranging from 20 to more than 300 grams per liter, with similar measurements in water samples collected from the Alberta Basin (figs. 5B and 6). The highest TDS measurements are from groundwater samples collected within

the north-central Williston Basin from strata overlying the Prairie Evaporite salt beds (fig. 6). The TDS values become progressively lower toward the modern day recharge zones in eastern Montana and western North Dakota.

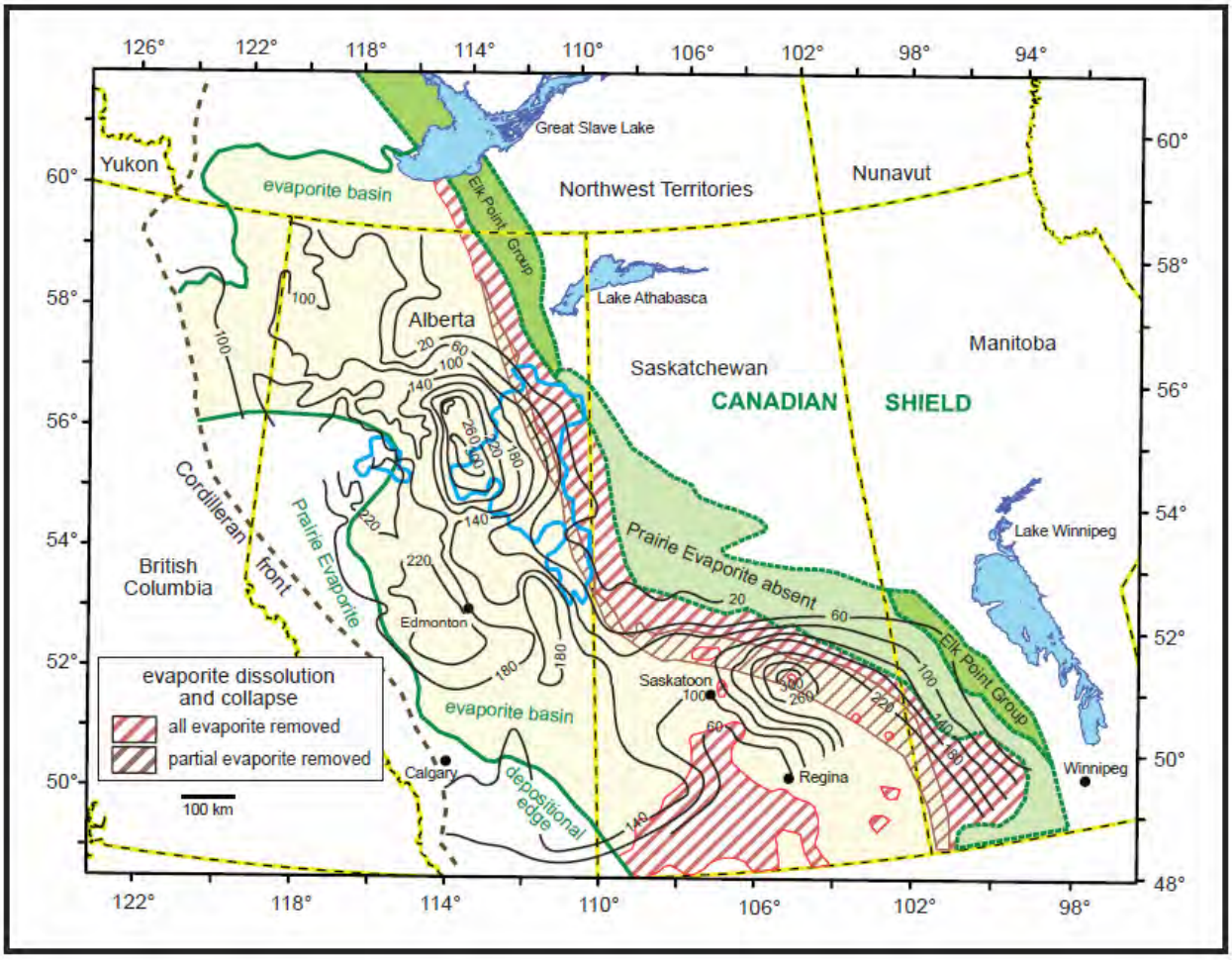

Figure 6. Distribution of total dissolved solids (TDS) in the Devonian aquifer system overlying the Prairie Evaporite basin across western Canada, based on drill-stem test data. Contour interval is 40 grams per liter TDS. Modified from Grasby and Chen (2005).

Grasby and others (2000) and Grasby and Chen (2005) calculated Na/Cl and Cl/Br ratios for groundwater samples, and interpreted the results as indicating mixtures of meteoric, glacial, and deep basin aquifer waters (fig. 7). The $\delta^{18}O$ (H_2O) depleted Na-Cl brines migrated to the northeast, up-structure, and discharged at numerous saline springs distributed along the eastern Prairie Evaporite basin margin in southeastern Saskatchewan and southwestern Manitoba, as well as across northeastern Alberta in topographically low areas such as the Athabasca River Valley.

Glacial meltwaters that invaded Devonian carbonate aquifers substantially diluted the brines that resulted in high Na/Cl but low Cl/Br ratios (fig. 7). Brines formed by the dissolution of halite have a substantially different Br/Cl ratio than residual evaporated seawater because during precipitation of halite from seawater bromide is excluded from the crystal structure. This results in a higher Cl/Br mass ratio in halite minerals and subsequently, in dissolution brines compared to seawater. The Cl/Br ratio in halite is generally greater than 3,000, but can be an order of magnitude higher, depending on re-dissolution/

re-precipitation cycles, whereas the Cl/Br ratio of meteoric water is much lower, generally less than 200 (Gue and others, 2015). The Cl/Br ratios in spring waters are generally consistent with halite dissolution sourced Na and Cl ions mixed with lower TDS of formation waters (fig. 7). This indicates that the brines discharged along the 1,000-km-long dissolution trend paralleling the eastern margin of the evaporite basin, have elevated salinities that resulted from dissolution of evaporite beds, and are mostly sourced from deep basin aquifer waters.

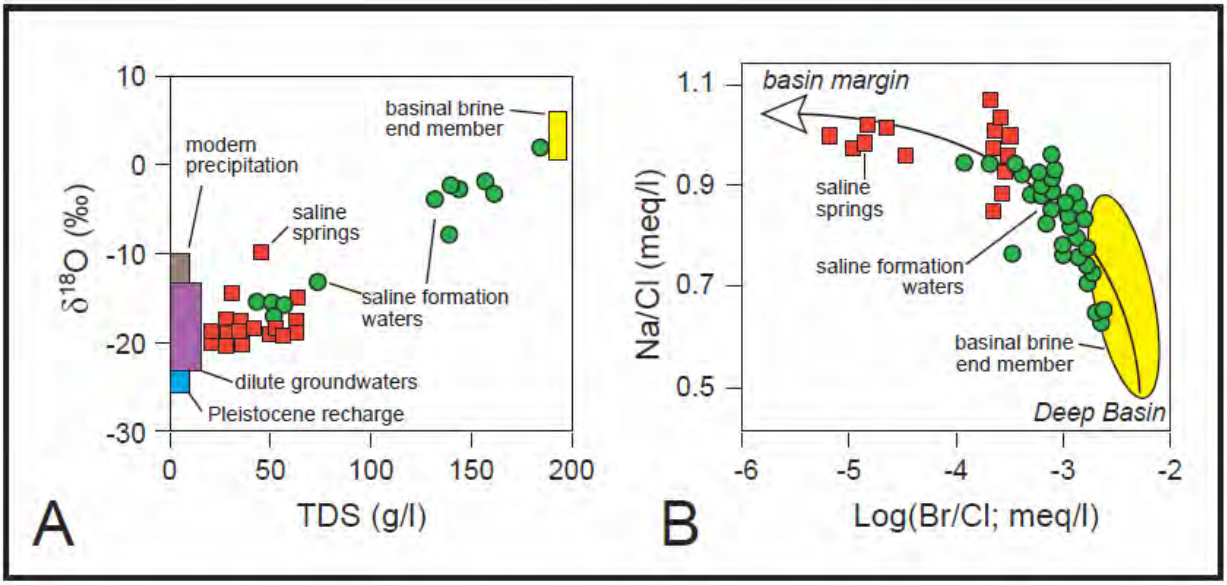

Figure 7. Geochemistry of multiple sourced waters. A, Oxygen isotope compositions of meteorically charged groundwater and basin brine samples collected from the Williston Basin, illustrating mixture of glacial meltwaters and saline waters. B, Na-Cl-Br in basin formation waters with high Na/Cl and low Cl/Br ratios. Isotopically depleted NaCl-rich waters discharged as brine seeps and saline springs at the surface along the eastern margin of the Prairie Evaporite salt basin. Modified from Grasby and others (2000), Grasby and Chen (2005), and Person and others (2007).

Glacial Loading and Reversal of the Regional Aquifer Flow System

Grasby and Chen (2005), Cowie and others (2014a, 2014b, 2015) and Broughton (2015, 2016) investigated the hydrogeological impact of aquifer water flows to the northeast toward the eastern margin of the WCSB and the largely coincidental edge of the Prairie Evaporite salt basin (figs. 1 and 8), as well as reversals in flow direction by an influx of glacial meltwaters driven by the hydraulic head associated with the height of the Laurentide ice sheet (Grasby and Betcher, 2000; Grasby and others, 2000). The ice sheet thickness varied from 1.5–2 km across Alberta and Saskatchewan to a 3-km-thick bulge over the present-day Hudson Bay in eastern Canada (Boulton and others, 1995; Margold and others, 2015).

Salinity data indicate that a chemical boundary between saline and fresh formation waters extended across southeastern Saskatchewan and southwestern Manitoba areas of the northern Williston Basin. This partition resulted from the influx of meltwaters into bedrock underlying topographic lows for distances up to 300 km, southwestward of the basin edge onlap with the Canadian Shield. This resulted in a geochemical and hydrologic divide between Williston Basin deep aquifer water flows up-structure to the northeast, and southwestward flows down-dip by invading glacial meltwaters (Betcher and others, 1995). Geochemical

evidence indicates that this invasion by fresh glacial meltwaters extended into areas characterized by high TDS, greater than 100,000 mg/L. The limits of the southwestward influx by freshwater may be approximated by the 2,000 mg/L boundary (Betcher and others, 1995; Grasby and Betcher, 2000; Grasby and others, 2000). The $\delta^{18}O$ (H_2O) stable isotope ratio values in formation waters along this northeast flank of the Williston Basin similarly indicate that fresh glacial meltwaters flowed into the Paleozoic strata and mixed with basin brines. These glacial meltwaters have end member $\delta^{18}O$ (H_2O) ratio values of -22‰ (Grasby and others, 2000).

Grasby and others (2000) interpreted the hydraulic head of the subglacial meltwaters as dependent upon whether the flow system was dominated by hydrostatic or lithostatic pressure. Free water under lithostatic load at the base of a 1.5-km-thick ice sheet would have pressures equivalent to a 1,400-m-high water column. The ice sheet was probably thicker, perhaps more than 2 km across northern Alberta, but less than the 3-km-high bulge over the present-day Hudson Bay (Dyke and others, 2002; Fisher and others, 2009; Margold and others, 2015). This thickness of a relatively porous ice sheet would have a hydraulic head sufficient to reverse the regional basin flow direction up-structure to the northeast. Provided that the modern regional aquifer water flow system of the WCSB was similar to the pre-Quaternary system, it underwent two flow reversals (fig. 8). The first resulted from glacial loading, and the second from reassertion of the earlier system following glacial retreat.

Discussion of Impact of Karst Collapse on Major Hydrocarbon Accumulations: The Athabasca Oil Sands

Oil migrations into the northern Alberta Basin from Exshaw Formation (Devonian-Mississippian) source rocks to the west were trapped by unconsolidated sand reservoirs of the McMurray Formation (Aptian), and overlying Wabiskaw sands, if present, accumulated as the basal member of the Clearwater Formation (Albian). Oil accumulations in these multi-kilometer-long sand reservoirs subsequently biodegraded into bituminous sand deposits (Head and others, 2003). The 45,000- km² Athabasca Oil Sand deposit consists of bituminous sand accumulations up to 100 m thick, resulting in a 200 billion cubic meter or a trillion barrel hydrocarbon resource (fig. 5A).

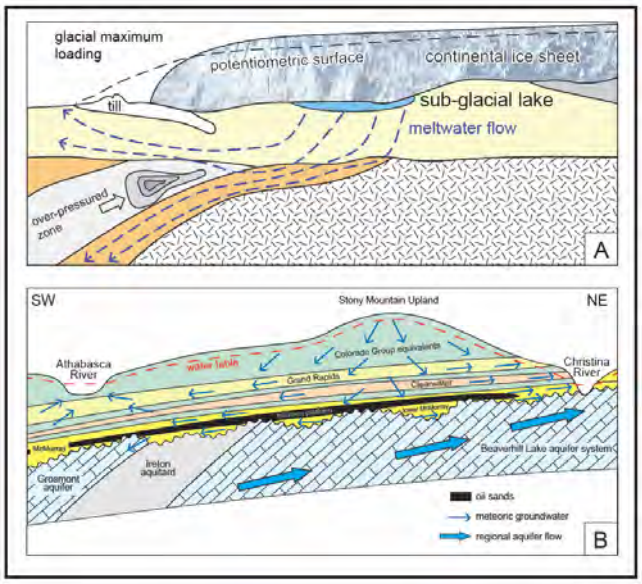

Figure 8. Schematic illustrations of the Quaternary water flows into Cretaceous and Devonian strata, such as at the Athabasca Oil Sands. A, Strongly pressured subglacial meltwaters driven into the subsurface by the hydraulic head of a 1.5-2-km-thick Laurentide ice sheet. Meltwater flowed into the subsurface to the southwest along Devonian strata, and reversed the direction of the regional aquifer water flows up-structure to the northeast, but reasserted upon retreat of the ice sheet (modified from Person and others, 2007). B, Holocene meteorically charged groundwater flows near river valleys in Cretaceous strata overlying the bitumen aquiclude were often counter to the regional aquifer water flows in Devonian strata below the aquiclude. Modified from Barson and others (2001).

The unusual geological aspect of the Athabasca Oil Sands is that the northern one-third of the deposit overlies a portion of the largest known halite-dominated evaporite karst collapse. Removal of 100–150 m of salt beds collapsed the overlying 175–250-m interval of Middle-Upper Devonian strata, resulting in a significant structural control on the fluvial-estuarine McMurray Formation sand depositional trend. This hypogene salt karst collapse resulted in mosaics of differentially subsided Devonian fault blocks above the salt removal areas (Broughton, 2013, 2015). Dissolution patterns developed in the Prairie Evaporite strata, concurrent with overlying McMurray deposition, resulting in 10s of km-long syndepositional sand trends. The dissolution fronts advanced along northwest- and northeast-oriented fracture-fault lineaments that dissected the salt beds, and subsequently coalesced into larger salt removal areas. These overarching structural trends configured the overlying Devonian karst topography.

A lattice-like organization by the lower McMurray braided river network resulted from draping onto the differentially subsided fault block pattern and resulting in a reticulated karstic Devonian topography. This resulted in 1–3-km-long reservoirs of pebble gravel and sand channel fills oriented to the northwest and to the northeast. The 50-km-long V-shaped Bitumount Trough, the largest of the salt collapse structures, filled with these lower McMurray channel sand deposits that paralleled salt dissolution patterns in the Middle Devonian substrate. The northern margin of the Bitumount Trough collapsed during lower McMurray deposition, as a result of extensive dissolution along a lineament that cross-cut the underlying salt scarp. This trough, as much as 100 m deep, extended along the northern margin of the Bitumount Trough and was floored by a 20-km-long linear chain of Devonian fault blocks. The resulting accommodation space filled as a syndepositional sand trend, 40–60 m thick, and was subsequently bitumen saturated (Broughton, 2013, 2015). The Horizon, Muskeg River, and Aurora North mines are located along this trend.

During the middle McMurray interval, salt dissolution fronts directed along cross-cutting lineaments migrated north of the Bitumount Trough. These advances resulted in salt removal patterns across the Central Collapse structure. Together, the Bitumount Trough and Central Collapse configured the northern Athabasca deposit as a lower estuary structural funnel. Incremental advances by the dissolution fronts underlying the Central Collapse area resulted in northeast-aligned terraces consisting of Upper Devonian-lower McMurray fault blocks that stepped down northward into the Central Collapse. Sand and fines were transported to the north along the relatively unstable Devonian substrate that floored the structural funnel.

The sinuous river channel belts to the south were constrained along the more stable substrate below the main paleovalley (fig. 5A). The main fairway branched onto the structural funnel as multiple, 10–30-km-long, sub-parallel fluvial-marine channel fairways. These aligned along the northwest-oriented structural grain imparted by salt dissolution trends only 200 m below. This resulted in the collinear alignments of 1–5-km-long stacked point bar complexes along these fluvial-marine fairways as they cascaded over the step-down terraces. This architecture permitted collinear alignments of detached aggradation sites, each consisting of overlying point bar complexes. The middle interval sand bar complexes, typically 2–5 km long and 20–40 m thick, resulted in giant scale reservoirs. Subsequent in-situ biodegradation during the early Paleogene resulted in giant commercially attractive sand complexes, each extending across 10s of km².

Regional salt dissolution continued during the middle-upper McMurray, below the northern margin of the western Bitumount Trough and adjacent areas of the Central Collapse. This resulted in an upper McMurray syndepositional sand trend. The 20-km-long accumulation paralleled a similar sand complex trend in the lower McMurray.

Conclusions

Multi-stage dissolution events occurred across southern Saskatchewan as responses to Paleozoic (Antler) and Jurassic-Cretaceous orogenic tectonism. In contrast, most of the salt removal patterns in northeastern Alberta resulted from Middle Jurassic to Early Cretaceous Columbian tectonism, followed by post-orogenic dissolution stages concurrent with deposition of the McMurray Formation (Aptian).

Deep basin aquifer water, recharged along Rocky Mountain terrain uplands, flowed up-structure to the northeast, resulting in a 1,000-km-long and 150-km-wide dissolution trend along the eastern margin of the Prairie Evaporite salt basin. Concurrent aquifer water recharged in the Montana Uplift flowed up-structure into the northern Williston Basin, resulting in extensive salt removal areas across southern Saskatchewan. These flows mixed with compaction driven vertical flows from the Keg River and other Devonian strata into the overlying Prairie Evaporite salt beds. The flows were directed to the northwest and to the northeast along cross-cutting sets of fracture-fault lineaments, which were propagated upward from Precambrian blocks responding to orogenic deformation of the underlying basement rocks. Removal of 100–150 m of salt in northeastern Alberta and up to 200 m across southern Saskatchewan resulted in the largest known hypogene halite karst collapse. The salt karst collapse structures in northeastern Alberta extensively impacted depositional trends in the overlying strata accumulated as the Athabasca Oil Sands.

During the Pleistocene, the hydraulic head of a 1.5–2-km-thick ice sheet resulted in subglacial meltwater influxes into the Devonian strata along the 1,000-km-long dissolution trend previously established along the eastern margin of the Western Canada Sedimentary Basin. These meltwaters were sufficiently pressured to temporarily reverse the basin water flows up-structure to the northeast until reasserted upon ice sheet withdrawal. The influx of fresh meltwaters came in contact with shallowly buried Middle Devonian salt beds, rejuvenating older collapse structure across southern Saskatchewan. Glacial meltwater flows into the subsurface and along lineaments within the salt beds resulted in aligned sinkholes on the subglacial topography in northeastern Alberta.

Acknowledgments

The author expresses his appreciation for commentaries by N. Pearson, Ph.D., Chevron Canada; M. Grobe, Ph.D., Alberta Geological Survey; Prof. J. Gibson, University of Victoria; Bryce Jablonski, Statoil Canada; and Tyler Hauck, Alberta Geological Survey. The manuscript was greatly improved with their peer reviews.

References Cited

Anfort, S.J., Bachu, S., and Bentley, L.R., 2001, Regional-scale hydrogeology of the Upper Devonian sedimentary succession, south-central Alberta Basin, Canada: AAPG Bulletin, v. 85, p. 637–660.

Bachu, S., 1995, Synthesis and model of formation-water flow, Alberta Basin, Canada: AAPG Bulletin, v. 79, p. 1159–1178.

Bachu, S., 1999, Flow systems in the Alberta Basin—Patterns, types and driving mechanisms: Bulletin of Canadian Petroleum Geology, v. 47, p. 455–474.

Bachu, S., and Underschultz, J.R., 1993, Hydrogeology of formation waters, northeastern Alberta: AAPG Bulletin, v. 77, p. 1745–1768.

Barson, D., Bachu, S., and Esslinger, P., 2001, Flow systems in the Mannville Group in the east-central Athabasca area and implications for steam-assisted gravity drainage (SAGD) operations for in situ bitumen production: Bulletin of Canadian Petroleum Geology, v. 49, p. 376–392.

Benyon, C., Leier, A.L., Leckie, D.A., Webb, A., Hubbard, S.M., and Gehrels, G.E., 2014, Provenance of the Cretaceous Athabasca Oil Sands, Canada—Implications for continental-scale sediment transport: Journal of Sedimentary Research, v. 84, p. 136–143.

Betcher, R., Grove, G., and Pupp, C., 1995, Groundwater in Manitoba—Hydrogeology, quality concerns, management: National Hydrology Research Institute, Saskatoon, Contribution CS-93017, 47 p.

Boulton, G.S., Caban, P.E., and Van Gijssel, K., 1995, Groundwater flow beneath ice sheets—Part 1-large scale patterns: Quaternary Science Reviews, v. 14, p. 545–562.

Broughton, P.L., 1977, Origin of coal basins by salt solution: Nature, v. 270, p. 420–423.

Broughton, P.L., 1985, Geology and resources of the Saskatchewan coalfields, *in* Patching, T.S., ed., Coal in Canada: Canadian Institute of Mining and Metallurgy, Special Volume 31, p. 87–99.

Broughton, P.L., 2013, Devonian salt dissolution-collapse breccias flooring the Cretaceous Athabasca Oil Sands deposit and development of lower McMurray Formation sinkholes, northern Alberta Basin, western Canada: Sedimentary Geology, v. 283, p. 57–82.

Broughton, P.L., 2015, Syndepositional architecture of the northern Athabasca Oil Sands deposit, northeastern Alberta: Canadian Journal of Earth Sciences, v. 52, p. 21–50.

Broughton, P.L., 2016, Alignment of fluvio-tidal bars in the middle McMurray Formation—Implications for structural architecture of the Lower Cretaceous Athabasca Oil Sands deposit, northern Alberta: Canadian Journal of Earth Sciences, v. 53, p. 896–930.

Christiansen, E.A., 1967, Collapse structures near Saskatoon, Saskatchewan, Canada: Canadian Journal of Earth Sciences, v. 4, p. 757–767.

Christiansen, E.A., 1971, Geology of the Crater Lake collapse structure in southeast Saskatchewan: Canadian Journal of Earth Sciences, v. 8, p. 1505–1513.

Christiansen, E.A., Gendzwill, D.J., and Meneley, W.A., 1982, Howe Lake—A hydrodynamic blowout structure: Canadian Journal of Earth Sciences, v. 19, p. 1122–1139.

Christiansen, E.A., and Sauer, E.K., 2002, Stratigraphy and structure of Pleistocene collapse in the Regina Low, Saskatchewan, Canada: Canadian Journal of Earth Sciences, v. 39, p. 1411–1423.

Cowie, B.R., 2013, Stable isotope and geochemical investigations into the hydrogeology and biochemistry of oil sands reservoir systems in northeastern Alberta, Canada, Ph.D. dissertation, University of Calgary, 239 p.

Cowie, B.R., James, B., and Mayer, B., 2015, Distribution of total dissolved solids in McMurray Formation water in the Athabasca Oil Sands region, Alberta, Canada—Implications for regional hydrogeology and resource development: AAPG Bulletin, v. 99, p. 77–90.

Cowie, B.R., James, B., Nightingale, M., and Mayer, B., 2014a, Determination of the stable isotope composition and total dissolved solids of Athabasca Oil Sands reservoir porewater—Part 1. A new tool for aqueous fluid characterization in oil sands reservoirs: AAPG Bulletin, v. 98, p. 2131–2141.

Cowie, B.R., James, B., Nightingale, M. and Mayer, B., 2014b, Determination of the stable isotope composition and total dissolved solids of Athabasca Oil Sands reservoir porewater—Part 2. Characterization of McMurray Formation waters in the Suncor-Firebag field: AAPG Bulletin, v. 98, p. 2143–2160.

DeMille, G., Shouldice, J.R., and Nelson, H.W., 1964, Collapse structures related to evaporites of the Prairie Formation, Saskatchewan: GSA Bulletin, v. 75, p. 307–316.

Dyke, A.S., Andrews, J.T., Clark, P.U., England, J.H., Miller, G.H., Shaw, J., and Veillette, J.J., 2002, The Laurentide and Innuitian ice sheets during the last glacial maximum: Quaternary Science Reviews, v. 21, p. 9–31.

Fisher, T., Waterson, N., Lowell, T.V., and Hajdas, I., 2009, Deglaciation ages and meltwater routing in the Fort McMurray region, northeastern Alberta and northwestern Saskatchewan, Canada: Quaternary Science Reviews, v. 28, p. 1608–1624.

Ford, D.C., 1997, Principal features of evaporite karst in Canada: Carbonates and Evaporites, v. 12, p. 15–23.

Garven, G., 1989, Hydrogeological model for the formation of the giant oil sands deposits of the Western Canada Sedimentary Basin: American Journal of Science, v. 289, p. 105–166.

Gibson, J.J., Fennell, J., Birks, S.J., Yi, Y., Moncur, M.C., Hansen, B., and Jasechko, S., 2013, Evidence of discharging saline formation water to the Athabasca River in the oil sands mining region, northern Alberta: Canadian Journal of Earth Sciences, v. 50, p. 1244–1257.

Grasby, S.E., and Betcher, R., 2000, Pleistocene recharge and flow reversal in the Williston Basin, central North America: Journal of Geochemical Exploration, v. 69–70, p. 403–407.

Grasby, S.E., and Chen, Z., 2005, Subglacial recharge in the Western Canada Sedimentary Basin— Impact of Pleistocene glaciations on basin hydrodynamics: GSA Bulletin, v. 117, p. 500–514.

Grasby, S.E., Osadetz, K., Betcher, R., and Render, F., 2000, Reversal of the regional-scale flow system of the Williston Basin in response to Pleistocene glaciation: Geology, v. 7, p. 635–638.

Grobe, M., 2000, Distribution and thickness of salt within the Devonian Elk Point Group, Western Canada Sedimentary Basin: Alberta Geological Survey Earth Sciences Report 2000-02, 12 p.

Gue, A.E., 2012, Geochemistry of saline springs in the Athabasca Oil Sands region and their impact on the Clearwater and Athabasca Rivers: University of Calgary M.Sc.thesis, 173 p.

Gue, A.E., Mayer, B., and Grasby, S.E., 2015, Origin and geochemistry of saline spring waters in the Athabasca Oil Sands region, Alberta, Canada: Applied Geochemistry v. 61, p. 132–145.

Head, I.M., Jones, D.M., and Larter, S.R., 2003, Biological activity in the deep subsurface and the origin of heavy oil: Nature, v. 426, p. 344–352.

Hein, F.J., Dolby, G. and Fairgrieve, B., 2013, A regional geologic framework for the Athabasca Oil Sands, northeastern Alberta, Canada, *in* Hein, F., Leckie, S., and Suter, J., eds., Heavy-oil and oil-sand petroleum systems in Alberta and beyond: AAPG Studies in Geology, v. 64, p. 207–250.

Holter, M.E., 1969, Middle Devonian Prairie Evaporite of Saskatchewan: Saskatchewan Department of Mineral Resources Report 123, 134 p.

Margold, M., Stokes, C.R., and Clark, C.D., 2015, Ice streams in the Laurentide ice sheet—Identification, characteristics and comparison to modern ice sheets: Earth Science Reviews, v. 143, p. 117–146.

McTavish, G.J., and Vigrass, L.W., 1987, Salt dissolution and tectonics, south-central Saskatchewan, *in* Carlson, C.G., and Christopher, J.E., eds., Proceedings, Fifth International Williston Basin Symposium: Saskatchewan Geological Society Special Publication 9, p. 157–168.

Person, M., McIntosh, J., Bense, V., and Remenda, V.H., 2007, Pleistocene hydrogeology of North America—The role of ice sheets in reorganizing groundwater flow systems: Reviews of Geophysics, v. 45, 28 p.

Qing, H., and Mountjoy, E.W., 1992, Large-scale fluid flow in the Middle Devonian Presqu'ile barrier, Western Canada Sedimentary Basin: Geology, v. 20, p. 903–906.

Rhodes, D., Lantos, E.A., Lantos, J.A., Webb, R.J., and Owens, D.C., 1984, Pine Point orebodies and their relationship to the stratigraphy, structure, dolomitization, and karstification of the Middle Devonian barrier complex: Economic Geology, v. 79, p. 991–1055.

Schneider, C.L., and Grobe, M., 2013, Regional cross-sections of Devonian stratigraphy in northeastern Alberta (NTS 74D, E): Alberta Geological Survey Open-File Report 2013-05, 25 p.

Tufa and Water Radiogenic Geochemistry and Tufa Ages for Two Karst Aquifers in the Buffalo National River Region, Northern Arkansas

By Mark R. Hudson[1], James B. Paces[1], and Kenzie J. Turner[1]

[1]U.S. Geological Survey, Geosciences and Environmental Change Science Center, Box 25046, MS980, Denver, CO 80225

Abstract

Radiogenic isotopes of uranium and strontium were measured for a set of water and tufa samples that were sourced from either Mississippian or Ordovician karstic carbonate aquifers exposed in and adjacent to the Buffalo River valley in northern Arkansas. Tufa samples and water from which they formed, where available, show similar geochemical signatures within the individual aquifers, but samples sourced from the Ordovician Everton Formation have $^{234}U/^{238}U$ activity ratios with a wider range and extend to higher values compared to samples sourced from the Mississippian Boone Formation that conversely, have a wider range of $^{87}Sr/^{86}Sr$ ratios that extend to higher values. Samples from 11 tufa deposits from 6 locations have ages that vary from 500 years to 169,000 years and record paleodischarge from two discrete Boone and Everton Formation spring horizons that lie at varying heights above river base level; discharge for individual deposits remained active for as long as 150,000 years. At Big Bluff, a 157,000-year average age for the oldest subsamples of three tufa deposits lying at a height of 116 meters above the Buffalo River provides an upper limit for the rate of valley incision of 0.74 millimeter per year.

Introduction

Buffalo National River, administered by the National Park Service, occupies a corridor along the 238-kilometer-long free flowing Buffalo River that lies within the southern Ozark Plateaus physiographic province in northern Arkansas (fig. 1). An approximately 500-meter (m)-thick section of Pennsylvanian, Mississippian, and Ordovician sandstone, shale, limestone, and dolomite is exposed within the Buffalo River valley (fig. 2). Abundant karst features and associated hydrologic systems are developed within Mississippian and Ordovician carbonate sequences (Hudson and others, 2011). Cherty limestone of the Lower to Middle Mississippian Boone Formation is the predominant host of karst features in the area and corresponds to the regional Springfield Plateau karst aquifer (Adamski and others, 1995). Sinkholes are common at the top of the Boone Formation where it is overlain by Batesville Sandstone, and springs are concentrated at the base of the Boone Formation within its basal chert-free St. Joe Limestone Member (Hudson and others, 2011). A lower karst aquifer, representing the upper part of the regional Ozark aquifer (Adamski and others, 1995), is recognized where erosion of structural highs has exposed lower parts of the Ordovician Everton Formation. The Everton Formation (Suhm, 1974) consists of predominantly sandy dolomite, but in western parts of the watershed also includes the 30-m-thick Newton Sandstone Member and an underlying thin limestone interval that commonly hosts springs. A series of Pleistocene to Holocene tufa deposits consisting of high-porosity, fine-grained calcite were deposited from near-surface discharge of springs and seeps, often sourced from solution conduits developed in Mississippian and Ordovician strata.

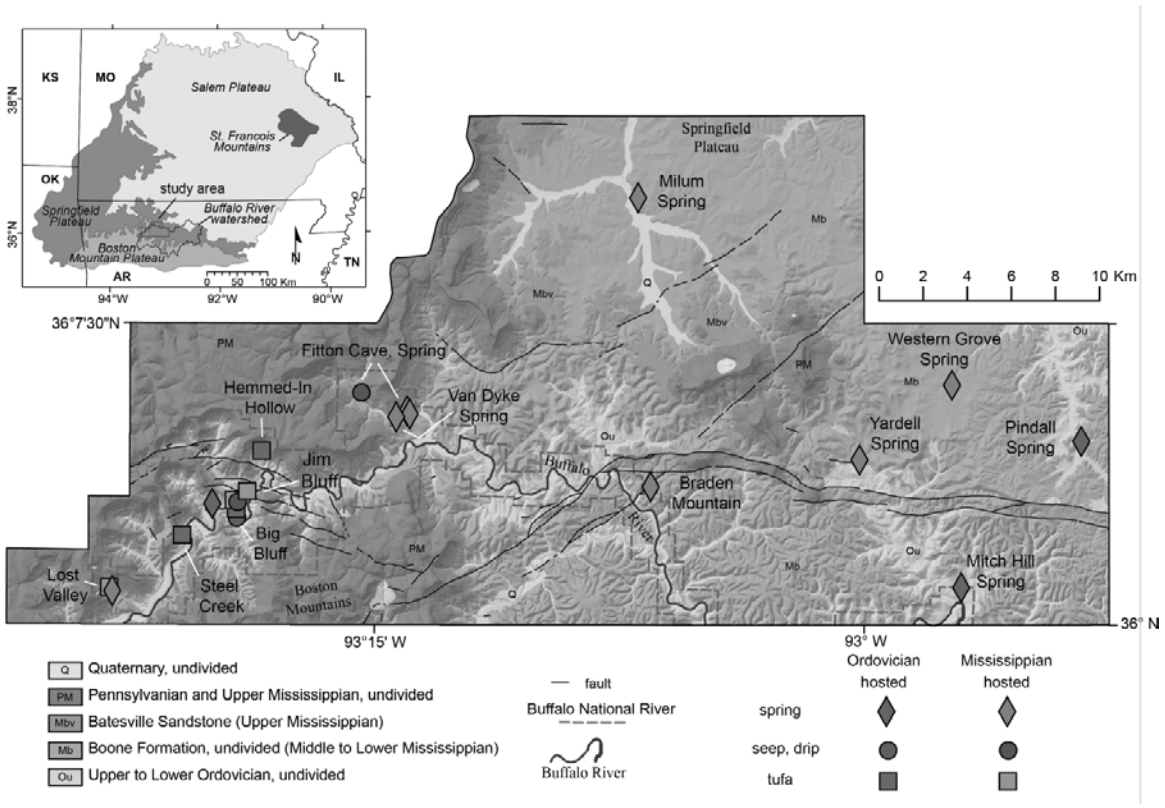

Figure 1. Simplified geologic map for the western part of the Buffalo River watershed and adjacent areas (modified from Hudson and Turner, 2014) with locations of water and tufa samples for this study. Inset shows location of study area within Ozark Plateaus physiographic province.

Radiogenic isotopes of strontium (Sr) and uranium (U) can permit geochemical discrimination of different source waters (Roback and others, 2001; Paces and others, 2002; Frost and Toner, 2004; Négrel and others, 2004; Durand and others, 2005; Ryu and others, 2009; Paces and Wurster, 2014) as well as provide age estimates for tufa deposits determined by U-series methods (Richards and Dorale, 2003; Bourdon, 2015). Isotopic compositions of Sr and U-thorium (Th) were determined for a set of samples of modern waters and tufas from both aquifers at Buffalo River to assess their geochemical signatures and tufa ages (tables 1 and 2).

Geologic Context of Samples

Water

Water samples were collected from springs, minor seeps, and a cave drip at 14 sites representative of discharge from both the Mississippian Boone Formation and the Ordovician Everton Formation (fig. 1, table 1). For the waters sourced from Mississippian units, those from Western Grove, Milum, Van Dyke, and Fitton Springs and from a small spring south of Braden Mountain, discharge from the main body of the Boone Formation, whereas those from Yardell Spring and Lost Valley as well as a small seep at the 150-m-high Big Bluff, discharge from the basal St. Joe Limestone Member of the Boone Formation. Two underground water samples were taken from (1) a stream in a shallow cave in the St. Joe Limestone Member of the Boone Formation in Lost Valley toward the west, and (2) a ceiling drip from within Fitton Cave formed in Boone Formation limestone.

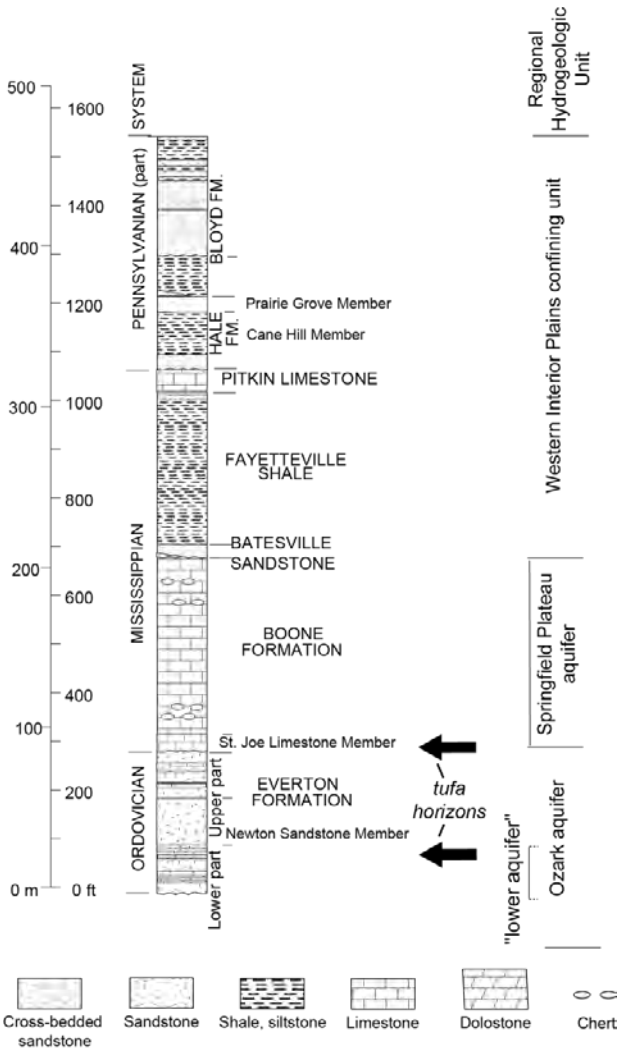

Figure 2. Representative stratigraphic column for the western part of the Buffalo River valley (modified from Hudson and others, 2011) with location of tufa horizons for this study. Regional hydrogeologic units follow Adamski and others (1995).

For water sourced from Ordovician units in the eastern part of the study area, Mitch Hill Spring (the largest in Buffalo National River Park) is hosted in the lower part of the Everton Formation, whereas Pindall Spring is hosted in the upper part of the Everton Formation. In the western part of the study area, a sample of ice associated with seepage from the lower part of the Everton Formation just below the Newton Sandstone Member was collected near the base of Big Bluff, whereas water from a spring discharging from the lower part of the Everton Formation just above its contact with the Powell Dolomite was collected about 1.5 km farther upstream.

Tufa Deposits

Tufa deposits were sampled in the western part of the Buffalo River watershed (fig. 1) where they are localized in either the basal St. Joe Limestone Member of the Boone Formation or the spring horizon in the lower part of the Everton Formation (table 2). Deposits typically form conical mounds associated with vadose seepage discharging in areas protected by cliff overhangs (fig. 3). Due to the location within the Buffalo National River Park, sparse sampling of one to three small pieces of tufa was conducted from unobtrusive lower or back parts of each deposit. Although innermost portions that potentially represent the oldest material present in the mounds were preferred, sampling was biased toward younger material to not destroy these features.

At Big Bluff, a series of five tufa deposits that lie at heights of 113 to 118 m above the Buffalo River were sampled along a 270-m-long traverse along a foot path named the Goat Trail. All tufa deposits are preserved in overhanging space of a cliff notch (fig. 3A) developed where the St. Joe Limestone Member of the Boone Formation overlies upper sandstone beds of the Everton Formation. Local draping of the tufa deposits across overhanging contacts with bedrock limestone demonstrates that these cliff-face notches predate the tufa deposition.

At Jim Bluff, a tufa deposit emerges from and drapes across the St. Joe Limestone Member (fig. 3C), like at Big Bluff. However, due to offset across a nearby normal fault that juxtaposes St. Joe Limestone Member against the lower part of the Everton Formation (Hudson and Murray, 2003), this tufa deposit lies only 3.6 m above the adjacent Buffalo River. At Lost Valley toward the west, a tufa deposit in St. Joe Limestone Member lies 1.3 m above Clark Creek, a tributary to the Buffalo River. This deposit formed directly below a prominent solution-enlarged joint (fig. 3E) that extends at least 5 m up into the overlying St. Joe Limestone Member.

Table 1. Initial $^{234}U/^{238}U$ activity ratios and $^{87}Sr/^{86}Sr$ ratios for water and bedrock samples from Buffalo National River area.

[Latitude, Longitude in decimal degrees, WGS84 coordinates; Fm, Formation; Everton, Everton Formation; St. Joe, St. Joe Limestone Member of Boone Formation; $^{234}U/^{238}U$ AR, $^{234}U/^{238}U$ activity ratio, corrected for mass fractionation, spike contributions, blank subtraction, and normalized to a standard value for NISTSRM4321b of $^{234}U/^{238}U$ atomic ratio=0.0000529; ±2σ, 2 sigma error; $^{87}Sr/^{86}Sr$ atomic ratios are corrected for mass fractionation and normalized to a standard value for NIST987 of $^{87}Sr/^{86}Sr$ =0.710248; ND, not determined; —, not calculated]

Sample name	Longitude	Latitude	Description	Sample type	Aquifer/Catchment	$^{234}U/^{238}U$ AR	±2σ	$^{87}Sr/^{86}Sr$	±2σ
BNR-140130-1	-93.2333	36.0880	Fitton Spring	Spring	Boone Fm, just above St. Joe	1.633	0.013	0.711970	0.000009
BNR-140130-2	-93.2326	36.0877	Cecil Creek	Surface water	Stream over Boone Fm	1.389	0.015	0.712008	0.000011
BNR-140131-1	-93.3202	36.0492	Lower Big Bluff	Vadose seep	Everton Fm, lower part	5.002	0.014	0.710395	0.000010
BNR-140201-1	-93.3857	36.0157	Lost Valley	Subsurface stream	St. Joe	1.189	0.009	0.712580	0.000010
BNR-140203-1	-92.9509	36.0149	Mitch Hill Spring	Spring	Everton, lower part	1.993	0.005	0.710347	0.000008
BNR-140203-2	-93.0028	36.0687	Yardelle Spring	Spring	St. Joe	1.520	0.004	0.711311	0.000008
BNR-140320	-93.2566	36.0962	Fitton drip	Vadose seep	Boone Fm	1.327	0.004	0.710798	0.000009
BNR-140321-1	-92.8897	36.0759	Pindall Spring	Spring	Everton, upper part	2.190	0.008	0.710532	0.000009
BNR-140321-2	-92.9559	36.0998	Western Grove Spring	Spring	Boone Fm	1.281	0.004	0.710083	0.000009
BNR-140321-3	-93.1091	36.0575	Braden Mtn. Spring 2	Spring	Boone Fm	1.225	0.005	0.710685	0.000008
BNR-140321-4	-93.1161	36.1774	Milum Spring	Spring	Boone Fm	1.402	0.006	0.710165	0.000009
BNR-140321-5	-93.2394	36.0862	Van Dyke Spring	Spring	Boone Fm	1.330	0.006	0.711961	0.000009
BNR-150630-1	-93.3326	36.0502	Near Cliff Hollow	Spring	Lower Everton/ above Powell Dolomite	2.092	0.006	0.710097	0.000009
BNR-150630-2	-93.3201	36.0502	Big Bluff Goat Trail	Vadose seep	St. Joe	1.185	0.003	0.710044	0.000011
BNR-140131-5BWR	-93.3211	36.0505	Big Bluff Goat Trail	Bedrock	St. Joe	ND	—	0.708822	0.000010
BNR-140131-5WR	-93.3211	36.0508	Big Bluff Goat Trail	Bedrock	St. Joe	ND	—	0.708846	0.000009
BNR-140201-3WR	-93.2707	36.0418	Bear Creek	Bedrock	St. Joe	ND	—	0.708980	0.000009
BNR-140203-3WR	-93.1388	36.0618	Bluff at Pruit	Bedrock	Everton Fm, lower part	ND	—	0.709023	0.000009

Table 2. Calculated $^{230}Th/U$ ages, initial $^{234}U/^{238}U$ activity ratios, and $^{87}Sr/^{86}Sr$ ratios for samples of tufa from Buffalo National River.

[Latitude, Longitude in decimal degrees, WGS84 coordinates; Height (m), meters above local valley bottom; Everton, Everton Formation; St. Joe, St. Joe Limestone Member of Boone Formation; $^{230}Th/U$ age calculated from detritally corrected $^{230}Th/^{238}U$ and $^{234}U/^{238}U$ activity ratios (Paces, 2015); ka, thousand years; ±2σ, 2 sigma error; Initial $^{234}U/^{238}U$ AR, $^{234}U/^{238}U$ activity ratio calculated at the time the sample formed (its $^{230}Th/U$ age); $^{87}Sr/^{86}Sr$ ratio reported as in Table 1. XS ^{230}Th indicates an excess of ^{230}Th that is not supported by U present in the sample and implies U loss. XDC indicates that an excessive detrital correction was required and that a reliable $^{230}Th/U$ age could not be calculated. *, excessive error due to large detrital corrections; ND, not determined; —, not calculated]

Sample name	Longitude	Latitude	Height (m)	Location	Source	$^{230}Th/U$ age (ka)	±2σ	Initial $^{234}U/^{238}U$ AR	$^{87}Sr/^{86}Sr$	±2σ
BNR-140131-1A1	-93.3204	36.0492	30	Big Bluff	Everton	1.41	0.09	4.574	0.710277	0.000009
BNR-140131-1A2	-93.3204	36.0492	30	Big Bluff	Everton	4.92	0.18	4.749	0.710262	0.000009
BNR-140131-1B1	-93.3204	36.0492	30	Big Bluff	Everton	4.99	0.08	4.945	0.710142	0.000009
BNR-140131-1B2	-93.3204	36.0492	30	Big Bluff	Everton	4.59	0.10	4.949	0.710143	0.000008
BNR-140131-2A1	-93.3197	36.0494	110.6	Big Bluff	St. Joe	34	11	1.246	0.710274	0.000009
BNR-140131-2A2	-93.3197	36.0494	110.6	Big Bluff	St. Joe	43.2	2.9	1.240	0.710013	0.000009
BNR-140131-2A3	-93.3197	36.0494	110.6	Big Bluff	St. Joe	25.7	2.7	1.231	0.709982	0.000009
BNR-140131-2B1	-93.3197	36.0494	110.6	Big Bluff	St. Joe	76.7	1.5	1.270	0.709774	0.000008
BNR-140131-2B2	-93.3197	36.0494	110.6	Big Bluff	St. Joe	XS ^{230Th}	—	—	0.709745	0.000009
BNR-140131-3A1	-93.3201	36.0502	113.3	Big Bluff	St. Joe	44.1	3.2	1.220	0.709394	0.000008
BNR-140131-3A2	-93.3201	36.0502	113.3	Big Bluff	St. Joe	114.3	2.8	1.274	0.709385	0.000009
BNR-140131-3B1	-93.3201	36.0502	113.3	Big Bluff	St. Joe	151	27	1.333	0.709682	0.000008
BNR-140131-4A	-93.3204	36.0503	117.2	Big Bluff	St. Joe	87	18	1.212	0.709813	0.000009
BNR-140131-4B	-93.3204	36.0503	117.2	Big Bluff	St. Joe	152	27	1.259	0.709907	0.000008
BNR-140131-5A1	-93.3211	36.0505	112.6	Big Bluff	St. Joe	XS ^{230Th}	—	—	0.711116	0.000009
BNR-140131-5A2	-93.3211	36.0505	112.6	Big Bluff	St. Joe	XS ^{230Th}	—	—	0.711056	0.000008
BNR-140131-6A1	-93.3215	36.0513	118.5	Big Bluff	St. Joe	19.2	0.9	1.140	0.709417	0.000009
BNR-140131-6A2	-93.3215	36.0513	118.5	Big Bluff	St. Joe	169	13	1.208	0.709570	0.000010
BNR-140131-6B1	-93.3215	36.0513	118.5	Big Bluff	St. Joe	XS ^{230Th}	—	—	0.709982	0.000009
BNR-140131-6B2	-93.3215	36.0513	118.5	Big Bluff	St. Joe	XS ^{230Th}	—	—	ND	—
BNR-140131-6C2	-93.3215	36.0513	118.5	Big Bluff	St. Joe	128	11	1.205	ND	—
BNR-140201-1A1	-93.3856	36.0156	1.3	Lost Valley	St. Joe	25	76*	1.173*	0.712276	0.000009
BNR-140201-1E1	-93.3856	36.0156	1.3	Lost Valley	St. Joe	20	25*	1.358*	0.711047	0.000010
BNR-140201-1F1	-93.3856	36.0156	1.3	Lost Valley	St. Joe	XS ^{230Th}	—	—	0.711137	0.000009
BNR150630-3A1	-93.3151	36.0546	3.6	Jim Bluff	St. Joe	2.9	3.6*	3.04*	0.709990	0.000009
BNR150630-3A2	-93.3151	36.0546	3.6	Jim Bluff	St. Joe	8	14*	3.23*	0.710273	0.000009
BNR150630-3B1	-93.3151	36.0546	3.6	Jim Bluff	St. Joe	XDC	—	—	0.710952	0.000009
BNR150630-3B2	-93.3151	36.0546	3.6	Jim Bluff	St. Joe	2	12*	1.156*	0.710309	0.000009
BNR150630-4A1	-93.3073	36.0721	30.7	Hemmed-In Hollow	Everton	0.46	0.07	1.712	0.710728	0.000009
BNR150630-4B1	-93.3073	36.0721	30.7	Hemmed-In Hollow	Everton	4.1	0.2	2.538	0.710379	0.000010
BNR150630-4C1	-93.3073	36.0721	30.7	Hemmed-In Hollow	Everton	2.3	0.5	2.619	0.710377	0.000009
BNR150702-1A1	-93.3482	36.0376	10	Steel Creek	Everton	5.7	9.6*	2.972*	0.710181	0.000009
BNR150702-1B1	-93.3482	36.0376	10	Steel Creek	Everton	5.3	1.9	1.189	0.710028	0.000010

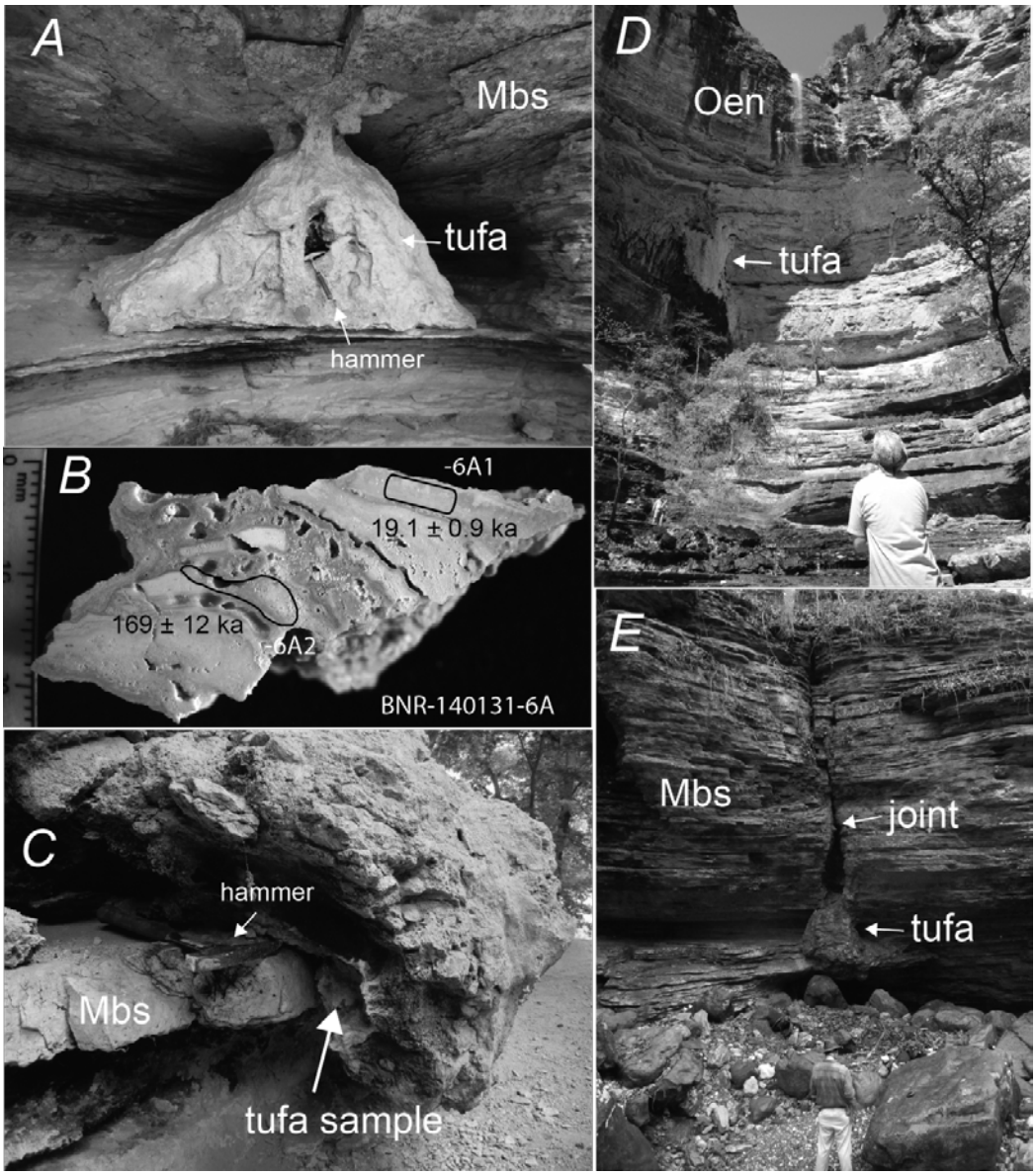

Figure 3. Photographs of tufa sample sites. Mbs–St. Joe Limestone Member, Boone Formation; Oen–Newton Sandstone Member, Everton Formation. Hammer head is 17 cm long. *A*, Tufa deposit preserved along Goat Trail of Big Bluff. *B*, Polished sample from tufa deposit of A with age determinations from inner and outer parts. *C*, Tufa deposit from Jim Bluff draping across Mbs bedrock with sample location indicated. *D*, View of 64-m-tall waterfall at Hemmed-In Hollow with tufa deposits preserved beneath overhang of Oen cliff. *E*, Tufa deposit from Lost Valley developed below joint through overlying St. Joe Limestone Member. Photos for A, C, and D by M.R. Hudson and for B and E by J.B. Paces.

Tufa deposits hosted by the Everton Formation were sampled directly adjacent to the Buffalo River at Steel Creek and at Big Bluff and also at the head of the Hemmed-In Hollow tributary. In each case the tufa formed from discharge along thin limestone beds that underlie the thick Newton Sandstone Member of the Everton Formation (fig. 3D), a lithologic position similar to cave horizons developed in older units of the Ozark aquifer in southeastern Missouri (Orndorff and others, 2006). At Steel Creek this discharge horizon is about 10 m above the Buffalo River from which the tufa deposit extends downward to where it was directly

sampled about 2 m above the river. At Big Bluff, the tufa forms from a discharge horizon that lies about 30 m above the river beneath an overhanging cliff of the Newton Sandstone Member. Due to inaccessibility, loose tufa blocks shed from the cliff were collected as samples. At the head of the Hemmed-In Hollow tributary, tufas formed at the base of the overhanging Newton Sandstone Member cliff (fig. 3D) lie about 30 m above the local base of a 64-m-tall waterfall; loose tufa blocks clearly derived from cliff-side mounds again provided samples.

Analytical Procedures

Tufa samples were cut and polished to examine their internal stratigraphy, and several subsamples from specific layers were collected with a microdrill for chemical analysis.

Ages (in 1,000s of years, or ka) for a series of subsamples collected from tufa deposits were calculated from detritus-corrected $^{234}U/^{238}U$ and $^{230}Th/^{238}U$ activity ratios (AR) using methods described elsewhere (Paces, 2015). Of the 34 subsamples analyzed for U-Th isotopes, 7 had excess ^{230}Th unsupported by ^{234}U present in the sample. This feature indicates that samples were subjected to relatively recent U mobility such that $^{230}Th/U$ ages and initial $^{234}U/^{238}U$ AR could not be calculated. However, fractionation of strontium isotopes likely remains unaffected by secondary processes, and measured 87Sr/86Sr values remain valid. Full data results are available at ScienceBase (doi.org/10.5066/P9L1J7BG).

Results and Implications

$^{234}U/^{238}U$ Activity Ratios and $^{87}Sr/^{86}Sr$ Variations

Modern spring waters and older tufas sourced from the Mississippian Boone Formation have $^{234}U/^{238}U$ AR that are distinct compared to similar materials sourced from the Ordovician Everton Formation (fig. 4). Water sourced from the Everton Formation and tufas derived therefrom have a wide range of measured (for water) or initial (for tufa) $^{234}U/^{238}U$ AR reaching values as high as 5 (for both water and tufa samples from Big Bluff). In contrast, tufa deposits sourced from the Mississippian St. Joe Limestone Member have a restricted range of initial $^{234}U/^{238}U$ AR from 1.1 to 1.3 with the exception of subsamples from the Jim Bluff tufa mound with values as high as 3.2. Because the St. Joe Limestone Member at Jim Bluff is down-faulted against the lower part of the Everton Formation (Hudson and Murray, 2003), it is likely that some groundwater from the adjacent lower part of the Everton Formation crossed the fault into the Boone Formation and provided a water source with elevated $^{234}U/^{238}U$ AR. A subsample from the same Jim Bluff mound does not have an elevated $^{234}U/^{238}U$ ratio, however, demonstrating that any such inter-aquifer groundwater mixing was heterogeneous.

To obtain higher $^{234}U/^{238}U$ AR, ^{234}U must be preferentially enriched relative to ^{238}U by various processes related to recoil from alpha decay (Porcelli, 2008; Porcelli, 2015). In terms of hydrologic properties, ^{234}U enrichment is typically related to porosity, travel time, water/rock ratios, and chemical aggressiveness. Smaller water/rock ratios along a given flow path will favor higher $^{234}U/^{238}U$ AR, especially if bulk dissolution of aquifer rock is limited. Likewise, groundwaters traversing longer flow paths are likely to have higher $^{234}U/^{238}U$ values than those of more local extent. Therefore, elevated $^{234}U/^{238}U$ AR in large volume springs are consistent with integration of flow and long residence time in the regional Ozark aquifer relative to shorter, more localized flow in the "flashy" Mississippian Springfield Plateau karst aquifer. Preferential incorporation of ^{234}U relative to ^{238}U in vadose seeps discharging from the stratigraphically lower Everton Formation may also be enhanced in that those pathways have been exposed to flow for shorter time intervals due to more recent exposure by base-level lowering as compared to seeps higher up in the Boone Formation.

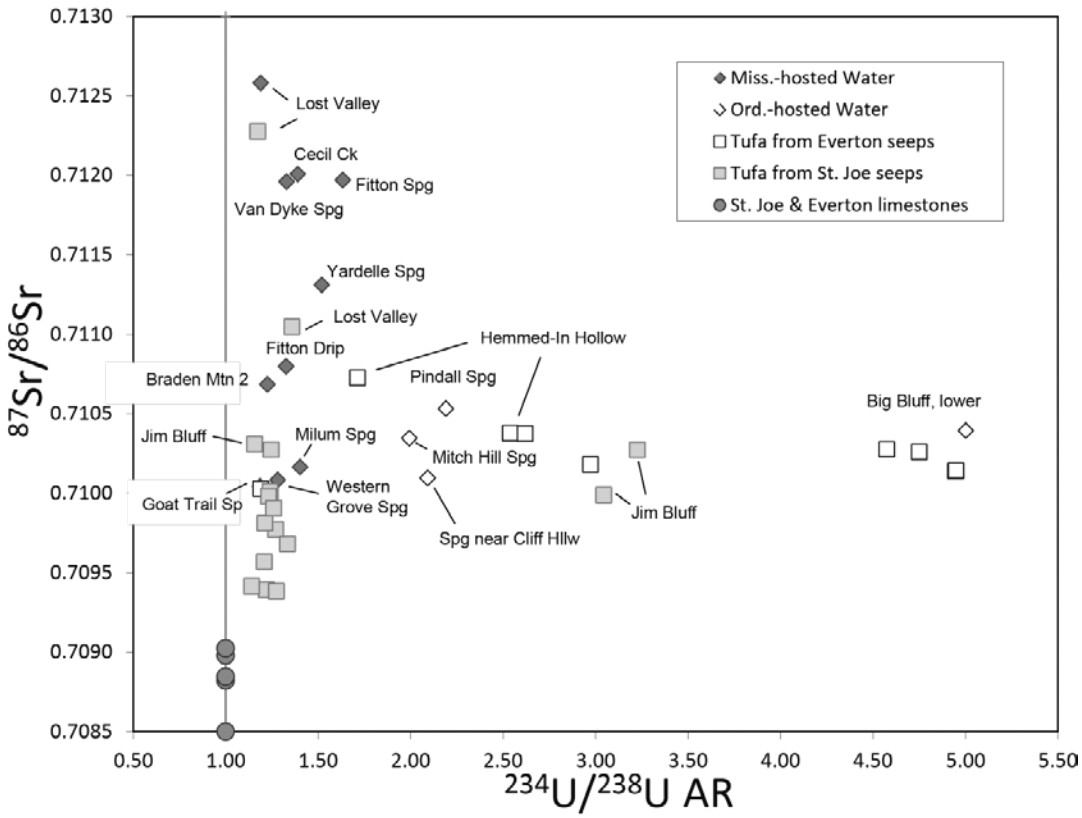

Figure 4. Plot of measured (for water) or initial (for tufa) $^{234}U/^{238}U$ activity ratios (AR) versus $^{87}Sr/^{86}Sr$ ratios for samples sourced from either the Mississippian Boone Formation or Ordovician Everton Formation. Also plotted are $^{87}Sr/^{86}Sr$ values for bedrock limestone samples of the St. Joe Limestone Member of the Boone Formation and of the Everton Formation (shown with an assumed $^{234}U/^{238}U$ AR of 1). Spg, Spring.

Water and tufa samples also have a considerable range in $^{87}Sr/^{86}Sr$, but with greater variability in the Boone Formation. The $^{87}Sr/^{86}Sr$ values from samples from the Everton Formation have a restricted range (0.7100–0.7107) compared to the 0.7093–07127 range for Boone Formation-hosted samples. These ratios are all elevated with respect to $^{87}Sr/^{86}Sr$ values of 0.709 or less determined on samples of Mississippian and Ordovician limestone from the area (fig. 4), or values expected for Paleozoic sea water during those periods (0.7076–0.7087; McArthur and others, 2012). The cause of the $^{87}Sr/^{86}Sr$ variation of the water and tufa samples in the Buffalo River area is speculative, but we note that Mississippian-hosted samples with high ratios are mostly from western locations where surface waters probably flowed across upper Mississippian and Pennsylvanian shales before infiltrating the Boone Formation. Those shales are likely to have much higher rubidium/strontium values than in the carbonate rocks, leading to elevated ^{87}Sr abundances in runoff and infiltration through those soils and bedrock units.

The different ranges for U and Sr isotopic compositions determined in this study add to other contrasts between groundwater sourced from Mississippian and Ordovician aquifers, including differences in major-ion chemistry (Galloway, 2004). The physical characteristics of springs from these aquifers also differ as unconfined springs with flashy discharge are typical for the Boone Formation, whereas partly confined springs with more steady flow are typical for the Everton Formation (Hudson and others, 2011).

U-series Ages from Tufa

U-series ages were determined from subsamples from 11 different tufa deposits at 6 different locations (table 2). Tufa samples yielded ages ranging from as young as 0.46 ± 0.07 ka to as old as 169 ± 13 ka. This age variation is partly linked to height above base level (fig. 5). Tufa deposits hosted by both the St. Joe Limestone Member and the Everton Formation that lie 30 m or less above the current Buffalo River level at Steel Creek, at the base of Big Bluff, and at Jim Bluff, all yielded tufa ages less than 8 ka. In contrast, the series of tufa deposits from the St. Joe Limestone Member from 113 to 118 m above the Buffalo River along the Goat Trail at Big Bluff yielded ages that ranged between 19.2 and 169 ka. Age ranges within four individual tufa deposits (a fifth did not yield reliable results) along the Goat Trail were 25.7–76.7 ka, 44.1–151 ka, 87–152 ka, and 19.2–169 ka. These ranges demonstrate that individual tufa deposits remained active for 51 to as long as 150,000 years (figs. 3B and 5), and reflect deposition from focused discharge along a perched horizon in the Springfield Plateau aquifer. We cannot be confident that the oldest part of each tufa deposit was dated given our sparse sampling protocol, yet it is notable that three of the four dated deposits along the Goat Trail yielded similar maximum ages of 151 ± 27 ka, 152 ± 27 ka, and 169 ± 13 ka. The 151–169 ka time interval falls within the prominent full glacial epoch of marine isotope stage 6 (Lisiecki and Raymo, 2005) during which precipitation and associated tufa deposition may have been enhanced. If paleoclimate did influence tufa deposition, older, dryer periods of exposure of the cliff face at Big Bluff may not have resulted in tufa deposition.

For the tufa samples from tributary locations, those taken from loose blocks derived from discharge from the lower part of the Everton Formation at Hemmed-In Hollow (fig. 3D) have a 0.5–4.1 ka range of ages that is similar to that of the other lower Everton Formation-sourced tufa deposits more closely associated with the Buffalo River. In comparison, the tufa deposit hosted by the St. Joe Limestone Member at Lost Valley yielded imprecise ages of 24.9 ± 76 ka and 20.3 ± 25 ka that are relatively old given that the deposit presently lies about 1.3 m above the bed of Clark Creek (fig. 3E). This tufa deposit is located at the base of a prominent joint enlarged by dissolution that extends at least 5 m into the overlying St. Joe Limestone Member, indicating that it could have initially formed several meters below the land-surface elevation due to sinking karst waters. It is unclear how deep deposits with high-porosity, fine-grained tufa texture could form, but we note that cave deposits in the area (Paces and others, 2017) typically contain only coarse crystalline calcite speleothems.

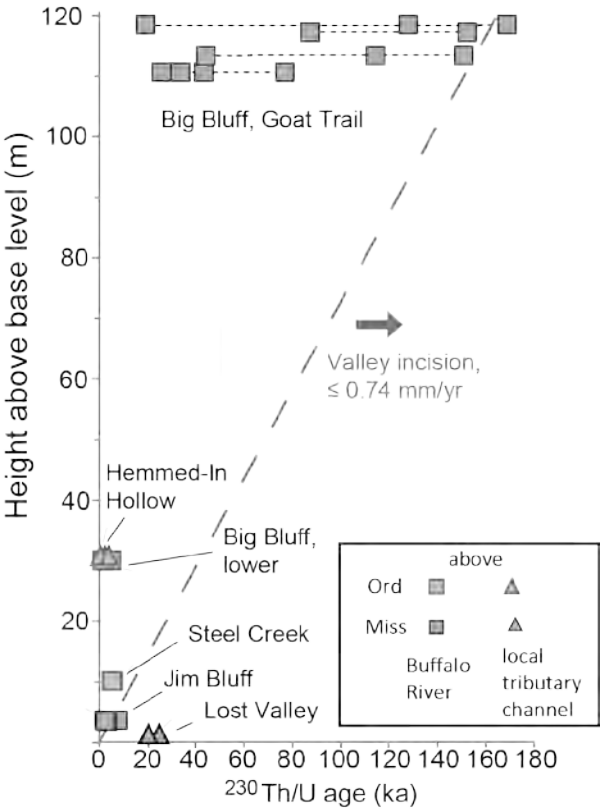

Figure 5. Plot of tufa age versus height of deposit (in meters) above base level. For tufa deposits from Goat Trail, dotted lines connect range of subsample ages within individual deposit. Ord–tufa hosted within Ordovician unit. Miss–tufa hosted within Mississippian unit.

The oldest tufa deposits at Big Bluff lying high above the Buffalo River provide an upper limit on valley incision rate at this location. The contact of the St. Joe Limestone Member above less permeable sandstone of the upper Everton Formation is well documented as a major modern spring horizon at the base of the Springfield Plateau aquifer throughout the western part of the Buffalo River valley (Mott and others, 2000; Turner and others, 2007; Hudson and others, 2011). The oldest dated tufa deposits at Big Bluff are preserved high above the modern valley bottom, which is consistent with deposition from spring discharge that began when valley incision first exposed the base of the St. Joe Limestone Member. Discharge at this horizon continued for as long as 150 ka afterward at one tufa deposit as valley incision continued to exhume the underlying Everton Formation and uppermost Powell Dolomite. Using a 157 ± 10 ka for the average age of the three oldest tufa deposits and a mean height of 116 m above the river yields an incision rate at Big Bluff of 0.74 millimeter per year (mm/yr) (fig. 5). However, because this 157 ka average age might be biased toward a period of enhanced precipitation during marine isotope stage 6, this age is probably a minimum for when the base of the St. Joe Limestone Member was exposed at Big Bluff. Thus, the 0.74 mm/yr incision rate should be considered an upper limit. For comparison, at Boxley Valley (upstream of fig. 1) where the Buffalo River flows over the Boone Formation (Hudson and Turner, 2007), Covington and others (2015) calculated a dissolution rate for pure limestone of 1.05 mm/yr based on the CO_2 undersaturation of river samples collected over a wide discharge range. Other research is ongoing to date cave and river terrace deposits elsewhere in the Buffalo River valley to add additional constraints on incision rate, so the 0.74 mm/yr upper limit at Big Bluff can be compared to any future estimates.

Conclusions

Radiogenic isotopes were measured for a set of water and tufa surface samples from karstic aquifers within Mississippian and Ordovician carbonate units located in the Buffalo River region in northern Arkansas. Key findings of this study were as follows:

- Tufa and water samples show similar geochemical signatures within the individual aquifers, but those from aquifers in Mississippian and Ordovician bedrock units have different ranges of $^{234}U/^{238}U$ activity ratios and $^{87}Sr/^{86}Sr$ values that can be used as natural tracers of groundwater sources.
- Tufa sample ages vary from 0.5 ± 0.07 to 169 ± 13 thousand years and record paleodischarge from two stratigraphic horizons, the basal St. Joe Limestone Member of the Boone Formation and the lower part of the Everton Formation along thin limestone beds beneath the Newton Sandstone Member. These horizons vary in height from 1 to as much as 118 meters above base level.
- Deposits located in the lower cliff heights above base level have younger ages than deposits present at greater heights above base level.
- The oldest, highest tufa deposits at Big Bluff were active for over 150,000 years.
- An upper limit for the rate of Buffalo River valley incision at Big Bluff is 0.74 millimeter per year.

References Cited

Adamski, J.C., Petersen, J.C., Freiwald, D.A., and Davis, J.V., 1995, Environmental and hydrologic setting of the Ozark Plateaus study unit, Arkansas, Kansas, Missouri, and Oklahoma: U.S. Geological Survey Water-Resources Investigations Report 94-4022, 69 p.

Bourdon, B., 2015, U-series dating, *in* Rink, W.J., and Thompson, J.W., eds., Encyclopedia of Scientific Dating Methods: Dordrecht, The Netherlands, Springer, p. 918–932, ISBN 978-94-007-6303-6.

Covington M.D., Gulley J.D., and Gavrovšek F., 2015, Natural variations in calcite dissolution rates in streams—Controls, implications, and open questions: Geophysical Research Letters, v. 42, no. 8, p. 2836–2843, DOI:10.1002/2015GL063044.

Durand, S., Chabaux, F., Rihs, S., Duringer, P., and Elsass, P., 2005, U isotope ratios as tracers of groundwater inputs into surface waters—Example of the Upper Rhine hydrosystem: Chemical Geology, v. 220, p. 1–19.

Frost, C.D., and Toner, R.N., 2004, Strontium isotopic identification of water–rock interaction and ground water mixing: Ground Water, v. 42, p. 418–432, http:// dx.doi.org/10.1111/j.1745-6584.2004.tb02689.x.

Galloway, J.M., 2004, Hydrologic characteristics of four public drinking-water supply springs in northern Arkansas: U.S. Geological Survey Water-Resources Investigations Report 03-4307, 68 p.

Hudson, M.R., and Murray, K.E., 2003, Geologic map of the Ponca quadrangle, Newton, Boone, and Carroll Counties, Arkansas: U.S. Geological Survey Miscellaneous Field Studies Map MF-2412, 1:24,000 scale, http://pubs.usgs.gov/mf/2003/mf-2412.

Hudson, M.R., and Turner, K.J., 2007, Geologic map of the Boxley quadrangle, Newton and Madison Counties, Arkansas: U.S. Geological Survey Scientific Investigations Map 2991, scale 1:24,000, http://pubs.usgs.gov/sim/2991/.

Hudson, M.R., and Turner, K.J., 2014, Geologic map of the west-central Buffalo National River region, Arkansas: U.S. Geological Survey Scientific Investigations Map 3314, 1:24,000 scale, http://pubs.usgs.gov/sim/3314/.

Hudson, M.R., Turner, K.J. and Bitting, C., 2011, Geology and karst landscapes of the Buffalo National River area, northern Arkansas: *in* Kuniansky, E.L., ed., U.S. Geological Survey Karst Interest Group Proceedings, Fayetteville, Arkansas, April 26–29, 2011: U.S. Geological Survey Scientific Investigations Report 2011–5031, p. 191–212, http://pubs.usgs.gov/sir/2011/5031/.

Lisiecki, L.E., and Raymo, M.E., 2005, A Pliocene-Pleistocene stack of 57 globally distributed benthic $\delta^{18}O$ records: Paleoceanography, v. 20, PA1003, doi:10.1029/2004PA001071.

McArthur, J.M., Howarth, R.J., and Shields, G.A., 2012, Strontium isotope chemistry, *in* Gradstein, F.M., Ogg, J.G., Schmidt, M.D., and Ogg, G., eds., The Geologic Time Scale 2012, v. 1, Amsterdam, Elsevier, p. 127–144.

Mott, D.N., Hudson, M.R., and Aley, T., 2000, Hydrologic investigations reveal interbasin recharge contributes significantly to detrimental nutrient loads at Buffalo National River, Arkansas: Proceedings of Arkansas Water Resources Center Annual Conference, MSC-284, Fayetteville, Ark., p. 13–20.

Négrel, P., Petelet-Giraud, E., and Widory, D., 2004, Strontium isotope geochemistry of alluvial groundwater—A tracer for groundwater resources characterization: Hydrology and Earth System Sciences, v. 8, p. 959–972.

Orndorff, R.C., Weary, D.J., and Harrison, R.W., 2006, The role of sandstone in development of an Ozark karst system, south-central Missouri, *in* Harmon, R.S., and Wicks, C., eds., Perspectives on karst geomorphology, hydrology, and geochemistry—A tribute volume to Derick C. Ford and William B. White: Geological Society of America Special Paper 404, p. 31–38, doi:10.1130/206.2402(04).

Paces, J.B., 2015, Appendix 1. $^{230}Th/U$ ages supporting geologic map of the Masters 7.5' quadrangle, Weld and Morgan Counties, Colorado, *in*, Berry, M.E., Slate, J.L., Paces, J.B., Hanson, P.R., and Brandt, T.R., 2015, Geologic map of the Masters 7.5' quadrangle, Weld and Morgan Counties, Colorado: U.S. Geological Survey Scientific Investigations Map 3344, 10 p., appendix, 1 sheet, 1:24,000 scale, accessed February 2017, at https://pubs.usgs.gov/sim/3344/sim3344_appendix_1.pdf.

Paces, J.B., Hudson, M.R., Hudson, A.M., Turner, K.J., Bitting, C., and Sugano, L., 2017, Isotope constraints on middle Pleistocene cave evolution, paleohydrologic flow and environmental conditions from Fitton Cave speleothems, Buffalo National River, Arkansas: *in* Kuniansky, E.L., and Spangler, L.E., eds., U.S. Geological Survey Karst Interest Group Proceedings, San Antonio, Texas, May 16–18, 2017: U.S. Geological Survey Scientific Investigations Report 2017–5023, p. 116–129.

Paces, J.B., Ludwig, K.R., Peterman, Z.E., and Neymark, L.A., 2002, $^{234}U/^{238}U$ evidence for local recharge and patterns of ground-water flow in the vicinity of Yucca Mountain, Nevada, USA: Applied Geochemistry, v. 17, p. 751–779.

Paces, J.B., and Wurster, F.C., 2014, Natural uranium and strontium isotope tracers of water sources and surface water-groundwater interactions in arid wetlands–Pahranagat Valley, Nevada, USA: Journal of Hydrology, v. 517, p. 213–225.

Porcelli, D., 2008, Investigating groundwater processes using U- and Th-series nuclides, *in* Krishnaswami, S., and Cochran, J.K., eds., U/Th series radionuclides in aquatic systems: Radioactivity in the Environment 13, p. 105–153.

Porcelli, D., 2015, Aquifer characteristics (U-series), *in* Rink, W.J., and Thompson, J.W., eds., Encyclopedia of Scientific Dating Methods, Dordrecht, The Netherlands, Springer, p. 54–58, ISBN 978-94-007-6303-6.

Richards, D.A., and Dorale, J.A., 2003, Uranium-series chronology and environmental applications of speleothems: Reviews in Mineralogy and Geochemistry, v. 52, p. 407–460.

Roback, R.C., Johnson, T.M., McLing, T.L., Murrell, M.T., Luo, S., and Ku, T.L., 2001, Groundwater flow patterns and chemical evolution in the Snake River Plain aquifer in the vicinity of the INEEL—Constraints from $^{234}U/^{238}U$ and $^{87}Sr/^{86}Sr$ isotope ratios: Geological Society of America Bulletin, v. 113, p. 1133–1141.

Ryu, J.-S., Lee, K.-S., Chang, H.-W., and Cheong, C.-S., 2009, Uranium isotopes as a tracer of sources of dissolved solutes in the Han River, South Korea: Chemical Geology, v. 258, p. 354–361.

Suhm, R.W., 1974, Stratigraphy of the Everton Formation (early Medial Ordovician), northern Arkansas: American Association of Petroleum Geologists Bulletin, v. 58, p. 685–707.

Turner, K.J., Hudson, M.R., Murray, K.E., and Mott, D.N., 2007, Three-dimensional geologic framework model for a karst aquifer system, Hasty and Western Grove quadrangles, northern Arkansas: U.S. Geological Survey Scientific Investigations Report 2007-5095, 12 p., http://pubs.usgs.gov/sir/2007/5095/.

Isotopic Constraints on Middle Pleistocene Cave Evolution, Paleohydrologic Flow, and Environmental Conditions From Fitton Cave Speleothems, Buffalo National River, Arkansas

By James B. Paces[1], Mark R. Hudson[1], Adam M. Hudson[1], Kenzie J. Turner[1], Charles J. Bitting[2], and Laura L. Sugano[3]

[1]U.S. Geological Survey, Geosciences and Environmental Change Science Center, Box 25046, Denver Federal Center, Denver, CO 80225-0046

[2]U.S. National Park Service, Buffalo National River, 402 N. Walnut Street, Harrison, AR 726013Kent State University, Department of Geology, 325 S. Lincoln St., Kent, OH 44242

[3]Kent State University, Department of Geology, 325 S. Lincoln St., Kent, OH 44242

Abstract

The evolution of Fitton Cave in the Buffalo National River Park Unit, northern Arkansas, is linked to karst processes and landscape development in the southern Ozark Plateau region. Clastic sediments in the cave were deposited from subterranean streamflow during the formation of cave passages. Karst incision and lowering of regional base levels resulted in cessation of active flow and sedimentation, after which flowstones associated with vadose seepage were able to form on the stabilized sediment. Uranium-series ages for capping flowstones commonly range from 400 to 700 thousand years (ka). These dates help to constrain incision rates that can be compared to estimates derived from other data. Variations in uranium and strontium isotopic compositions of speleothems from different areas within the cave are generally correlated and reflect differences in rock compositions and amounts of water/rock interaction along different flow paths. Speleothems also record changing paleoenvironmental conditions related to sources of meteoric water, temperatures, and plant communities contributing to soil CO_2. Three stalagmites contain material formed from about 165 to 185 ka and from about 240 to 350 ka. Age-calibrated shifts in isotopic composition can be related to climate changes near the transition from marine isotope stage (MIS) 8 (glacial) to stage 7 (interglacial) conditions.

Introduction

Fitton Cave, the largest known cave system in Arkansas, is developed in the Mississippian Boone Formation within the Buffalo National River Park Unit (Hudson and others, 2011). The cave is currently being studied to help understand its development and how this links to landscape evolution of the Buffalo River karst watershed within the Ozark Plateaus physiographic province. Accumulations of coarse clastic sediments in passages above the level of a modern cave stream reflect deposition when base levels were higher in the past, and can thus be used to help constrain longer-term incision rates if the ages of those deposits are known. Ongoing dating studies combining cosmogenic nuclides, optically stimulated luminescence, paleomagnetism, and U-series disequilibrium dating will help elucidate the history of cave formation and evolution, which can then be compared to other records of watershed incision (Keen-Zebert and others, 2016).

Clastic sediments in Fitton Cave are often capped by calcite flowstone or gypsum evaporative crusts; intercalated flowstone is uncommon. Flowstones provide minimum age constraints for deposition of underlying sediment, which in turn, provide minimum ages for initial formation of cave passages. Other forms of vadose speleothems are present in

Fitton Cave (stalactites, stalagmites, helictites); however, deposits suggesting extended periods of phreatic conditions are absent. Besides providing ^{230}Th/U ages to constrain cave formation, strontium (Sr) and initial uranium (U) isotopic compositions from speleothems represent records of vadose water chemistry that provide insight into flow paths, processes, and histories within the cave. Oxygen (O) and carbon (C) stable isotope compositions from speleothems can also provide records that can be used to evaluate changes in regional climate conditions associated with the past glacial/interglacial cycles.

This paper presents work on Fitton Cave speleothems collected in 2014 and 2015. We analyzed the speleothems for uranium-thorium (U-Th) isotopic compositions to establish ^{230}Th/U ages and initial ^{234}U/^{238}U activity ratios as well as Sr isotopes (^{87}Sr/^{86}Sr) to evaluate compositional variability in space and time. Besides flowstones, several broken stalagmites were analyzed to evaluate how chemical and environmental conditions may have varied over time at single drip sites. Data from those records will ultimately provide insight into regional conditions that will be important for climate-calibrated models of landscape evolution during the Pleistocene.

Hydrogeologic Setting

Buffalo National River is located on the southern flank of the Ozark dome (fig. 1), a late Paleozoic structural uplift developed in the foreland of the Ouachita orogenic belt (Hudson and others, 2011). The region is underlain by a series of relatively flat-lying Ordovician, Mississippian, and Pennsylvanian sedimentary rocks. The broadly uplifted strata form several regional-scale plateaus in southern Missouri and northern Arkansas that are variously dissected by fluvial systems. Fitton Cave is developed in the Boone Formation, a Lower to Middle Mississippian platform carbonate consisting of cherty limestone up to about 120 meters (m) thick. Near the cave, Boone Formation limestone is directly overlain by Upper Mississippian Batesville Sandstone (about 10 m thick) and Fayetteville Shale (about 90 m thick).

Upper Mississippian and Pennsylvanian clastic rocks in the region act as hydrologic confining units (Adamski and others, 1995). When removed by erosion, the underlying carbonate units become more exposed to dissolution by surface water, infiltration, and groundwater flow, resulting in karst features including cavernous porosity, sinkholes, sinking streams, and springs (Hudson and others, 2011). Dye-tracer tests indicate that groundwater can be transported through the Boone Formation at rates of several hundreds of meters per day (Mott and others, 2000). Springs in the area frequently discharge at or near the basal contact of the St. Joe Limestone Member of the Boone Formation (Hudson, 1998), lying unconformably above less permeable Ordovician sandstone. Silurian and Devonian rocks are not present in the section.

Fitton Cave consists of more than 30 kilometers of mapped passages (fig. 1). Multiple vertical levels span an elevation range of 120 m (Hudson and others, 2011) with four main levels characterized by gently sloping phreatic tube or base-level passages that are separated by more steeply dipping vadose passages (Keen-Zebert and others, 2016). Dye-tracer tests confirm a hydrologic connection between the water flowing in Fitton Cave and Fitton Spring, which discharges along Cecil Creek approximately 150 m east-southeast of the deepest mapped passages (fig. 1).

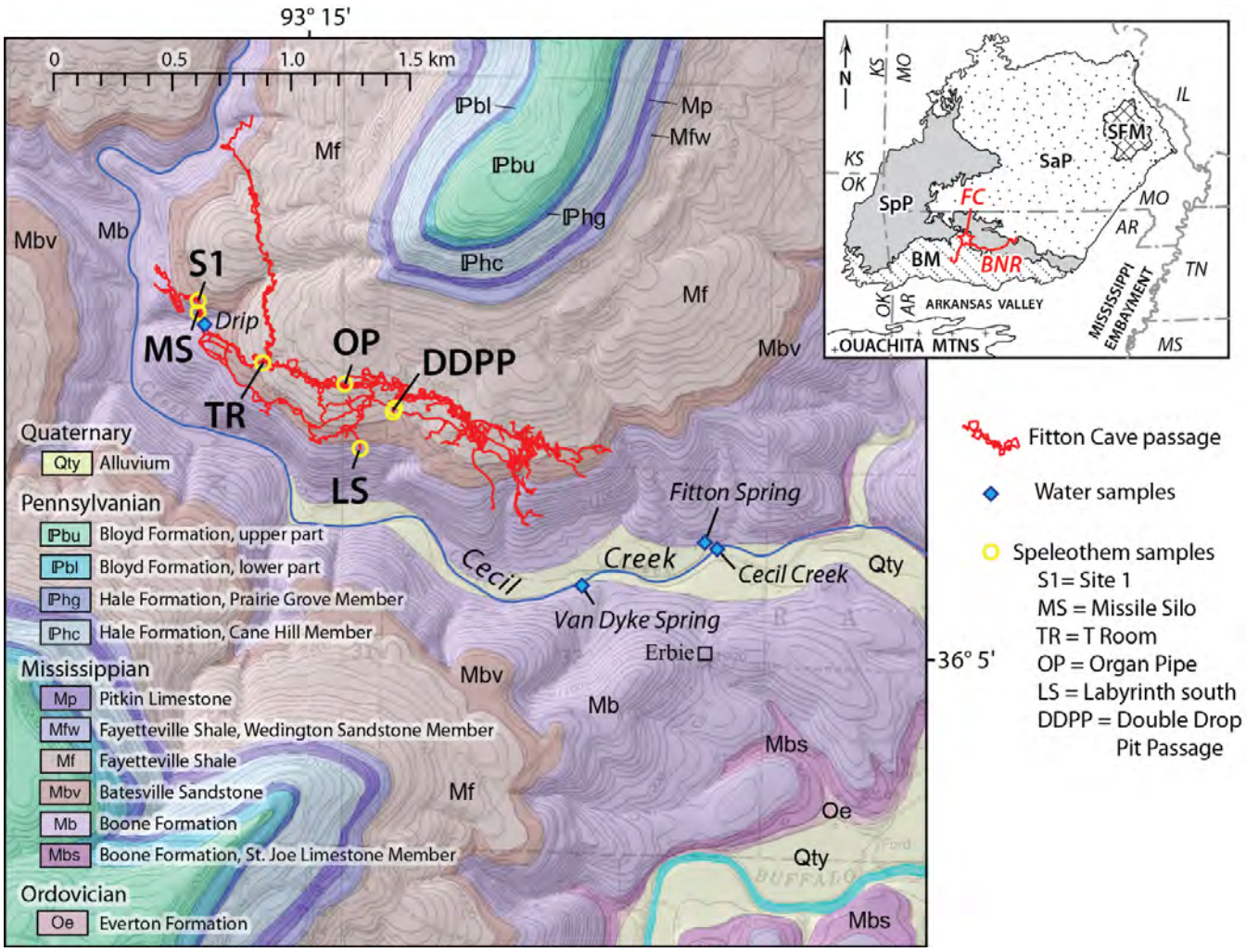

Figure 1. Geologic map showing projection of Fitton Cave passages to the surface along with speleothem and water sampling sites (base map from Hudson and Turner, 2014). Inset shows the Ozark Plateaus province in southern Missouri and northern Arkansas, consisting of the St. Francois Mountains (SFM), Salem Plateau (SaP), Springfield Plateau (SpP), and Boston Mountains (BM), and the location of Buffalo National River (BNR) and Fitton Cave (FC).

Samples

Nine samples of flowstone were collected from five different sites closely associated with clastic sediments. In addition, three stalagmites ranging from 20 to 40 centimeters (cm) in length were collected from two widely separated areas (fig. 1). Locations and elevations for underground sample sites were located on cave surveys (table 1). Elevations of the overlying land surface were determined to estimate overburden thickness, which varies from 34 to 107 m and includes the Boone Formation, Batesville Sandstone, and Fayetteville Shale.

Deposits of flowstone vary in thickness from several millimeters up to about 10 cm and consist of sparry calcite containing variable amounts of fine sediment. In one case (the T Room), gypsum constitutes the dominant phase, forming a 1- to 4-cm-thick crust capping sediments. In some areas, calcite deposits are corroded indicating partial dissolution at some time since their formation. No samples came from sites with active water flow or modern calcite precipitation.

Stalagmites were collected as broken fragments and could not be related to their original growth positions. Specimens are about 20 to 40 cm long and about 12 cm in diameter. Two samples (FC3A and FC11) retained growth tips (fig. 2), whereas the third (FC3B) was broken at both ends. All three show clear internal growth banding with several obvious discontinuities.

Table 1. Locations and sample types of speleothems and water from Fitton Cave and vicinity, Buffalo National River, northwest Arkansas.

Sample ID	Site name	Sample type	Latitude/Longitude (decimal degrees, WGS84 datum)		Elevation (meters)	Overburden thickness (m) and map unit
BNR-FC1	Site 1a	FS, intercal	36.09684	-93.25678	324.4	58.6 Mb, Mbv
BNR-FC2	Site 1b	FS, cap	36.09684	-93.25678	324.4	58.6 Mb, Mbv
BNR-FC3	Organ Pipe area	Stalag	36.09377	-93.24995	320.5	106.9 Mb, Mbv, Mf
BNR-FC4	T room	FS, crust (gyp)	36.09456	-93.25376	321.2	84.3 Mb, Mbv, Mf
BNR-FC5	Labyrinth south	FS, intercal	36.09139	-93.24936	339.7	33.7 Mb
BNR-FC6	Double Drop Passage Pit	FS, cap	36.09276	-93.24781	331.2	68.5 Mb, Mbv, Mf
BNR-FC7	Double Drop Passage Pit	TV	36.09276	-93.24781	331.2	68.5 Mb, Mbv, Mf
BNR-FC8	Double Drop Passage Pit	FS, cap	36.09286	-93.24766	332.3	70.3 Mb, Mbv, Mf
BNR-FC9	Missile Silo, lower room	FS, cap, corrode	36.09641	-93.25677	318.5	46.3 Mb
BNR-FC10	Missile Silo, upper room	FS, cap	36.09641	-93.25685	325.5	40.7 Mb
BNR-FC11	Missile Silo	Stalag	36.09632	-93.25661	318.5	47.8 Mb
BNR-140320	South of Missile Silo	Seep	36.09641	-93.25685	322.1	48.1 Mb
BNR-140130-1	Fitton Spring	Spring discharge	36.08803	-93.23331	276.5	0.0
BNR-140130-2	Cecil Creek	Surface water	36.08765	-93.23258	274.2	0.0
BNR-140321-5	Van Dyke Spring	Spring discharge	36.08623	-93.23935	281.5	0.0

Sample type: FS, intercal = Flowstone intercalated with sediment; FS, cap = Flowstone capping sediment; Stalag = Broken stalagmite; gyp = predominantly gypsum; TV = travertine vein; corrode = corroded flowstone.

Overburden thickness and map unit: Mb = Mississippian Boone Formation; Mbv = Mississippian Batesville Sandstone; Mf = Mississippian Fayetteville Shale

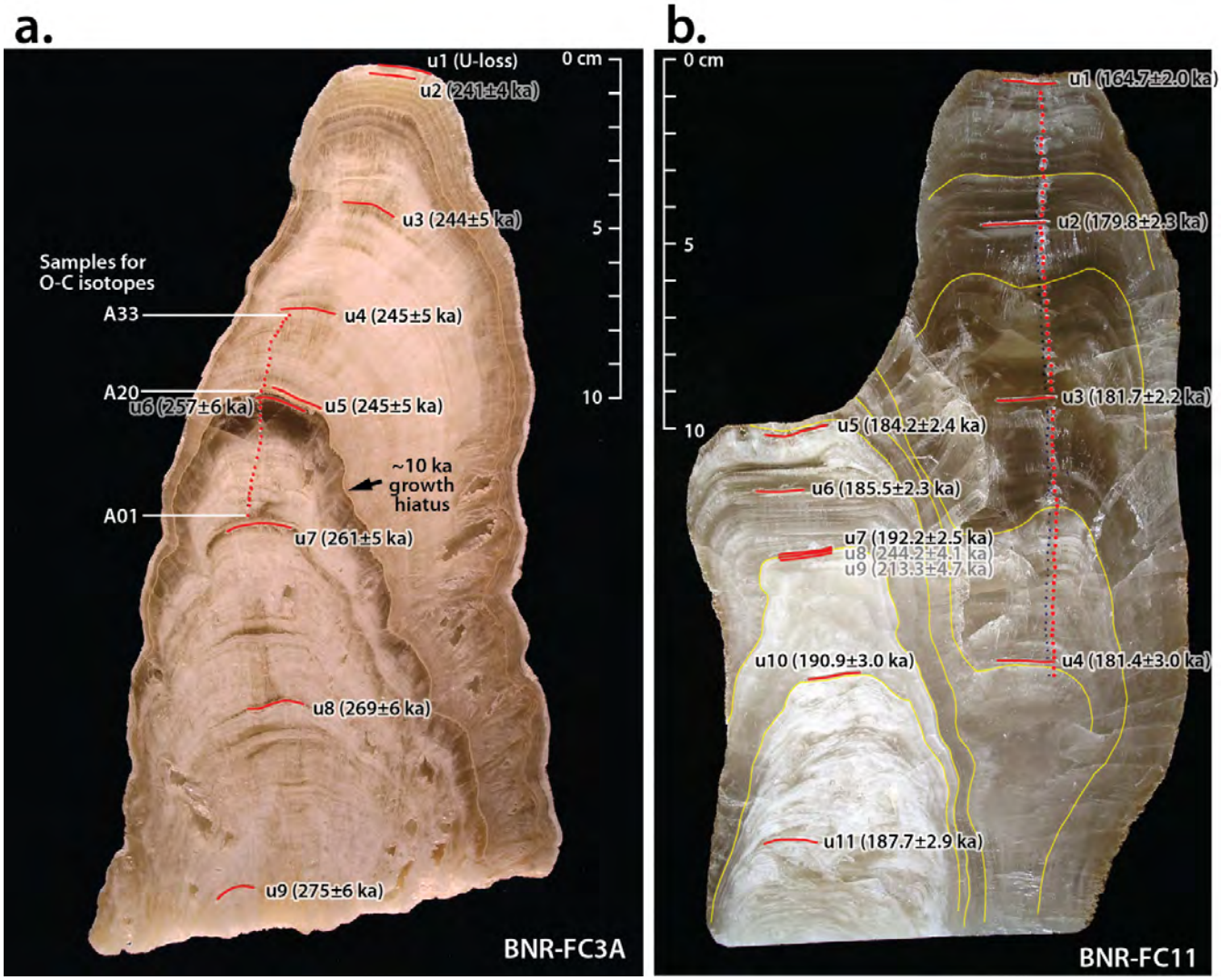

Figure 2. Photographs of slabbed stalagmite specimens (a) BNR-FC3A, and (b) upper half of BNR-FC11, showing locations of subsamples analyzed for uranium-thorium and strontium isotopes (identifier starting with "u"), and oxygen-carbon (O-C) isotopes (identifier starting with "A").

Analytical Methods

Specimens were cut perpendicular to growth axes and polished to allow subsampling of internal layers. Subsamples for radiogenic isotopes (U-Th, Sr) were collected using a 1-millimeter (mm)-diameter carbide dental bur to excavate shallow trenches parallel to growth bands, resulting in powder weights of 0.016 to 0.131 gram (median of 0.037 gram). Subsamples for O and C stable isotopes were collected along the growth axis of the stalagmites by drilling shallow 1-mm-diameter holes at 1- to 2-mm intervals over limited areas of interest.

The U and Th ($^{234}U/^{238}U$, $^{230}Th/^{238}U$, and $^{232}Th/^{238}U$) isotopic compositions were determined at the U.S. Geological Survey (USGS) Southwest Isotope Research Laboratory in Denver, CO, by thermal ionization mass spectrometry after total digestion and ion chromatographic separation/purification following procedures outlined elsewhere (Paces, 2015). The $^{87}Sr/^{86}Sr$ isotopic compositions were determined on the same digested aliquots by piggy-backing Sr columns to collect the initial effluent from U-Th

columns, with subsequent processing following the methods of De Muynck and others (2009).

The O and C stable isotope compositions were determined on CO_2 by phosphoric acid digestion using a custom automated sample preparation device attached directly to a VG Optima stable isotope ratio mass spectrometer at the USGS Southwest Isotope Research Laboratory in Denver, CO. Isotope compositions are expressed in standard δ notation in units of per mil (‰) relative to the Vienna Pee Dee Belemnite (VPDB) standard. Measured $\delta^{18}O$ and $\delta^{13}C$ values were corrected using internal standards calibrated to NBS-19. Uncertainties (2σ) are about 0.08‰ for $\delta^{13}C$ and 0.15‰ for $\delta^{18}O$.

Results of Analyses

Analytical results consisted of $^{230}Th/U$ ages, initial $^{234}U/^{238}U$ activity ratios (AR), and $^{87}Sr/^{86}Sr$ compositions on 77 aliquots from 19 individual specimens associated with the 6 sites identified in table 1 (data accessible in file "BNR_FittonCave_UTh_Sr_data.csv" at doi:10.5066/F7DZ06H6). Concentrations of U ranged from 0.32 to 24 ppm (median value of 4.93 ppm, N=77) with low Th concentrations (median concentration of 0.0023 ppm), making samples amenable to $^{230}Th/U$ dating.

Ages of Speleothems

Ages of Fitton Cave speleothems vary widely from 12 ka (thousand years) to 690 ka, although ages older than about 500 ka are close to the upper dating limit for the method and have large uncertainties. Typically, samples have low $^{232}Th/^{238}U$ AR (high $^{230}Th/^{232}Th$ AR) and require little correction for initial ^{230}Th. Only 4 of the 77 subsamples have $^{230}Th/^{238}U$ AR that are unsupported by U present in the sample, indicating that post-depositional U mobility is not a common problem.

Flowstones intercalated with sediments at Site 1 (FC1) and capping sediments at Double Drop Pit Passage (FC6, FC7, and FC8) consistently yield $^{230}Th/U$ ages between 415 and 690 ka, whereas younger ages were obtained for flowstone from Labyrinth south (FC5; 137±18 ka to 306±91 ka) and Missile Silo room (FC9; 159±21 ka to 304±62 ka). Flowstone and evaporative crusts capping sediment at Site 1 (FC2) and in the T Room (FC4) indicate deposition as young as 12 to 24 ka.

Stalagmites formed over discrete intervals of approximately 240–275 ka for FC3A (fig. 2a), 271–354 ka for FC3B, and 165–190 ka for FC11 (fig. 2b). Subsample ages generally are concordant with internal stratigraphy considering analytical uncertainties, although several apparent age reversals are present. Outermost surfaces show evidence of weathering and yield anomalously old ages or excess ^{230}Th, indicating post-depositional U loss (BNR-FC3A-u1 and BNR-FC3B-u1). Internal surfaces with anomalously old ages correspond to textural discontinuities that may reflect similar weathering periods (BNR-FC11-u7, -u8, and –u9). Growth rates range from 1.4 to 40 mm/ka and appear linear for tens of thousands of years before changing abruptly. Inflections are commonly associated with textural discontinuities (fig. 3).

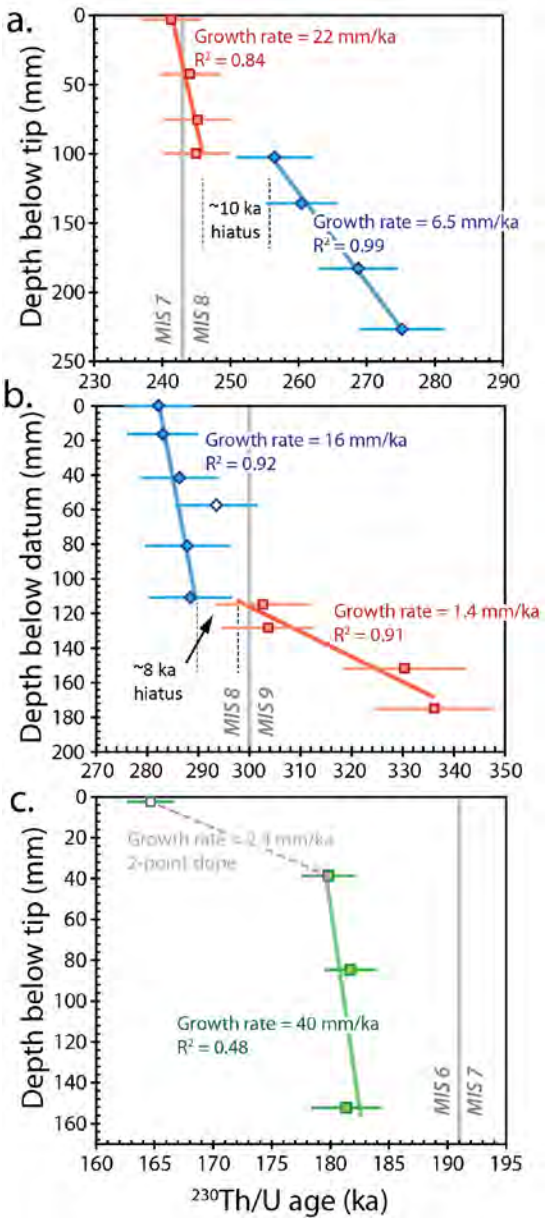

Figure 3. Depth versus age relations for Fitton Cave stalagmites (a) BNR-FC3A, (b) BNR-FC3B, and (c) BNR-FC11. Growth rates represent slopes of simple linear regressions using subsamples designated by filled symbols.

Compositions of Speleothems

In addition to obtaining ages from U-Th isotope analysis, values for the U isotopic composition at the time of mineral formation can be calculated (initial $^{234}U/^{238}U$ AR). Because very little U isotope fractionation takes place during calcite precipitation from aqueous solutions, initial $^{234}U/^{238}U$ AR values are equivalent to the values present in vadose water at the time the mineral formed. The same is true for $^{87}Sr/^{86}Sr$ compositions. Therefore, these isotopes are useful as natural tracers of water sources and how they vary both spatially and temporally.

Fitton Cave speleothems have a wide range of initial $^{234}U/^{238}U$ AR and $^{87}Sr/^{86}Sr$ compositions (fig. 4). Results for individual sites tend to cluster relative to the entire range; however, differences are also observed between multiple samples from the same site, as well as for different layers in a single stalagmite. Several specimens have initial $^{234}U/^{238}U$ AR less than 1.0 (FC2, FC3, FC4, FC10), which is uncommon for near-surface water sources that typically have $^{234}U/^{238}U$ AR greater than 1.0. Most Fitton Cave speleothems have initial $^{234}U/^{238}U$ AR in the range of 1.07 to 2.0.

All speleothems are enriched in radiogenic Sr (higher $^{87}Sr/^{86}Sr$ value) relative to values in the host limestone (median of 0.70850 for nine measurements). Therefore, vadose source water interacted with soil or bedrock having elevated $^{87}Sr/^{86}Sr$ values prior to reaching deposition sites. Younger clastic rocks overlying the Boone Formation likely have higher rubidium/strontium values than host limestones, resulting in more radiogenic $^{87}Sr/^{86}Sr$ values in infiltrating water.

Values of $^{87}Sr/^{86}Sr$ and initial $^{234}U/^{238}U$ AR observed in Fitton Cave speleothems are generally correlated (fig. 4). Because samples are widely dispersed within the cave, variations cannot be related to processes acting along any single vadose flow path. Samples from several sites have compositions that are consistent with values measured in vadose water as well as surface water or karst spring discharge (fig. 4). Variations are not clearly related to overburden thickness or the geologic units hosting overlying vadose pathways.

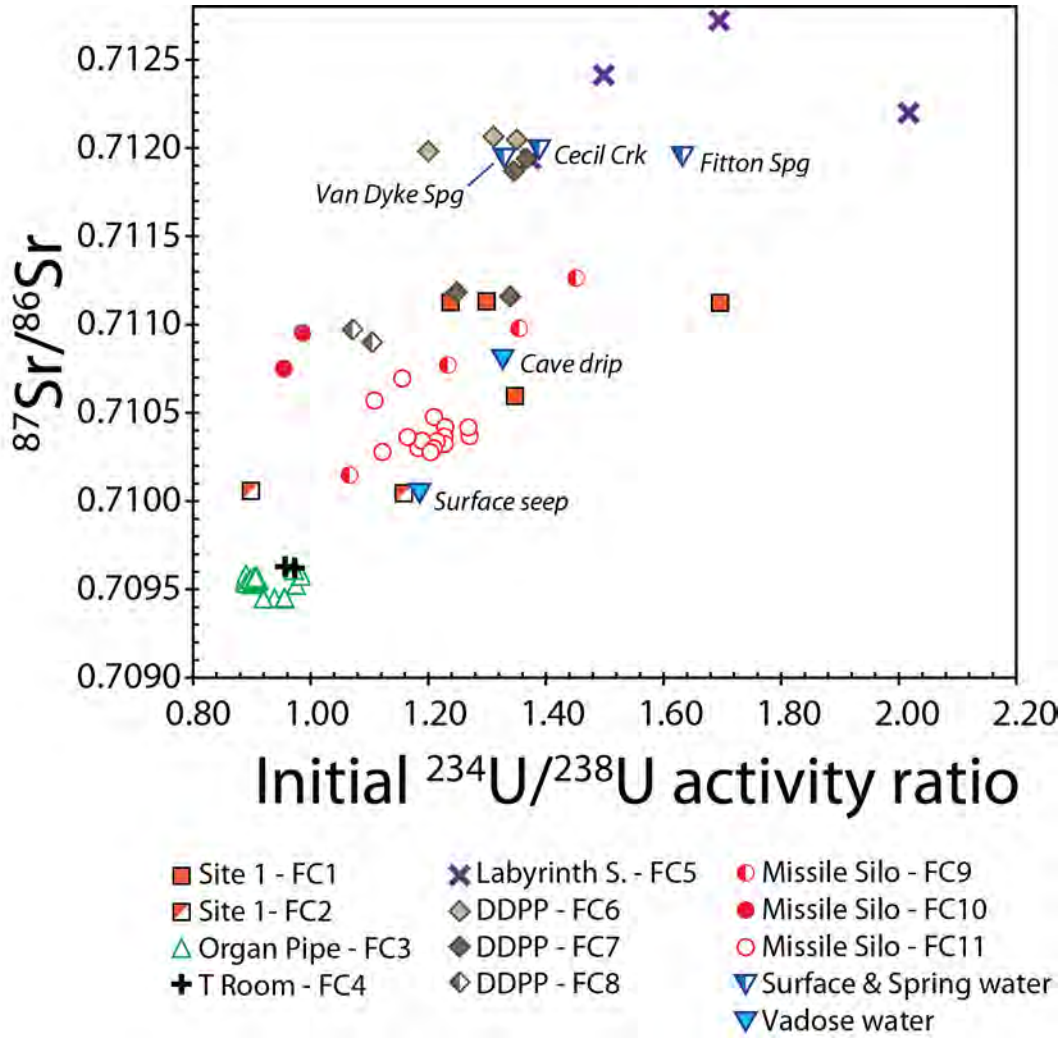

Figure 4. Strontium ($^{87}Sr/^{86}Sr$) and uranium ($^{234}U/^{238}U$) isotopic compositions for speleothems from Fitton Cave and associated water samples. Unfilled symbols represent stalagmites FC3 (triangles) and FC11 (circles). Water data from Hudson and others (2017).

A set of subsamples from stalagmites FC3A and FC3B were analyzed for O and C stable isotopes (data accessible in file "BNR_FittonCave_C-O_data.csv" at doi:10.5066/F7DZ06H6). Subsamples distributed at fine spatial resolution on either side of a distinct textural discontinuity representing a growth hiatus in FC3A (fig. 3) have $\delta^{18}O$ and $\delta^{13}C$ compositions ranging from -2.3 to -6.1 and 0.4 to -5.7 ‰, respectively. Overall, the two isotopes are poorly correlated, indicating that kinetic isotope fractionation within the cave environment is unlikely to fully explain the pattern of variability. However, compositions of calcite above and below the textural discontinuity show distinct differences (fig. 5), reflecting different compositions of infiltrating water likely related to climate-driven changes in moisture sources and plant communities at different time periods.

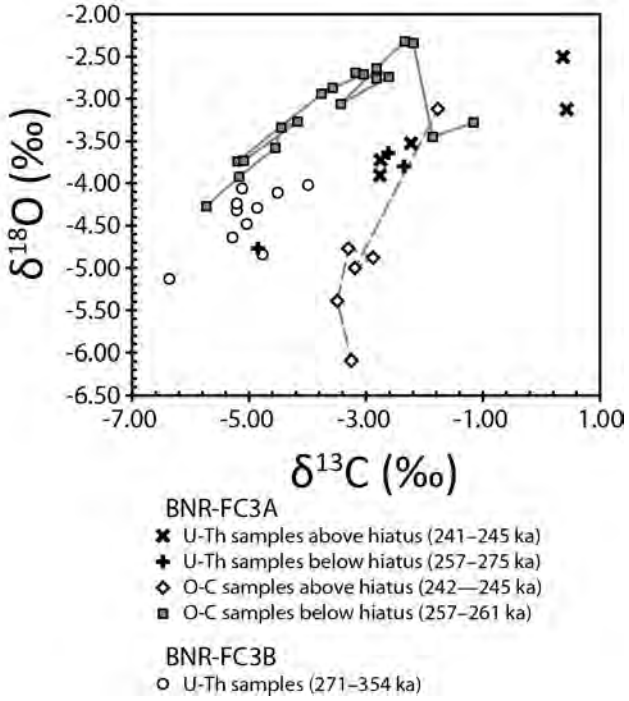

Figure 5. Relations between stable isotopic compositions of oxygen ($\delta^{18}O$) and carbon ($\delta^{13}C$) for Fitton Cave stalagmites FC3A and FC3B.

Discussion

Constraints on Cave Evolution

Ages for the oldest flowstones associated with cave sediments (400 to 700 ka) are substantially younger than preliminary cosmogenic nuclide burial ages of coarse clastic materials that vary from 740 to 2,200 ka (Keen-Zebert and others, 2016). However, the younger $^{230}Th/U$ ages are not an artifact of post-depositional open-system isotopic behavior. Older dates have remarkably consistent U-series systematics considering that a number of speleothems show textural evidence of corrosion, and that ages close to the dating limit are particularly sensitive to U loss but show none. Therefore, younger $^{230}Th/U$ ages for flowstones are interpreted as real periods of time that postdate active streamflow capable of carrying coarse sediment far underground.

The general absence of interbedded flowstone in coarse sediment sequences indicates that early, more-energetic stages of speleogenesis were not interrupted by periods of quiescence until base levels fell sufficiently to lower streamflow and allow flowstone caps to form on stabilized surfaces. Thus, flowstone ages are consistent with the older sediment burial ages that more closely reflect periods of passage formation, but may actually provide further constraints on periods of base level lowering related to regional incision.

Paleohydrologic Flow

Isotopic compositions of Sr and U are not affected substantially by many near-surface physical, chemical, or biological processes, allowing them to reflect values present in the water from which they precipitated (Ludwig and others, 1992; Paces and Wurster, 2014). Samples of vadose water, surface water, and karst spring sources associated with Fitton Cave have $^{87}Sr/^{86}Sr$ values and $^{234}U/^{238}U$ AR similar to those in speleothems (fig. 4). Cecil Creek and associated groundwater discharge have elevated values similar to speleothems collected from Labyrinth south (FC5) and Double Drop Pit Passage (FC6, FC7). Drip water from Fitton Cave, sampled near the Missile Silo, and a vadose seep discharging from the base of the St. Joe Limestone along the Goat Trail at Big Bluff, about 9 kilometers to the west, have lower values in the range of those observed in speleothems from Site 1 (FC1, FC2) and Missile Silo (FC9, FC10, FC11), although variability in speleothems is large.

Vadose water required to explain compositions of speleothems from Organ Pipe (FC3) and the T Room (FC4), which have the lowest $^{87}Sr/^{86}Sr$ values and initial $^{234}U/^{238}U$ AR less than 1.0, have not been sampled. The latter feature, though unusual, is not unique (Zhou and others, 2005). Water with $^{234}U/^{238}U$ AR less than 1.0 is presumed to have been the source for stalagmites and flowstone at these sites. Water depleted in ^{234}U relative to ^{238}U may be derived by dissolution of previously ^{234}U-leached bedrock (Osmond and Cowart, 2000), or by kinetics that inhibit the valence change of U(IV)

to U(VI) after alpha decay from the intermediate daughter ^{234}Th (Zhou and others, 2005). In either case, greater dissolution of the host limestone along these flow paths (or less dissolution in overlying clastic units) is likely required to explain the low $^{87}Sr/^{86}Sr$ values observed in these same materials.

Water compositions responsible for speleothems in Fitton Cave varied widely and likely reflect water/rock interactions at different spatial scales. Clustering of data observed for materials from different sites as well as the general positive correlation between $^{234}U/^{238}U$ and $^{87}Sr/^{86}Sr$ values imply that flow processes are not random but related to kinetic and compositional factors operating along a set of flow paths. These isotope data will ultimately provide important information to help understand those vadose zone hydrologic processes.

Past Environmental Conditions

The O and C stable isotope records preserved in speleothems have been widely used to evaluate histories of atmospheric flow patterns and temperatures ($\delta^{18}O$) or changing plant communities ($\delta^{13}C$) in continental settings (Winograd and others, 1992; Richards and Dorale, 2003; Fairchild and others, 2006). Many of those studies focus on late Pleistocene records when age uncertainties and temporal resolutions are optimal. Less is known about older, middle Pleistocene records like those available from the Fitton Cave stalagmites.

Initial investigations of parts of specimen FC3A show systematic variations of both $\delta^{18}O$ and $\delta^{13}C$ that are likely related to changing surface conditions that occurred during the marine isotope stages (MIS) 8/7 glacial-interglacial transition (fig. 6). Profiles are disrupted by a growth hiatus (about 245 to 257 ka) during MIS 8 full glacial conditions, but otherwise show clearly differing trends on either side of the discontinuity. Although substantial overlap is present, calcite deposited during MIS 7 tends to have higher $\delta^{13}C$ values for a given $\delta^{18}O$ value compared to that deposited during MIS 8, indicating a significant change in the surface environment. The MIS 8 calcite records a steep increase in $\delta^{13}C$ prior to the hiatus, which may be related to a shift toward reduced plant cover, or a change toward a prairie plant community during peak glacial conditions, similar to that noted in other speleothems from the region (Dorale and others, 1998). MIS 7 calcite trends sharply toward lower $\delta^{18}O$ values, and speleothem growth rate increases following the hiatus, possibly due to enhanced moisture availability coincident with deglaciation. Although these results are encouraging, data at similar spatial resolutions over the rest of this and other stalagmite records are needed to better interpret the significance of these variations. Ultimately, they should provide a history that can be compared to other detailed records to more clearly understand differences in the timing and degree of changes in the mid-continent region that can be related to their position with respect to the extent of the Laurentide ice sheet.

Isotopes of Sr and U also can provide information on how the vadose hydrologic system responded to changing environmental conditions through time. Both initial $^{234}U/^{238}U$ AR and $^{87}Sr/^{86}Sr$ values show differences in calcite deposited before and after the textural discontinuity in specimen FC3A. Assuming that the flow path to the drip site feeding this stalagmite remained fixed, the compositional shift is likely caused by differences in solubility related to water chemistry or water/rock volumes with time. Differences in composition between the two stalagmites may be more related to different flow paths feeding BNR-FC3A and FC3B, but where the record overlaps (BNR-FC3A-u9 and BNR-FC3B-u3), initial $^{234}U/^{238}U$ AR were identical, although $^{87}Sr/^{86}Sr$ values were not.

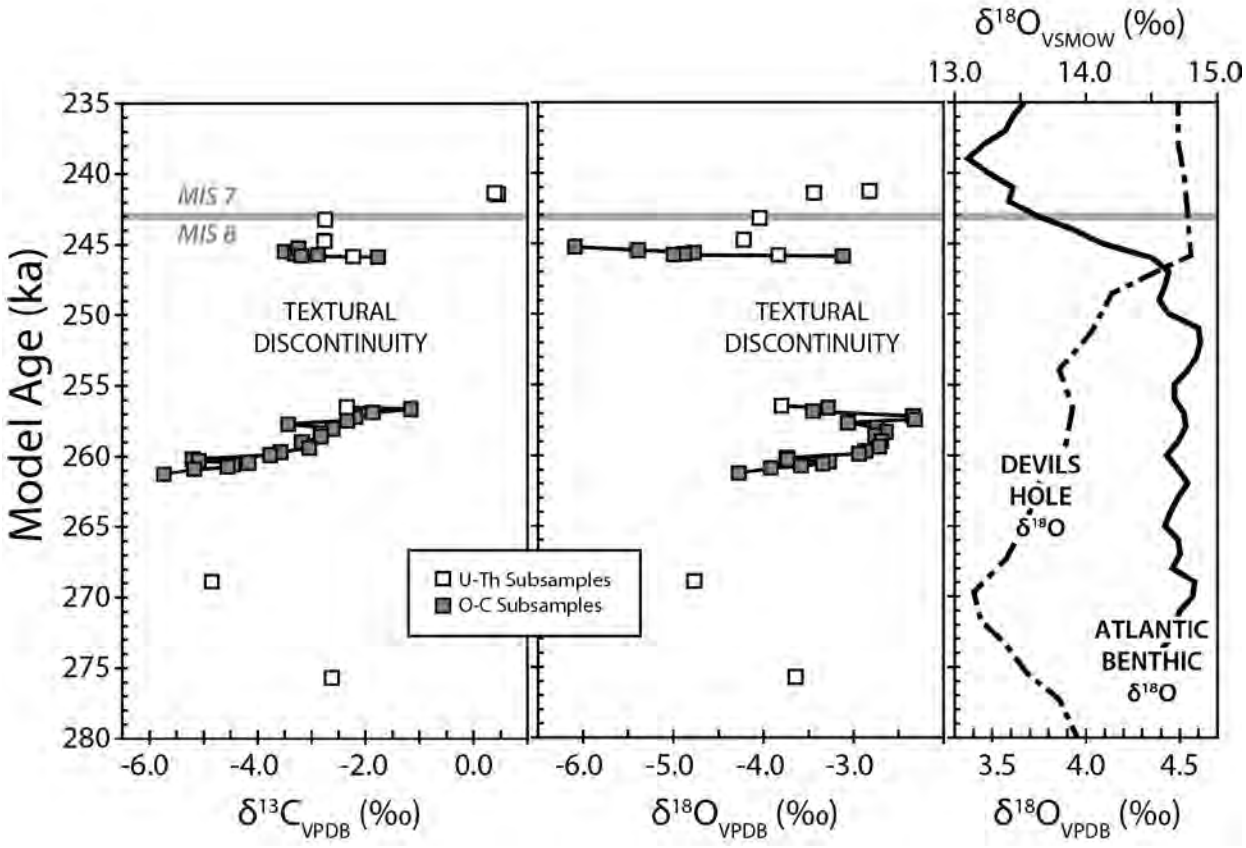

Figure 6. Profiles of $\delta^{13}C$ and $\delta^{18}O$ in Fitton Cave stalagmite BNR-FC3A compared to the Devils Hole continental hydrologic record (Winograd and others, 1992, expressed relative to Vienna Standard Mean Ocean Water [VSMOW]) and a stacked record of Atlantic benthic foraminifera $\delta^{18}O$ (global ice-volume proxy, Lisiecki and Raymo, 2009). The age model for Fitton Cave speleothems was produced using the StalAge algorithm of Scholz and Hoffmann (2011). Horizontal thick gray line marks the interglacial-glacial climate transition between marine isotope stages (MIS) 7 and 8, based on estimates from Lisiecki and Raymo (2005). See figure 2 for subsample locations.

Conclusions

Speleothems from Fitton Cave are being used to better understand karst processes and landscape evolution of the southern Ozark Plateau region. Ages of flowstones associated with clastic sediments using U-Th isotopes range from 400 to 700 ka. These dates are younger than cosmogenic burial ages for the sediment itself and reflect a younger hydrologic environment established after base levels lowered enough to allow stabilization of deposits.

Isotopic compositions of U and Sr in speleothems reflect those in the water from which they formed and provide a record of past water/rock interaction. Initial $^{234}U/^{238}U$ activity ratios and $^{87}Sr/^{86}Sr$ values for speleothems from different areas within the cave are generally correlated, and reflect variable rock compositions and processes involving water/rock interaction and flow.

Three stalagmites collected to evaluate changing paleoenvironmental conditions have ages that span middle Pleistocene depositional episodes from approximately 165 to 185 ka, and from about 240 to 350 ka. A preliminary O and C stable isotope record shows systematic shifts related to climate changes near the transition

between marine isotope stages (MIS) 8 (glacial) and MIS 7 (interglacial) conditions. Shifts in U and Sr isotopes are observed over this same period, reflecting changes in vadose paleohydrologic conditions and processes.

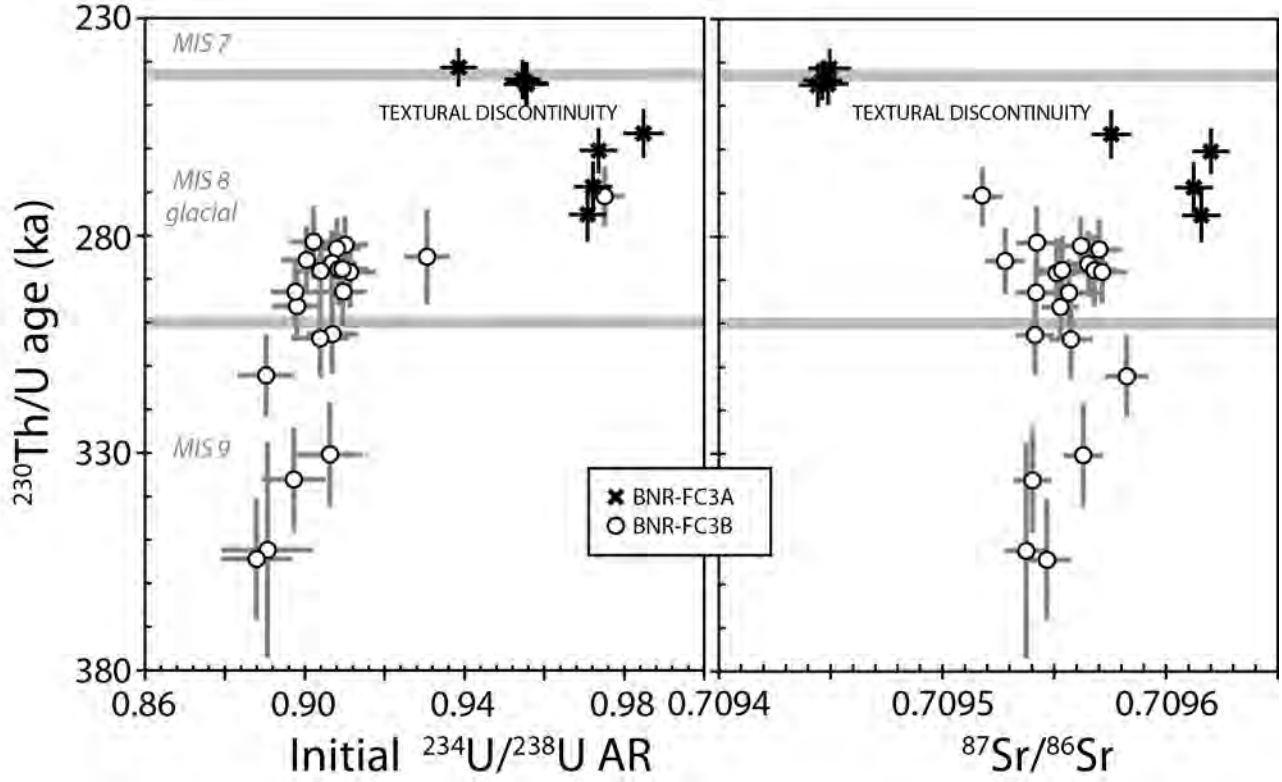

Figure 7. Profiles of radiogenic uranium (initial $^{234}U/^{238}U$ activity ratios) and strontium ($^{87}Sr/^{86}Sr$) isotopic compositions for dated subsamples of Fitton Cave stalagmites BNR-FC3A and BNR-FC3B. Horizontal thick gray lines mark interglacial-glacial climate transitions between marine isotope stages (MIS) 7, 8, and 9, based on estimates from Lisiecki and Raymo (2005). See figure 3 for BNR-FC3A subsample locations.

References Cited

Adamski, J.C., Peterson, J.C., Freiwald, D.A., and Davis, J.V., 1995, Environmental and hydrologic setting of the Ozark Plateaus study unit, Arkansas, Kansas, Missouri, and Oklahoma: U.S. Geological Survey Water-Resources Investigations Report 94-4022, 69 p., accessed Feb. 6, 2017, at https://pubs.usgs.gov/wri/wri944022/WRIR94-4022.pdf.

De Muynck, D., Huelga-Suarez, G., Van Heghe, Lana, Degryse, P., and Vanhaecke, F., 2009, Systematic evaluation of a strontium-specific extraction chromatographic resin for obtaining a purified Sr fraction with quantitative recovery from complex and Ca-rich matrices: Journal of Analytical Atomic Spectrometry, v. 24, p. 1498–1510, doi:10.1039/B908645E.

Dorale, J., Edwards, R.L., Ito E., and Gonzalez, L.A., 1998, Climate and vegetation history of the midcontinent from 75 to 25 ka—A speleothem record from Crevice Cave, Missouri, USA: Science, v. 282, p. 1871–1874, doi:10.1126/science.282.5395.1871.

Fairchild, I.J., Smith, C.L., Baker, A., Fuller, L., Spötl, C., Mattey, D., McDermott, F., and E.I.M.F., 2006, Modification and preservation of environmental signals in speleothems: Earth-Science Reviews, v. 75, p. 105–153, doi:10.1016/j.earscirev.2005.08.003.

Hudson, M.R., 1998, Geologic map of parts of the Gaither, Hasty, Harrison, Jasper, and Ponca quadrangles, Boone and Newton Counties, northern Arkansas: U.S. Geological Survey Open-File Report 98–116, scale 1:24,000.

Hudson, M.R., Paces, J.B., and Turner, K.J., 2017, Tufa and water radiogenic geochemistry and tufa ages for two karst aquifers in the Buffalo National River region, northern Arkansas: *in* Kuniansky, E.L., and Spangler, L.E., eds., U.S. Geological Survey Karst Interest Group Proceedings, San Antonio, Texas, May 16–18, 2017: U.S. Geological Survey Scientific Investigations Report 2017–5023, p. 107–118.

Hudson, M.R., and Turner, K.J., 2014, Geologic map of the west-central Buffalo National River region, Arkansas: U.S. Geological Survey Scientific Investigations Map 3314, 1:24,000 scale, http://pubs.usgs.gov/sim/3314/.

Hudson, M.R., Turner, K.J., and Bitting, C., 2011, Field trip guide—Geology and karst landscapes of the Buffalo National River area, northern Arkansas: *in* Kuniansky, E.L., ed., U.S. Geological Survey Karst Interest Group Proceedings, Fayetteville, Arkansas, April 26–29, 2011: U.S. Geological Survey Scientific Investigations Report 2011–5031, p. 191–212, accessed Feb. 6, 2017, at https://pubs.usgs.gov/sir/2011/5031/.

Keen-Zebert, A., Granger, D.E., Paces, J.B., Hudson, M.R., and Bitting, C., 2016, Combined use of cosmogenic nuclide, U-series disequilibrium, paleomagnetism, and optically stimulated luminescence within Fitton Cave to evaluate the landscape evolution of the Buffalo National River, Arkansas (abs.): Geological Society of America Abstracts with Programs, v. 48, no. 7, doi: 10.1130/abs/2016AM-285655.

Lisiecki, L.E., and Raymo, M.E., 2005, A Pliocene-Pleistocene stack of 57 globally distributed benthic $\delta^{18}O$ records: Paleoceanography, v. 20, PA1003, 17 p., doi:10.1029/2004PA001071.

Lisiecki, L.E., and Raymo, M.E., 2009, Diachronous benthic $\delta^{18}O$ responses during late Pleistocene terminations: Paleoceanography, v. 24, PA1732, 14 p., doi:10.1029/2009PA001732.

Ludwig, K.R., Simmons, K.R., Szabo, B.J., Winograd, I.J., Landwehr, J.M., Riggs, A.C., and Hoffman, R.J., 1992, Mass-spectrometric ^{230}Th-^{234}U-^{238}U dating of the Devils Hole calcite vein: Science v. 258, p. 284–287, www.jstor.org/stable/2879892.

Mott, D.N., Hudson, M.R., and Aley, T., 2000, Hydrologic investigations reveal interbasin recharge contributes significantly to detrimental nutrient loads at Buffalo National River, Arkansas: Proceedings of Arkansas Water Resources Center annual conference MSC-284, Fayetteville, AR., p. 13–20.

Osmond, J.K., and Cowart, J.B., 2000, U-series nuclides as tracers in groundwater hydrology, *in* Herczeg, A.L., ed., Environmental Tracers in Subsurface Hydrology: Boston, Kluwer Academic Publishers, p. 145–174, ISBN: 978-1-4615-4557-6.

Paces, J.B., 2015, $^{230}Th/U$ ages supporting geologic map of the Masters 7.5' quadrangle, Weld and Morgan Counties, Colorado, appendix 1 of Berry, M.E., Slate, J.L., Paces, J.B., Hanson, P.R., and Brandt, T.R., Geologic map of the Masters 7.5' quadrangle, Weld and Morgan Counties, Colorado: U.S. Geological Survey Scientific Investigations Map 3344, 10 p., 1 sheet, 1:24,000, accessed February 2017, at https://pubs.usgs.gov/sim/3344/sim3344_appendix_1.pdf.

Paces, J.B., and Wurster, F.C., 2014, Natural uranium and strontium isotope tracers of water sources and surface water–groundwater interactions in arid wetlands – Pahranagat Valley, Nevada, USA: Journal of Hydrology, v. 517, p. 213–225, doi.org/10.1016/j.jhydrol.2014.05.011.

Richards, D.A., and Dorale, J.A., 2003, Uranium-series chronology and environmental applications of speleothems: Reviews in Mineralogy and Geochemistry, v. 52, p. 407–460, doi:10.2113/0520407.

Scholz, D., and Hoffman, D.L., 2011, StalAge – An algorithm designed for construction of speleothem age models: Quaternary Geochronology, v. 6, p. 369–382, doi:10.1016/j.quageo.2011.02.002.

Winograd, I.J., Coplen, T.B., Landwehr, J.M., Riggs, A.C., Ludwig, K.R., Szabo, B.J., Kolesar, P.T., and Revesz, K.M., 1992, Continuous 500,000-year climate record from vein calcite in Devils Hole, Nevada: Science, v. 258, p. 255–260, doi:10.1126/science.258.5080.255.

Zhou, J., Lundstrom, C.C., Fouke, B., Panno, S., Hackley, K., and Curry, B., 2005, Geochemistry of speleothem records from southern Illinois—Development of (^{234}U)/(^{238}U) as a proxy for paleoprecipitation: Chemical Geology, v. 221, p. 1–20, doi:org/10.1016/j.chemgeo.2005.02.005.

Speleogenetic, Tectonic, and Sedimentologic Controls on Regional Karst Aquifers in the Southern Ozarks of the Midcontinent U.S., and Potential Problems at Site-Specific Scales From Aquifer Lumping

By Van Brahana

U.S. Geological Survey, Research Hydrologist Emeritus; University of Arkansas, Professor Emeritus, Department of Geosciences, 20 Gearhart Hall, Fayetteville, AR 72701

Abstract

The near-horizontal layering of Paleozoic aquifers in the southern Ozarks, many of which are in karstified carbonate rocks, offers a huge range of hydraulic characteristics, fluxes, mineralogy, flow mixing, land use, and speleogenesis. Regional aquifer system analysis (RASA) modeling conducted by the U.S. Geological Survey (USGS) in the 1980s and 1990s required combining (lumping) multiple carbonate aquifers into single hydrogeologic units, an oversimplification that has proven adequate for regional generalizations at scales of 10 kilometers and greater, but one that is misleading and oftentimes inappropriate at site-specific scales and in locally predictive hydrogeologic studies at scales of meters to hundreds of meters. Unfortunately, the conceptualization and utilization of regional hydrostratigraphic nomenclature has been widely accepted by many in the consulting industry, and coincidently, within the NAWQA program. Although the methodologies, purposes, and scopes of these regional studies have been clearly defined in USGS reports, the overall trend of generalization has taken a firm hold on the karst community. Accurately elucidating the speleogenesis of these karst aquifers, including their hydrogeologic attributes, hydraulic properties, tectonic settings, and sedimentologic histories is an essential component of resolving these scale-dependent problems, as case studies from (1) the Boone Formation in northern Arkansas, and (2) the Potosi Formation in southern Missouri, will show. Although the following explanation of speleogenesis in the Ozarks has a modicum of speculation, the problems it addresses are real.

The Boone and Potosi Formations encompass the full range of karst aquifers in this region of middle America, and highlight problems that lumping typically introduces at scales smaller than hundreds of meters, where most contamination problems occur. The Boone Formation, lumped as the Springfield Plateau aquifer, was part of the Ozark Plateaus aquifer system by Imes and Emmett (1994). The middle 70 meters of the Boone, with as many as 60 intervals of alternating thin limestone and chert couplets, represent a low-yield zone of very thin (from 5 to 50 centimeters) karst aquifers. Although this interval is only one part of a single regional hydrogeologically lumped unit, each of the limestone layers has the potential to be karstified, with variable attributes and boundaries. Above and below the chert-rich layers of the Boone are relatively pure limestones with completely different karst attributes, including greater spring yields, hydraulic conductivity, storage, and flow velocities, and completely different geomorphological characteristics. The continuity of the chert units, which act as confining units when indurated, decreases from south to north, resulting in an areal variability in hydrogeologic characteristics across the region. The source of much of this variability is hypothesized to be due to slight differences in karstification and sedimentation. The sedimentation appears to be related to distance from island arcs that provided air-fall ash that was spread across a shallow carbonate platform. The island arcs were above the subducting plate south of the Ouachita Mountains and resulted from the continent-to-continent Ouachita collision. Tectonic closure also resulted in a foreland bulge that produced slight uplift (200 meters), fracturing, and tilting in northern Arkansas. The chert interbedded with limestone confined groundwater flow, and systematic jointing and faulting limited groundwater

basin size. In Missouri, farther from the ash source and foreland bulge, chert nodules formed in place of continuous thin chert confining layers, and the Boone aquifers produced higher yielding springs that drew recharge from larger areas and stratigraphic intervals.

The Potosi Formation, on the other hand, is the dominant high-yielding groundwater source in the Ozark aquifer, which is made up of 14 individual geologic formations (Imes and Emmett, 1994). Three of the ten largest springs in the conterminous United States are attributed to the Potosi Formation, as are most of the public water-supply wells in southern Missouri. The karstification of the Potosi Formation appears to have been impacted most by an early-formed paleokarst, by geochemical alteration of limestone to dolomite, by tectonic reactivation of basement faults, and by tectonic expulsion of thermally heated hypogenic flow from the Arkoma Basin to the south. This latter stage of warm water served to precipitate drusy quartz into many of the voids in the dolomitic aquifer, thereby reducing its overall permeability and porosity. Whereas the Springfield Plateau aquifer includes many karstified thin zones separated by impermeable chert layers that impact site-specific contamination, the Ozark aquifer combines and mixes flow from a stratigraphic interval of 14 aquifers, with only minor confining units in a more than 500-meter-thick stratigraphic section. Aquifer attributes extrapolated from these projects that require lumping should be approached carefully and always with an intensive field data-collection program to verify that key karst components at an appropriate scale are included.

Reference Cited

Imes, J.L, and Emmett, L.F., 1994, Geohydrology of the Ozark Plateaus aquifer system in parts of Missouri, Arkansas, Oklahoma, and Kansas: U.S. Geological Survey Professional Paper 1414-D, 127 p.

Geologic Context of Large Karst Springs and Caves in the Ozark National Scenic Riverways, Missouri

By David J. Weary and Randall C. Orndorff

U.S. Geological Survey, MS926A, 12201 Sunrise Valley Drive, Reston, VA 20192

Abstract

The Ozark National Scenic Riverways (ONSR) is a karst park, containing many springs and caves. The "jewels" of the park are large springs that contribute substantially to the flow and water quality of the Current River and its tributaries. Completion of 1:24,000-scale geologic mapping of the park and surrounding river basin, along with synthesis of published hydrologic data, allows us to examine the spatial relations between the springs and the geologic framework, and develop a conceptual model for genesis of these springs and associated caves.

Large springs are present in the ONSR area because (1) the Ozark aquifer source is chiefly dolomite affected by solution via various processes over a long period of time, including late Paleozoic hydrothermal fluid migration, (2) a consistent and low regional bedrock dip of the Salem Plateau allows integration of subsurface flow into large groundwater basins with few discrete outlets, (3) locally to regionally continuous quartz sandstone and bedded chert in the carbonate stratigraphic succession serve as aquitards that locally confine and partition groundwater upgradient of the springs, creating artesian conditions. These partitions allow contributing aquifer compartments for different springs to overlap vertically, as evidenced by divergent and "crossing" dye traces in the study area, and (4) the springs are located where the rivers have cut down into structural highs, allowing access to groundwater confined lower in the section, thus draining aquifer compartments that have volumetrically larger storage than smaller springs higher in the section.

Introduction

The Ozark National Scenic Riverways (ONSR), located within the Salem Plateau subprovince of the Ozark Plateaus physiographic province in south-central Missouri, was created in 1964 to protect the riparian zone along 134 miles (mi) of the Current River and its major tributary, the Jacks Fork (figs. 1 and 2). The park includes numerous large artesian karst springs including Big Spring, by flow volume the largest spring in the National Park system. Base flow for the rivers is supplied chiefly by springs issuing groundwater that has traveled through the karst landscape from recharge areas 38 mi (61 kilometers [km]) or more away (Imes and Frederick, 2002). The springs and rivers provide habitat for numerous aquatic species as well as recreational resources for floaters, fishermen, and campers. The ONSR is also a major cave park with hundreds of known caves and diverse in-cave resources (Thornberry-Ehrlich, 2016).

Geologic mapping by the U.S. Geological Survey (USGS) and the Missouri Geological Survey (MGS) from 1997 to 2015 has provided complete coverage of the geology of the ONSR and parts of the surrounding region at a scale of 1:24,000 (fig. 2) (Weary and others, 2016). These maps and other unpublished field data allow us to examine the geologic context of many of the Ozark springs, make observations about possible relations between the geologic framework and the hydrology, and integrate published hydrologic data into a conceptual model addressing spring origins and speleogenesis in the southeastern Ozarks.

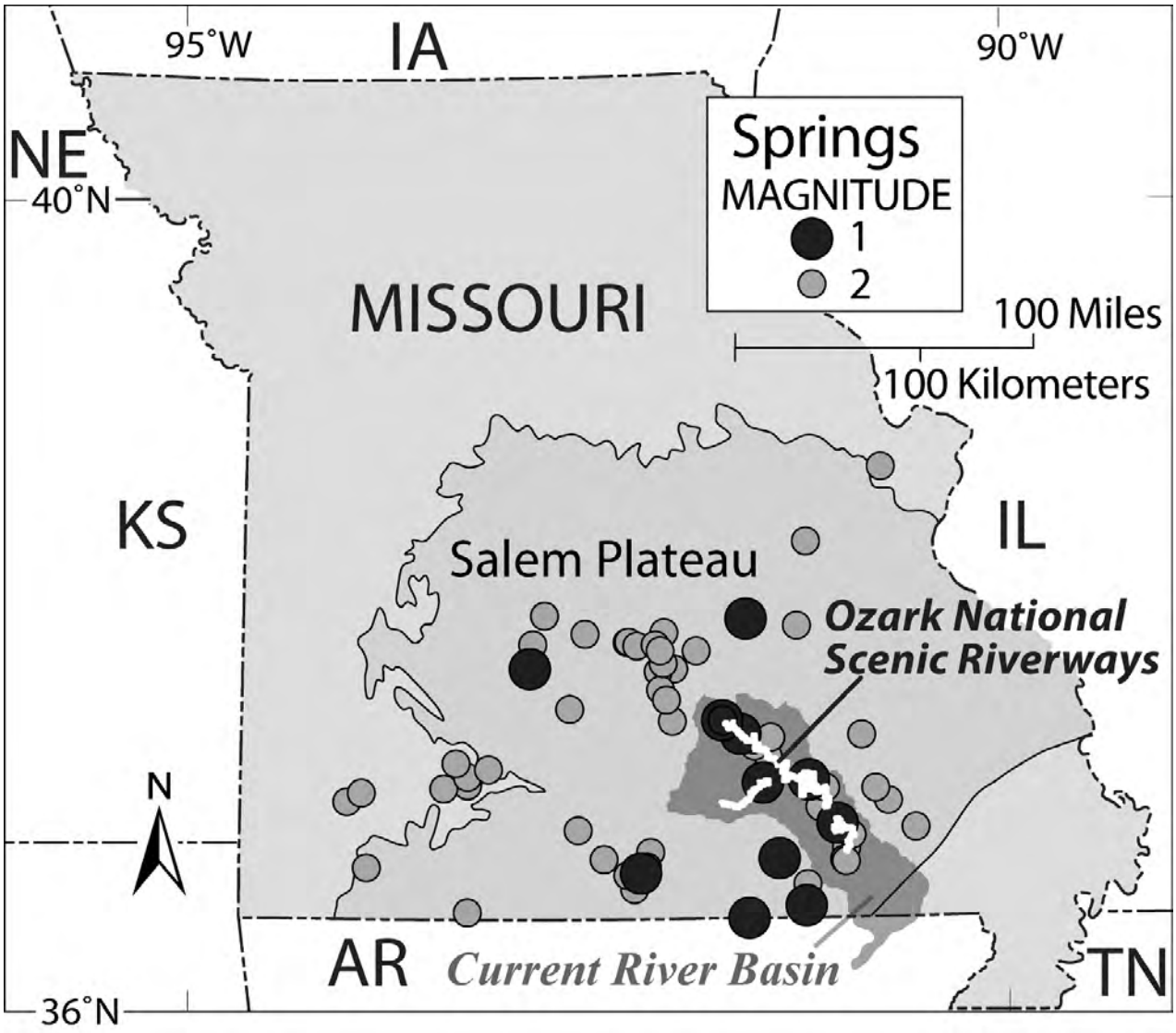

Figure 1. Location of the Ozark National Scenic Riverways, Current River Basin, and 1st and 2nd magnitude springs (Missouri Department of Natural Resources, 2002). Magnitude 1 flow—greater than 100 cubic feet/sec (2,800 liters/sec); magnitude 2 flow—10–100 cubic feet/sec (280–2,800 liters/sec).

Hydrologic Investigations

A comprehensive listing of previous hydrologic investigations in the study area can be found in reports by Mugel and others (2009), and Duley and others (2015). These reports also include information on dye-trace studies and delineations of recharge areas for many of the large springs. An unpublished Master's thesis by Keller (2000) provides detailed information on the flow and basin geometry of Welch Spring. Westerman and others (2016) published a regional report on the altitudes and thicknesses of hydrogeologic units within the Ozark aquifer.

Geohydrologic Framework

Geohydrologic units for the Salem Plateau have been classified as parts of the Ozark Plateaus aquifer system (Gann and others, 1976; Imes, 1989; Imes and Smith, 1990; Imes, 1990a, b). This vast system extends throughout southern Missouri, northern Arkansas, and eastern parts of Oklahoma and Kansas. The Ozark Plateaus aquifer system consists of four major geohydrologic units which, in ascending order,

include the (1) basement confining unit, (2) St. Francois aquifer, (3) St. Francois confining unit, and (4) Ozark aquifer. The basement confining unit comprises the Mesoproterozoic volcanic and plutonic basement rocks of the St. Francois terrane and Paleoproterozoic metamorphic rocks (Imes, 1989). The St. Francois aquifer comprises Upper Cambrian strata that disconformably overlie the basement confining unit and conformably underlie the St. Francois confining unit (Imes, 1990a). In the ONSR area, the St. Francois aquifer consists of the Lamotte Sandstone and the Bonneterre Formation (fig. 3).

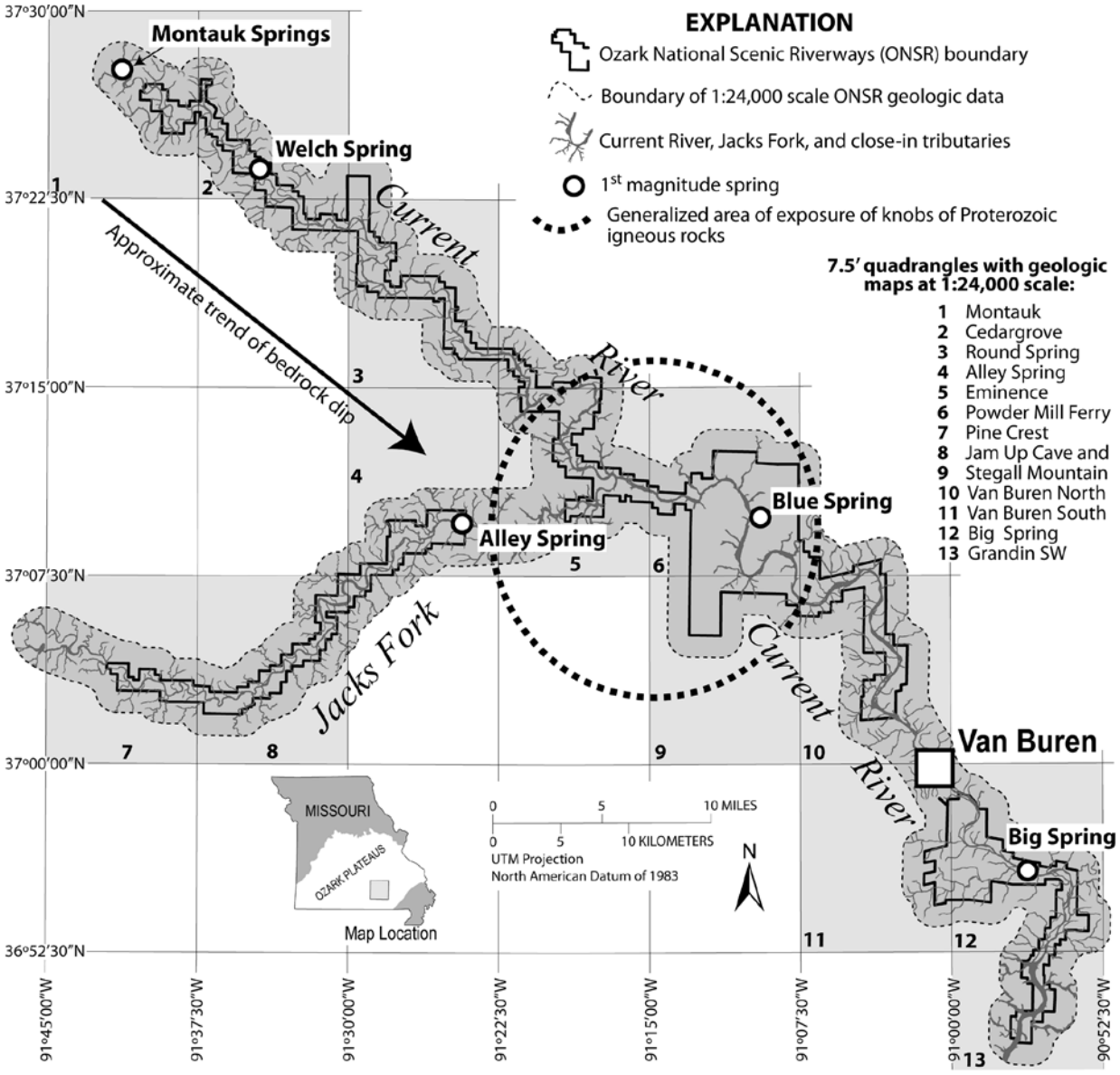

Figure 2. Map showing the Ozark National Scenic Riverways (ONSR) and areas of geologic map coverage. Most of the area is underlain by karstified lower Paleozoic dolomite; isolated knobs of Proterozoic volcanic rocks crop out in area encircled by dashed line. Gray shaded rectangles indicate locations of individual 1:24,000-scale geologic quadrangle maps published by the U.S. Geological Survey and the Missouri Geological Survey, 1997–2015. Irregular darker area with gray dashed outline delineates a 1:24,000-scale geologic map compilation covering the ONSR (Weary and others, 2016). The entire map area falls within the boundaries of 1:100,000-scale regional mapping (Weary and others, 2014).

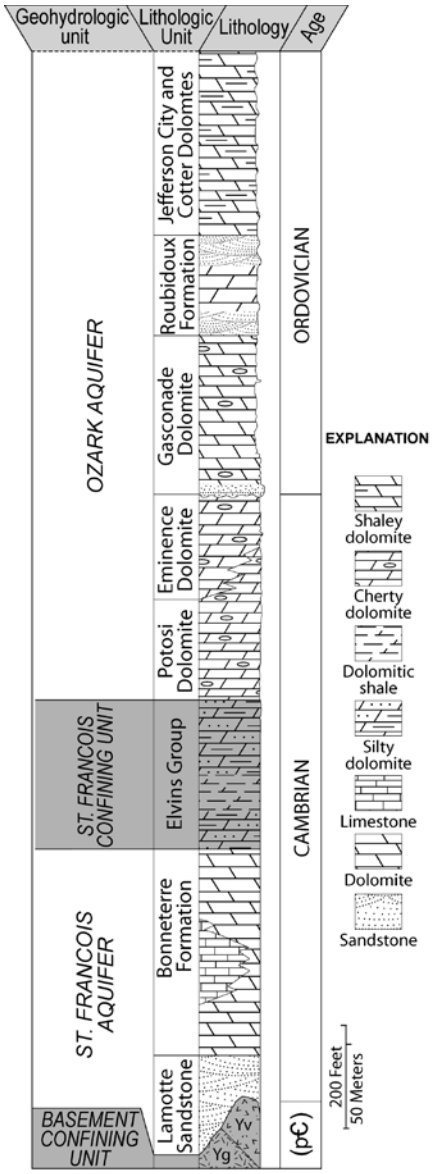

Figure 3. Idealized stratigraphic column showing geohydrologic and lithostratigraphic units in the Ozark National Scenic Riverways (ONSR) area, which include outcropping Paleozoic formations, buried Paleozoic formations, and Proterozoic rocks. Adapted from Lowell and others (2010). p€, rocks of Meso- and Neoproterozoic ages: Yg, Proterozoic granite, Yv, Proterozoic volcanic igneous rocks. Proterozoic igneous rocks are locally exposed adjacent to overlying units upsection into the Gasconade Dolomite. The Elvins Group, which occurs only in the subsurface in the ONSR area, consists of the Davis Shale and overlying Derby-Doerun Dolomite.

Bounding the top of the St. Francois aquifer is the St. Francois confining unit, which consists of the Cambrian Elvins Group, the Davis Formation, and the overlying Derby-Doerun Dolomite (usage of Missouri Geological Survey, 1979). These stratigraphic units contain beds of shale, shaley mudstone, and thinly bedded, dense, fine-grained dolomite, which analyses have shown are nonporous (primary porosity) and very impermeable (Kleeschulte and Seeger, 2000, 2001). No studies have been undertaken to evaluate the secondary porosity, potentially the result of faults and jointing, of these rocks.

From the top of the St. Francois confining unit to the topographic surface is the Ozark aquifer (Imes, 1990a), which in the study area, comprises in ascending order, the Potosi, Eminence, and Gasconade Dolomites, the Roubidoux Formation, and the Jefferson City Dolomite. The near-surface parts of the Ozark aquifer are generally unconfined and serve as the principal domestic water sources for most of southeastern Missouri, except in the St. Francois Mountains, where near-surface stratigraphic units of the St. Francois aquifer are commonly tapped. All of the springs in the ONSR area discharge from the Ozark aquifer.

Geologic Context for the Large Springs of the ONSR

The southern Ozarks are a landscape that has been exposed to surface erosion and development of subterranean drainage systems since the late Paleozoic. Over that time, the development of solution conduits and flow paths has been affected by the physical and chemical properties of the bedrock. These effects are recognizable in the observed spatial and stratigraphic relations among the rocks, caves, groundwater conduits, and springs in the ONSR and surrounding area.

Development of Enhanced Permeability in the Ozark Aquifer

Most of the lower Paleozoic rocks underlying the ONSR region were originally deposited as limestone under peritidal conditions in a shallow tropical inland sea. Deposition of marine sediments in the area probably occurred sporadically into the Early Pennsylvanian Period. Beginning in the Pennsylvanian and continuing to the present, the rocks of the Ozark Plateaus have been subject to subaerial weathering and erosion as well as diagenetic and hypogenic processes in the subsurface. Much of the alteration of the primary limestones to dolomite in the study area occurred during northward migration of hot brines from the Ouachita Mountains to the south (Leach, 1994). There was likely a cycle of transverse, hypogenic speleogensis associated with this fluid migration, and the horizontal permeability of these rocks was enhanced by mineralogic changes facilitating later development of solution conduits (Klimchouk, 2007). Kaufman and Crews (2013) have indicated that there is an increase in porosity and horizontal permeability that is stratigraphically concentrated near the tops of shallowing upward carbonate depositional sequences in the Ozarks due to a combination of stromatolitic fabrics, early diagenetic effects, and episodes of silicification and dolomitization. Faulting and jointing associated with the late Paleozoic ancestral Rocky Mountain-Ouachita-Alleghenian orogenies enhanced secondary vertical porosity (see Cox (2009) and Hudson (2000) for analyses of late Paleozoic faulting in the Ozark region).

The Large Scale Structural Setting and Aquifer Geometry Are Conducive to Formation of Long Flow Paths and Large Integrated Systems

Strata in the Salem Plateau are relatively flat-lying, with a very gentle dip toward the east and southeast with beds typically dipping less than 1 degree. For example, except for a relatively short stretch where the Current River flows over a structural high exposing the Potosi Dolomite and protruding Proterozoic rhyolites (fig. 2), the river flows down the regional dip surface with the channel of the river remaining in about the same stratigraphic position in the Eminence Dolomite. This reach, almost the entire distance of the length of the ONSR, is about 85 mi in a straight line from just below the headwaters at Montauk Springs toward the southeast to a point just downstream of Big Spring. The elevation loss for the top of the Eminence Dolomite between these points is about 440 feet (ft), indicating an average gradient of both the river and the strata of just over 5 ft per mile. This gentle incline, imposed on the sequence of laterally continuous strata, provides space for development of long strata-bound flow paths from recharge areas to groundwater outlets at the springs (fig. 4). Some recharge points proven by dye traces are at least 38 mi (61 km) away from the springs (Imes and Frederick, 2002). The maximum potential straight-line flow route is controlled by the length and width of the regional bedrock dip surface. Although there are many examples of interbasinal flow, and possibly underflow, deep incisions of the major streams segment the upper part of the aquifer and usually intercept flow routes that might otherwise continue farther down dip (fig. 4).

Laterally Continuous Siliceous Strata Are Aquitards That Vertically Segregate the Ozark Aquifer Into Vertically Stacked Compartments

Although the rocks that compose the Ozark aquifer are chiefly well-bedded dolomites, the sequence is punctuated by thin but laterally continuous siliceous strata that have significant effects on groundwater flow and speleogenesis in the ONSR area (fig. 5). As noted in earlier studies, most of the cave passages in the area are concentrated in dolomites beneath these relatively insoluble beds (Orndorff and others, 2006; Lowell and others, 2010; Kaufman and Crews, 2013). These siliceous horizons, from stratigraphically lowest to highest, are (1) bedded chert in the uppermost Potosi Dolomite, (2) an unnamed sandstone package in the upper part of the Eminence Dolomite, (3) the basal Gunter

Sandstone Member of the Gasconade Dolomite, (4) a *Cryptozoon* chert horizon at the base of the upper part of the Gasconade Dolomite, and (5) basal quartz sandstone of the Roubidoux Formation.

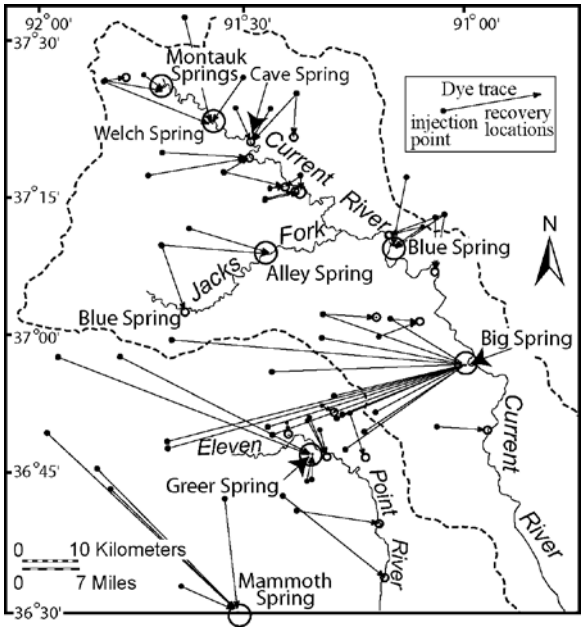

Figure 4. Selected dye traces to major springs in the Current River watershed area in southern Missouri (Aley and Aley, 1987; Imes and Kleeschulte, 1995). Large circles are 1st magnitude springs, smaller circles are other spring locations. Dashed line delineates the Current River surface basin. Note evidence of interbasin underflow and crossing flow paths. See Mugel and others (2009) and Duley and others (2015) for additional traces and more detailed discussion. Mammoth Spring, the largest spring in Arkansas, is located just south of the stateline.

A 1- to 3-ft-thick bed of porous chert near the top of the Potosi Dolomite was reported in the Eminence quadrangle (Orndorff and others, 1999) and in the Stegall Mountain quadrangle (Harrison and others, 2002). McDowell and Harrison (2000) reported a 3- to 6-ft-thick chert bed just above the Potosi–Eminence contact in the adjoining Powder Mill Ferry quadrangle. Although not noted in other geologic mapping in the study area, this siliceous interval is probably persistent across much of the study area and possibly confines the proximal part of the aquifer compartment feeding Blue (Current River), Cave, and Welch Springs (fig. 4). There may be other siliceous intervals lower in the Potosi that influence groundwater flow, but their existence is conjectural due to lack of exposure of the unit.

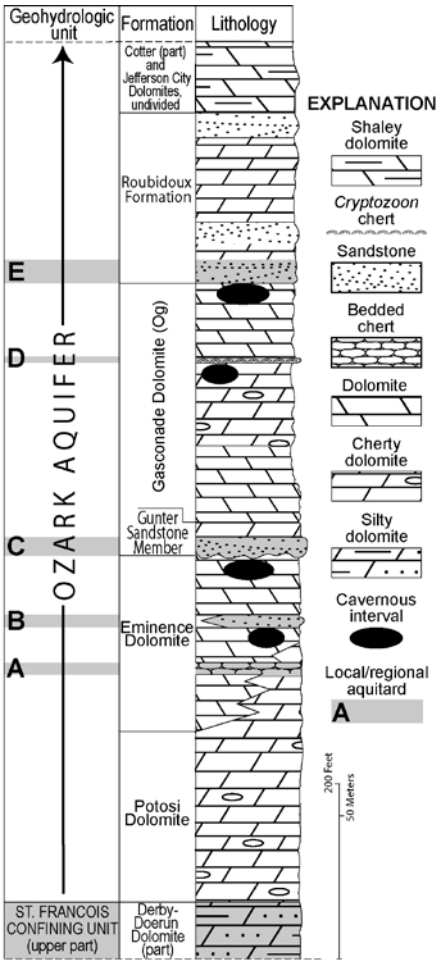

Figure 5. Idealized stratigraphic column showing geohydrologic and lithostratigraphic units composing the Ozark aquifer in the Ozark National Scenic Riverways (ONSR) area. Adapted from Lowell and others (2010). In the study area, laterally extensive thin siliceous strata punctuate the carbonate sequence and function as aquitards. **A**, bedded cherts near the Potosi/Eminence Dolomite contact, **B**, a quartz sandstone and orthoquartzite-rich interval in the Eminence Dolomite, **C,** quartz sandstone and orthoquartzite beds in the Gunter Sandstone Member of the Gasconade Dolomite, **D,** bedded *Cryptozoon* chert interval in the upper part of the Gasconade Dolomite, **E,** quartz sandstone beds in the basal part of the Roubidoux Formation.

A sandstone-rich interval in the Eminence Dolomite about 80–90 ft below the top of the formation is apparently horizontally continuous in the southeastern part of the study area and crops out in the Big Spring (Weary and McDowell, 2006), Van Buren South (Weary and Schindler, 2004), Van Buren North (Weary and Weems, 2004), and Stegall Mountain (Harrison and others, 2002) 7.5-minute quadrangles. Numerous caves are concentrated just below this horizon and although supplied by water from the underlying Potosi Dolomite, Big Spring issues from a conduit confined just beneath it as well (Weary and McDowell, 2006).

Many caves and springs occur in massive and thick-bedded dolomites of the uppermost Eminence Dolomite, beneath the basal Gunter Sandstone Member of the overlying Gasconade Dolomite. The Gunter Sandstone in the ONSR area comprises beds of relatively impermeable silica-cemented quartz sandstone and orthoquartzite. In other parts of the Ozark aquifer, outside of the ONSR area, the Gunter is not quartz cemented and is permeable, and regarded as an aquifer unit (Imes and Emmett, 1994; Elfrink, 2007). Alley and Montauk Springs both rise from confinement beneath the Gunter Sandstone. The main passage of Round Spring Cavern, the ONSR's tourist cave, is developed primarily just below the Gunter Sandstone and makes an almost perfect dry analogue for the subaqueous cave feeding Alley Spring (Lowell and others, 2010).

Numerous caves and springs occur about 100 ft below the top of the Gasconade Dolomite below a well-documented and laterally extensive bedded *Cryptozoon* chert interval (Lowell and others, 2010). None of the springs located at this horizon in the ONSR are very large, although 1st magnitude Greer Spring, near the Eleven Point River to the south of the ONSR, may rise from this level (fig. 4). Within the ONSR, 3rd magnitude Blue Spring (Jacks Fork) probably rises from confinement under this chert horizon.

Many caves and small springs in the ONSR area are located in non-cherty dolomite of the uppermost Gasconade Dolomite, just below the basal Roubidoux Formation quartz sandstones. Most of these occur in the upper reaches of Jacks Fork where the Gasconade is exposed in bluffs below Roubidoux cap rocks. Branson Cave and Jam Up Cave are two well-known examples (Weary and Orndorff, 2012; Weary and others, 2013). Strata above the basal Roubidoux Formation sandstones in the ONSR area are usually unsaturated and tend to host numerous small ephemeral, vadose springs that are perched on laterally discontinuous sandstone or chert beds.

Springs Are Localized by Intersections of Downcut River Valleys and Bedrock Structural Highs

Structural contours, commonly drawn on the elevation data for the base of the Roubidoux Formation, are available for most of the 7.5-minute geologic quadrangle maps that cover the ONSR. Undulations in this surface are interpreted to reflect tectonic folding and as such, this surface can be used as a proxy for elevation changes in parallel stratal surfaces, including the confining units below it (Lowell and others, 2010).

Most of the major springs in the ONSR area are located in the deep river valleys (figs. 2 and 4) and occur on the flanks of structural highs in the bedrock. Montauk Springs (a single conduit spring that has three separate outlets in the valley-fill alluvium) for example, are located where downcutting by Pigeon Creek and its continuation, the upper Current River, impinges on the flank of a structural high (fig. 6). This juxtaposition allows the ground surface to reach within a few tens of feet of the base of the subsurface Gunter Sandstone Member confining unit (Weary, 2015).

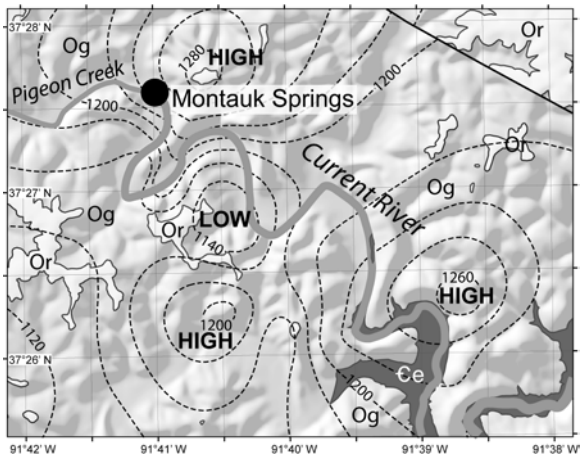

Figure 6. Map showing the location of Montauk Springs and their relation to bedrock geology. Map units in stratigraphic order, are Ce, Eminence Dolomite, Og, Gasconade Dolomite, including basal Gunter Sandstone Member, Or, Roubidoux Formation. Dashed lines are structural contours indicating the elevation of the base of the Roubidoux Formation, 20-foot contour interval. Geologic elements from Weary (2015).

Similar coincidences of springs adjacent to structural highs occur at all the first magnitude springs in the ONSR (Alley, Blue, Big, and Welch; see fig. 2 for locations). Hudson and others (2011) also noted that springs in the Ordovician Everton Formation in the Buffalo River, Arkansas area, about 120 mi (190 km) to the southwest of the ONSR, are localized over structural highs.

Discussion

The development of large artesian springs and their contributing groundwater basins in the Ozark aquifer of the Salem Plateau results from a long geologic history that has allowed development of secondary and tertiary permeability and integration of quick-flow routes across large recharge areas; for instance, the average quick-flow rate of dye traces to Big Spring ranges from slightly less than 1 to 3 mi/day (Imes and others, 2007). The potential base-flow magnitude of the springs is determined by the storage volume in the aquifer within the contributing area for that spring. The volume of storage is influenced by the topography and number of aquifer compartments, separated by aquitards that are vertically stacked upgradient of the springs. The largest springs tend to have large recharge areas and discharge from lower in the stratigraphic section. The geometry of the Salem Plateau, underlain by subhorizontal, continuous strata lends itself to development of large spring basins.

Large springs in the ONSR are located where downcutting streams erode into structural highs and lower the ground surface near the top of the locally confined part of the aquifer. At these places, unloading of downward hydrostatic pressure by erosion and surface drainage of the overlying rocks created strong upward pressure gradients. Over time, flow through fractures in the siliceous confining units has focused solution of the carbonate rocks above and below the aquitard. Ultimately, after solution of the adjoining dolomites, the siliceous units fail mechanically and collapse, opening the conduits to the surface and allowing concomitant increases in flow volume and velocity, further accelerating solution in the conduits proximal to the new large springs. Many of the large springs in the study area can be described as vauclusian, with large, single-conduit rise tubes that are steeply inclined to near-vertical (Vineyard and Feder, 1974). This geometry is the result of water rising steeply, under artesian pressure from the breach in the underlying local confining stratum. On its path to the surface, the water flow initially follows subvertical joints in the bedrock. Because most joints in the area are not throughgoing (continuous through more than a single bed), upward flow moves in a stepwise fashion, resulting in a slope determined by the thickness of the overlying rock beds and their joint spacing, as first described by Davis (1930, p. 549).

This process of spring creation and cave enlargement has been repeated over time as the landscape is lowered by erosion, focused in the large river valleys. Higher aquifer compartments are eventually drained by the large springs and by dissection of their upgradient contributing areas, leaving fossil conduits (dry caves) in the uplands. The spring rise tubes are almost never preserved as the valleys are deepened and enlarged over time by erosion. New springs open as deeper confined compartments in the aquifer are breached, often in the vicinity of, and in a similar structural setting as, the previous spring (fig. 7). The fact that geographically clustered caves are known from different stratigraphic levels in several places in the ONSR supports this hypothesis. Some of the elements of this model are similar to those proposed by Elfrink (2007) for speleogenesis in other parts of the Ozarks.

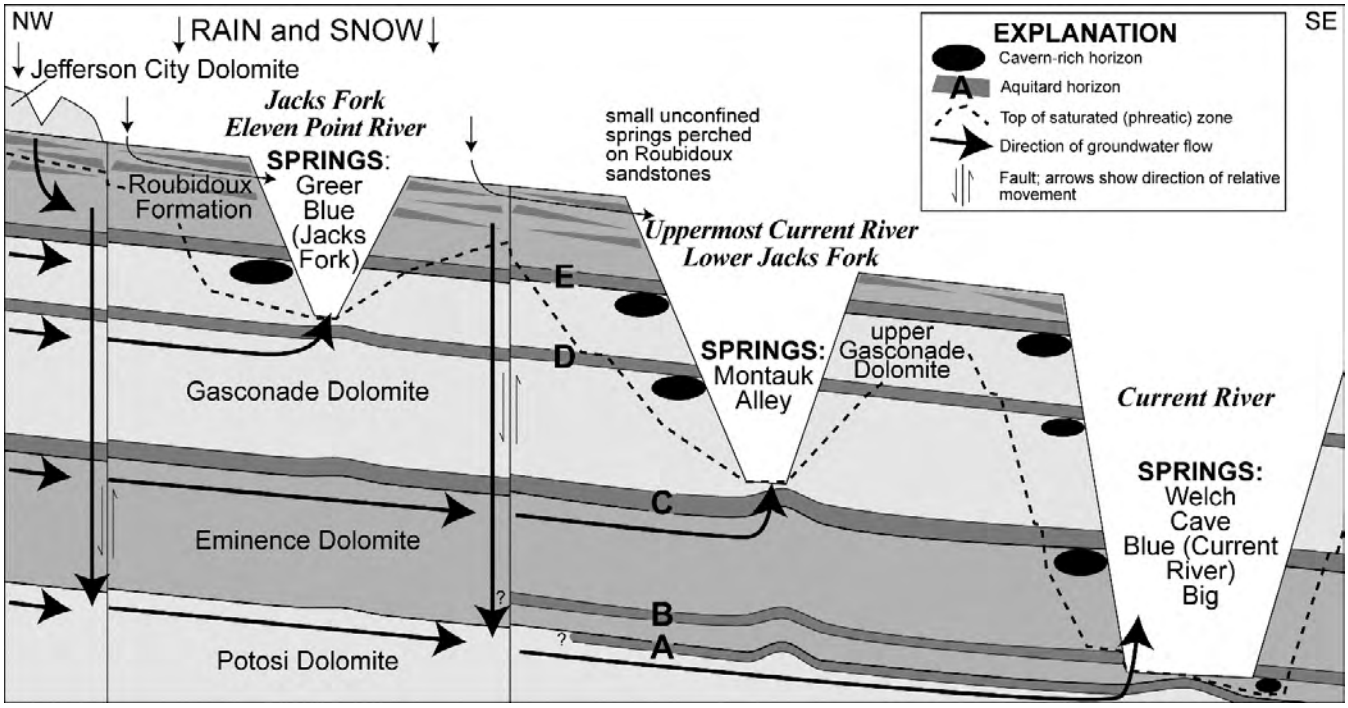

Figure 7. Generalized conceptual cross section showing spatial relations between groundwater flow to springs, cave locations, and geohydrologic units in the Ozark aquifer in the ONSR area of the Ozarks. Note that there is some geographic distortion to fit this simplistic model (see figure 2 for actual spring locations). Alphabetical labels on aquitard units correspond to those used on figure 5. Previous spring conduits are left as dry caves in the remnants of the upland stratigraphy as the rivers sequentially cut down and drain the upper artesian compartments. Geohydrologic effects of Proterozoic igneous rock knobs in the mid-Current River area (fig. 2) left out for simplicity.

There are several implications that arise from this model. The geographic extent of the individual vertically stacked aquifer compartments may not be coincident, resulting in groundwater spring basin boundaries that are not vertical but rather interfingering. These overlapping relations allow "crossing" dye traces, where a tracer input at a single location may tend to flow to one spring via the shallower compartments, but dye leakage into deeper compartments may flow to a different spring. The divergent traces from a single input to Blue Spring (Jacks Fork) and Alley Spring are a good example of this phenomenon (fig. 4). In addition, it can be assumed that the aquitard units that confine groundwater in upgradient areas proximal to the springs also seal off downward surface-water input into that part of

the aquifer. Therefore, an area exists for some distance upgradient of each spring and downgradient of the closest dye injection point that is effectively not a part of that springs' recharge area and should not be drawn as part of the recharge area for that spring in mapping exercises. This refinement alters the traditional shape of mapped recharge areas and affects the application of spring discharge and recharge area estimates.

Speleogenesis in the ONSR area probably began in the late Paleozoic with the development of a hypogenic intrastratal karst (Klimchouk, 2007), followed by later development of quick-flow routes to the large springs and associated conduit-forming and enlarging solution of the dolomite. Caves in the ONSR area tend to be stratabound, simple branchwork or single-conduit phreatic tubes and few are long. This indicates that processes controlling solutional enlargement of at least some of the caves are related to proximity to the springs they are feeding and that the age of cave enlargement is directly related to the history of Cenozoic dissection of the Salem Plateau.

References Cited

Aley, T.J., and Aley, Catherine, 1987, Groundwater study, Ozark National Scenic Riverways: National Park Service contract report CX 6000-4-0083, Protem, Mo., Ozark Underground Laboratory, 222 p.

Cox, R.T., 2009, Ouachita, Appalachian, and ancestral Rockies deformations recorded in mesoscale structures on the foreland Ozark plateaus: Tectonophysics, v. 474, no. 3-4, p. 674–683.

Davis, W.M. 1930, Origin of limestone caverns: Geological Society of America Bulletin, v. 41, no. 3, p. 475–628.

Duley, J.W., Boswell, C., and Prewett, J., 2015, Recharge area of large springs in the Ozarks, *in* Doctor, Daniel H., Land, Lewis, and Stephenson J. Brad, eds., Proceedings of the 14th Multidisciplinary Conference on Sinkholes and the Engineering and Environmental Impacts of Karst: National Cave and Karst Research Institute Symposium 5, October 5–9, 2015, Rochester, Minnesota, p. 85–91.

Elfrink, N., 2007, Transverse speleogenesis in the Ozarks, *in* 2007 National Cave and Karst Management Symposium Proceedings: Holiday Inn SW & Viking Conference Center, St. Louis, Missouri (USA), October 8–12, 2007, 13 p.

Gann, E.E., Harvey, E.J., and Miller, D.E., 1976, Water resources of south-central Missouri: U.S. Geological Survey Hydrologic Investigations Atlas HA–550, 4 sheets.

Harrison, R.W., Orndorff, R.C., and Weary, D.J., 2002, Geology of the Stegall Mountain 7.5-minute quadrangle, Shannon and Carter Counties, south-central Missouri: U.S. Geological Survey Geologic Investigations Series Map I–2767, scale 1:24,000.

Hudson, M.R., 2000, Coordinated strike-slip and normal faulting in the southern Ozark Dome of northern Arkansas—Deformation in a late Paleozoic foreland: Geology, v. 28, no. 6, p. 511–514.

Hudson, M.R., Turner, K.J. and Bitting, C., 2011, Geology and karst landscapes of the Buffalo National River area, northern Arkansas, *in* Kuniansky, E.L., ed., U.S. Geological Survey Karst Interest Group Proceedings, Fayetteville, Arkansas, April 26–29, 2011: U.S. Geological Survey Scientific Investigations Report 2011–5031, p. 191–212.

Imes, J.L., 1989, Major geohydrologic units in and adjacent to the Ozark Plateaus province, Missouri, Arkansas, Kansas, and Oklahoma—Basement confining unit: U.S. Geological Survey Hydrologic Investigations Atlas HA–711–B, 1 sheet, scale 1:750,000.

Imes, J.L., 1990a, Major geohydrologic units in and adjacent to the Ozark Plateaus province, Missouri, Arkansas, Kansas, and Oklahoma—Ozark aquifer: U.S. Geological Survey Hydrologic Investigations Atlas HA–711–E, 3 sheets, scale 1:750,000.

Imes, J.L., 1990b, Major geohydrologic units in and adjacent to the Ozark Plateaus province, Missouri, Arkansas, Kansas, and Oklahoma—St. Francois aquifer: U.S. Geological Survey Hydrologic Investigations Atlas HA–711–C, 2 sheets, scale 1:750,000.

Imes, J.L., and Emmett, L.F., 1994, Geohydrology of the Ozark Plateaus aquifer system in parts of Missouri, Arkansas, Oklahoma, and Kansas: U.S. Geological Survey Professional Paper 1414–D, 127 p.

Imes, J.L., and Fredrick, B.S., 2002, Using dye-tracing and chemical analyses to determine effects of a wastewater discharge to Jam Up Creek on water quality of Big Spring, southeastern Missouri, 2001: U.S. Geological Survey Fact Sheet 103–02, 6 p.

Imes, J.L., and Kleeschulte, M.J., 1995, Seasonal ground-water level changes (1990–93) and flow patterns in the Fristoe Unit of the Mark Twain National Forest, southern Missouri: U.S. Geological Survey Water-Resources Investigations Report 95–4096, 1 sheet.

Imes, J.L., Plummer, L.N., Kleeschulte, M.J., and Schumacher, J.G., 2007, Recharge area, base-flow and quick-flow discharge rates and ages, and general water quality of Big Spring in Carter County, Missouri, 2000–04: U.S. Geological Survey Scientific Investigations Report 2007–5049, 80 p.

Imes, J.L., and Smith, B.J., 1990, Areal extent, stratigraphic relation, and geohydrologic properties of regional geohydrologic units in southern Missouri: U.S. Geological Survey Hydrologic Investigations Atlas HA–711–I, 3 sheets, scale 1:750,000 and 1:1,000,000.

Kaufmann, J.E., and Crews, J., 2013, Stratigraphic control on conduit development in the Ozark karst, Missouri, USA, *in* Fong, D.W., Culver, D.C., Veni, G., and Engel, S.A. eds., Carbon and boundaries in karst: Karst Waters Institute Special Publication 17, p. 24, http://karstwaters.org/wp-content/uploads/2015/04/SP17_CarbonBoundaries.pdf.

Keller, A.E., 2000, Hydrologic and dye trace study of Welch Spring, Missouri: Rolla, University of Missouri–Rolla, M.S. thesis, 218 p.

Kleeschulte, M.J., and Seeger, C.M., 2000, Depositional environment, stratigraphy and vertical hydraulic conductivity of the St. Francois confining unit in the Fristoe Unit of the Mark Twain National Forest, Missouri: U.S. Geological Survey Water-Resources Investigations Report 00–4037, 65 p.

Kleeschulte, M.J., and Seeger, C.M., 2001, Stratigraphy and vertical hydraulic conductivity of the St. Francois confining unit in townships 25–27 N. and ranges 01–02 W., southeastern Missouri: U.S. Geological Survey Water-Resources Investigations Report 2001–4270, 64 p.

Klimchouk, A.B., 2007, Hypogene speleogenesis—Hydrogeological and morphogenetic perspective: National Cave and Karst Research Institute Special Paper No. 1, 106 p.

Leach, D.L., 1994, Genesis of the Ozark Mississippi Valley-type metallogenic province, Missouri, Arkansas, Kansas, and Oklahoma, USA, 1994: Society for Geology Applied to Mineral Deposits Special Publication 10, p. 104–138.

Lowell, G.R., Harrison, R.W., Weary, D.J., Orndorff, R.C., Repetski, J.E., and Pierce, H.A., 2010, Rift-related volcanism and karst geohydrology of the southern Ozark Dome, *in* Evans, K.R., and Aber, J.S., eds., From Precambrian rift volcanoes to the Mississippian shelf margin—Geological field excursions in the Ozark Mountains: Geological Society of America Field Guide 17, p. 99–158.

McDowell, R.C., and Harrison, R.W., 2000, Geologic map of the Powder Mill Ferry quadrangle, Shannon and Reynolds Counties, Missouri: U.S. Geological Survey Geologic Investigations Series Map I–2722, scale 1:24,000.

Missouri Department of Natural Resources, 2002, Springs, *in* Missouri Environmental Geology Atlas (MEGA): Geological Survey and Resource Assessment Division, Rolla, Mo., [CD-ROM].

Missouri Geological Survey, 1979, Geologic map of Missouri: Missouri Division of Geology and Land Survey, scale 1:500,000.

Mugel, D.N., Richards, J.M., and Schumacher, J.G., 2009, Geohydrologic investigations and landscape characteristics of areas contributing water to springs, the Current River, and Jacks Fork, Ozark National Scenic Riverways, Missouri: U.S. Geological Survey Scientific Investigations Report 2009–5138, 80 p.

Orndorff, R.C., Harrison, R.W., and Weary, D.J., 1999, Geologic map of the Eminence quadrangle, Shannon County, Missouri: U.S. Geological Survey Geologic Investigations Series Map I–2653, scale 1:24,000.

Orndorff, R.C., Weary, D.J., and Harrison, R.W., 2006, The role of sandstone in the development of an Ozark karst system, south-central Missouri, *in* Harmon, R.S., and Wicks, C., eds., Perspectives on karst geomorphology, hydrology, and geochemistry— Tribute volume to Derek C. Ford and William B. White: Geological Society of America Special Paper 404, p. 31–38.

Thornberry-Ehrlich, T.L., 2016, Ozark National Scenic Riverways Geologic Resources Inventory Report: National Park Service, Natural Resource Report NPS/NRSS/GRD/NRR—2016/1307, https://www.nature.nps.gov/geology/inventory/publications/reports/ozar_gri_rpt_view.pdf.

Vineyard, J.D., and Feder, G.L., 1974, Springs of Missouri (1982 ed.): Missouri Department of Natural Resources, Division of Geology and Land Survey Water Resources Report 29, 212 p.

Weary, D.J., 2015, Geologic map of the Montauk quadrangle, Dent, Texas, and Shannon Counties, Missouri: U.S. Geological Survey Scientific Investigations Map 3320, 1 sheet, scale 1:24,000.

Weary, D.J., Harrison, R.W., Orndorff, R.C., Weems, R.E., Schindler, J.S., Repetski, J.E., and Pierce, H.A., 2014, Bedrock geologic map of the Spring Valley, West Plains, and parts of the Piedmont and Poplar Bluff 30′ x 60′ quadrangles, Missouri, including the upper Current River and Eleven Point River drainage basins: U.S. Geological Survey Scientific Investigations Map 3280, scale 1:100,000.

Weary, D.J., and McDowell, R.C., 2006, Geologic map of the Big Spring quadrangle, Carter County, Missouri: U.S. Geological Survey Scientific Investigations Map 2804, scale 1:24,000.

Weary, D.J., and Orndorff, R.C., 2012, Geologic map of the Alley Spring quadrangle, Shannon County, Missouri: U.S. Geological Survey Scientific Investigations Map 3161, scale 1:24,000.

Weary, D.J., Orndorff, R.C., Harrison, R.W., and Weems, R.E., 2016, Digital geologic map data for the Ozark National Scenic Riverways and adjacent areas along the Current River and Jacks Fork, Missouri: U.S. Geological Survey data release, http://dx.doi.org/10.5066/F7CJ8BKB.

Weary, D.J., Orndorff, R.C., and Repetski, J.E., 2013, Geologic map of the Jam Up Cave and Pine Crest quadrangles, Shannon, Texas, and Howell Counties, Missouri: U.S. Geological Survey Scientific Investigations Map 3248, scale 1:24,000.

Weary, D.J., and Schindler, J.S., 2004, Geologic map of the Van Buren South quadrangle, Carter County, Missouri: U.S. Geological Survey Geologic Investigations Series Map 2803, scale 1:24,000.

Weary, D.J., and Weems, R.E., 2004, Geologic map of the Van Buren North quadrangle, Carter, Reynolds, and Shannon Counties, Missouri: U.S. Geological Survey Geologic Investigations Series Map 2802, scale 1:24,000.

Westerman, D.A., Gillip, J.A., Richards, J.M., Hays, P.D., and Clark, B.R., 2016, Altitudes and thicknesses of hydrogeologic units of the Ozark Plateaus aquifer system in Arkansas, Kansas, Missouri, and Oklahoma: U.S. Geological Survey Scientific Investigations Report 2016–5130, 32 p.

Utilizing Fluorescent Dyes to Identify Meaningful Water-Quality Sampling Locations and Enhance Understanding of Groundwater Flow Near a Hog CAFO on Mantled Karst, Buffalo National River, Southern Ozarks

By Van Brahana[1], Carol Bitting[2], Katerina Kosič-Ficco[3], Teresa Turk[4], John Murdoch[5], Brian Thompson[6], and Ray Quick[7]

[1]Professor Emeritus, Department of Geosciences, 20 Gearhart Hall, University of Arkansas, Fayetteville, AR 72701

[2]HC 73, Box 182 A, Marble Falls, AR 72648

[3]Faculty of Graduate Studies, Post Graduate Program of Karstology, University of Nova Gorica, Slovenia

[4]National Oceanographic and Atmospheric Administration, Research Fisheries Biologist (Retired), Seattle, WA 98115

[5]University of Arkansas, Department of Biologic and Agricultural Engineering (Retired), Fayetteville, AR 72701

[6]Tyson Foods, Inc. (Retired), Fayetteville, AR 72701

[7]Adjunct Professor, Department of Geosciences, 216 Gearhart Hall, University of Arkansas, Fayetteville, AR 72701

Abstract

The karst area of the Springfield Plateau in the southern Ozarks of north-central Arkansas is subject to numerous and varied land-use practices that impact water quality. In this region of the U.S., animal production and human activities have concentrated wastes within environmentally sensitive karst hydrogeologic settings. Groundwater flow in this region includes aquifers covered by a thin, rocky soil, and a variable thickness of regolith. The karst groundwater system is underlain by thin chert and limestone layers that have been fractured by slight uplift. The carbonate-rock aquifer intervals have been dissolved to form an open network of enlarged fractures, bedding-plane voids, conduits, sinkholes, swallets, sinking streams, caves, and springs. Flow in these aquifers is typically rapid, flow directions are difficult to predict, and interaction between surface water and groundwater is extensive, with little opportunity for contaminant attenuation. Herein, we show dispersive groundwater flow from multiple injection sites where groundwater basin boundaries can vary with fluctuations in groundwater level. Although the geologic framework appears simple, the results of tracing with fluorescent dyes from April to October 2014 indicates that a meaningful conceptual model is indeed complex, yet essential to use when sampling for water quality and fully understanding the movement of groundwater and its close interaction with surface streams and recharge.

Introduction

The landscape of the Springfield Plateau in the southern Ozarks (fig. 1) is a mantled karst, with few apparent topographic features such as sinkholes on the land surface, yet the region is underlain by a system of well-developed fast-flow pathways and voids that pass water and entrained contaminants downgradient to resurgent springs and streams quickly and with little attenuation of pollutants. Karst scientists have long been aware and are fully knowledgeable about this and related areas of mantled karst, covered by insoluble debris weathered from the original carbonate bedrock (White, 1988; Quinlan, 1989; Ford and Williams, 2007).

Unfortunately, consultants, some landowners, and water managers unfamiliar with mantled karst have difficulty in recognizing the vulnerability of groundwater in these settings and the close interaction with surface water in such areas (Kosič and others, 2016; Murdoch and others, 2016). This is the case of Big Creek basin, the second largest tributary of the Buffalo National River. Big Creek basin has a total area of about 115 square kilometers (km^2) (Center for Advanced Spatial Technology, 2006), within which permission was recently granted for an industrial hog factory housing 6,500 swine in a concentrated animal feeding operation (CAFO) (U.S. Department of Agriculture Farm Service Agency and U.S. Small Business Agency, 2015). Waste from this CAFO was permitted to be spread from lagoons onto 2.5 km^2 of mantled karst in 2012 using documents that did not discuss groundwater or karst (Pesta, 2012).

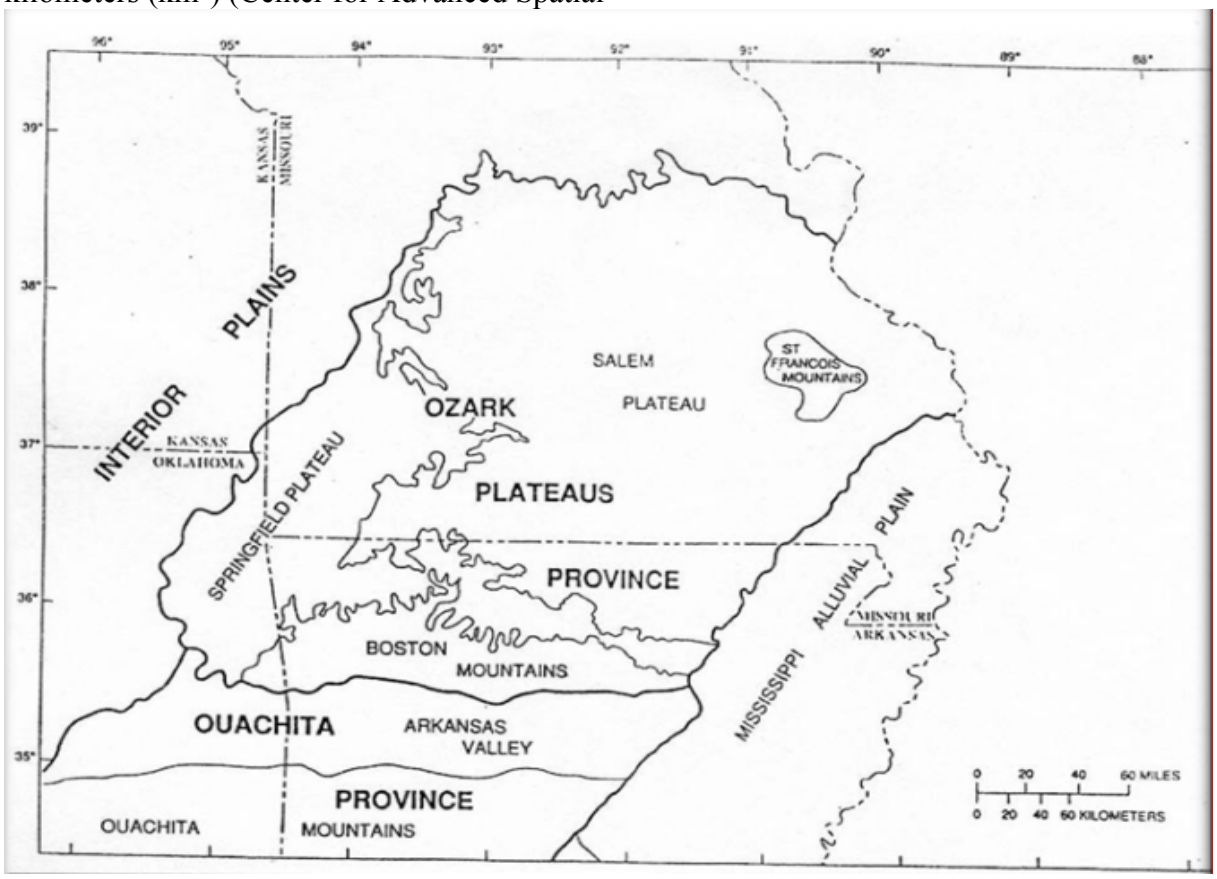

Figure 1. General physiographic regions of the Ozark Plateaus, including the Springfield Plateau, an alternating thinly bedded chert and limestone rock interval in northern Arkansas that develops mantled karst. The approximate study area is shown by the ellipse. From Imes and Emmett (1994).

Purpose and Scope

There are two objectives for conducting this research and writing this paper. The first is to present the results of five tracing events using three separate fluorescent dyes in Big Creek in the vicinity of the CAFO and its waste-spreading fields, focusing on point-to-point groundwater flow connections and time of travel. The long duration of the traces was intended to show natural variation of the groundwater flow system in the karst for varying recharge, and establish that the rates of flow do indeed characterize the fast-flow conditions of conduit transport. The second objective is to provide an explanation of why the groundwater moves in the manner that it

does, and to do so in terminology that will enlighten and educate lay people and other stakeholders, especially those who have the responsibility of promulgating regulations based on the established karst science. Documenting these karst attributes in peer-reviewed publications represents an important means to further educate all stakeholders.

Study Area

The study area was chosen to include the potential flow boundaries of the groundwater system that are known from previous karst studies in the Ozarks (Aley, 1988; Mott and others, 2000), which include an area of natural groundwater flow larger than the site-specific location of the CAFO and its spreading fields (fig. 2). The spreading fields extend from Dry Creek to Big Creek, and the confluence of these streams south along Big Creek to slightly north of the CAFO.

The reason for extending the study area boundaries in dye-tracing studies is to evaluate if surface-drainage basin boundaries and groundwater-basin boundaries are coincident or not. It is not uncommon for these boundaries to be different in karst (Quinlan, 1989; Imes and Emmett, 1994; Hobza and others, 2005). In addition to placing dye receptors on Big Creek, its unnamed tributaries, Buffalo National River, Little Buffalo River, Left Fork of Big Creek, Dry Creek, Rock Creek, Cave Creek, and the springs that flow into these surface drainages, wells tapping the Boone Formation proximal to the CAFO also were monitored.

Hydrogeologic and Karst Characterization of the Study Area

Big Creek is one of the largest tributaries to the Buffalo National River, encompassing slightly more than 10 percent of the total drainage of the entire Buffalo River basin (Scott and Hofer, 1995; Mott and Laurans, 2004). Topographically, tributaries head in uplands on terrigenous sediments of Pennsylvanian age on the Boston Mountains Plateau (fig. 1) and flow generally toward the north and east with relatively steep gradients, typically in the range of 3 to 5 meters (m) per kilometer (km).

The stratigraphic unit of greatest concern to this study is the Boone Formation (Braden and Ausbrooks, 2003), an impure limestone interval (fig. 3) that contains as much as 70 percent chert (Liner, 1978). The chert is hypothesized to have formed from atmospheric deposition of volcanic ash that was periodically ejected and carried by prevailing winds. In northern Arkansas, the setting was a shallow carbonate shelf (Brahana, 2014). The carbonate factory operating in this shallow marine setting at that time was hypothesized to have been overwhelmed by massive amounts of silica, which in the study area formed thin but fairly continuous layers of silica gel that typically ranged in thickness from 5 to 30 centimeters (cm). During periods of volcanic quiescence, carbonate sediments were deposited onto the thin layers of silica gel, and with successive sedimentation from these two sources, a sequence of approximately 80 m of these carbonate/silica couplets were laid down, compressed, and diagenetically altered and indurated into limestone and chert of the middle portion of the Boone Formation (Brahana, 2014).

Structural uplift resulting from compressive closure of the Ouachita orogeny created a foreland bulge. This uplift acted concurrently with the volcanism, causing jointing, faulting, and tilting that allowed and facilitated pathways of weathering and karstification (fig. 4) of the carbonate intervals of the middle Boone Formation.

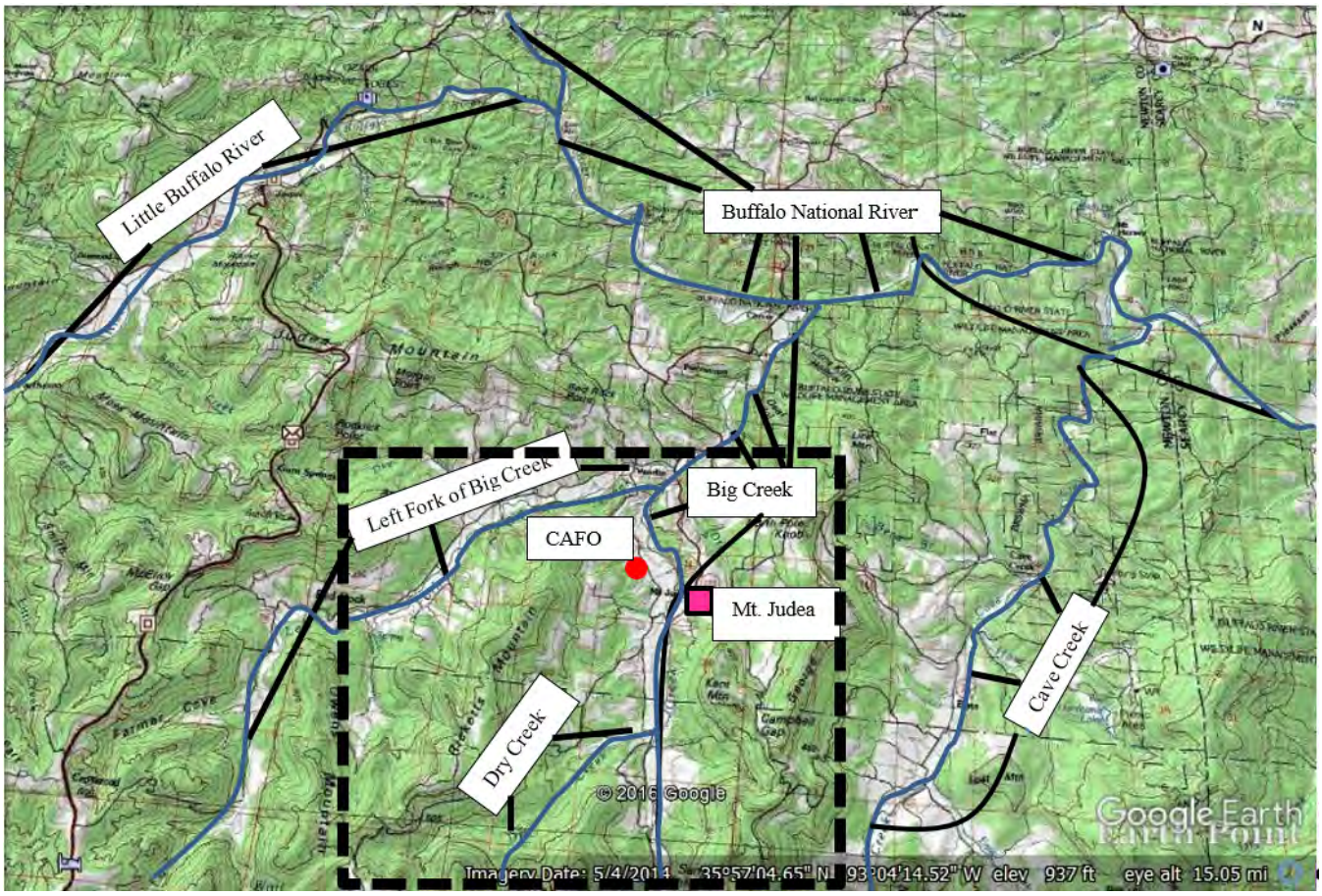

Figure 2. Expanded study area, showing location of the CAFO, the town of Mt. Judea, and the major surface-water bodies that receive groundwater from springs. The streams are approximately located by the blue lines, which are connected to the stream names. The dashed rectangle shows the approximate boundary of the focused study area, which has been enlarged on figures 7 to 9 to show specific details of the results of dye tracing.

Big Creek and its major tributary, Left Fork of Big Creek, flow in alluviated valleys on bedrock. Alluvium consists of nonindurated sediments, primarily chert and terrigenous rock fragments from younger, topographically higher formations. The alluvium in these valleys varies in thickness from a feather-edge to about 8 m. Outcrops of the Boone Formation are common in the streambed and bluffs along Big Creek and the Buffalo River. Springs are common along the entire reach of Big Creek, ranging from relatively small discharges in the tens of liters per minute range to large discharges in tens of liters per second. These larger flows discharge from relatively pure carbonate lithologies, with caves more commonly found in the lower Boone or in Ordovician-aged limestones and dolomites (Mott and others, 2000).

Methodology

Qualitative dye tracing was conducted from April 2014 through October 2014 in Big Creek and contiguous basins using three nontoxic, fluorescent dyes: fluorescein, rhodamine WT, and eosine. All dye injections were accomplished using liquid dyes, inasmuch as the powdered dyes (fluorescein and eosine) are easily caught up by air currents, and may cause severe cross-contamination if they are not in liquid form during injection. The liquid dyes were kept in impermeable containers, and dye receptors and personnel were isolated from incidental contact which would give false

positive results (Quinlan, 1989; Aley, 2003). For each test, a single dye was injected into flowing groundwater in the middle part of the Boone, characterized by chert/limestone couplets (fig. 5). Injection sites included hand-dug wells, a sinking stream in alluvium, and a swallet (table 1). The latter feature was a sinkhole that captured all of the flow of Dry Creek, a tributary upgradient from Big Creek and nearby spreading fields in limestone of the upper Boone. Fluorescein dye was introduced to a dug well about 500 m downgradient from the CAFO. At this location, groundwater is flowing on the epikarst, which is developed on the lower-middle Boone and overlain by Big Creek alluvium. Eosine was injected into a dug well that was surrounded by waste-spreading fields.

Passive dye receptors similar in appearance to a tea bag were constructed by placing approximately 10 grams of coconut charcoal in a permeable packet that allowed flowing groundwater to contact the charcoal. In most cases, the permeable external layer of the packet was a “milk sock”, whose manufactured purpose is to filter milk from automatic milking machines used by dairy barns. This fabric has enjoyed recent popularity within the dye-tracing community, especially for flow velocities of about 2 km/day or less. For greater flow velocities, such as surface streams, an additional packet was made with larger fabric openings approximately one-fourth the size of window screen. In high-velocity streams, the milk sock receptor was often too fine a mesh to allow full contact of the flowing water with the charcoal, and thus did not yield meaningful positive dye detections.

Passive dye receptors were placed in flowing groundwater and surface water throughout the study area, based on a previous karst inventory and discussions with local landowners. Receptors were placed in all available springs, wells, streams, and flowing water where we had been granted permission. Inasmuch as groundwater flow directions were not known at the start of the study, such a conservative approach is required (Quinlan, 1989).

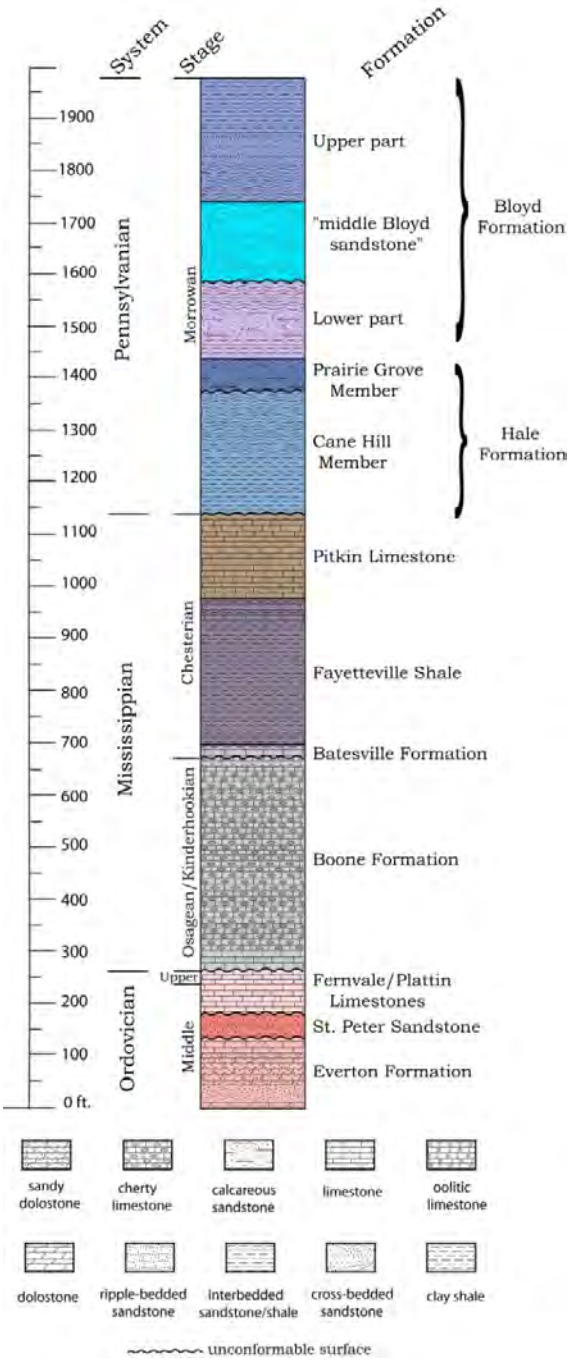

Figure 3. Stratigraphic column of the Big Creek study area, showing the stratigraphic extent of karst where the Boone Formation (light grey color) occurs at land surface. Arrows on the column bracket approximately 80 m of the chert-rich interval of the chert/limestone couplets of the Boone. Total thickness of the Boone Formation is about 110 m. Figure modified from Braden and Ausbrooks (2003).

Figure 4. Karst dissolution features in limestone interbedded with chert from the middle Boone Formation. The chert acts as an insoluble confining unit for the upper and lower dissolution zone. The size of these voids typically ranges from 2 to more than 5 cm.

If fluorescent dye were in the water, it was sorbed onto the charcoal in the receptor. These were left in place for periods of time varying from 1 day to 1 month, and were replaced by new receptors when the original receptors were retrieved. Receptors were identified by plastic tags with station number, date placed, and date retrieved noted in black permanent marker and placed into ziplock bags with additional information as appropriate recorded on the bag. Chain-of-custody forms were prepared and updated for the receptors through each transfer responsible for all remaining actions.

Upon receipt from the field, the receptors were rinsed with distilled water in the Hydrogeology Laboratory at the University of Arkansas to remove sediment and related debris. They were allowed to air dry for at least 24 hours, and were then analyzed on a calibrated Shimadzu scanning spectrofluoro-photometer (model RF 5000). One half of the dried charcoal was placed into plastic containers and an eluent of isopropyl alcohol and potassium hydroxide was added to mobilize any dye present on the charcoal into the residual solution (elutant). The elutant was then transferred by a disposable polyethylene pipette into a single-use cuvette, and analyzed for the wavelength of fluorescence specific to the three dyes that were used. Wavelength maxima for fluorescein were centered at 515 nanometers (nm), for eosine at 540 nm, and for rhodamine WT at 572 nm.

Data Verification

Verification of the accuracy of dye tracing is essential, and is documented by a process called quality assurance/quality control (QA/QC). QA/QC is a major component of all dye-tracing studies, and it provides unquestioned verification that the information gained from the passive detectors is valid. QA/QC also verifies that the study is accurate and represents only dye that was injected into the flowing groundwater. For this study, it involved verifying that (1) the hydraulic head of the groundwater is higher at the point of injection that at the point the dye receptor was placed, (2) that the injection point is part of a dynamic groundwater flow system, (3) that positive attributes of the dye at specific locations are duplicated by other dye analysts through a series of blind testing, (4) that the concept of clean hands/dirty hands (Shelton, 1994) is honored strictly and that receptor retrieval is done by different personnel than those that injected the dye, (5) that cross-contamination of receptors is avoided by means of gloves and ziplock bags, and (6) that duplicate receptors reflect the same results.

Tracing Results

Five dye traces were undertaken in the study area in 2014, and a detailed summary of each is provided in table 1. Dye-injection sites are shown on figure 7, overlain on a shaded relief map, and a summary of point-to-point dye connections is shown on figure 8. Important details of each trace are also described in the following section.

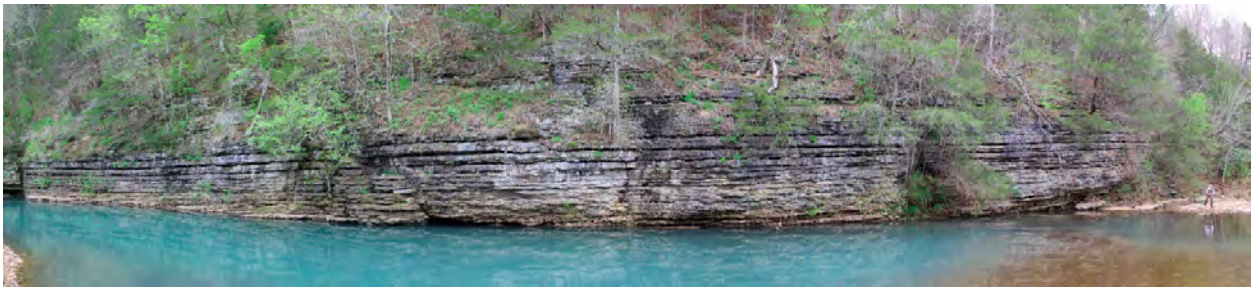

Figure 5. This spliced multi-image photo shows karstified zones in a sequence of limestone/chert couplets in an outcrop of the Boone Formation in a bluff along Big Creek. The dark, near-horizontal features are incompletely dissolved zones in the limestone, which figure 3 represents in a close-up view. Vertical fractures allow water from above to enter the karst and exit along Big Creek. The gentle dip of the layers reflects slight tilting, which is typically less than several degrees. Photo by John F. Murdoch.

Table 1. Selected dye injections in the study area during 2014. Locations of injection sites are shown on figure 7, overlying topography, and figure 8, overlying geology.

[FL, fluorescein; RWT, rhodamine WT; EO, eosine; m/d, meters per day; outside agencies providing verification of positive traces included Tom Aley, Ozark Underground Lab, Protem, Missouri, and Geary Schindel, Edwards Aquifer Authority, San Antonio, Texas. Instrumental confirmation was conducted using scanning spectrofluorophotometers; visual confirmation was assessed by observation of fluorescent color in the resurgence]

Injection Date	*Site Number*	*Hydrologic Setting*	*Geology*	*Tracer*	*Groundwater Flow*	*Comments*
4/22/14	BS-39	dug well perched	lower cherty Boone epikarst	FL	moderate; velocity about 660 m/d	multiple visual and instrument confirmations
4/27/14	BS-78	sinking stream	alluvial gravel over middle Boone	RWT	low; velocity not calculated	no observable confirmation; likely perched
5/12/14	BS-36	dug well perched on chert	middle cherty Boone	EO	very high; velocity about 800 m/d	widespread instrument and outside tracer confirmations; cross-basin and cross-formation flow; radial flow
7/10/14	BS-71	swallet perched	upper Boone limestone	RWT	moderate; velocity about 7,000 m/d	visible and instrument confirmation; surface flow part of the way
8/5/14	BS-36	dug well	middle cherty Boone	FL	very low; no velocity	no observable confirmation; dye density caused it to sink to lower reservoir; stagnant with no flow

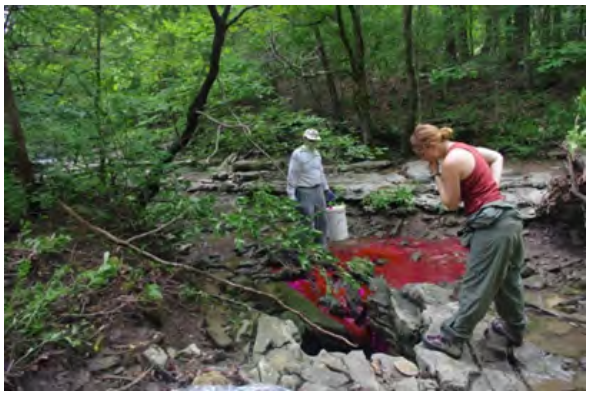

Figure 6. Swallet in Dry Creek in Ozark National Forest capturing all streamflow upgradient from CAFO spreading fields. In karst, surface water and groundwater interact as a single resource, with streams typically being pirated into the groundwater system as shown here, later resurging from downgradient springs back to the surface. Photo by Carol Bitting.

On April 22, 5 kilograms (kg) of fluorescein dye were injected into BS-39, a hand-dug well 13.17 m deep that had flowing groundwater on the epikarst perched on chert of the lower Boone Formation. BS-39 lies on an alluvial surface between the CAFO and Big Creek, about equidistant from both (fig. 6).

On April 27, 2 kg of rhodamine WT were injected at BS-78, a sinking stream at the intersection where a low-water county road crosses Sycamore Hollow (fig. 7). The dye was placed into alluvial gravel that overlaid limestone of the upper part of the middle Boone Formation. No positive instrument detections of the dye were confirmed from this trace. Insofar as passive dye receptors were only placed along Dry Creek and Big Creek for this test, results indicate there was no discernable eastern groundwater flow for the low-flow conditions at the time of this test. Positive traces were visually and instrumentally confirmed in an alluvial well downgradient and in multiple springs that resurge from below a chert layer in the bottom of Big Creek, upwelling about 660 m from the injection site 24 hours after injection. As with many of the other positive dye traces in the study area, the springs in the middle part of the Boone have multiple orifices and flow from a discrete karstified layer of a single limestone/chert couplet. This trace established that groundwater flowed from BS-39 to springs in Big Creek at a velocity of at least 660 meters per day (m/d). Springs associated with this resurgence would be an excellent place to sample for potential contamination from the CAFO, including feeding, waste-handling, and pond leakage.

On May 12, 8 kg of eosine dye were injected into BS-36, a hand-dug well 12.23 m deep in the middle Boone Formation with visible groundwater flow along several zones near the water table that had been studied intensively (Murdoch and others, 2016). Well BS-36 is located within the generalized area of waste spreading, with fields on three sides and within several hundred meters of the well. One day following dye injection, more than 15 cm of rainfall caused a water-level rise in the well of more than 1 m, mobilizing much of the dye into permeable zones above the pre-injection water level. The dye was dispersed in a radial pattern (fig. 8), with 36 confirmed positive eosine detections (fig. 9) at springs and surface streams in Big Creek and in different basins other than Big Creek, as well as downstream in the Buffalo River. One positive trace to Mitch Hill Spring, on the opposite side of the Buffalo River from the injection point, reflected how complex the karst flow system is and how far from the study area flow could be detected. This positive Mitch Hill Spring trace was reconfirmed by both of the dye analysts in an external review using split receptor samples provided in a blind test. Obviously, some of the groundwater flow resurfaced and moved downgradient in Big Creek and other surface channels, but this test documented that groundwater flow from the area of the spreading fields surrounding BS-36 is mobilized during intense rainfall events, and sampling sites at springs along Left Fork of Big Creek, the Buffalo River, and surface streams in contiguous basins would be excellent sites for

water-quality sampling at high-flow conditions. The radial pattern of flow resulting from this storm (fig. 8) is a common feature observed in other dye traces in the middle Boone Formation (Aley, 1988; Mott and others, 2000).

The traces shown by northwest-trending solid arrows from BS-36 to Left Fork of Big Creek (fig. 8) represent dye that was detected at receptors in 7 days, yielding a conservative straight-line velocity of about 800 m/d. These values, along with those from the BS-39 injection site, are comparable to the results of the fluorescein trace from BS-36 in the same geologic interval. As a comparison of velocity, later recovery of dye from receptors from BS-36 showed a static zone of very little groundwater movement that served as a storage reservoir in the lower part of the well. The remaining dye, which was denser than water, was not flushed from the deeper part of the well for more than 3 months, and thus, during that time indicated there was no movement of water out of the well.

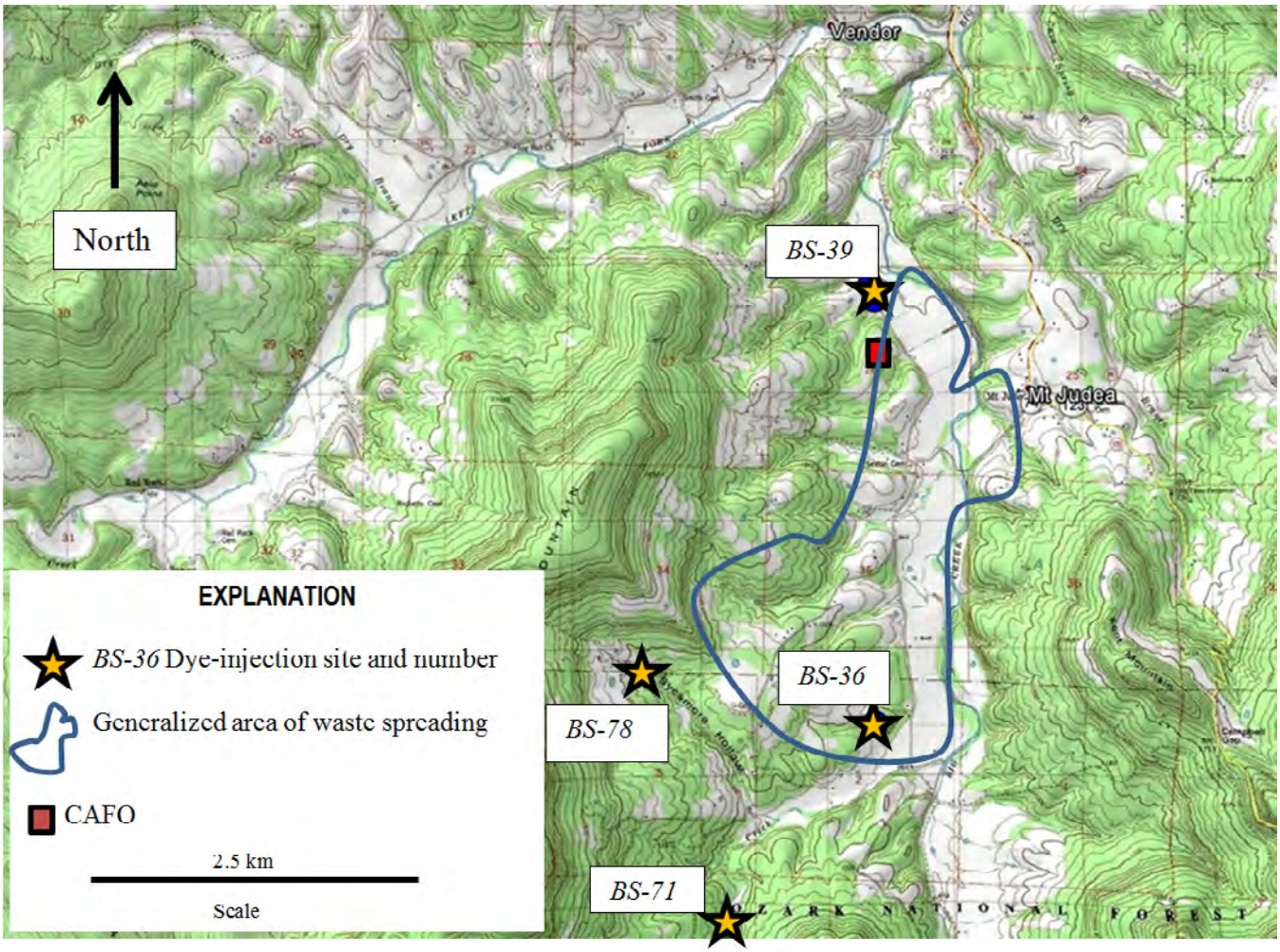

Figure 7. Topography of Big Creek basin near Mt. Judea in the area of the CAFO, including the locations of dye injections, and locations of CAFO structures housing 6,500 hogs and waste lagoons. BS-36 also was used to inject fluorescein dye 3 months later (table 1). Table 1 summarizes the important aspects of each dye-tracing test.

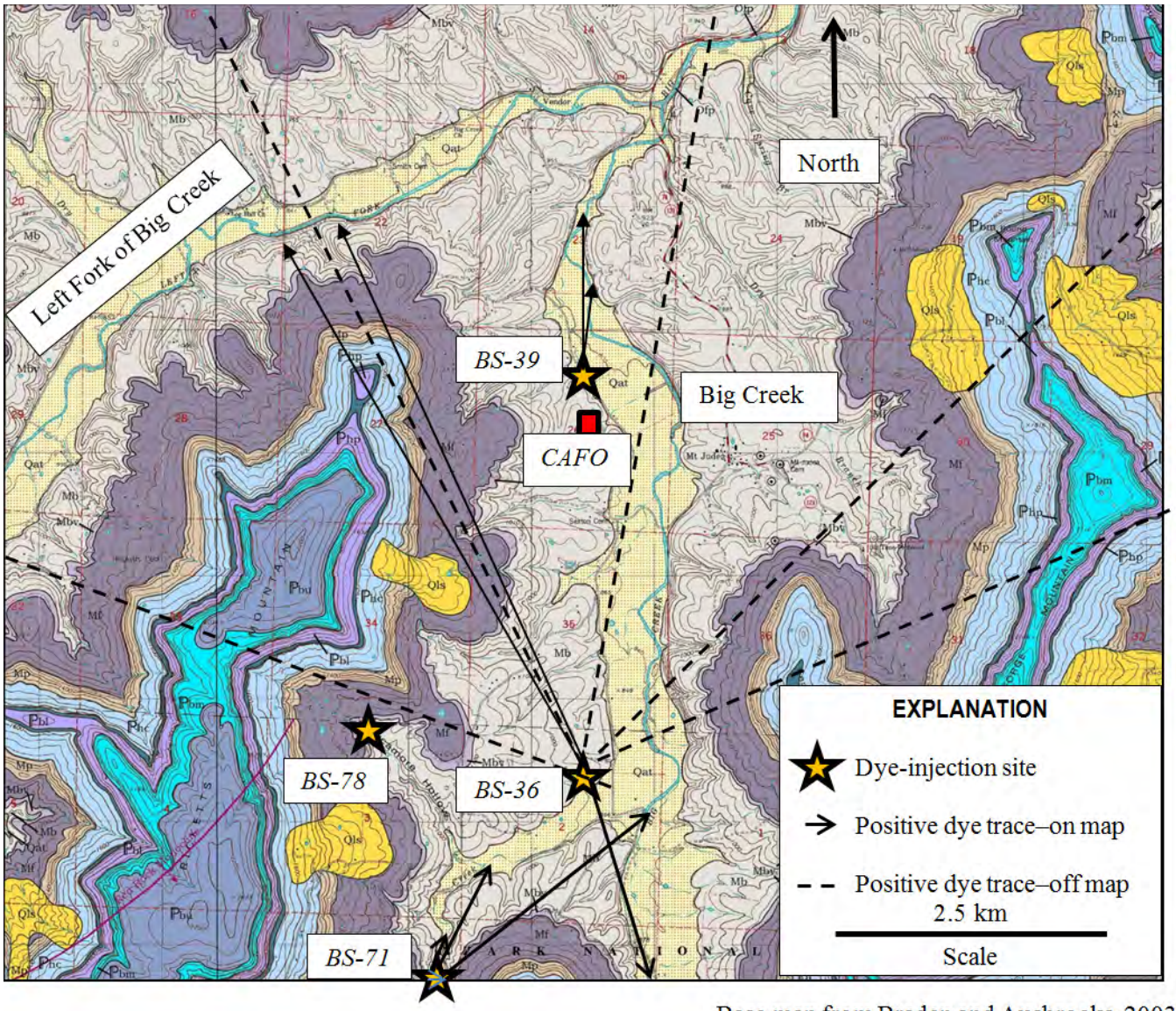

Base map from Braden and Ausbrooks, 2003

Figure 8. Geologic map showing point-to-point dye-tracing results in the area of the CAFO and its spreading fields. Solid arrows that emanate from the injection points show the locations of groundwater recovery sites on the map. Dashed lines from injection well BS-36 extend beyond the area shown on this map, with the full observed extent shown on figure 9. Actual flow paths in the subsurface are substantially more complex than the straight lines show. Tracing results shown here are groundwater-level dependent.

On July 10, 5 kg of rhodamine WT were injected in to a swallet that captured the entire discharge of Dry Creek upstream from BS-71 (fig. 7). This trace was initiated in the larger, more open voids of the upper Boone limestone (Stanton, 1994), which is chert free. This trace was visually confirmed at the confluence of Dry Creek and Big Creek, as well as instrumentally confirmed from dye receptors in springs along Dry Creek. This trace yielded the fastest groundwater velocity at nearly 7,000 m/d. Flow velocity based on this test was much greater than determinations made from tests in the karst in the middle Boone, and can be explained by less frictional flow from conduits in the pure-phase limestone of the upper Boone and a significant portion of the flow path occurring on the surface in Dry Creek.

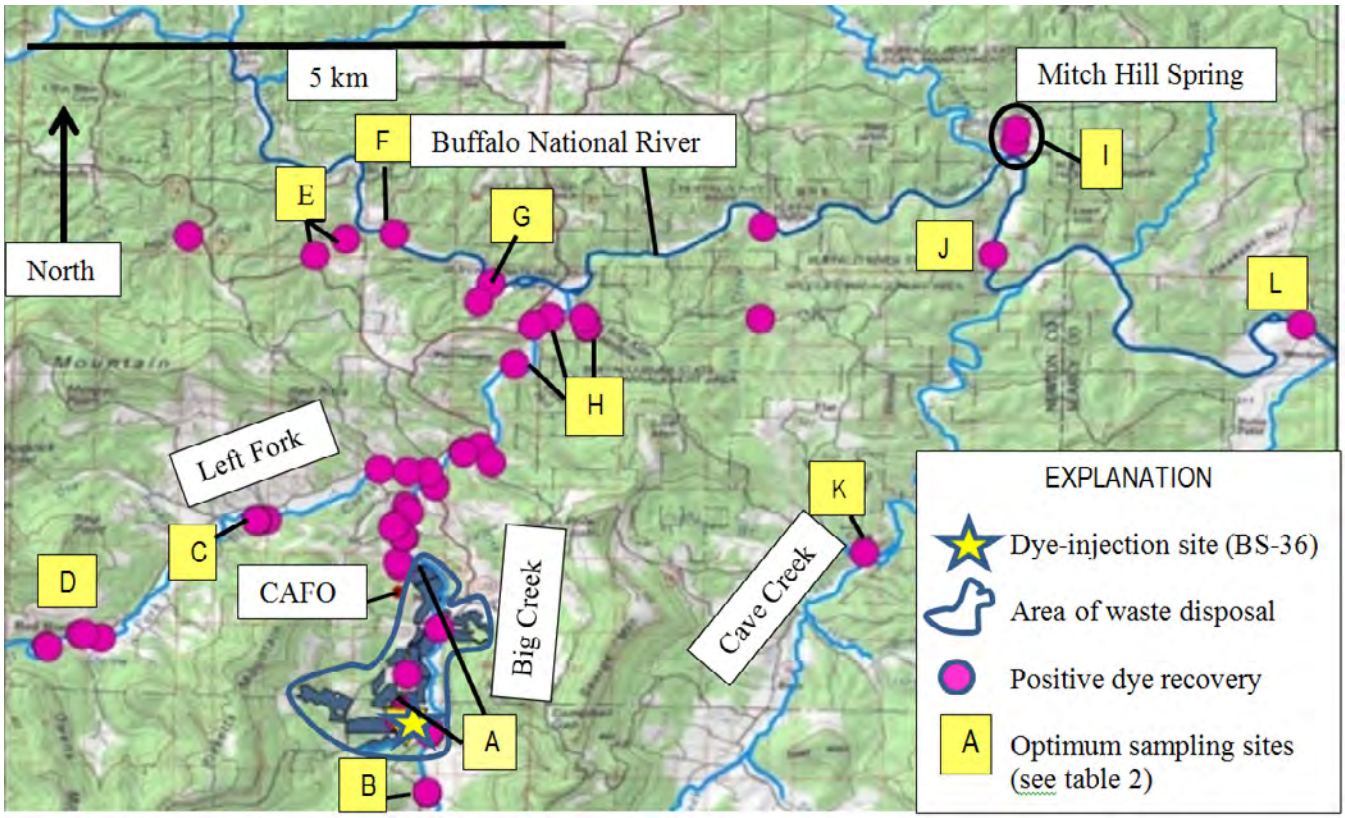

Figure 9. Flow from BS-36 during high flow after eosine injection on May 12, 2014. Dye was positively traced to 36 sites (springs and streams). Letters (yellow squares) show recommendations for sites to sample for evaluating contamination in the future. The dye-trace results show the full dispersive extent of karst flow in the subsurface into other surface-water basins, the Buffalo National River, and even beneath the Buffalo River to Mitch Hill Spring, identified by the black circle. Dark green rectangular patterns within area outlined around dye-injection site (yellow star) represent waste spreading fields. Five positive dye traces were recovered from the Buffalo National River during this test.

On August 5, 2 kg of fluorescein were injected into BS-36, this time under extremely low-flow conditions. As with the trace at BS-78, no positive confirmation at any dye receptor except within the injection well was observed. The variation in stage in BS-36 at the time of this test was substantially lower than during the eosine injection on May 12, and the conditions of groundwater flow were also substantially different from that test.

The May 12 test had 36 confirmed positive eosine traces (fig. 9); the August 5 fluorescein test had no confirmed traces. This result provides good insight for the water-level control on groundwater flow in the middle Boone, and helps explain our observations.

Discussion and Conclusions

Information from these dye traces can be used for designing a more reliable and relevant water-quality sampling network to assess the impact of the CAFO on the karst groundwater and for gaining further understanding of the flow in this karst area (table 2). On the basis of the results of the dye tracing described herein, the key observations made on groundwater flow in the Boone Formation in the Big Creek study area are as follows:

1. Although the study area is mantled karst, subsurface flow is very important, and forms a significant part of the hydrologic budget. Groundwater velocities in the

chert/limestone portion of the middle Boone Formation were conservatively measured to be in the range of 600 to 800 m/d.

2. Conduits in pure-phase limestones of the upper and lower Boone Formation have flow velocities that can exceed 5,000 m/d.
3. Groundwater flow in the Boone Formation is not limited to the same surface drainage basin, which means that anomalously large springs should be part of the sampling network (Brahana, 1997).
4. Because the Buffalo National River is the main drain from the study area, and is used intensively for activities such as canoeing, fishing, and swimming, large springs and high-yield wells close to the river should be included in the sampling network.
5. Potential transport velocities of CAFO wastes from the land surface appear to be most rapid during and shortly after intense rainfall. Minimum groundwater flow occurs during periods of low flow or during droughts. Sampling should accommodate these considerations.

The chert obviously plays a role as confining layers in the Boone Formation, and adds to the complexity of the flow systems in the karst. Interbasin transport of the dye is consistent with groundwater following faults, which are common in the study area, with many not mapped. Insoluble material can be washed into the fault plane and divert groundwater flow along the fault. The appearance of linear patterns truncating topography (fig. 7) and geology (fig. 8) are consistent with this interpretation, and can be further tested with additional dye traces.

Acknowledgments

The authors are most grateful to Chris Hobza and Dan Wagner for very helpful peer reviews, and to Eve Kuniansky and Larry Spangler for editorial advice and assistance. Funding for equipment, supplies, lab analyses, and partial travel costs were supplemented by the Ozark Society, the Buffalo River Watershed Alliance, Patagonia Environmental Grants Program, and five anonymous benefactors. We also thank the Slovene Human Resources Development and Scholarship Fund no. 11012-7/2014, and the innovative scheme to co-finance doctoral studies for the promotion of cooperation with the economy and solving current social challenges—generation 2012 from the Ministry of Education, Science and Sport of the Republic of Slovenia, and the University of Nova Gorica. These latter two sources funded coauthor Katarina Kosič- Ficco during her interval of working for the project. We sincerely acknowledge and thank all those individuals for their time and financial support.

References Cited

Aley, T., 1988, Complex radial flow of ground water in flat-lying residuum-mantled limestone in the Arkansas Ozarks, *in* Proceedings of the Environmental Problems in Karst Terranes and Their Solutions Conference, 2nd, Nashville, Tenn., November 16-18, 1988: Dublin, Ohio, National Water Well Association, v. 2, p. 159–170.

Aley, T., 2003, Groundwater tracing handbook: Ozark Underground Laboratory, Protem, Missouri, 38 p.

Braden, A.K., and Ausbrooks, S.M., 2003, Geologic map of the Mt. Judea quadrangle, Newton County, Arkansas: Arkansas Geological Commission, scale 1:24,000.

Brahana, J.V., 1997, Rationale and methodology for approximating spring-basin boundaries in the mantled karst terrane of the Springfield Plateau, northwestern Arkansas, *in* Beck, B.F., and Stephenson, J. Brad, eds., Sixth Multidisciplinary Conference on Engineering Geology and Hydrogeology of Karst Terranes, Springfield, Missouri, April 6–9, 1997: Rotterdam, A.A. Balkema, p. 77–82.

Brahana, Van, 2014, The role of chert in the karst hydrogeology and geomorphology of the southern Ozarks: Geological Society of America south-central meeting, March 17–18, 2014, Fayetteville, Arkansas, v. 46, no. 1.

Table 2. Recommended sites for collecting water-quality samples based on the results of dye tracing near the CAFO and its spreading fields near Big Creek, Newton County, Arkansas.

[Cl^-, chloride; nutrients, P and NO_3^-; pathogens, *E. coli* and fecal coliform; trace metals, isotopes of ^{31}P, ^{63}Cu,^{65}Cu, and ^{66}Zn; DO, dissolved oxygen; major constituents, Na^+, K^+, Ca^{+2}, Mg^{+2}, Cl^-, HCO_3^-, SO_4^{-2}; field parameters, temperature, pH, and specific conductance]

Site ID (see fig.9)	*Hydrologic Setting*	*Parameters to Sample*	*Justification for Recommendation*
A	springs, wells, surface streams that drain into Big Creek from waste-spreading fields	Cl^-, nutrients, pathogens, trace metals, DO, algae, major constituents, field parameters	dye tracing, proximity to source
B	perched bedding plane springs upstream on Big Creek	Cl^-, nutrients, pathogens, trace metals, DO, algae, major constituents, field parameters	dye tracing, upstream from CAFO source and waste spreading fields, anomalously large spring discharge
C	perched bedding plane springs upstream on Left Fork of Big Creek	Cl^-, nutrients, trace metals, DO, algae, major constituents, field parameters	dye tracing, larger spring indicates subsurface capture outside drainage basin, major algal blooms downstream from springs
D	upstream springs and surface streams on Left Fork of Big Creek	Cl^-, nutrients, trace metals, DO, algae, major constituents, field parameters	dye tracing, major algal blooms downstream from springs
E	Rock Creek upstream from Buffalo National River	nutrients, DO, algae, major constituents, field parameters	dye tracing
F	farthest upstream on Buffalo National River	nutrients, DO, algae, major constituents, field parameters	dye tracing
G	springs and cave streams less than 100 meters upstream from Buffalo National River	nutrients, DO, algae, major constituents, field parameters	dye tracing
H	Big Creek and springs downstream from confluence with Left Fork. Major gaining reach	Cl^-, nutrients, trace metals, DO, algae, major constituents, field parameters	dye tracing, downstream from CAFO source and waste spreading fields
I	Mitch Hill Spring and its spring run, on the north side of the Buffalo National River	Cl^-, nutrients, pathogens, trace metals, DO, algae, major constituents, field parameters	dye tracing, largest spring in the expanded study area, numerous dye traces recovered here from multiple injection sites
J	intermediate reach on Buffalo National River	Cl^-, nutrients, pathogens, DO, algae, major constituents, field parameters	dye tracing
K	below ponded resurgence of major spring on Cave Creek	Cl^-, nutrients, pathogens, DO, algae, major constituents, field parameters	dye tracing, anomalously large spring discharge
L	farthest downstream location on Buffalo National River	Cl^-, nutrients, pathogens, DO, algae, major constituents, field parameters	dye tracing

Center for Advanced Spatial Technologies, 2006, Arkansas Watershed Information System—Arkansas watersheds: University of Arkansas, Fayetteville, accessed March 10, 2017, at http://watersheds.cast.uark.edu/viewhuc.php?hucid=110100050302.

Ford, D.C., and Williams, P., 2007, Karst hydrogeology and geomorphology: New York, Wiley, 576 p.

Hobza, C.M., Moffit, D.C., Goodwin, D.P., Kresse, Timothy, Fazio, John, Brahana, J.V., and Hays, P.D., 2005, Ground-water quality near a swine waste lagoon in a mantled karst terrane in northwestern Arkansas, *in* Kuniansky, E.L., 2005, U.S. Geological Survey Karst Interest Group Proceedings, Rapid City, South Dakota, September 12–15, 2005: U.S. Geological Survey Scientific Investigations Report 2005-5160, p. 155–162.

Imes, J.L, and Emmett, L.F., 1994, Geohydrology of the Ozark Plateaus aquifer system in parts of Missouri, Arkansas, Oklahoma, and Kansas: U.S. Geological Survey Professional Paper 1414-D, 127 p.

Kosič, Katarina, Bitting, C.L., Brahana, J.V., and Bitting, C.J., 2015, Proposals for integrating karst aquifer evaluation methodologies into national environmental legislation—Case study of a concentrated animal feeding operation in Big Creek basin and Buffalo River watershed, Arkansas, USA: Sustainable Water Resources Management, v. 1, p. 363–374, doi10.1007/s-40899-015-0032-5.

Liner, J.L., 1978, Lithostratigraphy of the Boone Limestone, northwest Arkansas: Fayetteville, University of Arkansas, unpublished M.S. thesis, 88 p.

Mott, D.N., Hudson, M.R., and Aley, T., 2000, Hydrologic investigations reveal interbasin recharge contributes significantly to detrimental nutrient loads at Buffalo National River, Arkansas: Proceedings of the Arkansas Water Resources Center annual conference—Environmental Hydrology, Fayetteville, Arkansas, April 4–5, 2000: Fayetteville, University of Arkansas, Publication No. MSC-284, p. 13–20.

Mott, D.N., and Laurans, Jessica, 2004, Water resources management plan—Buffalo National River: U.S. Department of the Interior, National Park Service, Harrison, Arkansas, 145 p.

Murdoch, John, Bitting, Carol, and Brahana, John Van, 2016, Characterization of the karst hydrogeology of the Boone Formation in Big Creek Valley near Mt. Judea, Arkansas—Documenting the close relation of groundwater and surface water: Environmental Earth Sciences, v. 75;1160, 16 p., doi10.1007/s12665-016-5981-y.

Pesta, Nathan, for DeHaan, Grabs, and Associates, LLC, and Bates and Associates, Inc., 2012, NPDES Notice of Intent (NOI)—Concentrated Animal Feeding Operations (CAFO)— ARG590000, C&H Hog Farms, Section 26, T-15-N, R-20-E, Newton County, Arkansas: Unpublished document for Arkansas Department of Environmental Quality, 263 p., accessed June 28, 2015, at https://www.adeq.state.ar.us/downloads/webdatabases/permitsonline/npdes/permitinformation/arg590001_noi_20120625.pdf.

Quinlan, J.F., 1989, Ground-water monitoring in karst terranes—Recommended protocols and implicit assumptions: U.S. Environmental Protection Agency, Research and Development, 600/X-89/050, 88 p.

Scott, H.D., and Hofer, K.R., 1995, Spatial and temporal analyses of the morphological and land use characteristics of the Buffalo River watershed: Fayetteville, University of Arkansas, Arkansas Water Resources Center Publication No. MSC-170, 61 p.

Shelton, L.R., 1994, Field guide for collecting and processing stream-water samples for the National Water-Quality Assessment Program: U.S. Geological Survey Open-File Report 94-455, 42 p.

Stanton, G.P., 1994, Processes and controls affecting anisotropic flow in the Boone-St. Joe Limestone, northwest Arkansas: Fayetteville, University of Arkansas, unpublished M.S. thesis, 212 p.

U.S. Department of Agriculture Farm Service Agency and U.S. Small Business Administration, 2015, Final environmental assessment C&H Hog Farms, Newton County, Arkansas, 39 p., https://www.fsa.usda.gov/Assets/USDA-FSA-Public/usdafiles/Environ-Cultural/fonsi_hog_farms_final_assesment.pdf

White, W.B., 1988, Geomorphology and hydrology of karst terrains: New York, Oxford University Press, 464 p.

Using Quantitative Tracer Studies to Evaluate the Connection Between the Surface and Subsurface at Mammoth Cave National Park, Kentucky

By JeTara Brown[1], Rickard Toomey[2], Rick Olson[2], Lonnie Sharpe[1], and Thomas D. Byl[1,3]

[1]Tennessee State University, Dept. of Agricultural and Environmental Sciences, 3500 John H Merritt Blvd, Nashville, TN 37209

[2]Science and Resources Management, Mammoth Cave National Park, KY 42259

[3]U.S. Geological Survey, Lower Mississippi-Gulf Water Science Center, 640 Grassmere Park, Suite 100, Nashville, TN 37211

Abstract

The cave ecosystem at Mammoth Cave National Park, Kentucky, is linked to the surface through groundwater recharge. The cave was formed over hundreds of thousands of years through erosion and dissolution of limestone by groundwater. Water still plays a vital role in the continuing geomorphic processes that form the cave and the cave ecosystem. The objective of this study was to conduct quantitative tracer studies to evaluate the transport of an injected tracer from the surface into the cave under different hydrologic conditions. The study included three quantitative tracer studies originating from a potential contamination source on the surface and monitoring in upper and lower level cave passages. The distance between the tracer release point (injection site) and the sinkhole in the storm-runoff channel used in this study was approximately 1,500 feet. Rhodamine WT (20-percent solution) dye was released in conjunction with either the onset of storm runoff or as the storm was winding down. The dye was released in August and October 2014, and in January 2015. Prior to each dye release, streams in the cave were monitored for a minimum of three consecutive storms to verify the absence of dye from previous tests. Continuous monitoring from June 2014, through January 2015, was accomplished using two portable fluorometers. Additional monitoring for the second tracer study was achieved by using 12 passive activated charcoal sampling devices. The monitoring equipment was located in different levels of the cave. One fluorometer was located in an upper level passage called Cataract Hall. The second fluorometer was placed in a lower level passage of the cave system in Cascade Hall, which lies along Silliman's Avenue. In the first tracer study, two check dams were constructed in the surface channel, and 180 milliliters of the Rhodamine WT dye were released on the rising limb of the storm runoff hydrograph (1.2-inch storm). It took 9.7 hours for the dye to reach the fluorometer in the upper level cave passage. The dye concentrations and discharge rate in the upper level passage were used to calculate a 3-percent recovery of the released dye. We were unsuccessful at detecting any dye in the lower level passage because of the location of the second fluorometer. The two low-level check dams on the surface were removed before the second tracer study.

In the second study, 600 milliliters of Rhodamine WT dye were released during the rising limb of the storm runoff hydrograph (1.4-inch storm) and was detected in the upper level cave passage within 4 hours. Approximately 37 percent of the dye was accounted for in the upper level passage. The fluorometer in the lower level cave passage again failed to detect any dye; however, there were positive tracer results at 5 of the 12 passive sampler locations. The fluorometer in the lower level cave passage was moved to one of the locations with a positive recovery before the third tracer study was conducted. In the third tracer study, 600 milliliters of Rhodamine WT dye were released on the declining limb of the storm hydrograph (a 0.7-inch storm) and was detected in the upper level cave passage within 50 minutes. During that storm, approximately 38 percent of the dye was accounted for in the upper cave

passage. Trace amounts of the dye also were detected in the lower level passage approximately 3.5 days later. Furthermore, subsequent storms resulted in the detection of additional dye in the upper cave passage that accounted for another 7 percent of the original amount of dye injected in the study. Additional dye detections following subsequent storms had not occurred in the previous two tracer studies. The tracer peaks associated with successive storms after the third study were probably because of the timing of the tracer release in the receding portion of the storm runoff, resulting in dye becoming stranded as the storm flow ceased. In summary, these studies demonstrated that temporary check dams more than doubled travel time between the surface and the subsurface, and also resulted in a reduction in the percentage of dye recovered in the upper level cave passage. The third study also demonstrated that if a chemical is released during the later part of the falling limb of a storm hydrograph, it may be transported faster into the cave than if it were released during the rising limb, but a portion is prone to temporary storage. Additional work is needed to account for the remaining dye and to better understand transport and storage mechanisms into and within the cave.

Acknowledgment

The 12 passive charcoal samplers were analyzed by the Crawford Hydrology Lab at Western Kentucky University, C. Salley and L. Bledsoe, analysts.

Stalagmite $\delta^{13}C$ and $\delta^{18}O$ Records for the Past 130,000 Years From the Eastern Edge of the Chinese Loess Plateau (CLP): Responses of the CLP as a Carbon Sink to Climate Change

By Zhiguo Rao

College of Resources and Environmental Science, Hunan Normal University, South Lushan Road, Yuelu District, Changsha City, Hunan Province, P.R. China 410081

Abstract

Precisely dated high resolution stalagmite stable carbon $\delta^{13}C$ and oxygen $\delta^{18}O$ isotope records for the past 130,000 years from Zhenzhu Cave on the eastern edge of the Chinese Loess Plateau (CLP) indicate a high degree of co-variation between the isotopes. The $\delta^{13}C$ varies from about -9.4 to -2.9‰, with an average value of -6.3‰, relative to the Vienna Pee Dee Belemnite (VPDB) isotope standard. The $\delta^{18}O$ varies from about -10.8 to -6.5‰, with an average value of -9.2‰, relative to VPDB. The Zhenzhu Cave $\delta^{13}C$ record is consistent with pedogenic carbonate $\delta^{13}C$ data from the western edge of the CLP. The $\delta^{13}C$ records are indicators of the density of the land vegetation cover. The negative $\delta^{13}C$ values indicate that more organic carbon from the intensified overlying vegetation has been sequestrated into the inorganic carbonate. The Zhenzhu Cave $\delta^{18}O$ record is consistent with previously reported stalagmite $\delta^{18}O$ data from south China, and reveals its paleoclimatic significance as an indicator of the intensity of the Asian summer monsoon (ASM). The combination of all the evidence demonstrated that climatic amelioration due to enhanced ASM intensity (indicated by more negative stalagmite $\delta^{18}O$ data) increased terrestrial vegetation cover on the CLP, which resulted in the enlarged carbon sink in this region (indicated by the more negative loess carbonate and stalagmite $\delta^{13}C$ data).

Hydrogeochemical Characteristics of Precipitation and Cave Drip Water in Zhenzhu Cave, North China

By Yunxia Li[1,2], Zhiguo Rao[1], Yongli Gao[2], Xiaokang Liu[1], and Shengrui Zhang[3]

[1]Key Laboratory of Western China's Environmental Systems (Ministry of Education), College of Earth and Environmental Sciences, Lanzhou University, Lanzhou 730000, China

[2]Center for Water Research, Department of Geological Sciences, University of Texas at San Antonio, One UTSA Circle, San Antonio TX 78249

[3]College of Earth and Environmental Sciences, Hebei Normal University, Shijiazhuang, 050024, China

Abstract

This study summarizes the hydrogeochemical characteristics of precipitation and drip water in Zhenzhu Cave, North China. Two meteoric precipitation sites and six drip sites from Zhenzhu Cave were monitored during April 2012–April 2014. Local precipitation is characterized by a local meteoric water line (LMWL) with a slope close to 7.6 and an intercept value of 9.0 (R^2=0.94) in the study area, which is very close to the global meteoric water line and Chinese meteoric water line. This implies that secondary evaporation and other fractionation factors do not have significant influences on meteoric precipitation in this area. Monthly stable isotopic compositions of precipitation ($\delta^{18}O_p$ and δD_p) show negative correlation with monthly mean precipitation amounts at a low confidence level (R^2=0.18) and no significant correlation with surface air temperature. During 2 years of monitoring, the drip water line, based on the isotopic compositions ($\delta^{18}O_d$ and δD_d) of cave drip water, had a smaller slope value (3–5) than that of the LMWL, implying that the process from rainfall to drip water may be greatly impacted by other factors such as evaporation. Furthermore, $\delta^{18}O_d$ and δD_d values did not show any significant seasonal variability, which demonstrates that the drip water is a mixture of rainwater within a perched water reservoir in the epikarst zone integrated over a longer period. Results of monitoring in Zhenzhu Cave indicate that isotopic compositions of drip water are controlled by several factors; therefore, the change in $\delta^{18}O$ in cave calcite fed by drip water cannot be simply interpreted as a proxy for the original seasonal oxygen isotopic variability in local precipitation.

During the monitoring period, drip rates for all the sites were very low, ranging between 0.7–2 drips per hour. However, there was a significant seasonal variation in electrical conductivity at three of the six drip sites, with most peak values occurring during the rainy season. Interestingly, the drip water did not show significant variability in pH during the whole monitoring period except for an increasing trend at all six drip sites during September–October 2013, which may have been caused by abnormal changes in summer rainfall in 2013. On the other hand, concentrations of dissolved major cations (Mg^{2+}, Ca^{2+}) in the cave drip water do not show significant changes. In addition, concentrations of CO_2 and temperature in Zhenzhu Cave show significant seasonal variations, with peak concentrations in the summer and lowest concentrations in the winter. Changes in the concentration of CO_2 negatively correlate with seasonal temperature differences between the cave environment and the surface (from Shijiazhuang meteorological station) at a high confidence level (R^2=0.78). This may demonstrate that ventilation possibly caused seasonal variability in CO_2 in Zhenzhu Cave.

High-Resolution Summer Monsoon Intensity Variations in Central China From 26,000 to 11,000 Years Before Present as Revealed by Stalagmite Oxygen Isotope Ratios

By Dong Li[1], Liangcheng Tan[1,2], Yanjun Cai[1,2], Zhisheng An[1], Xiuyang Jiang[3], and Hai Cheng[2,4]

[1]Institute of Earth Environment, Chinese Academy of Sciences, Xi'an 710061, China

[2]Institute of Global Environment Change, Xi'an Jiaotong University, Xi'an 710054, China

[3]College of Geography Science, Fujian Normal University, Fuzhou 350007, China

[4]Department of Earth Sciences, University of Minnesota, Minneapolis, MN 55455, USA

Abstract

Asian summer monsoon intensity variations with a resolution of approximately 37 years from 26,000 to 11,000 years before present (ka BP) were reconstructed based on 14 thorium-230 ages and 344 oxygen isotope analyses from core profile samples obtained from stalagmite XL15 in Xianglong Cave, central China. The results are highly similar to the ice core oxygen isotope record from Greenland on orbital to millennial scales (Grootes and Stuiver, 1997). Our record is also similar to the previously published Hulu Cave record, but with larger amplitude (Wang and others, 2001). The larger amplitude may result from moisture sources farther north of Xianglong Cave. A distinct increase in oxygen isotope ratios ($\delta^{18}O$) in stalagmite core samples from XL15 at approximately 24 ka BP, 16 ka BP, and 12 ka BP was found, indicating three millennial-scale climate events (Heinrich 2, Heinrich 1, and Younger Dryas, respectively) since the last glacial maximum recorded in central China.

Selected References

Grootes, P.M., and Stuiver, M., 1997, Oxygen 18/16 variability in Greenland snow and ice with 10^{-3}- to 10^{5}-year time resolution: Journal of Geophysical Research, v. 102, issue C12, p. 26455–26470, doi: 10.1029/97JC00880.

Wang, Y.J., Cheng, H., Edwards, R.L., An, Z.S., Wu, J.Y., Shen, C.C., and Dorale, J.A., 2001, A high-resolution absolute-dated Late Pleistocene monsoon record from Hulu Cave, China: Science, v. 294, issue 5550, p. 2345–2348, doi: 10.1126/science.1064618.

Controls on the Oxygen Isotopic Variability of Meteoric Precipitation, Drip Water, and Calcite Deposition at Baojinggong Cave and Shihua Cave, China

By Lijun Tian[1], Yongli Gao[1], Ming Tan[2], and Wuhui Duan[2]

[1]Center for Water Research, Department of Geological Sciences, University of Texas at San Antonio, One UTSA Circle, San Antonio TX 78249

[2]Institute of Geology and Geophysics, Chinese Academy of Sciences, Beijing, 100029 China

Abstract

Oxygen isotopic compositions of speleothems ($\delta^{18}O_s$) in China caves have been used to interpret variations in East Asian summer monsoon (EASM) history based on the following assumptions: (1) the oxygen isotopic composition of meteoric precipitation ($\delta^{18}O_p$) reflects the local summer precipitation or EASM intensity, (2) the oxygen isotopic composition of drip waters ($\delta^{18}O_w$) follows changes in $\delta^{18}O_p$, and (3) the oxygen isotopic composition of calcite deposition ($\delta^{18}O_c$) is undergoing equilibrium fractionation with $\delta^{18}O_w$. Therefore, an understanding of the processes that control the $\delta^{18}O$ variability among meteoric precipitation, and drip waters and their corresponding calcite deposition, is essential for proper interpretation of speleothem $\delta^{18}O$ values.

A nearly 3-year-long (2011–2013) on-site monitoring program has been carried out with monthly sampling at Baojinggong Cave in South China and Shihua Cave in North China. Although there are differences in climatic conditions and cave geology between the two caves, we find that consistent controls on the $\delta^{18}O_p$, $\delta^{18}O_w$, and $\delta^{18}O_c$ at Baojinggong Cave and Shihua Cave are as follows:

1) The "Circulation effect" of $\delta^{18}O_p$

The $\delta^{18}O_p$ values at the two caves do not correlate well with rainfall amount or temperature at seasonal or inter-annual scales. We find a similar seasonal circulation effect of $\delta^{18}O_p$ at the two caves in the summer monsoon season—the $\delta^{18}O_p$ value is relatively high if the short-distance water vapor is from the Pacific Ocean, whereas the $\delta^{18}O_p$ value is relatively low if the long-distance water vapor is from the Indian Ocean.

2) The "Evaporation effect" of $\delta^{18}O_w$

The amplitudes of the $\delta^{18}O$ values decrease greatly from precipitation to drip water, which is "smoothed" when waters infiltrate through the vadose zone at the two caves. The $\delta^{18}O$ versus δD plots of drip waters are slightly below the corresponding local meteoric water line. The average values of $\delta^{18}O_w$ at all drip sites are higher than the annually weighted $\delta^{18}O_p$ values. The "peaks" of $\delta^{18}O_w$ correspond with the droughts above the cave or low humidity inside the cave. Therefore, seasonal changes in $\delta^{18}O_w$ are due to evaporation processes in the vadose zone and inside the cave.

3) The "Ventilation effect" of $\delta^{18}O_c$

The CO_2 concentration is higher in the summer season and lower in the winter season at the two caves. The drip sites closer to cave entrances were affected by strong cave ventilation and have lower CO_2 concentrations. Spatial variations in the carbon and oxygen isotopic composition of calcite deposited on glass plates show good positive correlations, which indicate a kinetic fractionation effect. The $\delta^{18}O_c$ values during enhanced ventilation periods are isotopically heavier than those of calculated results based on $\delta^{18}O_w$ and temperature under equilibrium fractionation.

Use of Seismic-Reflection and Multibeam-Bathymetry Data to Investigate the Origin of Seafloor Depressions on the Southeastern Florida Platform

By Kevin J. Cunningham[1], Jared W. Kluesner[2], Richard L. Westcott[3], Daniel R. Ebuna[4], and Cameron Walker[5]

[1]U.S. Geological Survey, Caribbean-Florida Water Science Center, 3321 College Avenue, Davie, FL 33314

[2]U.S. Geological Survey, Pacific Coastal and Marine Science Center, 2885 Mission Street, Santa Cruz, CA 95060

[3]Cherokee Nation Technology Solutions, 3321 College Avenue, Davie, FL 33314

[4]Earth and Planetary Sciences Department, University of California, Santa Cruz, CA 95084

[5]Walker Marine Geophysical Inc., 7061 NE 8th Drive, Boca Raton, FL 33487

Abstract

Numerous large, semicircular, deep submarine depressions on the seafloor of the Miami Terrace, a bathymetric bench that interrupts the Atlantic continental slope on the southeastern Florida Platform, have been described as submarine sinkholes resulting from freshwater discharge at the seafloor and dissolution of carbonate rock. Multibeam-bathymetry and marine, high-resolution multichannel 2D and 3D seismic-reflection data acquired over two of these depressions at water depths of about 250 m ("Miami sinkhole") and 336 m ("Key Biscayne sinkhole") indicate the depressions are pockmarks. Seafloor pockmarks are concave, crater-like depressions that form through the outburst or venting of fluid (gas or liquid or both) at the sea floor and are important seabed features that provide information about fluid flow on continental margins. Both the Miami sinkhole and Key Biscayne sinkhole (about 25 and 48 m deep, respectively) have a seismic-chimney structure beneath them that indicates an origin related to seafloor fluid expulsion, as supported by multi-attribute analysis of the Key Biscayne sinkhole. Further, there is no widening of the depressions with depth as in the northern Fort Worth Basin, where widening of similar seismic, subcircular, karst-collapse structures is common. However, hypogenic karst dissolution is not ruled out as part of the evolution of the Miami Terrace depressions. Indeed, a hypogenic karst pipe plausibly extends downward from the bottom of the Key Biscayne sinkhole, providing a pathway for focused upward flow of fluids to the seafloor. In the Key Biscayne sinkhole, the proposed karst pipe occurs above the underlying seismic chimney that displays flat bright spots (a hydrocarbon indicator) in the seismic data, showing that possible fluids are currently trapped beneath the pockmark within a tightly folded popup structure. The Miami Terrace depressions have seismic-reflection features similar to modern pockmarks imaged on the Maldives carbonate platform. The seismic-reflection data also show that ancient satellite expulsions formed buried pockmarks, slumps, and paleo-collapse structures in the carbonate sediments near the Key Biscayne sinkhole. Additional processing of the 3D seismic data will aid in elucidating the origin of these seafloor depressions.

Characterization of Microkarst Capping Lower Eocene High-Frequency Carbonate Cycles, Southeast Florida

By Shakira A. Khan[1] and Kevin J. Cunningham[2]

[1]Cherokee Nation Technologies c/o U.S. Geological Survey, Caribbean-Florida Water Science Center, 3321 College Avenue, Davie, FL 33314

[2]U.S. Geological Survey, Caribbean-Florida Water Science Center, Carbonate Aquifer Characterization Laboratory, 3321 College Avenue, Davie, FL 33314

Abstract

Carbonate rocks of the lower Eocene Oldsmar Formation, which compose the lower Floridan aquifer, are a result of depositional processes influenced by low-amplitude, high-frequency sea-level fluctuations. These rocks have been subjected to repeated subaerial exposure during low stands in sea level, resulting in dissolution-formed secondary porosity. A 17-foot length of limestone core acquired from the Oldsmar Formation was recovered from a water utility well (G-2994) within the City of Hollywood, Broward County, Florida. The core section contains a vertical succession of eight shallowing-upward, high-frequency cycles deposited in peritidal environments. Six of these cycles, deposited in shallow marine subtidal to tidal flat depositional environments, are capped with lime mudstone permeated with decimeter-scale microkarst. These six microkarstic cycle caps were selected for detailed examination.

Microkarst morphology and associated sedimentary features, including depositional texture and constituents present at cycle boundaries, were described using data from thin sections and core samples. In addition, a 6-inch section of the core, which spans a cycle boundary, was scanned by using high-resolution computed tomography. The tomography scan was used to produce three-dimensional visualizations that show the detailed geometry of a single microkarstic surface contained in the core sample. The High-Resolution X-ray Computed Tomography Facility at the University of Texas at Austin conducted the computed tomography scan and its computer image rendering.

Eight high-frequency cycles, identified in the cored interval from 2,630 to 2,647 feet below land surface, are defined by an idealized vertical lithofacies succession characterized by benthic foraminiferal packstone and grainstone in the lower part that has indications of shallowing upwards through wackestone and packstone to a lime mudstone or ostracod-rich lime mudstone cap. Each cycle is bounded above and below by subaerial exposure surfaces. The upper part of the cycles exhibits microkarst with millimeter- to decimeter-scale paleotopography. The extent of karstification may affect only the upper few millimeters of the bed in which it developed, or it may extend downward a distance of up to 2 decimeters into the lime mudstone to wackestone units that form the uppermost part of the cycles. The morphology of these microkarstic surfaces varies depending on the intensity of dissolution that has occurred and possibly on the duration of subaerial exposure. One morphology appears on some slabbed core faces as an irregular linear feature that forms sharp, small-scale pinnacles separated by deep channels created by dissolution that create an intricate network of cavities. Another morphology has a more subdued, undulating surface with round-bottomed dissolution channels. Channels are open upward or semi-enclosed due to overhanging tips of adjacent pinnacles. Along slabbed core surfaces, areas of extensive dissolution can appear as isolated “floating” lime mudstone to wackestone clasts in a grain-dominated host rock, but actually are connected downward to the karstic mud-rich bed.

Dissolution induced by subaerial exposure is responsible for many examples of secondary porosity associated with high permeability in aquifers, as well as in oil and gas field units around the world. A detailed description of small-scale karst and its relation to subaerial exposure at the high-frequency cycle scale has generally not been done extensively. This study of microkarstic features associated with high-frequency cycle boundaries in the Oldsmar Formation may provide insight into the occurrence and extent of this type of secondary porosity within platform carbonates.

Overview of the Revised Hydrogeologic Framework of the Floridan Aquifer System, Florida and Parts of Alabama, Georgia, and South Carolina

By Eve L. Kuniansky[1] and Jason C. Bellino[2]

[1]U.S. Geological Survey, Water Mission Area, 1770 Corporate Drive, Suite 500, Norcross, GA 30093

[2]U.S. Geological Survey, Caribbean-Florida Water Science Center, 4446 Pet Lane, Suite 108, Lutz, FL 33559

Abstract

The hydrogeologic framework for the Floridan aquifer system (FAS) has been revised (Williams and Kuniansky, 2015; Williams and Dixon, 2015) as part of a national program to assess groundwater availability by the U.S. Geological Survey Water Availability and Use Science Program. New studies and data that have become available since the original framework established by the U.S. Geological Survey in the 1980s (Miller, 1986; Bellino, 2011) were used in the revised framework, which is a product intended for regional (greater than 10,000 square miles [mi^2]) and subregional (1,000 to 10,000 mi^2) investigations, rather than site-scale (less than 1 mi^2) investigations. This overview describes differences in the revised mapping of the Floridan aquifer system from Miller (1986) as published in Williams and Kuniansky (2015) and how the revised framework was used in the development of layers for a regional groundwater flow model.

The Floridan aquifer system (FAS) underlies all of Florida and some of the less densely populated parts of southern Alabama, Georgia, and South Carolina (fig. 1), and is one of the principal regional aquifer systems in the United States. The FAS consists predominantly of permeable Tertiary-age carbonate rocks and some equivalent clastic units in the updip areas of Alabama, Georgia, and South Carolina. In Georgia and Florida, the aquifer system is the principal source of freshwater for agricultural irrigation, and industrial, mining, commercial, and public-supply use (Miller, 1986; Maupin and Barber, 2005). The FAS also locally yields abundant water supplies in southeastern Alabama and South Carolina. In all four States, the aquifer system covers approximately 100,000 mi^2. The aquifer system dips steeply into southeastern Mississippi and contains poor quality water; thus, it is not utilized for water supply in Mississippi and was not mapped by Miller (1986) or Williams and Kuniansky (2015). The FAS crops out in parts of southwest Georgia, southeast Alabama, and the western part of peninsular Florida where numerous karst features are present. In much of Florida and parts of Georgia and South Carolina, the FAS is overlain by an upper confining unit, which in local areas contains the Brunswick aquifer (Georgia) and the Intermediate aquifer system (Florida). Above the upper confining unit is the Surficial aquifer system (fig. 2). Below the FAS are less permeable rocks of the Cedar Keys Formation that also forms a confining unit.

The revised extent of the FAS (fig. 1) includes some of the updip clastic facies, which grade laterally into the Lower Floridan aquifer, and that have been previously included in the Southeastern Coastal Plain aquifer system, the FAS, or both. Additionally, the updip limit of the most productive part of the FAS was revised and indicates the approximate updip limit of the carbonate facies (former extent of FAS from Miller, 1986). The system includes Paleocene- to Miocene-age rocks that combine to form a vertically continuous sequence of mostly carbonate rocks that are interconnected, to varying degrees, vertically and horizontally within the system (Miller, 1986). In this revision, the system includes deeper rocks in a small area of Georgia where upper Cretaceous rocks are permeable and hydraulically connected to Paleocene rocks.

The most significant difference in the revised framework is the delineation of internal boundaries between the Upper and Lower Floridan aquifers. In the previous framework, discontinuous numbered middle confining units (MCUI through MCUVII; and MCUVIII in the Lower Floridan) were used to subdivide the system, some of which overlap each other vertically. Where units overlap, the least permeable rock unit within the middle part of the system was used to subdivide the system. Subregional variations in permeability, caused by facies changes, led to the use of different stratigraphic units to delineate the Upper and Lower Floridan aquifers in peninsular Florida by local hydrogeologists. Where none of these units exist, the entire thickness of the FAS acts as a single hydrogeologic unit and was named the Upper Floridan aquifer. This variability in the way the system was subdivided at the sub-regional scale presents a challenge for regional studies of the system as a whole. Additionally, many of the previously numbered middle confining units could no longer be defined as low permeability or confining units (Williams and others, 2013; Williams and Kuniansky, 2015), based on results from numerous packer tests and flowmeter log data collected from the late 1980s to 2010, when work on the revised framework started.

In the revised framework, internal boundaries between the Upper and Lower Floridan aquifers are mapped using results from local studies; regional correlations of lithostratigraphic and hydrogeologic units or zones; and new information from digital televiewers, flowmeter logging analyses, and thousands of new borehole logs and aquifer tests (Kuniansky and Bellino, 2012; Kuniansky and others, 2012; Williams and others, 2013). The nomenclature for the previously numbered middle confining units (MCUI–MCUVIII) of Miller (1986) is abandoned. Although the term "confining unit" is not totally abandoned within the revised framework, a new term "composite unit" is introduced for lithostratigraphic units that cannot be defined as either a confining or aquifer unit over their entire extent. This naming convention and mapping approach is a departure from the previous framework of the late 1980s in that three regionally mappable lithostratigraphic units are used to consistently subdivide the aquifer system into upper and lower aquifers across the entire aquifer system, but does not change the conceptual flow system. General hydraulic properties subareas of composite units (for example, confining, semi-confining, leaky, or permeable) are delineated and indicate where the Upper and Lower Floridan aquifers behave as one aquifer system or are hydraulically separate. The revised framework uses stratigraphic names for the composite units within the middle part of the FAS rather than numbers. The three laterally extensive units used to subdivide the FAS into the Upper and Lower Floridan aquifers, from shallowest to deepest are the Bucatunna Clay confining unit (BCU), the Lisbon-Avon Park composite unit (LISAPCU), and the middle Avon Park composite unit (MAPCU). All three of these units are subregional in extent, with the BCU present in the Florida panhandle; the LISAPCU present in Georgia, southeast Alabama, South Carolina, and northern peninsular Florida; and the MAPCU present in central and southern peninsular Florida. In southeast Georgia and northeast Florida both the LISAPCU and MAPCU are present.

The revised framework introduces more zones of distinctly higher or lower permeability along narrower stratigraphic intervals within either the Upper or Lower Floridan aquifer to allow finer delineation of permeability variations within the aquifer system. The zones and units that subdivide the system are subregional in extent; thus, one or more geologic formations may be grouped to represent an important zone or unit while attempting to stay within the narrowest stratigraphic interval possible. Important considerations for mapping were (1) the mappability of the units or zones, (2) the stratigraphic position and continuity of hydraulic properties in subregional areas for logical grouping, (3) the degree of hydraulic head separation between zones or units, and (4) the use of geophysical log markers to define the positions of units or zones within the aquifer system. A schematic diagram of the

relative vertical and horizontal relations of aquifers, zones, composite and confining units, and model layers by regions of the FAS is shown on figure 2.

As the FAS thickened to over 3,000 feet (ft) southward, more zones were delineated. In peninsular Florida, from top to bottom, there are three zones in the Upper Floridan aquifer: the uppermost permeable zone (UPZ), the Ocala-Avon Park lower permeability zone (OCAPLPZ), and the Avon Park permeable zone (APPZ) (fig. 2). The uppermost part of the Upper Floridan is extremely permeable and mapped as the UPZ. There is a facies change within the Avon Park where it is less permeable and part of the LISAPCU in northern Florida, but the formation becomes thicker and more permeable to the south. The upper part of the Avon Park is somewhat less permeable than the APPZ or UPZ and mapped as the OCAPLPZ, but is part of the Upper Floridan. The middle part of the Avon Park is less permeable than the Upper or Lower Floridan aquifer zones and mapped as the MAPCU; it is used in southern peninsular Florida to divide the FAS into the Upper and Lower Floridan aquifers. The Lower Floridan aquifer in peninsular Florida is subdivided into the lower Avon Park permeable zone (LAPPZ) and the Oldsmar permeable zone (OLDSPZ) by a mappable, generally less permeable unit called the Glauconite marker unit (GLAUCU). This unit is mapped by using the geophysical log signature for a distinctive glauconitic interval located in the uppermost part of the Oldsmar Formation. In the lower part of the Oldsmar Formation are extremely permeable cavernous areas locally named the Boulder Zone in south Florida and the Fernandina permeable zone in northeastern Florida and southeastern Georgia. In the revised framework, the Boulder Zone and Fernandina permeable zone are within the OLDSPZ.

In developing the updated regional model of the FAS with MODFLOW-2005 (Harbaugh, 2005), much thought and discussion went into the determination of how to incorporate the revised framework into the model with the least number of model layers while retaining the important subregional variations in hydraulic properties. The maximum number of layers discussed was 11, but the final number retained was 9. All model layers are continuous and have a minimum thickness of 50 ft. Thus, many of the layers may be composed of several different aquifers, or confining or composite units or zones within an aquifer (fig. 2). Because there are actually three different discontinuous units that are used to separate the Upper and Lower FAS, and more zonations of permeability variations occur vertically in peninsular Florida, model layer 5 is composed of both the Lower FAS in the northern part of the study area and the Upper FAS in peninsular Florida. The variation in hydraulic properties of subregions is based on the revised framework (Williams and Kuniansky, 2015) using the spatial datasets for the framework (Williams and Dixon, 2015) and using aquifer test datasets (Kuniansky and Bellino, 2012; Kuniansky and others, 2012). The current regional model of the freshwater part of the system has an equal-spaced model grid with 5,000-ft sides, and has a total of 863,971 active cells. Once the model of the freshwater part of the system is calibrated to historic flow and head datasets, it will be used to quantify current fresh groundwater resources, evaluate how these resources have changed over time, and provide forecast response tools for climate change/weather extremes, sea-level rise, and projected groundwater pumpage.

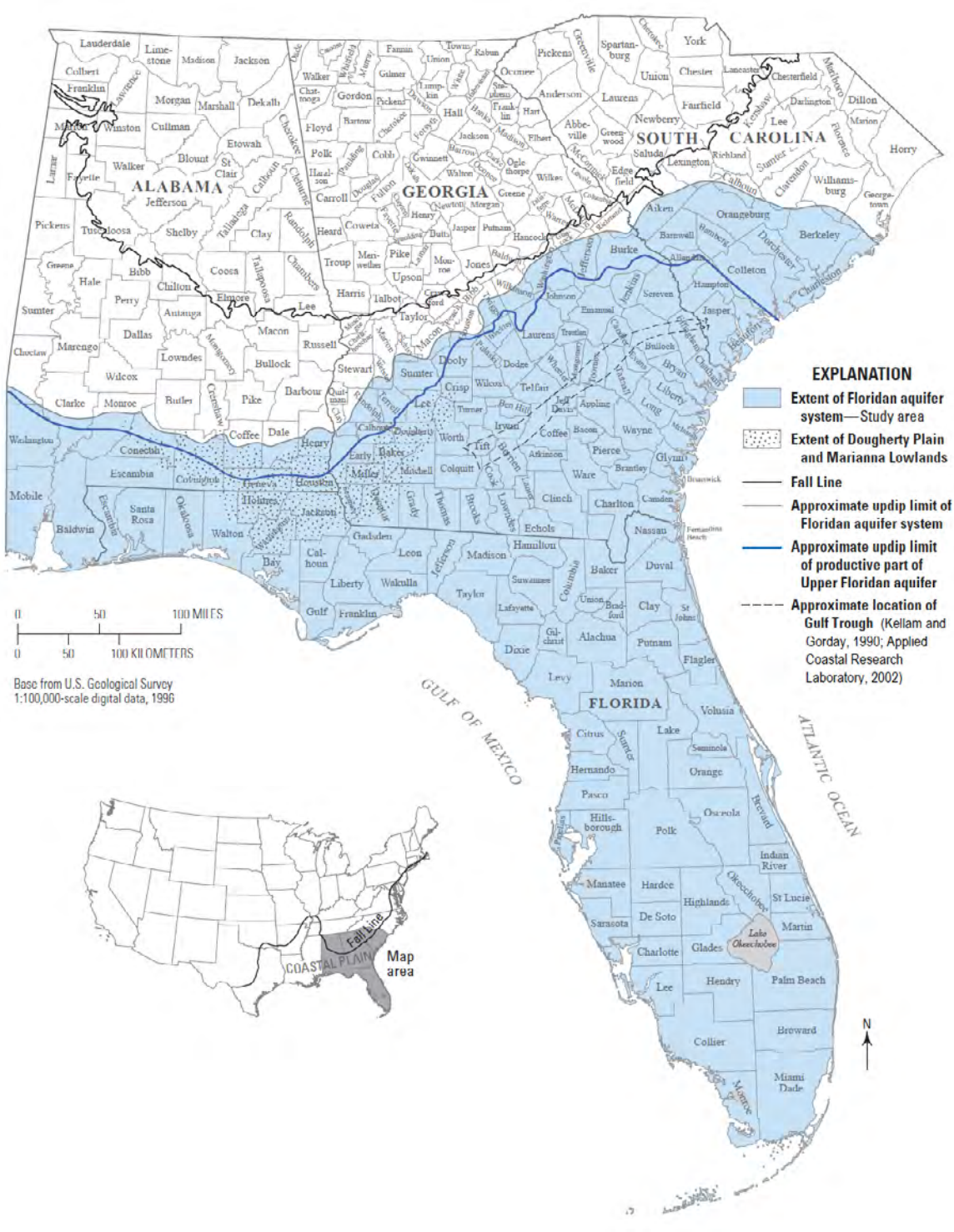

Figure 1. Location of the study area and approximate updip limit of the Floridan aquifer system, southeastern United States (from Williams and Kuniansky, 2015).

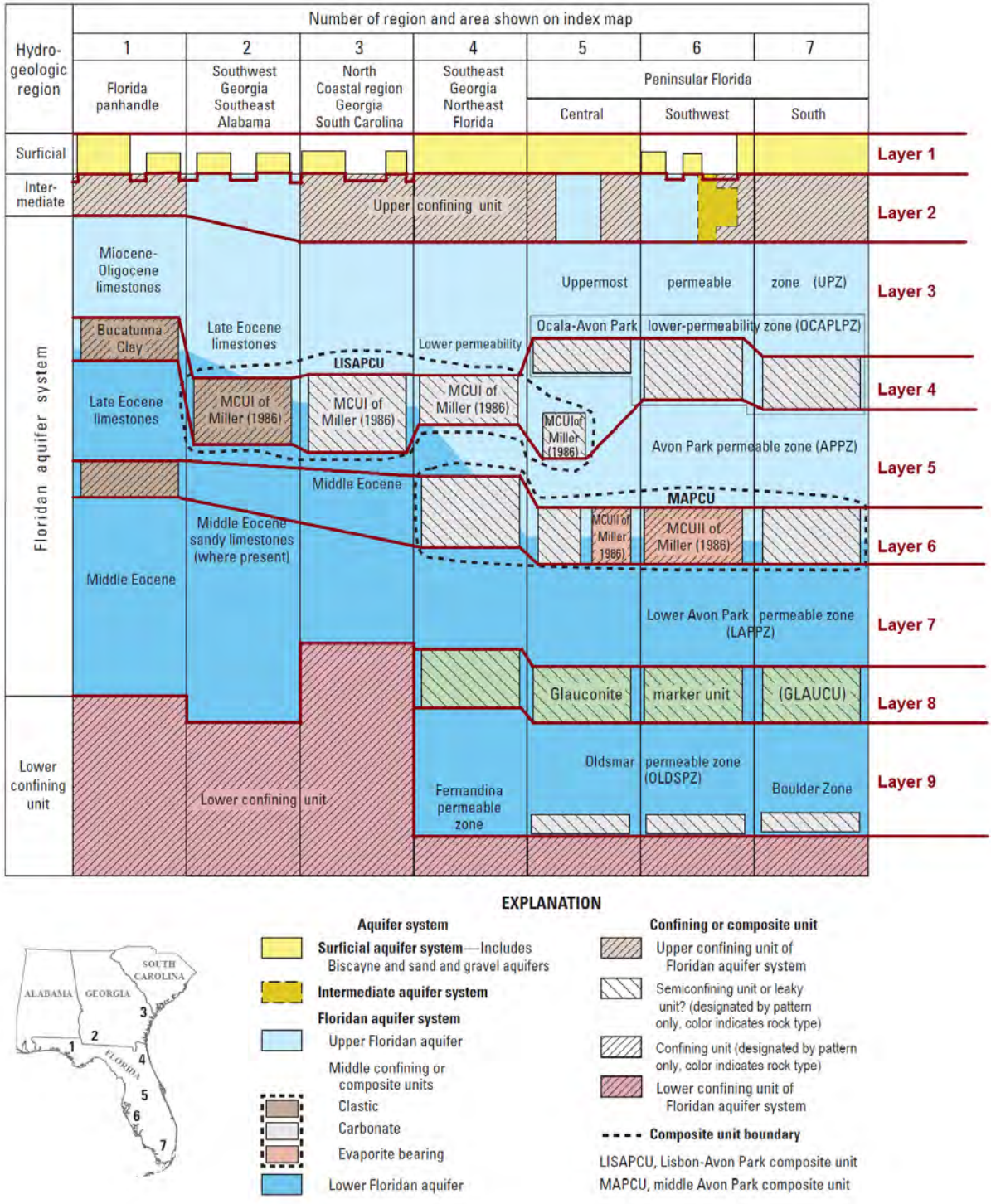

Figure 2. Aquifers, composite and confining units, and model layering of the Floridan aquifer system, southeastern United States (modified from Williams and Kuniansky, 2015, figure 6).

References Cited

Applied Coastal Research Laboratory, 2002, Gulf trough and Satilla line data analysis: Georgia Southern University, project report 48 prepared for the Georgia Environmental Protection Division of the Department of Natural Resources, Georgia Geologic Survey, 16 p.

Bellino, J.C., 2011, Digital surfaces and hydrogeologic data for the Floridan aquifer system in Florida and in parts of Georgia, Alabama, and South Carolina: U.S. Geological Survey Data Series 584, http://pubs.usgs.gov/ds/584/.

Harbaugh, A.W., 2005, MODFLOW-2005—The U.S. Geological Survey modular ground-water model—The ground-water flow process: U.S. Geological Survey Techniques and Methods 6-A16.

Kellam, M.F., and Gorday, L.L., 1990, Hydrogeology of the Gulf Trough—Apalachicola Embayment area, Georgia: Georgia Geologic Survey Bulletin 94, 74 p.

Kuniansky, E.L., and Bellino, J.C., 2012, Tabulated transmissivity and storage properties of the Floridan aquifer system in Florida and parts of Georgia, South Carolina, and Alabama: U.S. Geological Survey Data Series 669, 37 p., http://pubs.usgs.gov/ds/669 .

Kuniansky, E.L., Bellino, J.C., and Dixon, J.F., 2012, Transmissivity of the Upper Floridan aquifer in Florida and parts of Georgia, South Carolina, and Alabama: U.S. Geological Survey Scientific Investigations Map 3204, 1 sheet.

Maupin, M.A., and Barber, N.L., 2005, Estimated withdrawals from principal aquifers in the United States, 2000: U.S. Geological Survey Circular 1279, 46 p.

Miller, J.A., 1986, Hydrogeologic framework of the Floridan aquifer system in Florida and in parts of Georgia, Alabama, and South Carolina: U.S. Geological Survey Professional Paper 1403–B, 91 p.

Williams, L.J., and Dixon, J.F., 2015, Digital surfaces and thicknesses of selected hydrogeologic units of the Floridan aquifer system in Florida and parts of Georgia, Alabama, and South Carolina: U.S. Geological Survey Data Series 926, 24 p., http://doi.org/10.3133/ds926.

Williams, L.J., and Kuniansky, E.L., 2015, Revised hydrogeologic framework of the Floridan aquifer system in Florida and parts of Georgia, Alabama, and South Carolina: U.S. Geological Survey Professional Paper 1807, 140 p., 23 pls., http://doi.org/10.3133/pp1807.

Williams, L.J., Raines, J.E., and Lanning, A.E., 2013, Geophysical log database for the Floridan aquifer system and southeastern Coastal Plain aquifer system in Florida and parts of Georgia, Alabama, and South Carolina: U.S. Geological Survey Data Series 760, 11 p., http://pubs.usgs.gov/ds/760/.

Numerical Simulation of Karst Groundwater Flow at the Laboratory Scale

By Roger Pacheco Castro[1], Ming Ye[1], Xiaohu Tao[2], Jian Zhao[2], and Xiaoming Wang[3]

[1]Florida State University, Geophysical Fluid Dynamics Institute and Department of Scientific Computing, 600 W. College Avenue, Tallahassee, FL 32306

[2]Hohai University, College of Water Conservancy and Hydropower Engineering, 1 Xikang Road, Nanjing 210098, P.R. China

[3]Florida State University, Department of Mathematics, 600 W. College Avenue, Tallahassee, FL 32306

Abstract

A three-dimensional sand box was built to explore flow exchange between porous media and karst conduits in order to improve our understanding of groundwater flow in karst aquifers. A tank is filled with sand as the porous medium, which is coupled with a pipe used to simulate a conduit. Measured heads and flow rates of the laboratory experiments, development of a numerical model with MODFLOW-Conduit Flow Process mode 1 (MODFLOW-CFP1), and model calibration are discussed. The calibration is performed manually using FloPy, which allows the integration of MODFLOW-CFP1 with Python to make the modeling process more user friendly. With the use of FloPy, we adjusted hydraulic gradient and the exchange coefficient of MODFLOW-CFP1 within a given range, and generated response surfaces for flow rates. This allowed us to find a combination of calibration parameter values that yielded satisfactory agreement between simulated and measured flow rates. Our future work is to focus on the integration of automatic calibration tools and the comparison of simulated results with other models such as the Darcy-Stokes model.

Introduction

Karst aquifers develop in soluble rocks such as carbonates. They are characterized by a large heterogeneity in hydraulic properties owing to dissolution of the rocks, creating preferential flow paths. It is estimated that 25 percent of the world's population depends on karst aquifers for water supply (Ford and Williams, 2007). Goldscheider and others (2007) presented an example where almost half the population of a city was affected by contaminant transport through preferential flow paths in a karst aquifer. Flow modeling in karst is challenging because the assumption of equivalent porous media may not be valid, and the assumption may cause risk to public health due to the presence of preferential flow paths where contaminants can move faster. There are several approaches to modeling karst groundwater flow depending on the conceptualization of porous media and karst conduits. This study only considered a coupled discrete-continuum model (Teutsch and Sauter, 1991, 1998), a type of hybrid model (Kuniansky, 2014), in which the porous media are assumed to be a three-dimensional (3-D) equivalent porous media, and the conduits are simulated by using a network of one-dimensional discrete pipes that can flow under laminar and non-laminar conditions. Hybrid models have the advantage of integrating all of the existent information about the conduit system (Shoemaker and others, 2008). This study used MODFLOW-CFP mode 1 [MODFLOW-CFP1] (Shoemaker and others, 2008), a hybrid modeling approach. Examples of using MODFLOW-CFP1 for field applications are found in Gallegos and others (2013), Hill and others (2010), and Kuniansky (2016 a, b), for areas in Florida where the spring conduits have been previously mapped.

Gallegos and others (2013) also applied MODFLOW-CFP1 to simulate one lab experiment.

With the objective of evaluating the performance of hybrid models and improving our understanding of karst flow, a 3-D sand box was built to simulate a simple karst system to which MODFLOW-CFP1 could be applied (fig. 1). In this paper we present some results of the laboratory experiments and the process of a manual calibration for MODFLOW-CFP1 using FloPy (Bakker and others, 2016), a Python package that integrates MODFLOW with Python. The FloPy package facilitates the generation of MODFLOW input files, the execution of MODFLOW, and the analysis of modeling results. Because the current version of FloPy does not work with MODFLOW-CFP, we have developed new code for FloPy to make it compatible.

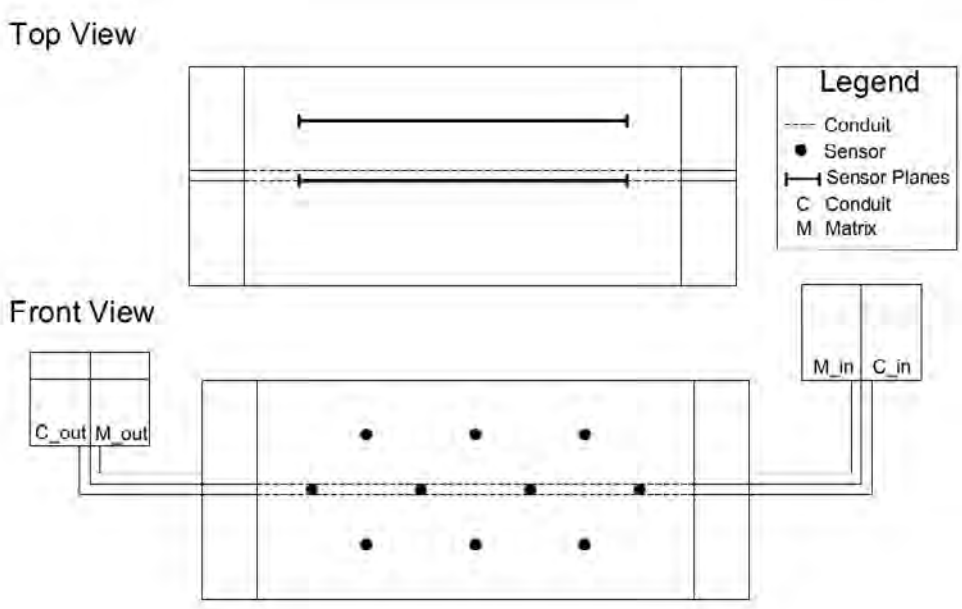

Figure 1. Schematic view of the sand box used to simulate the simplified karst system.

Experimental Data Collection

Figure 1 shows a schematic diagram of the 3-D sand box. The tank is made of Plexiglas and is 100 centimeters (cm) long, 43.5 cm wide, and 41.8 cm high. Along the length, at each end of the sand box, a reservoir is used to maintain constant head, which controls the inflow and outflow of the system. Each reservoir is 10 cm in length. The remaining 80 cm of the sand box is filled with fine sand. A stainless steel pipe is placed in the center of the sand box to simulate a karst conduit. The pipe is 80 cm in length and 1.9 cm in diameter. A number of holes 0.2 cm in diameter are drilled in the pipe to allow water exchange between the porous medium and the karst pipe. A fine mesh was used to prevent sand infiltration into the porous pipe. Two reservoirs are also placed at the two ends of the pipe. A total of four external reservoirs are used to control inflow to and outflow from the porous medium and conduit by controlling hydraulic head in the reservoirs. The heads within the system are recorded using 20 sensors. As shown in the top view of figure 1, the sensors are placed in two parallel planes, each one containing 10 sensors. One plane is located next to the conduit, and the other is 11 cm from the first plane (fig. 1). The system is sealed at the top with Plexiglas, thus representing a confined karst aquifer. The porous medium is

fine sand with a hydraulic conductivity of 0.788 cm/s that was measured in the laboratory using a Darcy column. For the data presented here, the outflow tank for the matrix and conduit are kept at the same height of 46.4 cm above an established datum. At the beginning of the experiment, the inflow tanks of matrix and conduit are also set at the same height of 60 cm. After the experiment starts, the conduit tank is raised incrementally by 2.5 cm until a height of 75 cm is reached. This gives a total of seven sets of head measurements that were made when the system reached steady state. In addition to the head measurements by the sensors, heads and flow rates at the inflow and outflow ends of the sand box are recorded. Heads at the inflow are measured before the water enters the system, and heads at the outflow are measured after water leaves the system. The flow rates are calculated by measuring pressure drops in the pipes connected to the tank.

Results

Figure 2 plots the heads and flow rates measured at the inflow and outflow ends of the sand box for the matrix and conduit for the seven experimental configurations. Figure 2(a) shows that at the inflow the heads for the matrix and conduit have almost the same values as the conduit head increases. At the outflow end, the head for the conduit becomes increasingly higher than the head for the matrix as the conduit head at the inflow end increases. For the flow rates, figure 2(b) shows that the flow rate in the conduit increases as the conduit head increases; however, the matrix inflow rate decreases at a similar rate. This is caused by the increase in water flow from the conduit to the matrix. In all the cases, the mass balance error was less than 3.5 percent.

(a) (b)

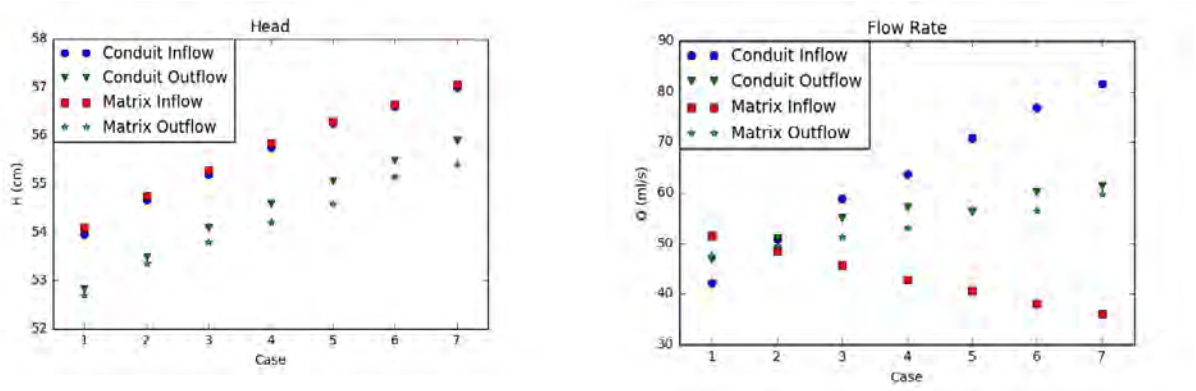

Figure 2. Graphs showing (a) Heads measured at the inflow and outflow for the conduit and matrix for the seven configurations, and (b) Flow rates measured at the inflow and outflow for the conduit and matrix for the seven configurations.

A numerical model was developed using MODFLOW-CFP1 to simulate the measured heads and flow rates. The model consisted of 31 rows, 54 columns, and 31 layers, as shown on figure 3. The conduit is located in layer 16 and row 16, between columns 3 and 52, and the grid is finer close to the conduit. For the conduit layer, its height is 1.9 cm, the diameter of the conduit. In the numerical simulation, we used a critical Reynolds number between 2000 and 4000 because a straight stainless steel pipe was being used. The tortuosity for a straight pipe is 1, and 0.01 cm was used for the roughness. The roughness for new stainless steel has a range of

0.1 to 0.015 cm, depending on the surface finish (Albright, 2009). The measured water temperature was 12 ^{o}C. The boundary conditions are constant head at the inflow and outflow for the matrix and the conduit, using the values measured in the laboratory. The experimental values used for case 5 are listed in table 1.

Table 1. Measured values of head and flow rate in the laboratory.
[cm, centimeters; ml/s, milliliters per second]

	Head In (cm)	Head Out (cm)	Flow Rate In (ml/s)	Flow Rate Out(ml/s)
Conduit	56.25	55.05	70.81	56.35
Matrix	56.30	54.60	40.62	56.52

Before model calibration, the response surfaces of the measurements were plotted for matrix hydraulic conductivity and the matrix-conduit flow exchange coefficient (α). These two variables were chosen as calibration parameters, because they are unknown. Although matrix hydraulic conductivity of the sand was measured in a Darcy column, the value may have changed when packing the sand into the tank. When evaluating the response surface, the matrix hydraulic conductivity (K) varied in the range 0.5 to 1.7 cm/s, and the exchange coefficient (α) ranged from 0.001 to 31. The range of the exchange coefficient is large, because its value is completely unknown. By visually checking the response surfaces we observed that it was possible to get a combination that may calibrate the matrix flow rates; however, the conduit flow rates were always overestimated by the model.

During the manual model calibration, the roughness was increased from 0.01 cm to 0.1 cm to account for the extra roughness caused by the pipe holes. With this change, a closer match between measured and simulated conditions was obtained. Figure 4 shows a plot for the root mean square error (RMSE). From this plot, an evaluation can be made with regard to whether a pair of parameters can be used to calibrate the model. The minimum error is given at $K = 1.5$ cm/s and $\alpha = 7$ cm^2/s, and the simulated flow rates for those parameters are shown on figure 5. There is a satisfactory match between measured and simulated values; however, simulated head values are overestimated.

Conclusion and Future Work

A MODFLOW-CFP1 model was developed to simulate groundwater flow in a confined karst aquifer. The preliminary results show that satisfactory agreement between simulated and measured flow rates can be achieved, although measured heads at the sensors are being overestimated. Future work is focused on the use of automatic calibration tools such as PEST (Doherty, 2016). In addition, we will test other experimental configurations to better understand groundwater flow in karst aquifers.

Acknowledgments

Roger Pacheco acknowledges Fulbright and CONACYT for their financial support, and to Hohai University for giving me the opportunity to do an internship and for the use of their facilities for the experimental work.

(a) (b)

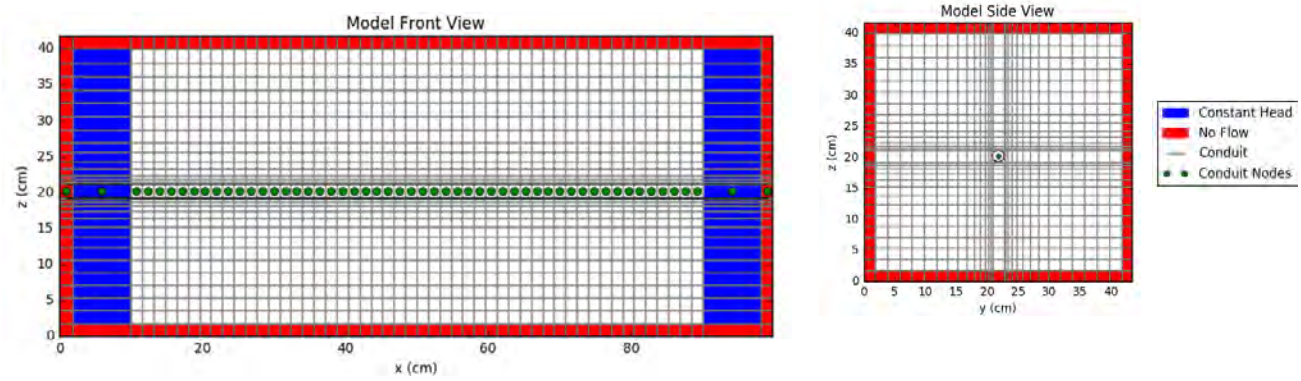

Figure 3. Model discretization showing (a) Front view of vertical cross section along row 16 where conduit is located, and (b) Side view of vertical cross section along column 16.

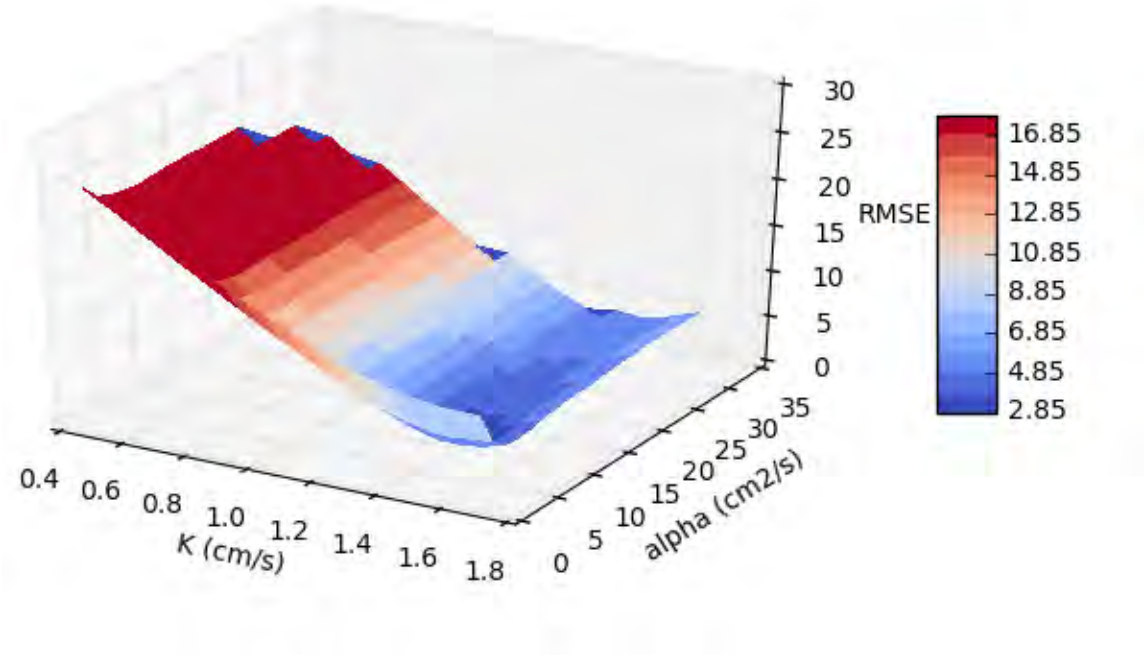

Figure 4. Surface response for the root mean square error (RMSE). The color bar is truncated for a better visualization of the minimum value.

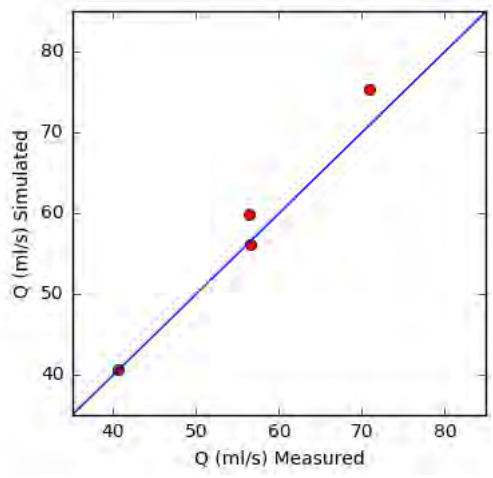

Figure 5. Comparison of measured and simulated flow rates. The blue line is the identity line.

References Cited

Albright, L., 2009, Albright's chemical engineering handbook, CRC Press, Taylor & Francis Group, p. 421.

Bakker, M., Post, V., Langevin, C.D., Hughes, J.D., White, J.T., Starn, J.J., and Fienen, M.N., 2016, FloPy v3.2.4: U.S. Geological Survey Software Release, 08 February 2016, http://dx.doi.org/10.5066/F7BK19FH

Doherty, J., 2016, PEST model-independent parameter estimation user manual part I: PEST, SENSAN and Global Optimizers, 6th ed., Watermark Numerical Computing, 390 p.

Ford, D.C., and Williams, P.W., 2007, Karst geomorphology and hydrology: John Wiley & Sons Ltd., 576 p.

Gallegos, J.J., Hu, B.X., and Davis, Hal, 2013, Simulating flow in karst aquifers at laboratory and sub-regional scales using MODFLOW-CFP: Hydrogeology Journal, v. 21, no. 8, p. 1749–1760.

Goldscheider N., Drew D., and Worthington S., 2007, Introduction—Methods in karst hydrogeology, *in* Goldscheider, N., and Drew, D., eds, International Association of Hydrogeologists, International Contributions to Hydrogeology Report 26, 264 p.

Hill, M.E., Stewart, M.T., and Martin, A., 2010, Evaluation of the MODFLOW-2005 Conduit Flow Process: Ground Water, v. 48, p. 549–559.

Kuniansky, E.L., 2014, Taking the mystery out of mathematical model applications to karst aquifers—A primer, *in* Kuniansky, E.L., and Spangler, L.E., eds., U.S. Geological Survey Karst Interest Group Proceedings, Carlsbad, New Mexico, April 29–May 2, 2014: U.S. Geological Survey Scientific Investigations Report 2014–5035, p. 69–81, http://dx.doi.org/10.3133/sir20145035 .

Kuniansky, E.L., 2016a, Simulating groundwater flow in karst aquifers with distributed parameter models—Comparison of equivalent porous media and hybrid flow approaches: U.S. Geological Survey Scientific Investigations Report 2016–5116, 14 p., https://dx.doi.org/10.3133/sir20165116

Kuniansky, E.L., 2016b, MODFLOW and MODFLOW Conduit Flow Process data sets for simulation experiments of the Woodville Karst Plain, near Tallahassee, Florida with three different approaches and different stress periods: U.S. Geological Survey data release, http://dx.doi.org/10.5066/F7PK0D87

Shoemaker, W., Kuniansky, E.L., Birk, S., Bauer, S. and Swain, E.D., 2008, Documentation of a Conduit Flow Process (CFP) for MODFLOW-2005: U.S. Geological Survey Techniques and Methods, book 6, chap. A24, 50 p.

Teutsch, G., and Sauter, Martin, 1991, Groundwater modeling in karst terranes—Scale effects, data acquisition and field validation, *in* Proceedings of the Third Conference on Hydrogeology, Ecology, Monitoring, and Management of Ground Water in Karst Terranes, Nashville, Tennessee, December 4–6, 1991: National Ground Water Association, Association of Ground Water Scientists and Engineers, and U.S. Environmental Protection Agency, p. 17–35.

Teutsch, G., and Sauter, Martin, 1998, Distributed parameter modelling approaches in karst hydrological investigations: Bulletin d'Hydrogeologie, v. 16, p. 99–110.

Hydrograph Recession Curve Analysis to Identify Flow Regimes in Karst Systems

By Rebecca B. Lambert and Cassi L. Crow

U.S. Geological Survey, Texas Water Science Center, South Texas Program Office, 5563 De Zavala Rd., Suite 290, San Antonio, TX 78249

Abstract

Analyzing the recession curves of groundwater-level hydrographs can be useful for identifying the types of flow regimes that characterize groundwater flow paths in karst systems. Flow regimes generally present in karst systems include conduit, mixed, and diffuse (matrix) and are related to the effective porosity and permeability of the aquifer strata through which groundwater flows. Recession curve analysis looks at inflection points (or breaks) in the water level measured in a well as the water level is declining after a rise or in the recession limb of a springflow hydrograph. These inflection points, or breaks, in the slopes of the water level or springflow discharge hydrographs are indicative of a change in flow regime or a change within a particular flow regime. In general, higher coefficient values indicate a steeper slope in the recession curve associated with movement or release of groundwater through conduit-type features of a karst aquifer, whereas lower coefficient values indicate a gentler, less steep recession slope associated with movement or release of water from diffuse (matrix) features of a karst aquifer. Recession coefficients with moderate slopes may indicate mixed flow regime types. Recession coefficients (α) were calculated for each part of the groundwater-level hydrograph for the karstic Edwards aquifer system by using a previously published equation (Milanović, 1976) related to the release or movement of water through an aquifer. Additional information on recession coefficient calculations in the Edwards aquifer can be found online at https://pubs.usgs.gov/sir/2007/5285/.

Reference Cited

Milanović, P.T., 1976, Water regime in deep karst—Case study of the Ombla Spring drainage area, *in* Yevjevich, V., ed., Karst hydrology and water resources–v. 1, Karst hydrology: Littleton, Colorado, Water Resources Publications, p. 165–191.

Surface-Water and Groundwater Interactions in the Upper Cibolo Creek Watershed, Kendall County, Texas

By Christopher Ray, John Ricci, and Yongli Gao

Center for Water Research, Department of Geological Sciences, University of Texas at San Antonio, One UTSA Circle, San Antonio TX 78249

Abstract

The interaction between groundwater and surface-water flow within karstic systems can be quite complex. Kendall County, Texas, underlain by both confined and unconfined segments of the Trinity aquifer, is situated along the southeastern edge of the Edwards Plateau and is dominated by outcroppings of the limestones in the upper and lower Glen Rose Formation. Two studies of the water quality of, and the interactions between, groundwater and surface water have been conducted by students from the University of Texas at San Antonio. The primary goal of these studies was to characterize the geochemical and isotopic composition of waters within the Trinity aquifer, the Guadalupe River, and Cibolo Creek, as well as to determine if there were any distinguishing characteristics of these waters that could be used as tracers to track the flow of these waters upon entering the Edwards aquifer.

The first study utilized hierarchical clustering analysis, k-means clustering analysis, and principal component analysis of geochemical data to gauge if there was a significant difference between the waters of the Trinity aquifer and the waters of both the Guadalupe River and Cibolo Creek. Over a 2-month period in the fall of 2013, water samples were collected from sections of Cibolo Creek flowing through Boerne, Texas and the Cibolo Preserve, the section of the Guadalupe River flowing between the river's intersections with Hwy 1376 and Eagle Falls Road, and 16 wells located in the southeastern portion of Kendal County. Temperature, pH, conductivity, and alkalinity were measured at the time of sample collection, and the water samples were analyzed for major cations and anions as well as the stable isotopic composition of oxygen ($\delta^{18}O$) and deuterium (δD) in water.

The second study was a monitoring program designed to evaluate differences in the quality of waters from the 1-mile-long segment of Cibolo Creek that flows through the Cibolo Preserve, which is predominantly fed by two wastewater treatment plants during drought conditions. During August 2013 to May 2014, water samples were collected from three locations along Cibolo Creek on a biweekly to monthly basis. The same parameters described for the first study were measured for the second study with the addition of the stable isotopic composition of dissolved inorganic carbon ($\delta^{13}C$) in water.

Overall, the waters from the section of Cibolo Creek flowing through the Cibolo Preserve bear little resemblance to the waters from the Guadalupe River and Trinity aquifers. On the basis of the difference in geochemical signatures, it is unlikely that this section of Cibolo Creek is gaining any groundwater. The waters flowing out of the lower Cibolo Creek watershed have slightly elevated concentrations of both chloride and nitrate. The elevated levels of chloride in waters from Cibolo Creek may serve as a possible tracer for groundwater flow into the Edwards/Trinity aquifer system.

An Integrated Outcrop and Subsurface Study of the Late Cretaceous Austin Group in Bexar County, Texas

By John R. Cooper and Alexis Godet

University of Texas at San Antonio, Dept. of Geological Sciences, One UTSA Circle, San Antonio, TX 78249

Abstract

Interbedded chalks and marls of the Austin Group are considered to be one of several confining units to the Edwards aquifer (Maclay and Small, 1984). However, recent studies by the U.S. Geological Survey in Bexar County, Texas, indicate that the Austin Group may be in hydrologic connectivity with the underlying Edwards, a highly productive carbonate (karst) aquifer, through associated en echelon, normal faults of the Balcones system (Banta and Clark, 2012). An integrated outcrop and subsurface study was conducted to refine the local stratigraphic architecture of the Austin Group in Bexar County. Selected outcrops were measured and described; in addition, hand-held gamma ray scintillometer profiles were obtained from the measured sections (fig. 1). Key marker horizons, first identified by C.O. Durham (1957) at Cibolo Creek on the Bexar-Guadalupe County line, allowed for correlation of outcrops several miles apart. Geophysical logs of boreholes drilled through the Austin Group provided data to better link the subsurface with the surface outcrops (Pedraza and Shah, 2010). Outcrop and subsurface data illustrate lateral variations in thickness of stratigraphic units within the Austin Group that are truncated at multiple discontinuity surfaces with some beds completely pinching out. There are three distinct oyster horizons in the uppermost 60 feet of the Austin Group in Bexar County: a 2-foot-thick layer of tightly packed *Gryphaea wratheri* and Inoceramid fragments within a glauconitic matrix occurring 50 feet below the top of the Austin Group, a 2-foot-thick layer of tightly packed *Exogyra laevuiscula* occurring 30 feet below the top, and a 5-foot-thick layer rich in *Gryphaea aucella* with abundant glauconite that is overlain by a bored hardground representing the Austin-Taylor Group contact. The Austin Group in Bexar County can be divided into lower, middle, and upper units that are distinct lithologic units bounded by laterally extensive discontinuity surfaces (fig. 1). The lower and middle units together compose the Coniacian-age Atco Formation, recognizable at the type section in Travis County. The upper unit comprises the Santonian to Campanian-age Vinson and Dessau Formations, also recognized in Travis County. The Atco Formation thins toward the San Marcos Arch to the northeast. The Vinson and Dessau Formations, which are thin in Bexar County, thicken toward the San Marcos Arch to the northeast. Integrated outcrop and subsurface stratigraphic work can be applied to understanding hydrologic units within the Austin Group in Bexar County that may be in connectivity with the underlying Edwards aquifer through associated faults and fractures of the Balcones system.

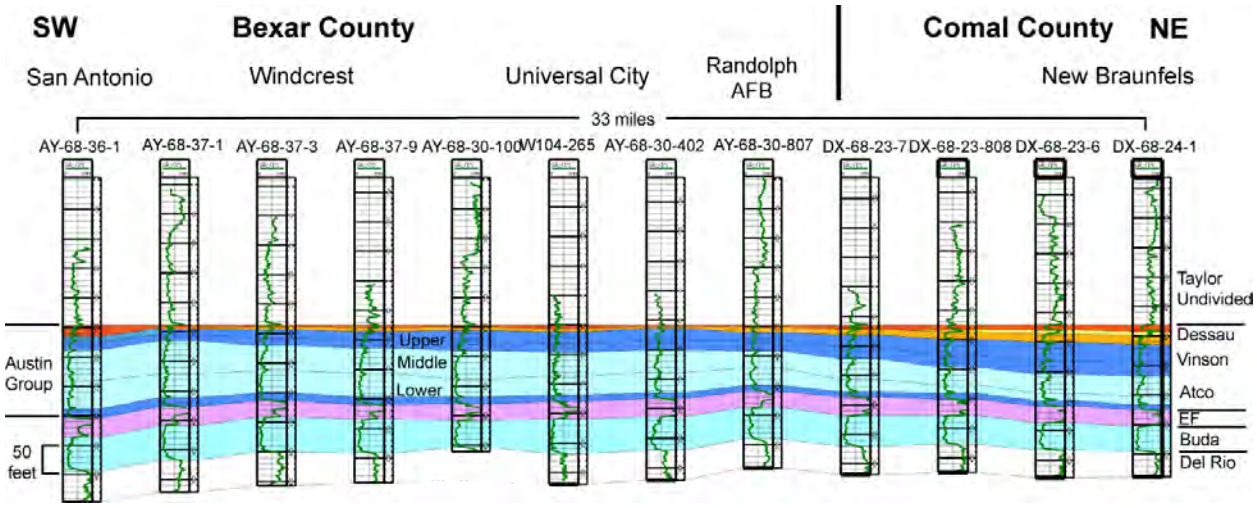

Figure 1. Stratigraphic cross section along the outcrop trend from San Antonio to New Braunfels, showing the lateral thickening and thinning of the lower, middle, and upper units of the Austin Group. Water wells with gamma ray logs were used to construct the cross section, referenced to the top of the Austin Group. EF=Eagle Ford Group

Acknowledgments

The authors would like to thank the Edwards Aquifer Authority and the U.S. Geological Survey in San Antonio for access to their geophysical log archives. The authors would also like to thank Dr. Michael Pope from Texas A&M University and Dr. Daniel Lehrmann from Trinity University for providing use of hand-held gamma ray scintillometers. We would also like to thank the Geological Society of America, the Gulf Coast Association of Geological Societies, and the South Texas Geological Society for providing additional support for this project.

References Cited

Banta, J.R., and Clark, A.K., 2012, Groundwater levels and water-quality observations pertaining to the Austin Group, Bexar County, Texas, 2009–11: U.S. Geological Survey Scientific Investigations Report 2012–5278, 18 p., 2 appendixes.

Durham, C.O., 1957, The Austin Group in central Texas: Ph.D. Dissertation, Columbia University, New York, p. 1–54.

Maclay, R.W., and Small, T.A., 1984, Carbonate geology and hydrology of the Edwards aquifer in the San Antonio area, Texas: U.S. Geological Survey Open-File Report 83-537, 72 p.

Pedraza, D.E., and Shah, S.D., 2010, Geodatabase design and characteristics of geologic information for a geodatabase of selected wells penetrating the Austin Group in central Bexar County, Texas, 2010: U.S. Geological Survey Data Series 522, 39 p.

Microbial Indicators and Aerobic Endospores in the Edwards Aquifer, South-Central Texas

By MaryLynn Musgrove

U.S. Geological Survey, Texas Water Science Center, 1505 Ferguson Lane, Austin, TX 78754

Abstract

Microbiological contaminants in groundwater can be of concern for human health. This is especially true in karst aquifers where rapid recharge from direct surface inputs is common. The Edwards aquifer in south-central Texas is a highly productive fractured karst aquifer that responds rapidly to changes in hydrologic conditions in a region characterized by cyclic periods of drought and wet conditions. An ongoing study by the U.S. Geological Survey's National Water-Quality Assessment (NAWQA) Project in the Edwards aquifer—to better understand how groundwater quality changes over short (daily to monthly) and long (seasonal to decadal) timescales—provides a framework ideal for also assessing the variability of microbiological constituents, including aerobic endospores and pathogens. Three groundwater wells in the Edwards aquifer have been instrumented to provide near-continuous (subhourly) water-quality data (temperature, pH, specific conductance, and dissolved oxygen). To augment these data, discrete samples were collected and analyzed for a range of geochemical constituents. Some of these constituents are useful for describing microbial groundwater quality: the presence of E. coli, total coliforms, coliphage, and enterococci might be indicative of fecal contamination; aerobic endospores are non-fecal indicators of groundwater under the influence of surface water. Additionally, pathogenic microorganisms (Cryptosporidium and Giardia) and viruses were analyzed in a subset of samples. The wells are near San Antonio, Texas, along an updip-to-downdip aquifer transect, and consist of one monitoring well in the unconfined (recharge) zone and two public-supply wells in the confined zone of the aquifer. Microbiological constituents were commonly detected in the updip recharge zone, but were infrequently detected in the deeper confined wells. Aerobic endospores were detected throughout the aquifer, but concentrations and detections generally decreased downdip. These results are consistent with other geochemical indicators that indicate updip-to-downdip patterns in groundwater geochemistry with respect to water-rock interactions and groundwater residence time, and provide insight into the vulnerability of karst groundwater resources to contamination.

Onset, Development, and Demise of a Rudist Patch Reef in the Albian Glen Rose Formation of Central Texas

By Alexis Godet and J. Douglas Grosch

Dept. of Geological Sciences, The University of Texas at San Antonio, 1 UTSA Circle, San Antonio, TX 78249

Introduction and Geological Setting

The Comanche platform developed on the northern margin of the Gulf of Mexico after the breakup of Pangea in the late Permian–Triassic and the deposition of a thick succession of evaporitic sediments (Louann Salt) in the Jurassic (Salvador, 1991a, b). Its evolution during the Cretaceous is marked by periods of carbonate production punctuated by the deposition of more siliciclastic and organic-rich sediments (for example, Phelps and others, 2014). During the Albian (Early Cretaceous), rudist biostromes developed in the shallow marine environments that occupied the northern margin of the Gulf of Mexico (Perkins, 1974, 1985). Such bioconstructions are preserved in the subsurface of Maverick County in Texas (Loucks and Kerans, 2003). Although the geometry and facies of these patch reefs are well constrained, the reasons for their initiation, unfolding, and demise has yet to be investigated. We hypothesize that nutrient supply and oxygenation of seawater, in addition to sea-level changes, played an important role in their development. This assumption was tested by investigating a rudist patch reef outcropping at the Cibolo Preserve in the city of Boerne, Texas (fig. 1).

Methods

Field description of the patch reef defines its core, which consists of caprinid rudist bivalves that are capped by a thin layer of monopleurid and toucasid rudists (fig. 1). Petrographic analysis of thin sections (optical and cathodoluminescence microscopy) aids in defining four microfacies corresponding to peritidal (stromatolitic dolostone), restricted subtidal (miliolid-rich packstone), reefal (rudist-rich rudstone and boundstone), and open marine subtidal (bioclastic grainstone) environments, which alternate vertically throughout the studied section. This stratigraphic evolution of the stacking pattern of microfacies mirrors changes in sea levels and thus helps constrain the sequence stratigraphic interpretation of the sedimentary succession. Carbon stable isotope analysis is used to refine the age interpretation of the succession at Cibolo Preserve to the middle Albian by correlating its $\delta^{13}C$ curve with well-dated ones, such as the reference $\delta^{13}C$ curve for the Comanche platform proposed by Phelps and others (2014, 2015), as well as identify subaerial exposure surfaces. Nutrient supply and oxygen level are monitored by the phosphorus content and the vanadium/(vanadium+nickel) (V/(V+Ni)) ratio, respectively, based on the geochemical analysis of powdered samples by means of WD-XRF spectrometry.

Discussion and Conclusion

Sequence stratigraphic analysis of the sedimentary succession indicates that the biostrome developed during a period of high sea level, whereas the subsequent drop in relative sea level facilitated the installation of more restricted, slightly supersaline and mesotrophic conditions. This is confirmed by the occurrence of miliolid-rich facies directly on top of the rudist patch reef, prior to a sequence boundary and an associated period of subaerial exposure indicated by a negative shift in both the carbon and oxygen stable isotope composition of whole rock samples. Moreover, the switch from caprinid-dominated to monopleurid- and toucasid-rich facies corresponds to a slight increase in the phosphorus content, from 25 to 35 ppm. Phosphorus is a biophile element that usually constitutes a proxy for trophic

level (Föllmi, 1996); its content in the ocean influences the type of carbonate ecosystems that develop (Hallock, 1988; Mutti and Hallock, 2003). On the other hand, the V/(V+Ni) ratio reflects redox conditions (Hatch and Leventhal, 1992; Riquier and others, 2006); reported values indicate the installation of suboxic conditions during the subsequent phase of sea-level rise that follows sequence boundary (SB) 2 (fig. 1). We conclude that the monopleurid-toucasid association is adapted to slightly more mesotrophic conditions, but that the lack of well-oxygenated bottom seawater prevents their resilience and induces the demise of this rudist patch reef that eventually became subaerially exposed. Meteoric diagenesis induced dissolution of the aragonitic part of the rudist shells and the development of a fabric selective porosity, similar to that associated with rudist biostromes in the upper Glen Rose Formation. There, the moldic porosity is associated with nonfabric selective porosity that enhances the overall permeability of the biostrome and makes it one of the most permeable intervals in these carbonate rocks (Clark, 2003; Pantea and others, 2014).

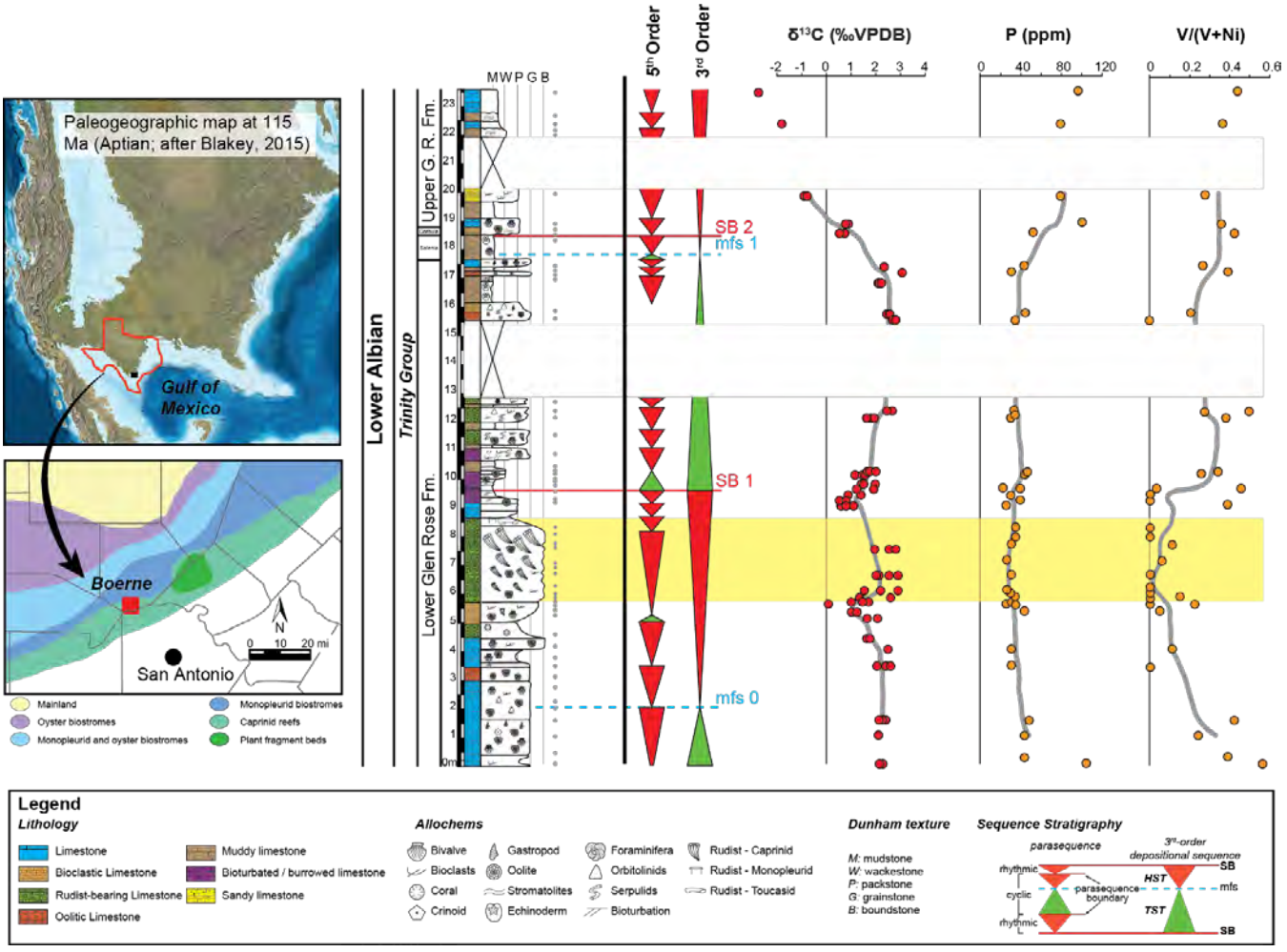

Figure 1. Synthetic section of the Glen Rose Formation outcrop at the Cibolo Preserve in Boerne, Texas. The gray band highlights the position of the rudist patch reef. The slight increase in the phosphorus content in the upper part (24 to 35 ppm) and directly above the rudist patch reef (35 to 48 ppm) may reflect the onset of slightly more mesotrophic conditions. Above SB1, the increase in V/(V+Ni) values indicates a lack of oxygen in seawater during a transgressive systems tract. Facies belts on the present day location maps were redrawn from Perkins (1974).

Acknowledgments

This project was completed under a research agreement between UTSA and the Cibolo Preserve, Boerne, Texas. We extend our acknowledgment to the Trustees of the Cibolo Preserve, especially Bill Lende and J.W. Pieper for their help and support in the field. We thank the Office of Vice President for Research at UTSA for financial support. The comments by Stéphane Bodin (University of Aarhus, Denmark) and Chris Lowery (University of Texas at Austin) are greatly appreciated.

References Cited

Blakey, R., 2015, Western Interior Seaway paleo-geographic maps and cross sections: Deep Time Maps, Albian (115 Ma), http://deeptimemaps.com/western-interior-seaway-map-list/.

Clark, A.K., 2003, Geologic framework and hydrogeologic features of the Glen Rose Limestone, Camp Bullis Training Site, Bexar County, Texas: U.S. Geological Survey Water-Resources Investigations Report 03-4081, p. 1–9.

Föllmi, K.B., 1996, The phosphorus cycle, phosphogenesis and marine phosphate-rich deposits: Earth-Science Reviews, v. 40, p. 55–124.

Hallock, P., 1988, The role of nutrient availability in bioerosion—Consequences to carbonate buildups: Palaeogeography, Palaeoclimatology, Palaeoecology, v. 63, p. 275–291.

Hatch, J.R., and Leventhal, J.S., 1992, Relationship between inferred redox potential of the depositional environment and geochemistry of the Upper Pennsylvanian (Missourian) Stark Shale Member of the Dennis Limestone, Wabaunsee County, Kansas, U.S.A: Chemical Geology, v. 99, p. 65–82.

Loucks, R.G., and Kerans, C., 2003, Lower Cretaceous Glen Rose "Patch Reef" reservoir in the Chittim Field, Maverick County, south Texas: Gulf Coast Association of Geological Societies Transactions, v. 53, p. 490–503.

Mutti, M., and Hallock, P., 2003, Carbonate systems along nutrient and temperature gradients—Some sedimentological and geochemical constraints: International Journal of Earth Sciences, v. 92, p. 465–475.

Pantea, M.P., Blome, C.D., and Clark, A.K., 2014, Three-dimensional model of the hydrostratigraphy and structure in and around the U.S. Army-Camp Stanley storage activity area, northern Bexar County, Texas: U.S. Geological Survey Scientific Investigations Report 2014–5074, p. 1–13.

Perkins, B.F., 1974, Paleoecology of a rudist reef complex in the Comanche Cretaceous Glen Rose Limestone of central Texas: Geoscience and Man, v. 8, p. 131–173.

Perkins, B.F., 1985, Caprinid reefs and related facies in the Comanche Cretaceous Glen Rose Limestone of central Texas, *in* Bebout, D.G., and Ratcliff, D., eds., Lower Cretaceous depositional environments from shoreline to slope–a core workshop: GCAGS-GCS/SEPM, Austin, Texas, p. 129–140.

Phelps, R.M., Kerans, C., Da Gama, R.O.B.P., Jeremiah, J., Hull, D., and Loucks, R., 2015, Response and recovery of the Comanche carbonate platform surrounding multiple Cretaceous oceanic anoxic events, northern Gulf of Mexico: Cretaceous Research, v. 54, p. 117–144.

Phelps, R.M., Kerans, C., Loucks, R.G., Da Gama, R.O.B.P., Jeremiah, J., and Hull, D., 2014, Oceanographic and eustatic control of carbonate platform evolution and sequence stratigraphy on the Cretaceous (Valanginian-Campanian) passive margin, northern Gulf of Mexico: Sedimentology, v. 61, p. 461–496.

Riquier, L., Tribovillard, N., Averbuch, O., Devleeschouwer, X., and Riboulleau, A., 2006, The Late Frasnian Kellwasser horizons of the Harz Mountains (Germany)—Two oxygen-deficient periods resulting from different mechanisms: Chemical Geology, v. 233, p. 137–155.

Salvador, A., 1991a, Triassic-Jurassic, *in* Salvador, A., ed., The geology of North America: Geological Society of America, Boulder, Colorado, p. 131–180.

Salvador, A., 1991b, Origin and development of the Gulf of Mexico, *in* Salvador, A., ed., The geology of North America: Geological Society of America, Boulder, Colorado, p. 389–444.

Environmental Reconstruction of an Albian Dinosaurs Track-Bearing Interval in Central Texas

By Beau Johnson[1,2], Alexis Godet[1], Thomas Adams[3], Alixandria Cain[1], Dan Lehrmann[4],and Marina Suarez[1]

[1]Dept. of Geological Sciences, The University of Texas at San Antonio, 1 UTSA Circle, San Antonio, TX 78249

[2]Chesapeake Energy Corporation, Oklahoma City, OK 73154

[3]The Witte Museum, 3801 Broadway Street, San Antonio, TX 78209

[4]Trinity University, 1 Trinity Pl, San Antonio, TX 78212

Introduction and Geological Setting

After the breakup of the continent of Pangea in the late Permian–Triassic and the deposition of a thick succession of evaporitic sediments in the Jurassic (Salvador, 1991, and references therein), the Comanche carbonate platform developed in epicontinental seas on the northern margin of the ancestral Gulf of Mexico. The shallow marine environment resulted in the deposition of thick layers of platform carbonates, preserving a record of environmental and ecological changes (Hallock, 2001; Mutti and Hallock, 2003; Pomar and Hallock, 2008; Phelps and others, 2014).

Belonging to the Trinity Group, the Glen Rose Formation is a thick shallow marine carbonate succession deposited during the Albian Stage (Early Cretaceous) in south-central and north-central Texas (Hill, 1901; Wilmarth, 1938; Lozo and Stricklin, 1956; Phelps and others, 2014). The Glen Rose Formation is known for its dinosaur tracks and trackways (Perkins, 1974), which can be observed in numerous locations, such as Canyon Lake Gorge in Comal County (Ward and Ward, 2007). Recently, Adams and others (2015) described well-preserved tracks and trackways (theropod and sauropod) at Government Canyon State Natural Area (GCSNA), located northwest of San Antonio, Texas. This is a significant discovery as this outcrop represents the first Glen Rose track site to be identified within Bexar County. However, its precise stratigraphic location and depositional environment have yet to be determined in detail. This study aims to determine the position of this dinosaur track-bearing section within the overall stratigraphy of the Glen Rose Formation and to assess the paleoenvironmental and paleoclimatic conditions that prevailed at this location during deposition.

Methods and Results

Field description of the dinosaur tracks and of the studied stratigraphic succession included the in-situ measurement of the natural radioactivity using a handheld scintillometer (Terraplus RS-125 Super Gamma-Ray Spectrometer/Scintillometer). Petrographic analysis of thin sections (optical and cathodoluminescence microscopy) aids in defining four microfacies: (1) fine crystalline dolomite, peritidal environment; (2) miliolid-rich mudstone to wackestone, very shallow subtidal to lower intertidal environment; (3) lime mudstone, shallow subtidal, lagoonal environment; and (4) bioclastic, peloidal packstone, shallow subtidal, shelfal environment.

The sequence stratigraphic interpretation of the studied sedimentary succession derives from the stratigraphic repartition and evolution of these microfacies. An analysis of the carbon stable isotope composition of carbonate samples helped refine correlation of the stratigraphic succession at GCSNA by comparing the $\delta^{13}C$ curve with well-dated isotope records, such as the reference $\delta^{13}C$ curve for the Comanche platform proposed by Phelps and others (2014, 2015). This chemostratigraphic correlation is supported by the correlation of the total natural radioactivity with the gamma-ray curve of a water well

located northeast of San Antonio that penetrates the upper Glen Rose Formation. The intensity of weathering on land is recorded by the kaolinite/mica ratio and the Chemical Index of Alteration (CIA) (Nesbitt and Young, 1982, 1984) derived from mineralogical (XRD) and geochemical (WD-XRF) data, respectively.

Discussion and Conclusion

The contact between the Trinity and Edwards Groups can be observed in the slope of the hill above the top of the measured section (Allan Clarke, U.S. Geological Survey, oral commun., 2016). This implies that the studied sedimentary section belongs to the upper member of the Glen Rose Formation. The evolution of carbon isotopic composition within the section and the outcrop gamma-ray profile will hopefully help precisely date this location. Bulk-rock geochemical data indicate that dinosaurs responsible for the tracks were living under warm and humid conditions characteristic of intertropical regions where strong weathering occurred, as deduced from the CIA values between about 78 and 98, as shown on figure 1 (Nesbitt and Young, 1982). Based on the beds stacking pattern and evolution of microfacies, we developed a sequence stratigraphic framework for the studied section. A third-order sequence boundary is identified at the top of a shallowing-upward trend that corresponds to the transition from fine crystalline dolomite with quartz (shallow subtidal, restricted environment), to limestones with miliolids (shallow subtidal environment). This sequence boundary separates a late highstand systems tract from an early transgressive systems tract. Dinosaur tracks and trackways are preserved at the tops of parasequences belonging to this late highstand systems tract. Depositional environments correspond to shallow subtidal settings affected by a warm and humid climate that promoted strong weathering on land. This high-resolution study of facies, including diagenesis, of part of the upper Glen Rose Formation highlights the localized development of secondary vuggy porosity linked to meteoric diagenesis directly below the sequence boundary. Such enhanced porosity horizons may serve as discrete carrier beds and may play a role in the recharge mechanisms of the upper Trinity aquifer.

Acknowledgments

This research was conducted under an established Memorandum of Agreement between GCSNA and the Witte Museum. We acknowledge the logistic help of Chris Holm, superintendent of GCSNA, and the field assistance of Caroline Kelleher and Dianna Price. The comments of Allan Clarke (U.S. Geological Survey) and Lance Lambert (University of Texas at San Antonio) are greatly appreciated.

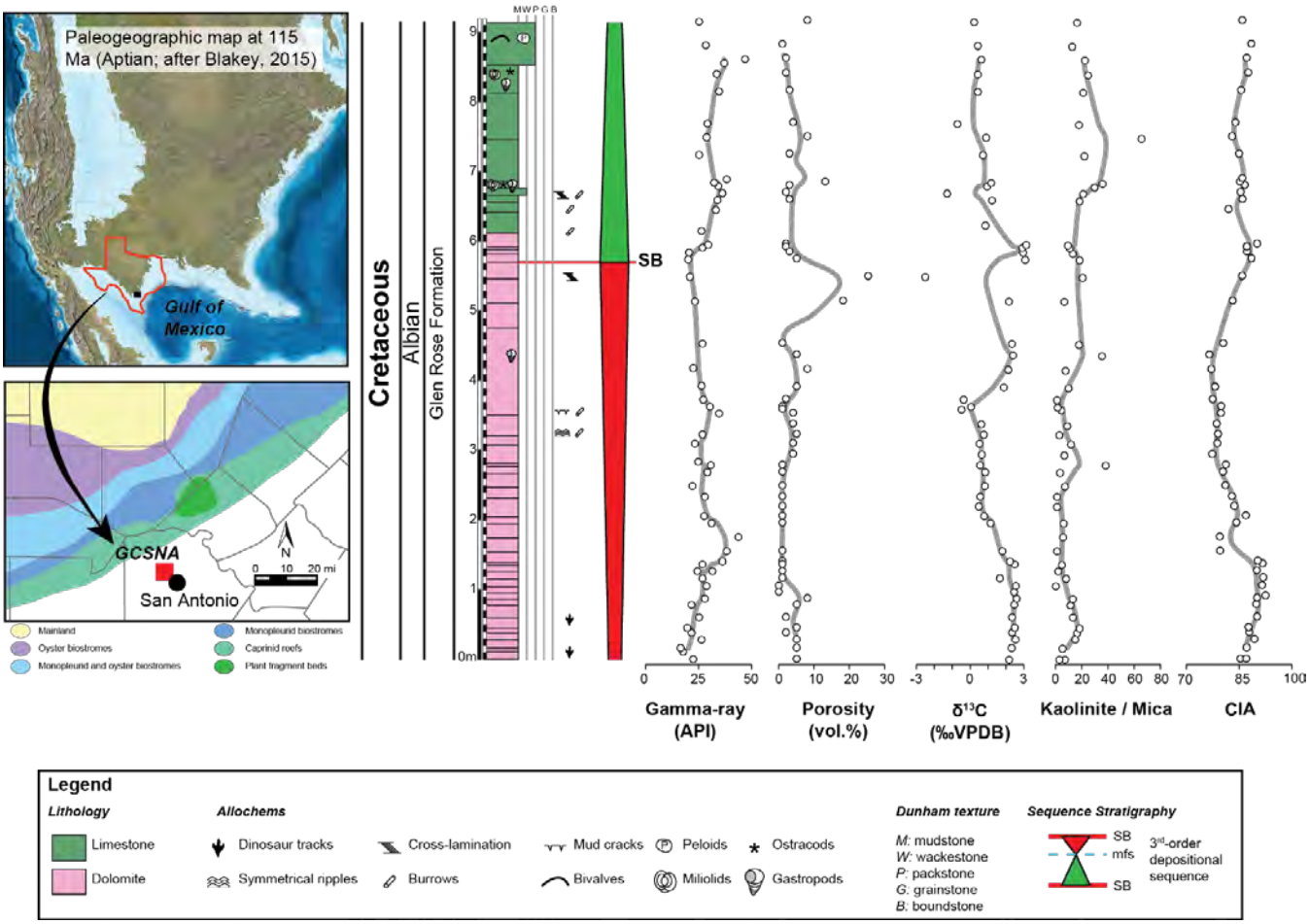

Figure 1. During the Early Cretaceous, the study area was located in an epicontinental setting on the northern margin of the ancestral Gulf of Mexico. A, Albian paleogeographic map after Blakey (2015). B, The study area is located in the Government Canyon State Natural Area (GCSNA), which is approximately 25 kilometers northwest of San Antonio in central Texas. The lithologic column of the studied section is plotted along with a gamma-ray log profile, percent porosity estimates, carbon stable isotope composition ($\delta^{13}C$), kaolinite to mica ratio, and chemical index of alteration (CIA) curves.

References Cited

Adams, T.L., Koepke, J.H., Gonzalez, R., Azouggagh, D., Price, D., Shaffer, J., Ellis, A., Weissling, D., and Choate, J., 2015, Museums, parks, and dinosaur footprints—Developing partnerships in paleontology: Society of Vertebrate Paleontology, 75th annual meeting, Dallas, Texas.

Blakey, R., 2015, Western Interior Seaway paleogeographic maps and cross sections: Deep Time Maps, Albian (115 Ma), http://deeptimemaps.com/western-interior-seaway-map-list/.

Hallock, P., 2001, Coral reefs, carbonate sediments, nutrient, and global change, *in* Stanley, G.D.J., ed., The history and sedimentology of ancient reef systems: New York, Kluwer-Plenum, p. 387–427.

Hill, R.T., 1901, Geography and geology of the Black and Grand prairies, Texas with detailed descriptions of the Cretaceous formations and special reference to artesian waters: Twenty-First Annual Report of the United States Geological Survey to the Secretary of the Interior, 1899–1900, Part VII–Texas, 666 p.

Lozo, F.E., and Stricklin, F.L.J., 1956, Stratigraphic notes on the outcrop basal Cretaceous, central Texas: Transactions of the Gulf Coast Association of Geological Societies, v. 6, p. 67–78.

Mutti, M., and Hallock, P., 2003, Carbonate systems along nutrient and temperature gradients—Some sedimentological and geochemical constraints: International Journal of Earth Sciences, v. 92, p. 465–475.

Nesbitt, H.W., and Young, G.M., 1982, Early Proterozoic climates and plate motions inferred from major element chemistry of lutites: Nature, v. 299, p. 715–717.

Nesbitt, H.W., and Young, G.M., 1984, Prediction of some weathering trends of plutonic and volcanic rocks based on thermodynamic and kinetic considerations: Geochimica and Cosmochimica Acta, v. 48, p. 1523–1534.

Perkins, B.F., 1974, Paleoecology of a rudist reef complex in the Comanche Cretaceous Glen Rose Limestone of central Texas: Geoscience and Man, v. 8, p. 131–173.

Phelps, R.M., Kerans, C., Da Gama, R.O.B.P., Jeremiah, J., Hull, D., and Loucks, R., 2015, Response and recovery of the Comanche carbonate platform surrounding multiple Cretaceous oceanic anoxic events, northern Gulf of Mexico: Cretaceous Research, v. 54, p. 117–144.

Phelps, R.M., Kerans, C., Loucks, R.G., Da Gama, R.O.B.P., Jeremiah, J., and Hull, D., 2014, Oceanographic and eustatic control of carbonate platform evolution and sequence stratigraphy on the Cretaceous (Valanginian-Campanian) passive margin, northern Gulf of Mexico: Sedimentology, v. 61, p. 461–496.

Pomar, L., and Hallock, P., 2008, Carbonate factories—A conundrum in sedimentary geology: Earth-Science Reviews, v. 87, p. 134–169.

Salvador, A., 1991, Triassic-Jurassic, in Salvador, A., ed., The geology of North America: Geological Society of America, Boulder, Colorado, p. 131–180.

Ward, W.C., and Ward, W.B., 2007, Stratigraphy of middle part of Glen Rose Formation (lower Albian), Canyon Lake Gorge, central Texas, U.S.A., *in* Scott, R.W., ed., Cretaceous rudists and carbonate platforms: Environmental Feedback, Tulsa, Oklahoma, SEPM, p. 193–210.

Wilmarth, M.G., 1938, Lexicon of geological names of the United States: U.S. Geological Survey Bulletin, v. 896, 2,396 p.

Field Trip Guide Book for USGS Karst Interest Group Workshop, 2017: The Multiple Facets of Karst Research Within the Edwards and Trinity Aquifers, South-Central Texas

Field trip planning committee: Allan K. Clark[1] and Amy R. Clark[2]

Field trip guides: Allan K. Clark[1], Amy R. Clark[2], George Veni[3], Geary Schindel[4], Keith Muehlestein[2], Alexis Godet[2], James Golab[5], Marcus Gary[4], Carter Keairns[2], and Ron Green[6]

UTSA logistics committee: Amy R. Clark[2], Lance Lambert[2], and Yongli Gao[2]

[1]U.S. Geological Survey, Texas Water Science Center, South Texas Program Office, 5563 De Zavala Rd., Suite 290, San Antonio, TX 78249

[2]University of Texas at San Antonio, Department of Geosciences, 1 UTSA Circle, San Antonio, TX 78249

[3]National Cave and Karst Research Institute, 400-1 Cascades Avenue, Carlsbad, NM 88220

[4]Edwards Aquifer Authority, 900 E. Quincy, San Antonio, TX 78215

[5]University of Kansas, Department of Geology, 1475 Jayhawk Blvd, Lawrence, KS 66045

[6]Southwest Research Institute, Geosciences and Engineering Division, 6220 Culebra, San Antonio, TX 78238

Contents for Karst Interest Group Field Trip Guide

Field Trip Safety

Hazards of concern are traffic, heat-related illness, snakes and insects (bites and stings), plants ("poisonous" or thorny), falling rocks, falling, and cuts/scraps. If there are any safety concerns during the field trip, please inform the field trip leaders immediately.

During the field trip, we will be making a number of stops to observe various hydrogeologic features. Please be aware that some of the stops will be along busy roadways. Please do not walk within a body length of the road unless you are crossing the road. We will have safety personnel on the trip to flag/warn traffic of the group's activity as needed.

A major concern in south-central Texas is heat. Please stay hydrated during the field trip by drinking plenty of fluids. Seek assistance and shade if you feel like the heat is beginning to affect you, and inform the field trip leaders.

Snakes, insects, and "poisonous" or thorny plants are always an issue when you are in the field. The best defense against these is to remain vigilant and refrain from sticking hands into holes or under rock ledges if you can't see what is underneath. If you see a potential hazard from snakes, insects, or plants, warn the people around you and contact a field trip leader, so that they can make an announcement to the group.

Falling rocks and falling off steep inclines, ledges, and cliffs is always a danger. When approaching the outcrop, look above you to identify potential hazards, and warn people if you are going to be on an outcrop above them. If you dislodge a rock on the outcrop, warn people below you by yelling "ROCK!" If you are on an outcrop with a steep incline, ledge, or cliff, maintain a safe distance from the edge for your own safety and for the safety of the individuals who may be below you.

In the event that an individual suffers a cut/scrap, please proceed to the first aid truck for appropriate medical attention. If the bleeding is severe, inform the field trip leaders so that they can assist.

There will be a designated truck containing a first aid kit, water, and other emergency equipment including an automated external defibrillator (AED). The designated truck will be identified during the safety briefing at the beginning of the field trip and will be marked with a first aid sticker on the back tailgate area.

To summarize:

- Watch for traffic
- Stay hydrated and avoid overheating
- Be aware of the flora and fauna
- Don't stand too close to edges with steep inclines, ledges, or cliffs

If you witness an injury that requires assistance, please contact the field trip leaders. If the emergency appears life threating, please call 911 immediately. It is the responsibility of everyone who attends a field trip to not only be mindful of their own safety but also for the safety of their fellow attendees.

Introduction to Karst Interest Group Field Trip

Welcome to the Karst Interest Group field trip. This field trip will take you to various sites in Bexar, Comal, and Hays Counties. A total of eight stops are planned for the field trip which will look at issues related to hydrology, paleontology, stratigraphy, depositional history, recharge and discharge, surface geomorphology, biology, and anthropogenic effects on karst (figs. 1, 2, and 3). At these sites, various presenters will discuss the current understanding of the Edwards and Trinity aquifers related to research being conducted on these aquifers.

The field trip will begin at 7:15 AM on May 18 and proceed from stops 1 through 3 in northern Bexar County. Lunch (Stop 4) will be at the Old 300 Bar-B-Que in Blanco, Texas, at approximately 11:30 AM. During lunch, a presentation on the depositional history of the Edwards and Trinity Groups will be given. After lunch, the field trip will proceed to sites 5 through 8. Stop 8 will culminate with pizza while watching the bat flight out of Bracken Bat Cave, which contains the largest colony of bats in the world. The field trip will end at approximately 8:30 PM.

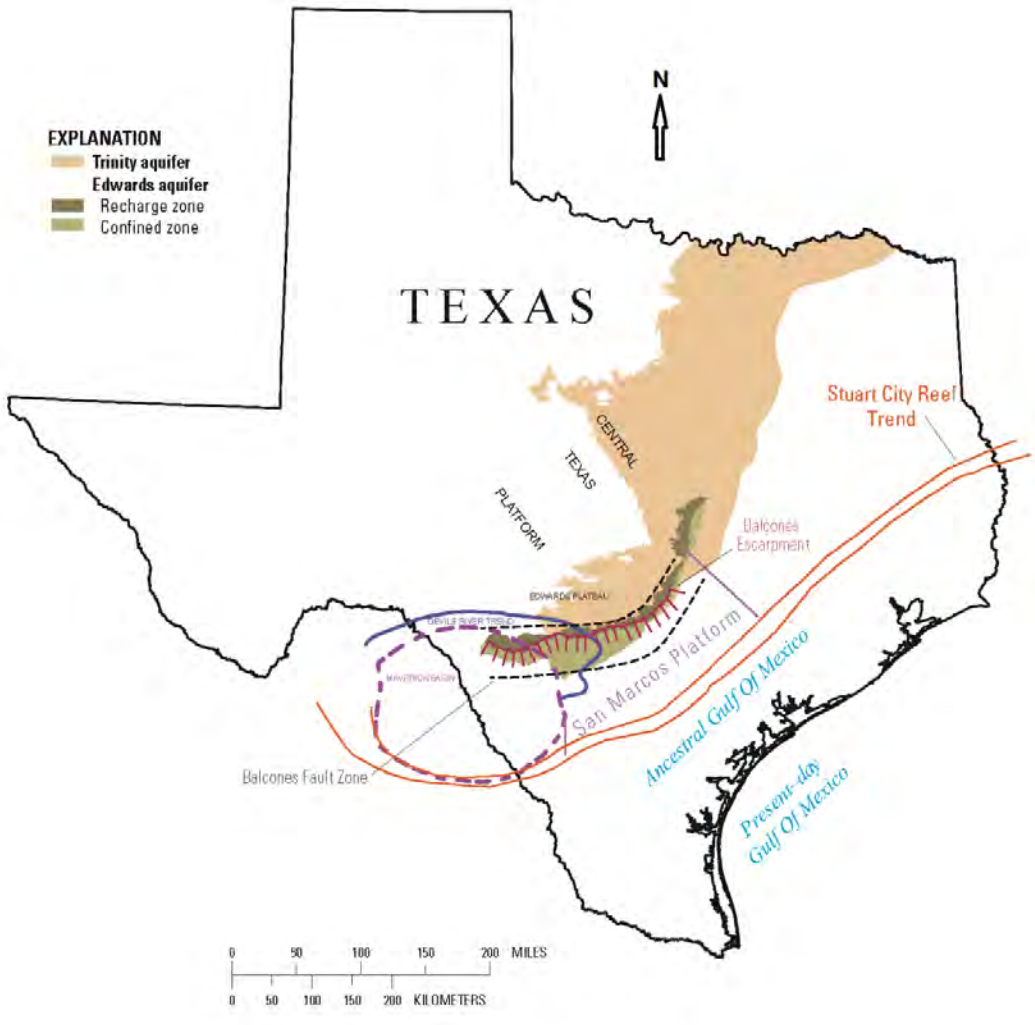

Figure 1. Map of Texas showing location of outcrops of the Edwards and Trinity aquifers, recharge and confined zones, and the Balcones Escarpment and Fault Zone along the margin of the Edwards Plateau.

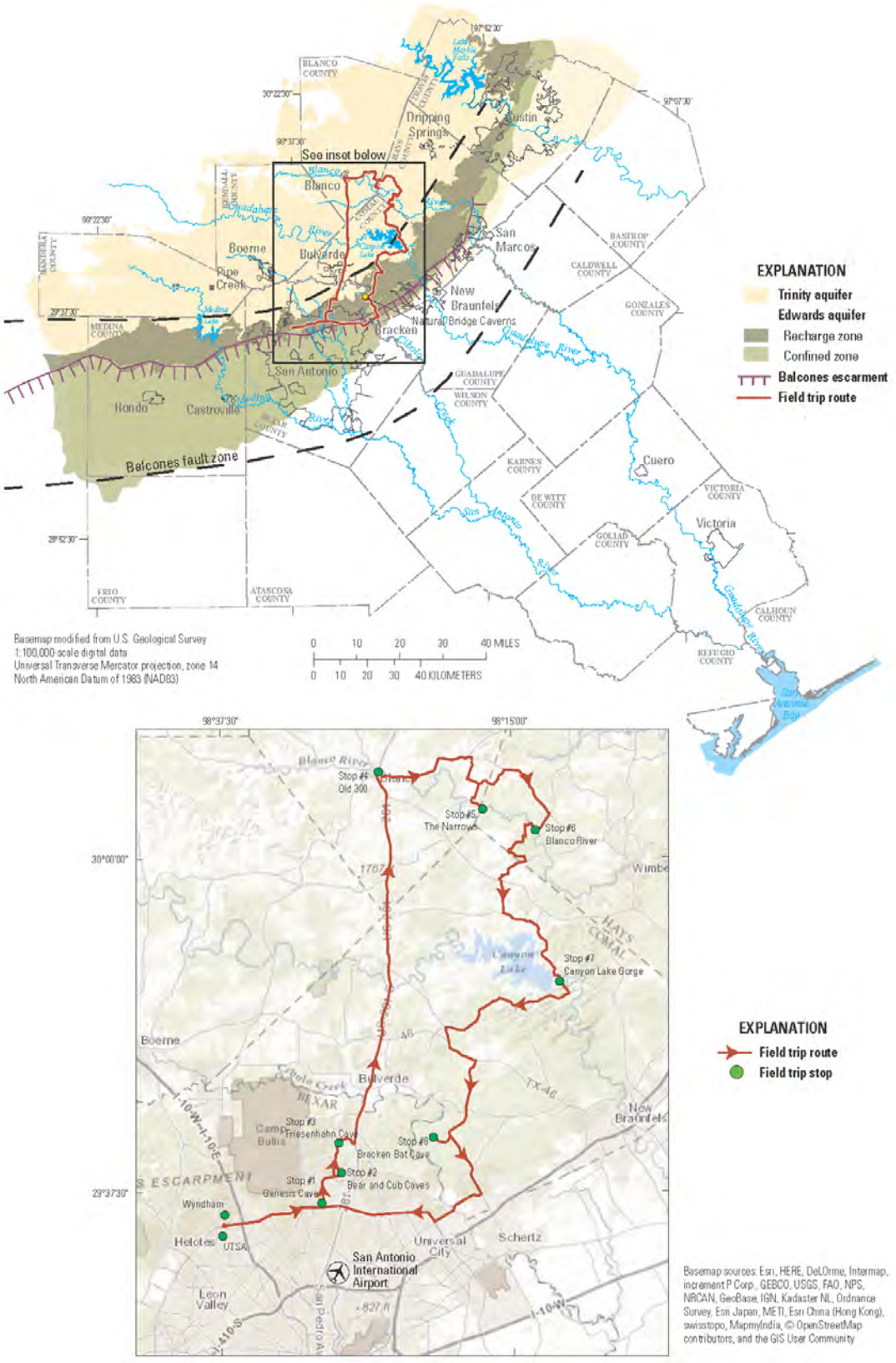

Figure 2. Location map showing the field trip route relative to the Edwards and Trinity aquifers in central Texas, and a detailed route map showing individual stops in Bexar, Blanco, Comal, and Hays Counties, Texas.

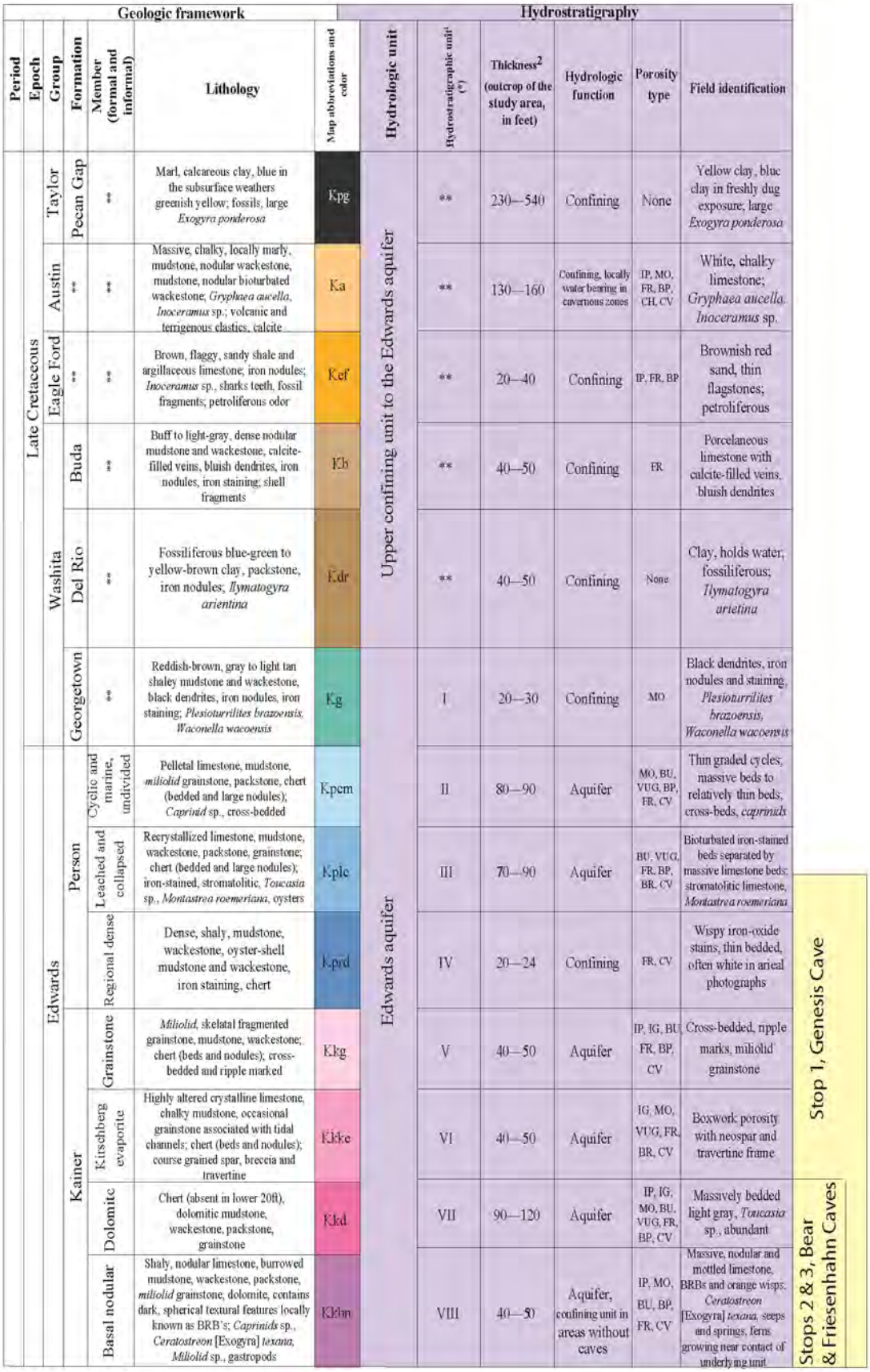

Figure 3. Summary of the geologic framework and hydrostratigraphy of the Edwards and Trinity aquifers within Bexar and Comal Counties, Texas. [[1]Informal, [2]Thickness based on field mapping]

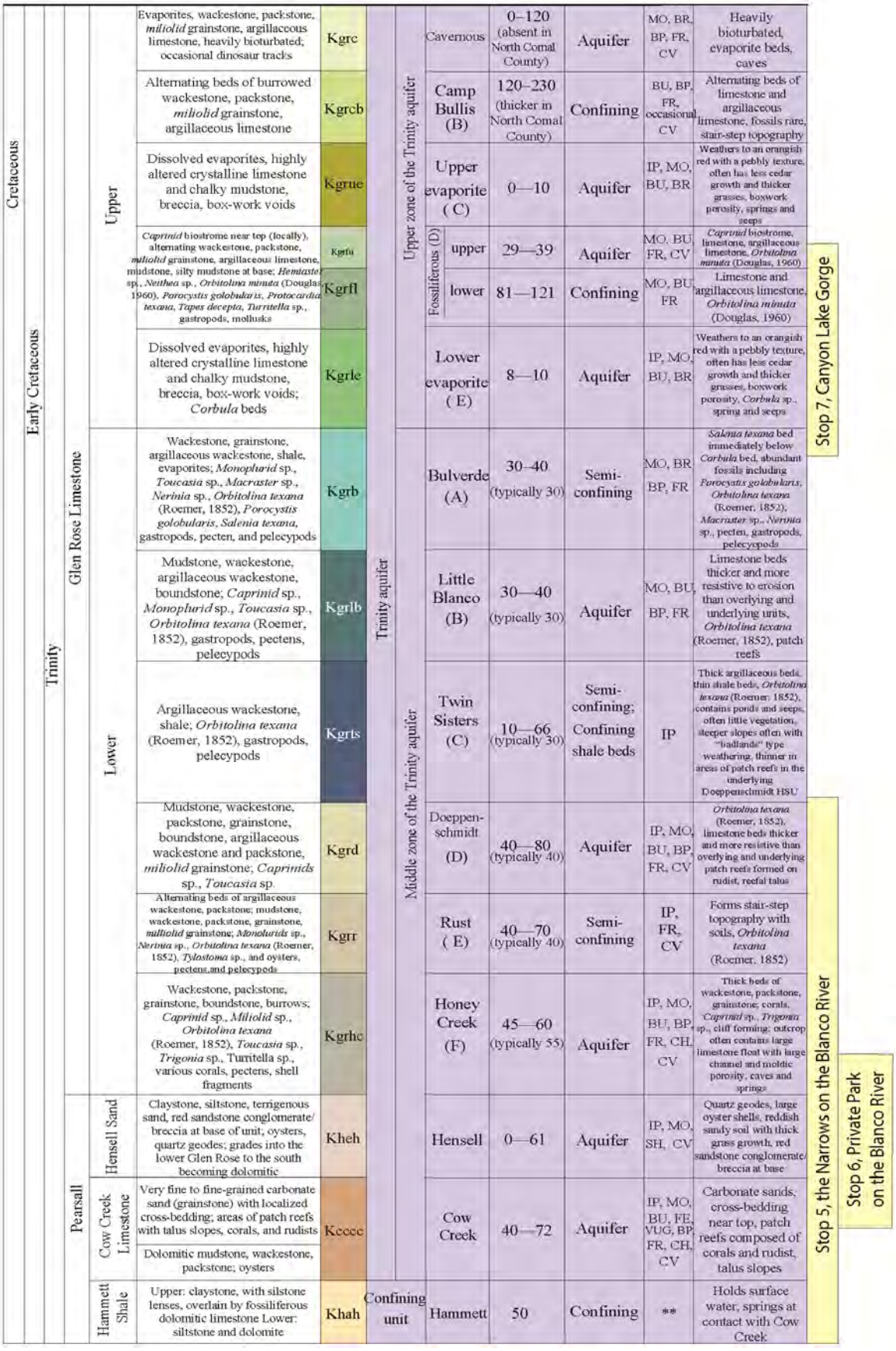

Cretaceous	Early Cretaceous	Trinity	Glen Rose Limestone	Upper	Evaporites, wackestone, packstone, *miliolid* grainstone, argillaceous limestone, heavily bioturbated; occasional dinosaur tracks	Kgrc	Upper zone of the Trinity aquifer		Cavernous	0–120 (absent in North Comal County)	Aquifer	MO, BR, BP, FR, CV	Heavily bioturbated, evaporite beds, caves	Stop 7, Canyon Lake Gorge
					Alternating beds of burrowed wackestone, packstone, *miliolid* grainstone, argillaceous limestone	Kgrcb			Camp Bullis (B)	120–230 (thicker in North Comal County)	Confining	BU, BP, FR, occasional CV	Alternating beds of limestone and argillaceous limestone, fossils rare, stair-step topography	
					Dissolved evaporites, highly altered crystalline limestone and chalky mudstone, breccia, box-work voids	Kgrue			Upper evaporite (C)	0—10	Aquifer	IP, MO, BU, BR	Weathers to an orangish red with a pebbly texture, often has less cedar growth and thicker grasses, boxwork porosity, springs and seeps	
					Caprinid biostrome near top (locally), alternating wackestone, packstone, *miliolid* grainstone, argillaceous limestone, mudstone, silty mudstone at base; *Hemiaster* sp., *Neithea* sp., *Orbitolina minuta* (Douglas, 1960), *Porocystis golobularis*, *Protocardia texana*, *Tapes decepta*, *Turritella* sp., gastropods, mollusks	Kgrfu		Fossiliferous (D)	upper	29—39	Aquifer	MO, BU FR, CV	*Caprinid* biostrome, limestone, argillaceous limestone, *Orbitolina minuta* (Douglas, 1960)	
						Kgrfl			lower	81—121	Confining	MO, BU FR	Limestone and argillaceous limestone, *Orbitolina minuta* (Douglas, 1960)	
					Dissolved evaporites, highly altered crystalline limestone and chalky mudstone, breccia, box-work voids; *Corbula* beds	Kgrle			Lower evaporite (E)	8—10	Aquifer	IP, MO, BU, BR	Weathers to an orangish red with a pebbly texture, often has less cedar growth and thicker grasses, boxwork porosity, *Corbula* sp., spring and seeps	
				Lower	Wackestone, grainstone, argillaceous wackestone, shale, evaporites; *Monopluria* sp., *Toucasia* sp., *Macraster* sp., *Nerinia* sp., *Orbitolina texana* (Roemer, 1852), *Porocystis golobularis*, *Salenia texana*, gastropods, pecten, and pelecypods	Kgrb	Middle zone of the Trinity aquifer		Bulverde (A)	30–40 (typically 30)	Semi-confining	MO, BR BP, FR	*Salenia texana* bed immediately below *Corbula* bed, abundant fossils including *Porocystis golobularis*, *Orbitolina texana* (Roemer, 1852), *Macraster* sp., *Nerinia* sp., pecten, gastropods, pelecypods	
					Mudstone, wackestone, argillaceous wackestone, boundstone; *Caprinid* sp., *Monopluria* sp., *Toucasia* sp., *Orbitolina texana* (Roemer, 1852), gastropods, pectens, pelecypods	Kgrlb			Little Blanco (B)	30—40 (typically 30)	Aquifer	MO, BU, BP, FR	Limestone beds thicker and more resistive to erosion than overlying and underlying units, *Orbitolina texana* (Roemer, 1852), patch reefs	
					Argillaceous wackestone, shale; *Orbitolina texana* (Roemer, 1852), gastropods, pelecypods	Kgrts			Twin Sisters (C)	10—66 (typically 30)	Semi-confining; Confining shale beds	IP	Thick argillaceous beds, thin shale beds, *Orbitolina texana* (Roemer, 1852), contains ponds and seeps, often little vegetation, steeper slopes often with "badlands" type weathering, thinner in areas of patch reefs in the underlying Doeppenschmidt HSU	
					Mudstone, wackestone, packstone, grainstone, boundstone, argillaceous wackestone and packstone, *miliolid* grainstone; *Caprinids* sp., *Toucasia* sp.	Kgrd			Doeppen-schmidt (D)	40—80 (typically 40)	Aquifer	IP, MO, BU, BP, FR, CV	*Orbitolina texana* (Roemer, 1852), limestone beds thicker and more resistive than overlying and underlying patch reefs formed on rudist, reefal talus	Stop 5, the Narrows on the Blanco River
					Alternating beds of argillaceous wackestone, packstone; mudstone, wackestone, packstone, grainstone, *miliolid* grainstone; *Monolurids* sp., *Nerinia* sp., *Orbitolina texana* (Roemer, 1852), *Tylostoma* sp., and oysters, pectens,and pelecypods	Kgrr			Rust (E)	40—70 (typically 40)	Semi-confining	IP, FR, CV	Forms stair-step topography with soils, *Orbitolina texana* (Roemer, 1852)	
					Wackestone, packstone, grainstone, boundstone, burrows; *Caprinid* sp., *Miliolid* sp., *Orbitolina texana* (Roemer, 1852), *Toucasia* sp., *Trigonia* sp., Turritella sp., various corals, pectens, shell fragments	Kgrhc			Honey Creek (F)	45—60 (typically 55)	Aquifer	IP, MO, BU, BP, FR, CH, CV	Thick beds of wackestone, packstone, grainstone; corals, *Caprinid* sp., *Trigonia* sp., cliff forming; outcrop often contains large limestone float with large channel and moldic porosity, caves and springs	
		Pearsall		Hensell Sand	Claystone, siltstone, terrigenous sand, red sandstone conglomerate/ breccia at base of unit; oysters, quartz geodes; grades into the lower Glen Rose to the south becoming dolomitic	Kheh			Hensell	0—61	Aquifer	IP, MO, SH, CV	Quartz geodes, large oyster shells, reddish sandy soil with thick grass growth, red sandstone conglomerate/ breccia at base	Stop 6, Private Park on the Blanco River
				Cow Creek Limestone	Very fine to fine-grained carbonate sand (grainstone) with localized cross-bedding; areas of patch reefs with talus slopes, corals, and rudists	Kcrcc			Cow Creek	40—72	Aquifer	IP, MO, BU, FE, VUG, BP, FR, CH, CV	Carbonate sands, cross-bedding near top, patch reefs composed of corals and rudist, talus slopes	
					Dolomitic mudstone, wackestone, packstone; oysters									
				Hammett Shale	Upper: claystone, with silstone lenses, overlain by fossiliferous dolomitic limestone Lower: siltstone and dolomite	Khah	Confining unit		Hammett	50	Confining	**	Holds surface water, springs at contact with Cow Creek	

Figure 3. Summary of the geologic framework and hydrostratigraphy of the Edwards and Trinity aquifers within Bexar and Comal Counties, Texas. [[1]Informal, [2]Thickness based on field mapping] —Continued

Road Log

Access the directions at: ftp://ftpext/pub/cr/tx/san.antonio/Clark/

1. Meet in parking lot of Wyndham Garden San Antonio near La Cantera at 7:15 AM for a mandatory briefing about field trip safety and logistics.
2. Field trip convoy leaves parking lot at 7:30 AM.

   (Estimated travel time to first stop is 13 minutes)

3. Exit Wyndham Garden San Antonio near La Cantera parking lot, and turn right on to Market Hill.
4. Turn right (west) onto North Loop 1604 (hereinafter referred to as Loop 1604) West frontage road.
5. Take turnaround from the 1604 West frontage road to the 1604 East frontage road
6. Continue east on the Loop 1604 East frontage road through the light at the La Cantera Pkwy./Peace Blvd. intersection. (Cumulative distance 0.5 mi). After passing the La Cantera Pkwy./Peace Blvd. intersection, merge onto Loop 1604 East from the left lane using the entrance ramp (Cumulative distance – 0.7 mi).
7. Continue east on Loop 1604 to the Voigt Dr./Stone Oak Pkwy. exit (cumulative distance 8.1 mi).f
8. Follow the Loop 1604 East frontage road, staying in the left lane, to the turnaround at Stone Oak Pkwy/Voigt Dr. (cumulative distance – 8.4 mi).
9. Take the turnaround and go west on the Loop 1604 West frontage road. Merge into the right lane and continue to Sonterra Place (cumulative distance – 8.8 mi).
10. Turn right (north) onto Sonterra Place.

    Genesis cave is on the right within a fenced-in playground; the approximate address is 18514 Sonterra Place. Parking is in the Cornerstone Church parking lot. (cumulative distance – 9.4 mi).

Field Trip Stop 1: Genesis Cave (presentation by George Veni)

Planned time at stop 1 is from 7:45 AM to 8:30 AM

11. Leaving the parking area for Field Trip Stop 1 turn right (east) on Sonterra Place, and ead east toward Stone Oak Pkwy.

12. Turn right onto Stone Oak Pkwy, and go past the first left turn (only 200 ft from where you turned on to Stone Oak Pkwy) to the following turnaround at Tuscany Stone (cumulative distance – 9.6 mi).

13. After making the turnaround from southbound Stone Oak Pkwy to northbound Stone Oak Pkwy, follow Stone Oak Pkwy north and east for about 3.6 mi to a turnaround located just past the entrance to the northernmost of two parking areas for Stone Oak Park (cumulative distance – 13.2 mi).
14. Make the turnaround to go the opposite direction on Stone Oak Pkwy, and turn right (north) at the entrance to Stone Oak Park that is less than 100 ft past the turnaround. Follow the entrance road to the parking area (cumulative distance – 13.3 mi).

Field Trip Stop 2: San Antonio River Authority Flood Control Dam (Site 8), and Bear and Cub Caves (presentation by Geary Schindel)

Planned time at stop 2 is from 8:45 AM to 9:30 AM

15. Leaving the parking area at Field Trip Stop 2, turn right (west) on Stone Oak Pkwy., and follow it about 0.8 mi (first traffic light) to Canyon Golf Rd. (cumulative distance – 14.1 mi).
16. Turn right (north) on Canyon Golf Rd., and follow it about 2.8 mi to the entrance to Friesenhahn Cave (less than 0.2 mi after passing under some high voltage power lines). Turn right through the gate and park in the designated area (cumulative distance – 16.9 mi).

Field Trip Stop 3: Friesenhahn Cave (presentation by Keith N. Muhlestein)

Planned time at stop 3 is from 9:45 AM to 10:30 AM

17. Leaving Friesenhahn Cave, turn right (north) on Canyon Golf Rd., and go about 0.25 miles to Overlook Pkwy (cumulative distance – 17.1 mi).
18. Turn right (east) on Overlook Pkwy, and go 1.5 miles to US Hwy 281 (cumulative distance – 18.6 mi).
19. Turn left (north) on US Hwy. 281 North, and follow it north about 30 miles to the town of Blanco (cumulative distance – 48.2 mi).
20. In Blanco turn right on 4th St. and go one block east to the 'OLD 300 BBQ' which is at the northwest corner of 4th and Pecan St. Parking is usually available around the Old Blanco County courthouse (cumulative distance – 48.3 mi).

Field Trip Stop 4: Lunch Presentation: Cretaceous Sedimentation in Central Texas (presentation by Alexis Godet)

Planned time at stop 4 is from 11:30 AM to 12:30 PM

21. Leaving Field Trip Stop 4, continue east and south on Loop 163/RR-165, across the Blanco River for about 0.5 mi to the point where RR-165 turns left (east) and Loop 163 continues ahead (cumulative distance – 48.9 mi).

    Note: In the Texas, rural roads can be designated as FM (Farm to Market), FR (Farm Road), RM (Ranch to Market) or RR (Ranch Road); and it is not uncommon for the same road to be designated as "RR" in one location and as "FM" in another. Do not get confused if the route you are following changes from, "FM" to "RM". As long as the numerical designation does not change, you are on the correct road.

22. Turn left (east) onto RR-165 East, and follow it about 7.5 mi to FR-2325 (cumulative distance – 56.4 mi).
23. Turn right (east) on FR-2325, and go 0.3 mi to Chimney Valley Rd. (cumulative distance – 56.7 mi).
24. Turn right (south) on Chimney Valley Rd., and follow it about 1.8 mi to Red Corral Ranch Rd. (cumulative distance – 58.4 mi).
25. Turn left (east) on Red Corral Ranch Rd., and follow it about 1.0 mi to Taylor Ranch Rd. (cumulative distance – 59.4 mi).

26. Turn right (south) on Taylor Ranch Rd., and follow it about one mile to where it makes a 90 degree curve to the left (east). Almost at the end of that curve, two roads, only 50 ft apart, will join from the right. Turn right (south) on the nearer of the two roads, Conservancy Trace (cumulative distance – 60.4 mi).
27. Follow Conservancy Trace about 0.2 mi, go through the gate, and park in the designated area (cumulative distance – 60.6 mi).

Field Trip Stop 5 is on private property and is reached via a 1.5 mile ranch road that may be difficult to traverse without a high clearance or non-4WD vehicle. Participants not wishing to take their vehicles farther may park them at the gate and ride in other vehicles. (cumulative distance – 62.1 mi).

Field Trip Stop 5: The Narrows on the Blanco River (presentations by James Golab, Amy Clark, and Allan Clark

Planned time at stop 5 is from 1:00 PM to 2:45 PM

28. Leaving Field Trip Stop 5, retrace your route north about 2.7 mi via Conservancy Trace and Taylor Ranch Rd. to Red Corral Rd. (cumulative distance – 64.8 mi).
29. Turn right on Red Corral Ranch Rd., and go about 2.9 mi to RR-2325 (cumulative distance – 67.7 mi).
30. Turn right (east) on RR–2325, and go 5.4 mi to Burnett Ranch Rd. (cumulative distance – 73.1 mi).
31. Turn right (SW) on Burnett Ranch Rd., and go 1.2 mi to Valley View Rd. (cumulative distance – 74.3 mi).
32. Turn right (west) on Valley View Rd., and go 0.6 mi (cumulative distance – 74.9 mi) to the entrance to Burnett Ranch Community Park, on the left. Turn left, and park in the designated area (cumulative distance – 75.0 mi).

Field Trip Stop 6: Burnett Ranch Community Park (optional stop, presentation by Marcus Gary)

Planned time at stop 6 is from 3:45 PM to 4:30 PM

33. Leaving Burnett Ranch Community Park, turn left (north) on Valley View Rd., and go 1.1 mi to Days End Rd. (cumulative distance – 76.2 mi).
34. At Days End Rd. turn left (south), and go one mi to a **very sharp** 135 degree turn to the right (cumulative distance – 77.2 mi). Continue on Days End Rd. for another 0.3 mi (cumulative distance – 77.5 mi) until Days End Rd. makes a turn to the left (south) and Curry Ranch Rd. continues straight ahead (west). Turn left and stay on Days End Rd for another 2.4 mi (cumulative distance – 78.5 mi) until it makes a turn to the left (south) and its name changes to Cottonwood Rd.
35. Continue on Cottonwood Rd. for an additional 1.8 mi to Fischer Store Rd (Cumulative distance 80.3 mi)

Note: The Corbula Bed, which marks the dividing line between the upper and lower members of the Glen Rose Limestone, is exposed in the drainage ditch at the intersection of Fischer Store Rd. and Cottonwood Rd.

36. Turn right (west) at Fischer Store Rd., and go 2.8 mi to the community of Fischer (cumulative distance – 83.1 mi).

37. Turn left (east) at Fischer on RR-484, and go 0.2 mi to the stop light at RR-32 (cumulative distance – 83.3 mi).

> CAUTION: RR-32 is one of the major roads that connect the I-35 corridor with the US-281 corridor, and it can have heavy truck traffic. Use care when crossing RR-32 because of limited sight distance due to hills in both directions.

38. Cross RR-32, and continue south on RR-484 for an additional 2.6 mi to FM-306 (cumulative distance – 85.9 mi).
39. Turn left (east) on FM-306, and follow it 7.1 mi to South Access Rd. (cumulative distance – 93.0 mi).
40. Turn right (south) on South Access Rd., and pass by the base of Canyon Dam. Normal pool elevation in Canyon Lake is 100 ft above South Access Rd.
41. Follow South Access Rd. about 1.3 mi to the entrance to the Canyon Lake Gorge Visitor Center, a small gravel driveway on the right (cumulative distance – 94.3 mi).

Field Trip Stop 7: Canyon Lake Gorge (presentation by Carter Keairns)

Planned time at stop 7 is from 5:00 PM to 5:50 PM

42. Leaving stop 7 turn right (south) on South Access Rd., and go 1.3 mi to FM-2673 (cumulative distance – 95.6 mi).
43. Turn right (west) on FM-2673, and go 6.0 mi to the intersection with FM-3159 in Startzville (cumulative distance – 101.6 mi).
44. Turn left (west) on FM-3159, and go 5.4 mi to the intersection with FM-311 (cumulative distance – 107.0 mi).
45. Turn left (south) on FM-311, and go 1.2 mi to the intersection with TX-46 (cumulative distance – 108.2 mi).
46. Turn left (south) on TX-46, and go 2.8 mi to FM-3009 (cumulative distance – 111.0 mi).
47. Turn right (south) on FR-3009 (Natural Bridge Caverns Road), and go 6.9mi to the entrance to the Bracken Bat Cave on the right (cumulative distance – 117.7 mi).

> The road to the bat cave is an unmarked Private Road; personnel from the UTSA Student Geological Society and/or Bat Conservation International will meet us at the gate. The parking area at the bat cave is 1.7 mi (cumulative distance – 119.4 mi) past the entrance gate.

Field Trip Stop 8: Bracken Bat Cave (presentations by Ron Green and George Veni)

Planned time at stop 8 is from 6:30 PM to 7:30 PM; bat flight begins at 7:30PM

Field trip ends after the bat flight; we will caravan back to the parking lot of the Wyndham Garden San Antonio near La Cantera.

(Estimated travel time from Stop 8 back to hotel is 45 minutes)

Driving directions from Bracken Bat Cave to Wyndham Garden San Antonio near La Cantera

48. From the Bracken Bat Cave parking area, proceed back toward the entrance to the bat cave preserve on FM-3009 (cumulative distance – 121.1 mi).
49. At FR-3009 turn right (south), and go about 5.3 mi to Nacogdoches Rd. (cumulative distance – 126.4 mi).
50. Turn right on Nacogdoches Rd., and go 4.4 mi to the Loop 1604 West frontage road (cumulative distance – 130.8 mi).
51. Turn right (north) on the Loop 1604 West frontage road and go about a quarter of a mile to the Loop 1604 West entrance ramp. Enter Loop 1604 West and follow it 16.3 mi to the La Cantera Pkwy/Fiesta Texas/ Chase Hill Blvd exit (cumulative distance – 147.1 mi).
52. Follow the Loop 1604 West frontage road for about 0.4 mi to Market Hill (cumulative distance – 147.5 mi).
53. Turn right on Market Hill and go 0.1 mi to the hotel, on the left (cumulative – distance 147.6 mi).

Field Trip Stop 1: Genesis Cave

By George Veni

Introduction

The narrow entrance to Genesis Cave, and the adjacent shallow sinkhole, belies that fact that this is the deepest cave in Bexar County and one of the deeper caves in Texas. It has a surveyed depth of 78 meters (m) (Texas Speleological Survey, 2016) and continues deeper. Genesis is the deepest cave known in the recharge zone in the Edwards aquifer (Balcones Fault Zone) (fig. 1). The aquifer's water table often rises to flood the cave's lower portions.

The cave can be described as having three main sections (fig. 4). The upper section, from the surface to a depth of 44 m, is a series of short drops and steep-floored passages over a horizontal length of about 70 m. The middle section is "The Crawl," a 47-m long horizontal passage that averages 1 m wide by 0.5 m high. The Crawl ends at the top of the cave's lower section, which begins with "The Drain," a 22.8-m deep pit, and continues steeply 10 m deeper to the cave's surveyed end in a small room. The floor of the room was excavated a short distance to reveal a clean-washed pit estimated to be 6 m deep. This pit has not been explored due to high levels of carbon dioxide in the cave's atmosphere that often occur through the cave and increase with depth.

Genesis Cave was discovered in early June 1985 and surveyed over the next couple of months. A year after the map was completed, the Mud Pit in the lower section was explored to a muddy bottom but was not surveyed. The cave was named after a plot subject in a *Star Trek* movie and not for any religious reason. When named, the cavers who discovered it did not know a church would be built on the property a year later. The 6-m deep pit at the bottom was opened in the early 1990s.

The cave provides valuable insight into the karst hydrogeology of the Edwards aquifer. It is also biologically important, containing the federally listed endangered carabid beetle, *Rhadine infernalis infernalis* (U.S. Fish and Wildlife Service, 2011). A stygobitic salamander was reported in an isolated pool in the cave, but this has not been confirmed with collected specimens. If accurate, it would represent the stranding of a salamander following high aquifer levels. More importantly, it may indicate the presence of groundwater flow paths from the aquifer in the adjacent Glen Rose Limestone (figs. 2 and 3) where some of these salamanders are known. For more details about the cave and its early history, see Veni (1988).

Hydrogeology

The first and most important thing to do when examining the cave's geology is to ignore the stratigraphy shown on the popularly used maps. The mapped stratigraphy in 1985 was inaccurate as there was no detailed mapping of the Edwards Group (fig. 3) and its members. Admittedly, the general morphology of the cave (fig. 4) fit well with the stratigraphy that was interpreted. The interpretation was that the upper part of the cave was in the Person Formation of the Edwards Group, "The Crawl" was perched on the regional dense member of the Person Formation, and the lower portion of the cave was in the Kainer Formation of the Edwards Group (figs. 3 and 5).

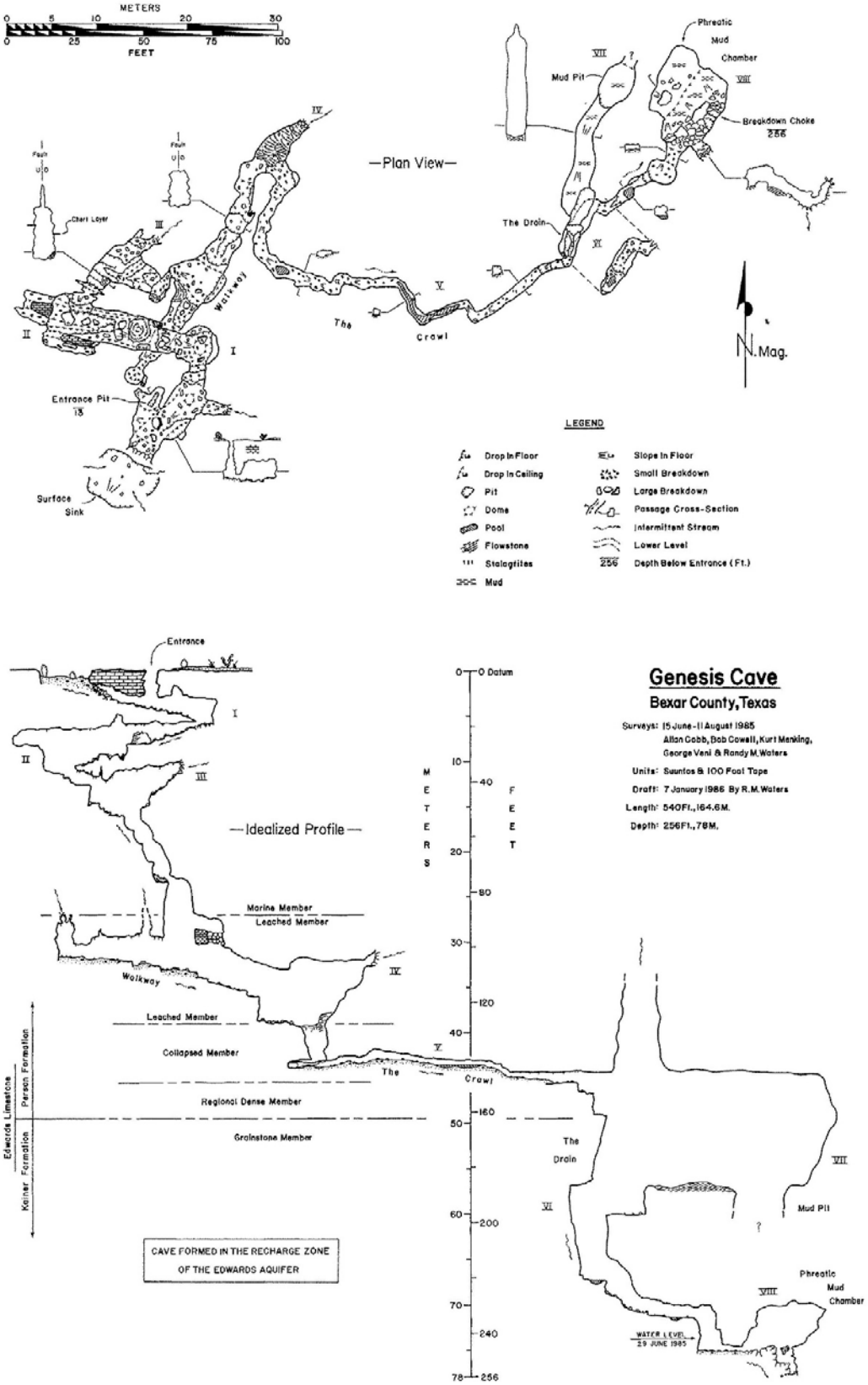

Figure 4. Map of Genesis Cave, Bexar County, Texas (Veni, 1988).

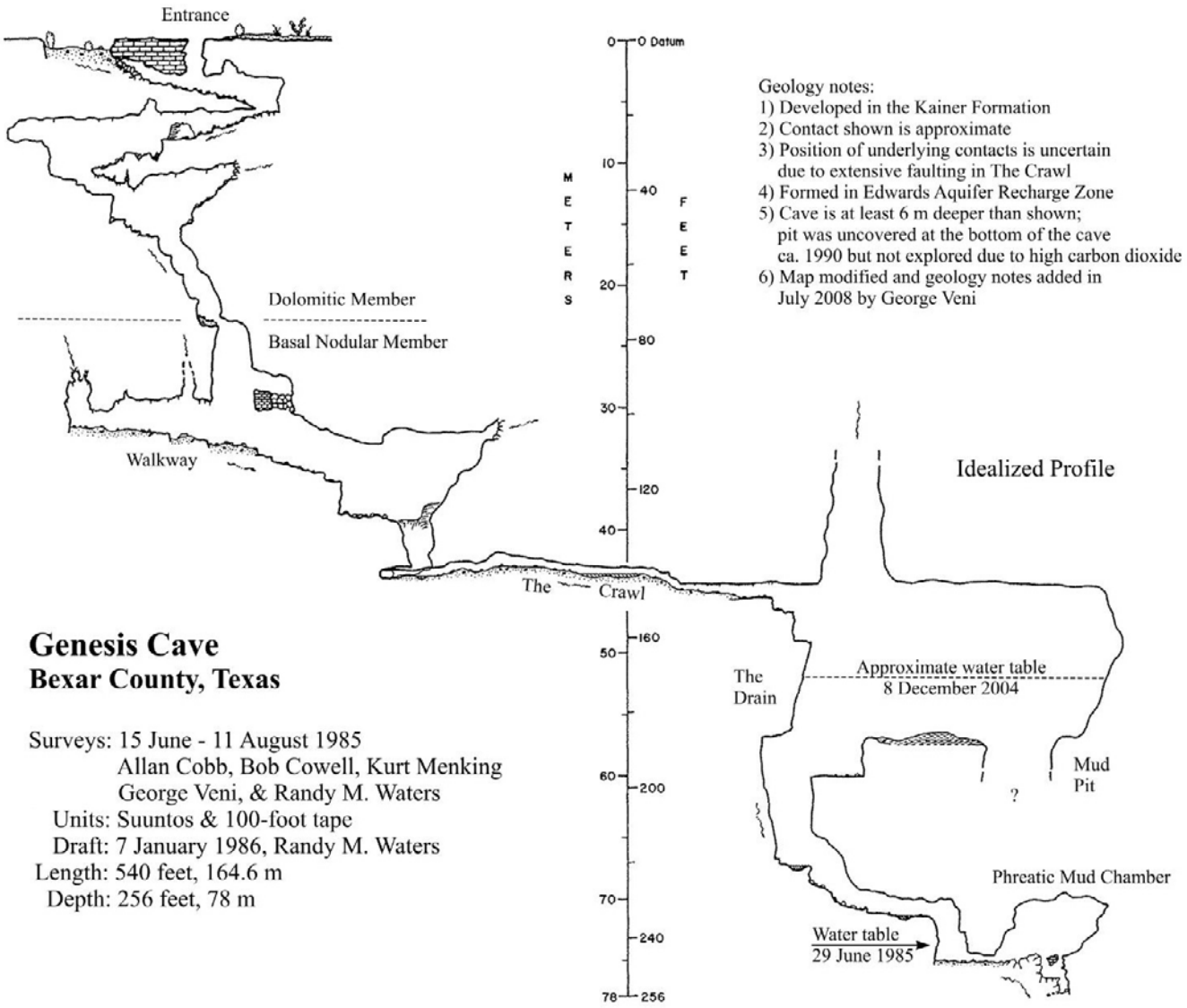

Figure 5. Updated geological and water-table profile of Genesis Cave, Bexar County, Texas.

Ten years later, Stein and Ozuna (1995) published the first detailed map of the geology in the Bexar County portion of the Edwards aquifer recharge zone. They identified the surface as the dolomitic member (figs. 3 and 5) of the Kainer Formation, which is near the bottom of the Edwards Group. Their mapping also placed the cave in the middle of a 360-m-wide horst that strikes northeast-southwest, the major trend of faults in that area. Caves in the Edwards aquifer recharge zone are most often formed along joints (Veni, 1988). Faults rarely guide passage development but one passage in Genesis Cave is formed along two parallel faults that strike N30°E and have a combined 1-m throw down to the east.

In 2004, the cave was verified (by the author) that its roughly upper 23 m occurred in the dolomitic member and that the Kainer's basal nodular member (figs. 3 and 5) was below. However, the situation became complicated in "The Crawl," which based on this new interpretation as shown on figure 5, should be located well within the cavernous hydrostratigraphic unit (fig. 3) of the upper member of the Glen Rose Limestone. The brecciated to highly disrupted beds in the walls and ceiling of "The Crawl," that led the author 19 years earlier to conclude it was in the collapsed member of the Person Formation and perched on the regional dense member (fig. 3), left the stratigraphic position uncertain. The walls of the first 10 m of "The Crawl" are probably within a fault breccia. At the end of "The Crawl" the beds are not disrupted, but the mud covering the walls and high levels of carbon dioxide prevented identification of the unit, and from there extrapolating the stratigraphy to the bottom of the cave. It is believed that they are in the upper member of the Glen Rose Limestone, but a careful study of "The Crawl" and deeper portions of the cave are still needed to verify the stratigraphy and explain the origin of the disrupted beds.

The sinkhole near the cave's entrance drained an area of over 10,000 m^2 prior to urbanization; runoff from only about a third of that area is now captured. Based on morphology, recharge through the sinkhole was the primary driving force in the cave's development. As the sinkhole filled with sediment, its permeability diminished, resulting in increased overland flow, which probably enlarged a joint-controlled dome in the cave's first room to create its present entrance.

Considerable, but unquantified recharge enters the cave through other permeable fractures. Genesis is one of many caves in the Edwards aquifer recharge zone where water is observed dripping to gushing (as is the case with Bear Cave, seen at the next field trip stop) from solutionally enlarged fractures into passages within 10 to 30 minutes of rainfall. The combined flow from these fractures and the cave's sinkhole result in a stream that reaches the water table within minutes. This behavior is especially prevalent in the dolomitic member of the Kainer Formation because of its high fracture permeability, which also limits overland flow resulting in predominantly small sinkholes and many barely-enterable cave entrances (Veni, 2005). The size of the drainage area for the Genesis sinkhole is a rare exception.

Aquifers levels are known to fluctuate at least 26 m in the cave, with the highest level observed on December 8, 2004 (fig. 5). These levels have not been correlated with monitoring wells in the area, but at least a small amount of groundwater mounding in the cave is possible. Such rises could have also stranded the reported stygobitic salamander in the vadose zone.

The only recharge zone cave known in Bexar County to contain such salamanders is Elm Springs Cave, located in the Person Formation about 7 kilometers (km) to the southwest. Sweet (1978) identified them as *Eurycea tridentifera*, which are otherwise mostly known from the caves in the lower member of the Glen Rose Limestone (the uppermost unit of the Middle Trinity aquifer) with most localities occurring along Cibolo Creek about 20 km to the north. However, a recent genetic study of *Eurycea tridentifera* discovered them in Stealth Cave (Bendik and others, 2013), located almost halfway between

Cibolo Creek and Elm Springs Cave and at the top of the upper member of the Glen Rose Limestone (fossiliferous hydrostratigraphic unit) (Clark and others, 2009). This locality suggests that fault juxtaposition of permeable limestone units has allowed the migration of the salamanders through conduits, as well as potential direct lateral recharge of the Edwards aquifer from the Glen Rose. Unfortunately, although the salamander is on the Texas list of threatened species, Elm Springs Cave was sealed in the middle to late 1990s, and its salamanders cannot be accessed for genetic study. If a stygobitic salamander is found again in Genesis Cave, it should be collected and genetically assessed for DNA evidence of this potential Cibolo/Glen Rose flow path into the Edwards aquifer.

In the meantime, Johnson and others (2010) conducted a series of more conventional tracer tests with fluorescent dyes at Genesis and caves as much as 4 km west and northwest in the Panther Springs Creek drainage basin. When eosine dye was injected during the aforementioned high conditions on December 8, 2004, it was detected in low concentrations at two wells, 1.75 km and 1.89 km to the southwest about a month later, demonstrating groundwater velocities of about 50 m/day. In contrast, dye injected at another cave during the same period yielded groundwater velocities of nearly 5,000 m/day. The main mass of dye injected into Genesis Cave was not found. These and other results indicate that Genesis Cave may straddle the divide between the groundwater drainage basin below Panther Springs Creek and groundwater to the east. Potentially, the eosine dye from Genesis may not have appeared in the Panther Springs Creek basin wells except for the high aquifer levels at the time. Additional tracer work is needed to find the major groundwater flow path fed by Genesis Cave.

Cave and Aquifer Management

The church, which owns the cave, has long been an active partner in its protection and has supported access for its study, although there were a couple of early missteps. In 1987, the church's parking lot proved smaller than anticipated. A quick expansion of the lot resulted in asphalt poured to within 5 m of the cave's entrance, no curb installed, and parking lot runoff pouring into the cave. This was a violation of the church's water pollution abatement plan for the original parking lot's design. The Edwards Underground Water District (EUWD), predecessor agency to the current Edwards Aquifer Authority, worked with the church and the asphalt was removed, land surface restored, and the parking lot moved to 30–40 m from the entrance. However, two factors were not adequately considered: the low gradient topography and that the expanded parking area still extended over nearly half of the cave. A curb was installed this time, but for several years water flowed to the ends of the curb and again into the cave. Some of this water never reached the cave entrance, presumably recharging the cave via many of the permeable fractures in the intervening area. In the late 1990s, the parking lot was moved back 80–90 m from the cave and curbed so that no parking lot runoff now reaches the entrance or flows over the known parts of the cave. Also in the late 1990s, the road Sonterra Place was constructed, cutting off about two-thirds of the runoff into the cave.

Construction of Sonterra Place, which is not owned by the church, encountered another cave. Like Genesis Cave 180 m to the west, Godchildren's Sink was not named for religious reasons. This pit was a trash dump when the property was a ranch. Excavation of the trash by cavers reached a depth of 6 m in October 1985 without finding the end to the trash or cave (a mangled baby doll pulled out of the trash was placed where it could "watch" the excavations and it became known as "the godchild," hence the cave's name). Road construction did not remove the trash but preserved the cave within a 90-m long by 7- to 15-m-wide vegetated median in the middle of the road. The cave's entrance was filled with rocks and a storm water detention and filtration basin occupies the eastern half of the median.

Genesis Cave extends a third of the way and directly toward Godchildren's Sink. Unexplored domes in Genesis could lead to passages that drain Godchildren's, or the caves may connect in the aquifer below the currently explored levels in Genesis Cave. In any case, their proximity suggests they are similarly related hydrologically to the Edwards aquifer. It is not known what effects the unexcavated trash and the storm water basin are having on the quality of water transmitted through these caves.

While access to Godchildren's Sink was blocked by rocks, in 1988, the EUWD contracted my consulting firm, George Veni and Associates, to gate Genesis Cave. EUWD did not approve the gate design that was recommended but insisted on a different design. The EUWD designed gate was installed and it was breached within a month as predicted by George Veni and Associates. The gate was then chained shut and the church built two fences around the cave a few years later. A decorative fence was put around the entrance and sinkhole, and a chain-link fence was constructed along the edge of the parking lot.

Field Trip Stop 2: San Antonio River Authority Flood Control Dam (Site 8), and Bear and Cub Caves

By Geary Schindel and George Veni

Since 1971, the San Antonio River Authority has constructed 15 flood control dams in the Salado Creek watershed. The Site 8 dam was completed across Mud Creek in 1973. It measures 510 m long by 19 m high and can hold up to 5.16 million cubic meters (m^3) of water that drains from its 28.95-square kilometer (km^2) drainage basin. Total volume of fill to create the dam was approximately 310,000 m^3. During record flooding in October 1998, following 46 centimeters (cm) of rainfall in a 24-hour period (mean annual precipitation is only 76 cm), the spillway for the dam overflowed for the first time. The overflow was so forceful that it carried a 20-m-long by 10-m-wide slab of concrete for a few meters downstream until stopped by a tree.

Some of the flood control dams have also served to enhance recharge into the Edwards aquifer. The Site 8 dam is particularly notable in this regard to the presence of three caves within the reservoir area. The most significant cave is Bear Cave, which is a transitional cave originally formed as a large chamber by previous hydrologic regimes. The cave is most likely of hypogenic origin and may represent a paleo spring site (fig. 6). The collapse of its roof by valley downcutting modified it into an important recharge site. Prior to the construction of the dam, water had never been observed to flow into the cave's entrance. However, parts of the cave extend under the creek bed and capture substantial volumes of water when the stream flows. At such times, water pours into the cave through numerous fractures, including one "fire-hydrant" sized downspout. These inflows carry sediment, which demonstrate no filtration of the water. Examination of the surface stream has thus far found no single eddy or site of recharge to account for the flow found in the cave, indicating rapid combined recharge through the many solutionally enlarged fractures in the limestone. Flow into the cave and overall recharge into the aquifer behind the Site 8 dam has not been gauged. Increased urbanization of the drainage basin has raised concern about the quality of the impounded water recharging the aquifer. During the October 1998 and July 2002 flood events, water levels formed by the dam were as much as 4.5 m above the entrance to Bear Cave.

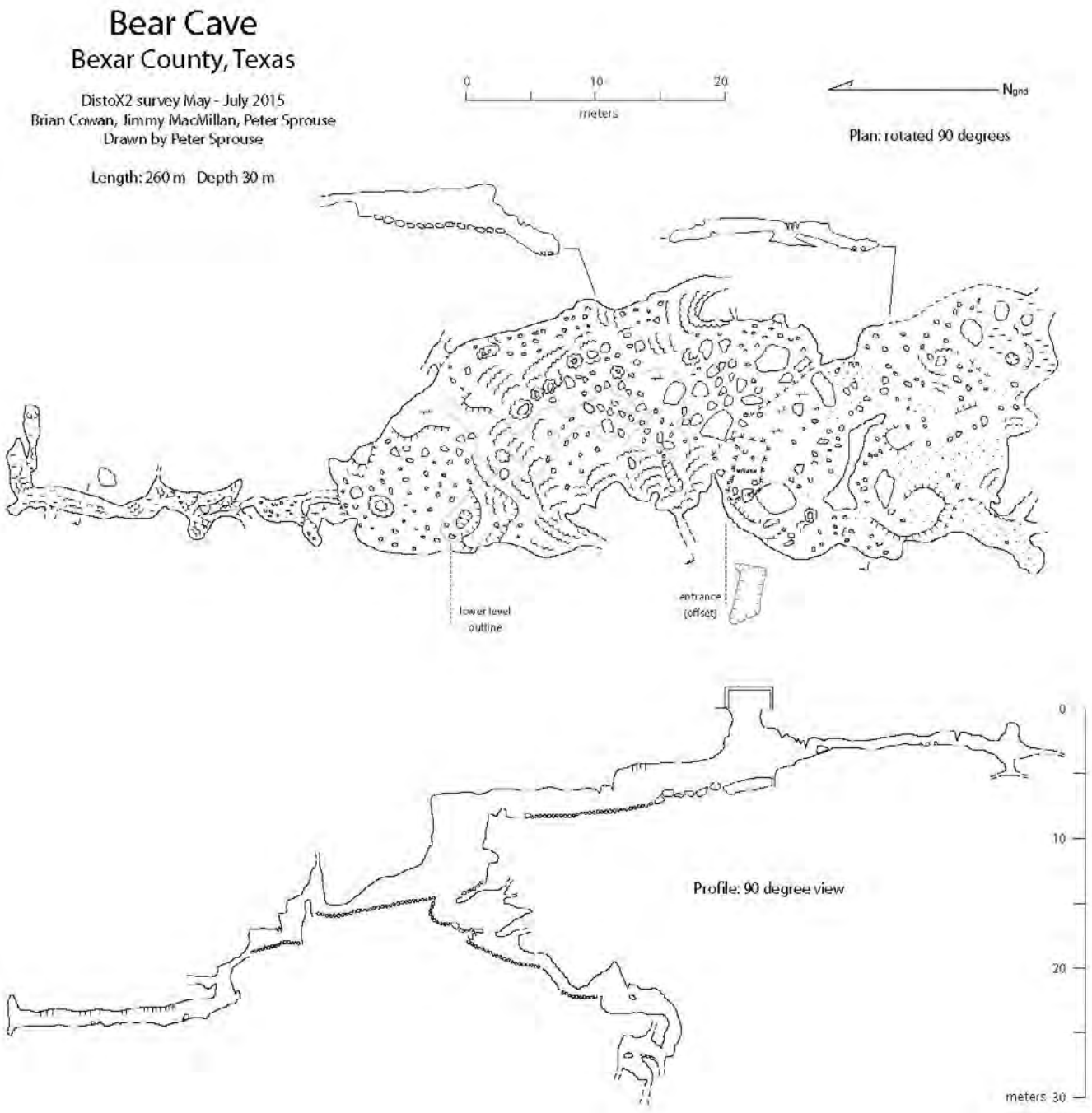

Figure 6. Map of Bear Cave, Bexar County, Texas.

Since the construction of the dam and semi-regular flooding of the cave, the bat population that once inhabited Bear Cave has now been displaced. Flooding has also modified the cave, washing open sediment plugs that had once blocked exploration and study. The map also shows the cave as having two entrances, but the natural bridge separating them was broken in an attempt to fill the cave in 1984. Flooding a year later washed away the fill.

The next most notable cave behind the Site 8 dam is Cub Cave (fig. 7). At 18 m wide by 5.5 m high, it has the largest cave entrance known in the county. Cub Cave is also an old chamber truncated by valley incision. However, it does not appear to have developed a pathway to the aquifer as permeable as at Bear Cave. New interpretations of the genesis of Cub Cave indicate that it might have formed as a mixing chamber from ascending water and represent a paleo spring site. The roof of the cave contains a number of cupolas and rise tubes from bedding enlarged conduits. A third smaller cave, a pit about 6 m deep, is located in the middle of the reservoir. Although this cave appears to be formed by vadose action to recharge the aquifer, sedimentation behind the dam is filling the cave faster than the sediments can be transported into the aquifer. The cave was last seen in 1985. Recent attempts to relocate it have failed.

Both Bear Cave and Cub Cave entrances do not appear to be related to the current topography as they have not captured the nearby surface stream even though both caves lie below the level of the valley bottom. The urbanization of the basin and construction of the flood control structure resulted in more frequent flooding of both caves. In addition, both caves exhibit some structures that indicate they may have been formed by ascending water. Both Bear Cave and Cub Cave contain a number of cupolas and wall channels that indicate upward flow. Do these caves represent the abandoned conduit of a paleo spring complex and are now being overprinted by epigenic processes?

Stone Oak Park is also an excellent location to view the rapid and dense urbanization of the recharge zone of the Edwards aquifer in northern Bexar County. Note the presence of large houses and apartment complexes along the parameter of the park as well as along the roadways leading to the park. San Antonio is experiencing a growth rate of fewer than 3 percent. The City of New Braunfels and City of San Marcos have approached 7 percent. The Austin–San Antonio growth corridor continues to expand and development over the recharge zone appears to be accelerating.

Urbanization of the recharge and contributing zone creates the potential for water-quality degradation in the aquifer from sanitary effluent, application of landscaping products, hazardous materials spills, increased sedimentation and erosion, and urban non-point runoff, among other things.

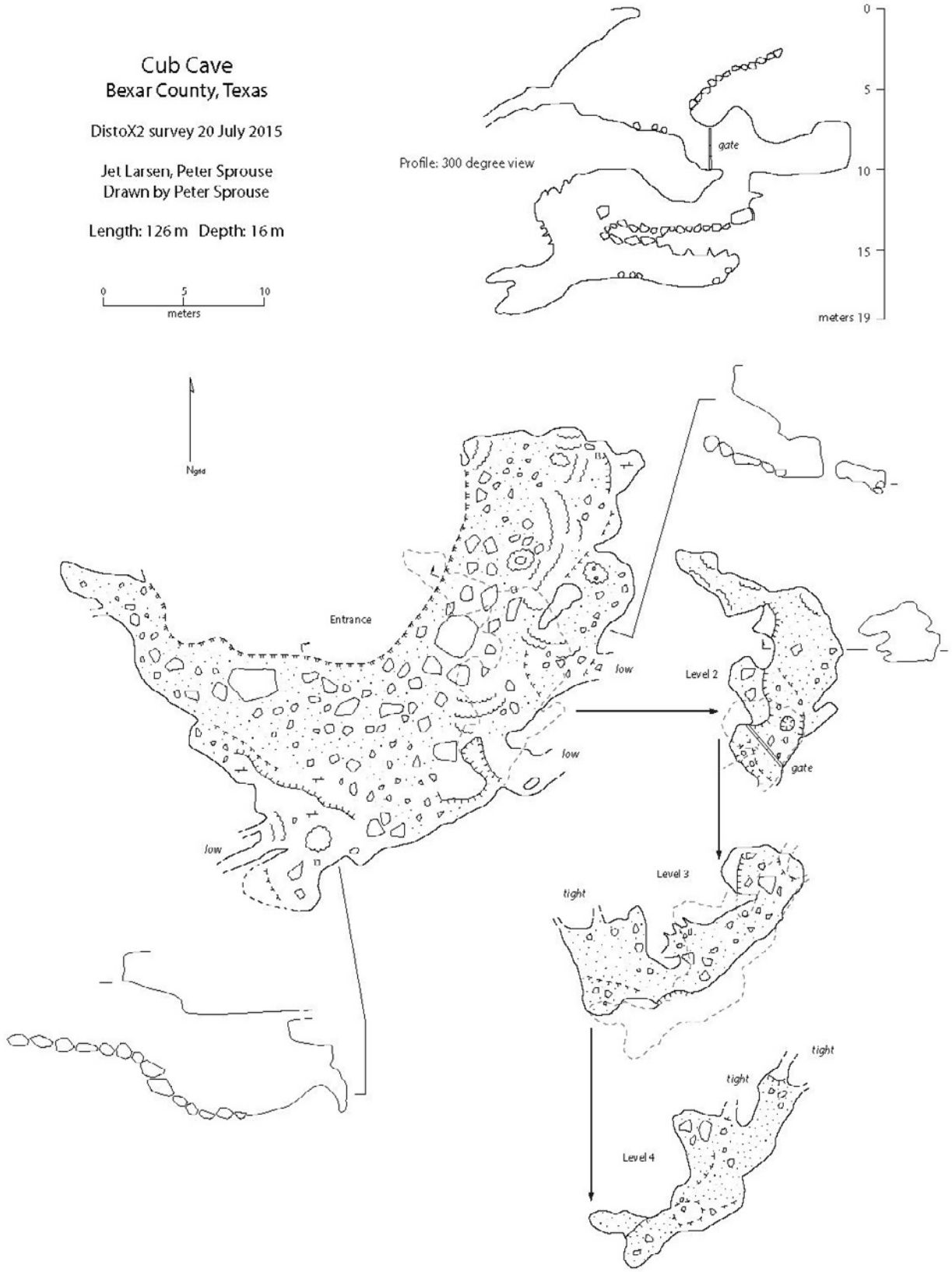

Figure 7. Map of Cub Cave, Bexar County, Texas.

Field Trip Stop 3: Friesenhahn Cave

By Keith N. Muhlestein

Friesenhahn Cave is located near the Balcones Escarpment along the Edwards Plateau of central Texas in northern Bexar County and is well known as a Pleistocene Epoch predator cave. Friesenhahn contains an exceptional variety of megafauna fossils including *Homotherium serum*, the scimitar cat, and *Mammuthus columbi*, or mammoth.

The area around the cave today is completely built out in residential neighborhoods and minimarket gas stations. The once sprawling ranchland is now lost to San Antonio's appetite for suburban housing. A tiny preserve, around 3 acres, surrounds the cave and provides a sliver of habitat for wildlife. It is covered with a mix of vegetation common to the area such as juniper, oak, and mesquite as well as various grasses and understory growth. The full extent of the cave system has not been defined because of rock and sediment filling the lower portions of the cave making them inaccessible without further excavation. It has been known for some time however, that substantial volumes of water drain into the cave and flow through it to parts unknown.

Recent 3-D resistivity research has revealed substantially more cave than is currently known. Research done by Muhlestein and Green in 2010 shows the cave extending deeper and substantially farther than previously thought. This evidence substantiates the dynamic recharge observations made by Meissner as well.

The Pleistocene cave entrance has collapsed and is currently inaccessible; however, the present day entrance consists of a 9-meter (m)-deep vertical shaft formed by solution and collapse. It is currently rigged with a ladder for easy access to the cave pit. This current entrance passes through the lower part of the Edwards Group and is a conduit to the Edwards aquifer. The known cave dimensions are roughly 10 m measured horizontally from east to west, and 20 m north to south.

The 3-D electrical resistivity survey was designed to characterize the subsurface features using a dipole-dipole array. Four overlapping grids were laid out on the site with the corner of each of the four grids meeting directly over the vertical entrance of the cave. Each grid was set to 5-m intervals for a total grid dimension of 35 m by 55 m. With an electrode overlap in both the X and Y directions, the dimensions of the four joined grids are 70 m by 110 m.

AGI Earth Imager software was used for visualization of the 3-D survey data and to statistically validate the 3-D data set. This arrangement provided a depth resolution of just over 12 m. The survey indicates additional void space associated with Friesenhahn and indicates that the cave is substantially greater in horizontal and vertical extent.

Field Trip Stop 4: Lunch Presentation: Cretaceous Sedimentation in Central Texas

By Alexis Godet

Introduction

The Cretaceous Period (ca. 66–145 Ma, Gradstein and others, 2012; fig. 8) was a time of heightened plate tectonics, rifting, and volcanism associated with the rapid breakup of the supercontinent Pangea (fig 8). These transformations affected ecological, climatic, and oceanic conditions across the planet (see Föllmi, 2012, and references therein), and resulted in a warmer climate directly related to increased levels of atmospheric greenhouse gasses including carbon dioxide. In particular during the Early Cretaceous, major volcanic pulses and increased mid-ocean ridge activity pumped vast amounts of CO_2 into the atmosphere (four times present-day concentrations) (Larson, 1991; Barron and others, 1995), triggering a climate that oscillated from "normal" greenhouse conditions coupled with widespread aridity, to intensified greenhouse conditions causing widespread humidity (Hay, 2008; Föllmi, 2012; Millán and others, 2014; Phelps and others, 2014). During this time multiple Oceanic Anoxic Events (OAEs) occurred (Schlanger and Jenkyns, 1976; Weissert and Erba, 2004; Föllmi, 2012; Phelps and others, 2014). They are commonly identified in the rock record by pronounced carbon isotope excursions (Arthur and others, 1990; Erbacher and Thurow, 1997; Leckie and others, 2002; Trabucho and others, 2010), significant marine extinctions (Erbacher and others, 2001), and a widespread (interoceanic/interbasinal) occurrence of well-preserved sedimentary organic matter in open marine deposits (Wilson and others, 1998; Erbacher and others, 2001; Leckie and others, 2002; Millán and others, 2014).

The North American continent has been affected by the aforementioned sea-level changes and environmental perturbation. A direct consequence is the inundation of North America that resulted in the development of the Western Interior Seaway (Schröder-Adams, 2014) (fig. 9). This large interior sea existed between Laramida and Appalachia, and was estimated to be 980 feet deep (Kaufmann, 1977). The fragmentation of Pangea also greatly increased the length of available coastline for passive margin and thus, epicontinental seas (fig. 9) development, where carbonate ecosystems thrived (Philip, 2003). In such a contrasted world, carbonate platforms represent ideal recorders of environmental changes, such as enhanced greenhouse conditions, rise in global temperature, and strengthened nutrient supply into the oceans (Föllmi and others, 1994; Weissert and Erba, 2004). These parameters may have had profound impacts on the development of these passive margin platforms in terms of their general morphology and their facies distributions (Föllmi and others, 2006).

Central Texas presently encompasses the Hill County (mostly Cretaceous limestones) and the Coastal Plains (Cenozoic siliciclastics). The Hill County is affected by the Balcones Fault Zone, which formed following downwarping near the Gulf Coast and moderate uplift inland during the Tertiary. The transition between these two regions corresponds to the lower Cretaceous shelf break, where the Stuart City Reef developed.

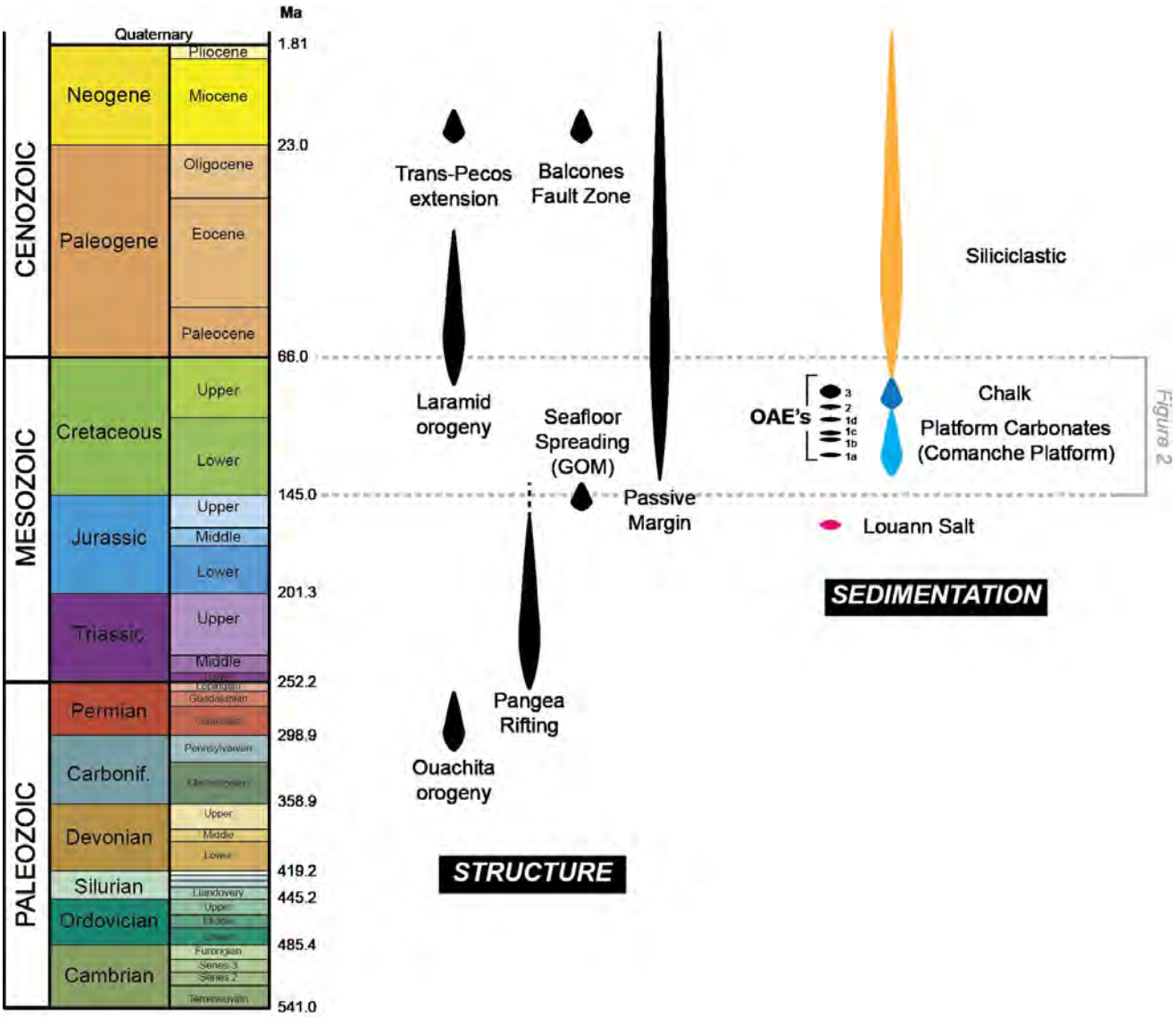

Figure 8. Key structural, paleoceanographic, and sedimentation events of central Texas plotted along the geological timescale (Gradstein and others, 2012). GOM, Gulf of Mexico; OAE, oceanic anoxic event.

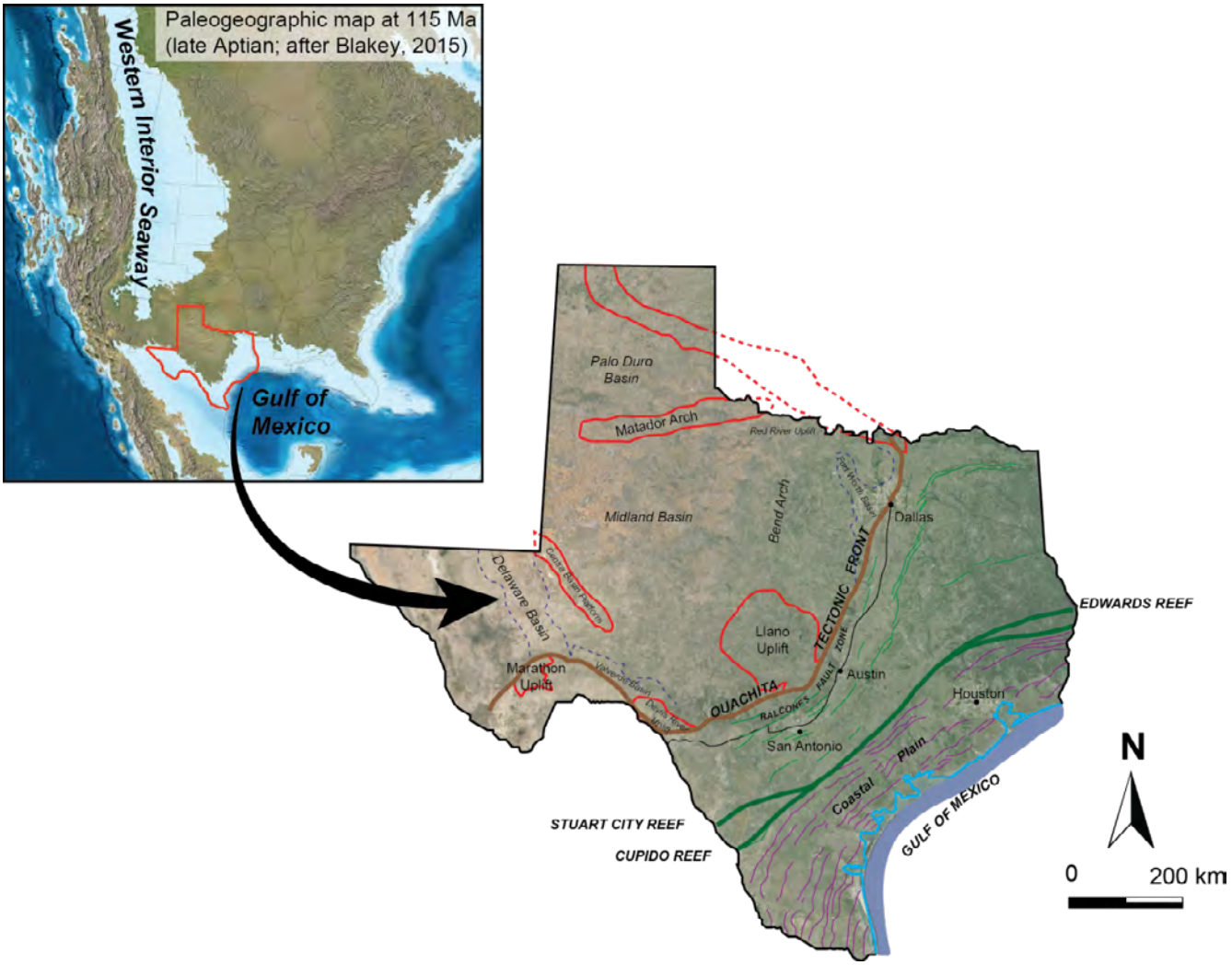

Figure 9. Simplified tectonic map of Texas outlining the main structural features and basins.

From Pangea to the Comanche Platform

The Comanche platform formed along the northern border of the present-day Gulf of Mexico, at a paleolatitude between 20 and 30° north of the equator (Scotese and others, 1988; Winker and Buffler, 1988), and provides an almost complete reference section for the Cretaceous Period in this part of the world (Phelps and others, 2014). The thick platform sequence shows very little influence from regional tectonic events as it was deposited on a passive shelf margin.

The Late Paleozoic Ouachita collision and the subsequent rifting during the Early-Mid Mesozoic (fig. 9) resulted in (1) a seaward shelf edge, (2) the San Marcos Arch, and (3) the Maverick Basin (Montgomery, 1990). After the breakup of Pangea and rifting in the Late Permian and Triassic (fig. 10), arid conditions during the Jurassic promoted deposition of the thick Louann salt (fig. 10) in basins within and around the Gulf of Mexico (fig. 9). These basins became zones of increased subsidence and sedimentation during the Cretaceous Period (Salvador, 1991; Phelps and others, 2014). During the late Jurassic, the transitional continental crust was attenuated and later became the foundation for the Comanche platform (Buffler and Sawyer, 1985; Winker and Buffler, 1988; Phelps and others, 2014). The San Marcos Arch was a high point between the Maverick Basin in south-central Texas and the East Texas Basin, and separated these two basins from each other during the Late Cretaceous (Luttrell, 1977). The Rio Grande Embayment is bounded by the Balcones Fault Zone to the north with abundant volcanic ash in the Austin and Taylor Groups, and the Salado-Tamaulipas Arch as well. Cretaceous and Tertiary sediments accumulated in the rapidly subsiding Rio Grande Embayment (Luttrell, 1977), where upper Cretaceous deposits reached a maximum thickness, whereas they are the thinnest over the San Marcos Arch (Montgomery, 1990).

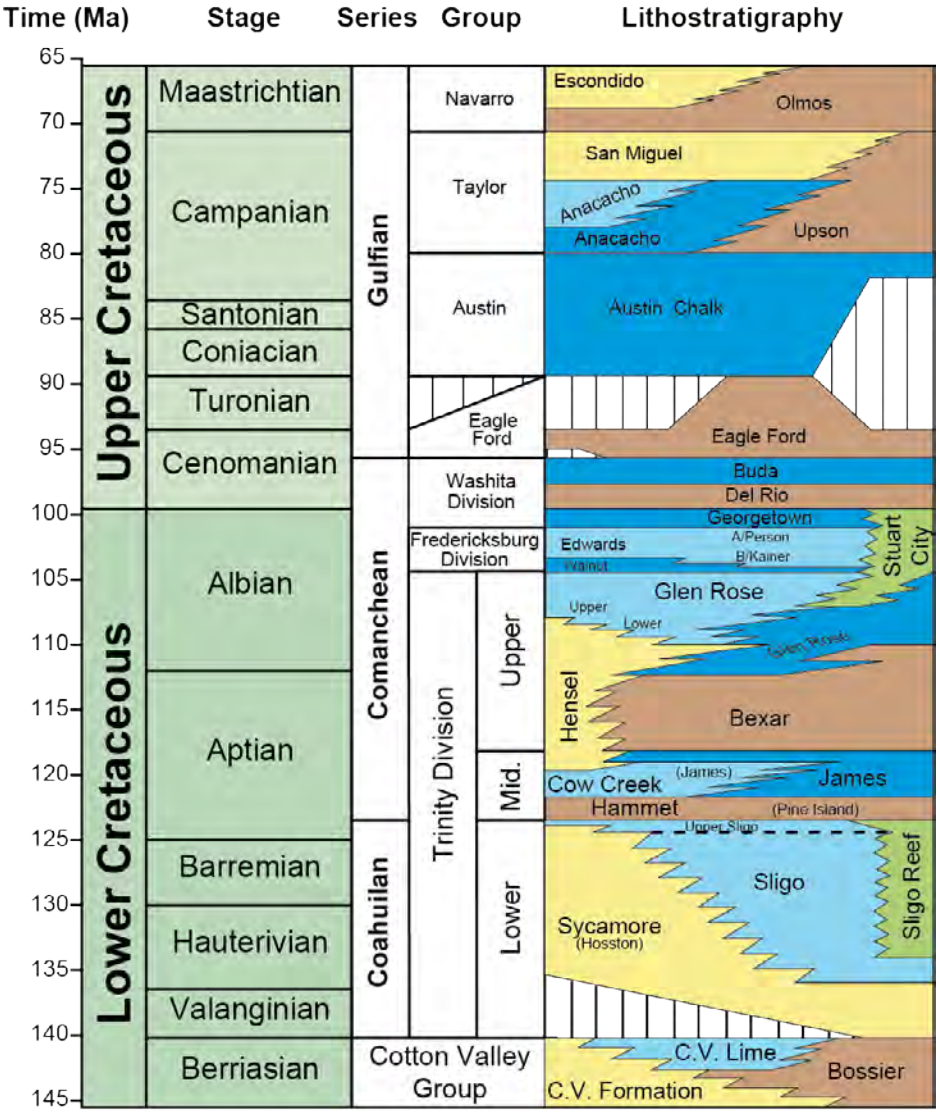

Figure 10. Lithostratigraphic units of the Cretaceous succession of central Texas (Phelps and others, 2014).

Lithostratigraphic Division of the Cretaceous in Central Texas

The lower Cretaceous Comanche Series and the upper Cretaceous Gulf Series are classically differentiated in central Texas. The lower Cretaceous Comanche Series consists of the Trinity (Hill, 1887; Lozo and Stricklin, 1956), Fredericksburg (Hill, 1887, 1891) and Washita (Hill, 1901) Groups, whereas the upper Cretaceous Gulf Series consists of the Eagle Ford (Hill, 1887; Adkins, 1932), Austin (Shumard, 1860; Murray, 1961), Taylor (Hill, 1892; Young, 1965) and Navarro (Shumard, 1862; Wilmarth, 1938) Groups (fig. 3). After its original definition, this lithostratigraphic framework evolved. The deposition of the Coahuilan Series (Valanginian to earliest Aptian; Imlay, 1944) (fig. 8) on top of the Cotton Valley Group (Berriasian; Weeks, 1938; Shearer, 1938; Swain, 1944) (fig. 8) predates the Comanchean (early Aptian to middle Cenomanian) and the Gulfian Series (middle Cenomanian to end of Cretaceous) (fig. 8).

More recently, Phelps and others (2014) broke the sedimentary succession of the Comanche platform into three second-order supersequences: the Valanginian-Barremian (140–124 Ma), the Aptian-Albian (124–100 Ma), and the Cenomanian-Campanian (100–80 Ma) (fig. 8). They are defined based on marine transgressions (either eustatic in origin or the result of drastic environmental change brought about by an OAE) and subsequent recovery of the platform during periods of sea-level highstand.

Berriasian Sedimentation (145 to 140 Ma)

Dated to the Late Jurassic to the Early Cretaceous (Tithonian to Berriasian) (fig. 10), the Cotton Valley Group (Mann and Thomas, 1964) consists of sandstone, shale, and limestone, and is found across much of the northern coastal plain of the Gulf of Mexico. Its basal formation (Boissier Shale; Swain, 1944) (fig. 8) consists of dark-gray calcareous fossiliferous marine shale deposited in an open marine setting. Following on top of the Boissier Shale, the Cotton Valley Sandstone (Shearer, 1938) (fig. 8) includes braided-stream, fan-delta, and wave-dominated deltaic sandstones. Siliciclastic sedimentation may be retrained to the upper Jurassic part of the Cotton Valley Group; a regional regression allowed the deposition of carbonates during the Berriasian (Cotton Valley Limestone; Dyman and Condon, 2006) (fig. 8).

Valanginian–Barremian Supersequence (140 to 124 Ma)

The Valanginian-Barremian supersequence (fig. 8) consists of siliciclastic-dominated lowstand (Hosston and Sycamore Formations, Valanginian, 140–136 Ma; Hill, 1901; Cuyler, 1939; Imlay, 1940), transgressive, and highstand (Sligo Formation, Hauterivian-Barremian, 136–124 Ma; Imlay, 1940; Warner and Moody, 1992) systems tracts.

Hosston Formation

Preferentially found in eastern Texas, the Hosston Formation (fig. 8) consists of a package of sandstone marking deltaic and shoreline environments (Ewing, 2010). Its contact with the underlying Cotton Valley Group corresponds to an unconformity at 140 Ma (Phelps and others, 2014), above which basal conglomerate of the Sycamore Formation (fig. 8) was deposited in a fluvial environment.

Sligo Formation

The Hauterivian-Barremian Sligo Formation (fig. 8) corresponds to the first episode of widespread carbonate sedimentation in central Texas, where it reaches a thickness of 735 feet in the subsurface of Karnes County (Phelps and others, 2014).

Aptian–Albian Supersequence (124 to 101 Ma)

The Aptian-Albian supersequence (fig. 8) began with another rapid transgression, the inundation of the carbonate platform (Sligo Formation), and widespread deposition of siliciclastic sediments (Hammett Shale and Hensell Sandstone; Imlay, 1940; Warner and Moody, 1992); the deposition of the Hammett Shale is coeval to the lower Aptian OAE1a (fig. 10). The carbonate ramp subsequently began to rebuild and prograde outward into the basin during the early Aptian (124-119 Ma), before the subsequent OAE1b (fig. 10) stalled carbonate production and triggered another episode of platform inundation. This second inundation episode resulted in the widespread deposition of black sediments, the Bexar Shale (119-110 Ma; Forgotson, 1957) (fig. 8). The Pine Island and Bexar Shales exhibit high organic carbon content (up to 1.86 and 1.73 weight percent total organic carbon, respectively), and decreased bioturbation as a result of deposition under anoxic conditions (Hull, 2011). Bexar Shale deposition ceased with a marine transgression during the Albian (110-104 Ma). The transgression marked the beginning of a gradual return to normal marine conditions as the platform began to recover from the damaging environmental impacts of the preceding OAE1a and 1b. The platform developed a distinct progradational shelf margin profile with the installation of abundant reef buildups along an emerging shelf margin. A marine transgression in the late Albian (104-101 Ma) prompted a shift from shelf progradation to aggradation (Phelps and others, 2014).

Although erosion has removed the majority of upper Cretaceous strata within the Comanche platform, Aptian-Albian carbonates are well preserved because of early cementation (Galloway and others, 1982; Fullmer and Lucia, 2005; Phelps and others, 2014). These Albian units of the Comanche platform include, from oldest to youngest, the Glen Rose Limestone (Hill, 1901; Wilmarth, 1938; Lozo and Stricklin, 1956), the Walnut Formation (Loeblich and Tappan, 1949), the Edwards Group (Hill and Vaughan, 1898; Adkins, 1932; Wilmarth, 1938; Rose, 1972), the Georgetown Formation, and the Stuart City Formation of the Atascosa Group (fig. 9).

Glen Rose Limestone

The Glen Rose Limestone is a thick shallow-marine carbonate succession deposited above the Bexar Shale during a series of minor marine transgressions and regressions (Phelps and others, 2014). Evolution of the Glen Rose tracks the recovery of the platform following the disruptive OAE1b. The Glen Rose Limestone is part of the Upper Trinity sequence and is divided into lower and upper members (Mb; Hazzard, 1939; Scott and others, 2007) by a thin, laterally continuous accumulation of shells of the small bivalve *Corbula martinae*, known as the *Corbula* bed (Whitney, 1952; Lozo and Stricklin, 1956).

The lower member of the Glen Rose Limestone primarily comprises alternating layers of limestone, dolomite, and thin shale. The carbonate layers consist of shell fragments with micritic sparry calcite or dolomite matrices (Stricklin and others, 1971). Deposition of the lower member of the Glen Rose Limestone occurred along a carbonate ramp as sea level transgressed. Dinosaur tracks are preserved in intertidal to supratidal environmental facies of the lower Glen Rose. Although less common, some dinosaur footprints and trackways have been identified in shallow subtidal environments within the lower member of the Glen Rose (Hawthorne, 1990). The upper member of the Glen Rose Limestone comprises layers of evaporites, dolomite, and marl with evidence of periodic subaerial exposure (Stricklin and others, 1971). Carbonate production was also restored with the installation of widespread, thick rudist patch reefs, such as at Canyon Lake Gorge (Ward and Ward, 2007).

Walnut Formation

The Walnut Formation is the lowermost formation of the Fredericksburg Division (fig. 8) and consists primarily of clay, limestone and marl. The Walnut Formation was deposited atop the Glen Rose Limestone in response to a normal marine transgression at about 104 Ma. This transgression marked the shift from progradational to aggradational shelf trajectories on the Comanche platform.

Edwards Group

The Edwards Group comprises the remainder of the Fredericksburg Division and is a thick sequence of limestone deposited during a series of minor marine transgressions and regressions. It is characterized by rudist bioherms, carbonate mudstone to grainstone, and evaporites. The depositional history of the Edwards Group reflects a general shallowing of depositional environments from bottom to top of the formation.

Stuart City Formation

The Stuart City Reef defined the shelf edge during middle to late Albian and was preferentially developed along a hinge line separating more slowly subsiding, thick transitional continental crust from more rapidly subsiding, thin transitional continental crust (Buffler and Sawyer, 1985; Winker and Buffler, 1988; Phelps and others, 2014). The Stuart City Formation consists of rudist reefs surrounded by deeper water, lagoonal and shelf slope deposits. The Stuart City Reef persisted for a short time after the inundation documented within the Edwards Group in the inner platform, but ultimately could not keep up with sea-level rise and was overlain by the Del Rio Clay.

Cenomanian–Campanian Supersequence (101 to 80 Ma) and the Maastrichtian

The third and final supersequence started with another rapid marine transgression in the early Cenomanian (101–96 Ma) (fig. 10) that triggered the inundation of the platform, embodied by the demise of the Georgetown Formation and associated Stuart City Formation. This transgression was associated with a third anoxic event (OAE1d) that occurred between late Albian and early Cenomanian time and resulted in the widespread deposition of the Del Rio Clay of the Washita Group (Hill and Vaughan, 1898) of the Comanche Series.

The Buda Limestone (Vaughan, 1900; Wilmarth, 1938) is recognized in the south, central, and Trans-Pecos regions of Texas (Sellards and others, 1932). The Buda Limestone is part of the Washita Group of the Comanche Series (Wilmarth, 1938; Montgomery, 1990; Reaser and Dawson, 1995). It overlies the Del Rio Clay and is in turn, unconformably overlain by the Eagle Ford Group (Barnes, 1982) (fig. 8). The unconformity between the Buda Limestone and the Eagle Ford Group corresponds to a period of subaerial exposure resulting from a drop in global sea level (Haq and others, 1987; Salvador, 1991; Phelps and others, 2014). The contact between the Buda Limestone and the Eagle Ford Group is easily distinguished by a change from the bioturbated gray wackestone (Buda), to the organic-rich mudrock of the lower part of the Eagle Ford Group. In the subsurface, this contact appears as a very sharp gamma ray excursion. The Buda Limestone was deposited on a wide flooded shelf, landward of the Stuart City shelf margin (Ruppel and others, 2012). It is a light grey, very fine textured, very hard, dense, micritic limestone. The Buda Limestone is highly fractured, contains numerous stylolites, and is fossiliferous. The thickness of the Buda ranges from less than 3.3 feet to a maximum of 350 feet (Snyder and Craft, 1977; Stapp, 1977; Scott, 1977; Montgomery, 1990; Reaser and Dawson, 1995).

Organic-rich shales of the Eagle Ford Group were deposited from 96–80 Ma and are associated with the maximum flooding of the Cenomanian–Campanian supersequence. Widespread deposition and preservation of organic material results from the unfolding of the OAE2 at the end of the Cenomanian, an event recognized worldwide and that corresponds to the highest sea-level stand of the Phanerozoic (Jenkyns, 1980; Erba, 2004; Keller and others, 2004; Mort and others, 2007; Haq, 2014). Rocks of the Eagle Ford Group cropping out near the city of Austin can contain up to 8.3 weight percent of total organic carbon (Robison, 1997).

The Taylor Group was deposited on top of the Eagle Ford Group and is divided into the Anacacho (Wilmarth, 1938) and San Miguel Formations (Dumble, 1892), which consist mainly of carbonate and siliciclastic deposits, respectively. The remainder of the Cretaceous consists of the Olmos (Stephenson, 1927) and Escondido Formations (Dumble, 1892; Stephenson, 1927) (fig. 8). Sediments constituting these formations were deposited in a wave-modified fluvial-dominated delta system. These upper Campanian–Maastrichtian lithostratigraphic units mark the onset of the siliciclastic sedimentation that will dominate this part of the northern Gulf of Mexico in the Cenozoic (fig. 8).

Field Trip Stop 5: The Narrows on the Blanco River

By Amy R. Clark, Allan K. Clark, and James Golab

Introduction

An approximately 194-foot (ft) stratigraphic column was measured along the Blanco River in western Hays County, Texas, which includes the Pearsall Formation and the lower part of the lower member of the Glen Rose Limestone. The units were also described hydrostratigraphically such that the Pearsall Formation includes the Hammett Shale, Cow Creek Limestone, and Hensel Sand, and the Glen Rose Limestone includes the Honey Creek, Rust, Doeppenschmidt, and Twin Sisters hydrostratigraphic units (HSUs).

The stratigraphic column was measured with a hand level and a Jacob's staff that were demarcated in decimal feet (ft) and extended up to 25 ft in height. Beds were described lithologically, sedimentologically, and ichnologically. Lithologies were described using the Dunham (1962) classification system for carbonates, the Embry and Klovan (1971) expansion of the Dunham classification system to include rudist reef material, and the Wentworth (1922) classification system for siliciclastics. Sedimentological features and ichnofossils were examined and described *in situ*; some representative ichnofossil samples were collected for photographs. Ichnofossils were described using morphology, surface textures, and burrow fill. Ichnofabric index (ii) was also recorded throughout the section.

Hammett Shale

The basal 6.4 ft of the measured section is the Hammett Shale (fig. 3), a confining unit within the Trinity aquifer. The Hammett Shale in this location is primarily massive, very-fine grained sandstone to siltstone with carbonate cement. Laminated siltstone was observed 5 ft from the base of the section. Some rhizoliths are present near the upper contact of this unit.

Cow Creek Limestone

The Cow Creek Limestone (figs. 3 and 11) extends from 6.4–44.4 ft of the measured section and primarily consists of a coral-dominated bafflestone and floatstone. The basal 2 ft of the section is a fossiliferous grainstone containing oyster, bivalve, and gastropod shells as well as fragmented coral

fragments. The overlying 16 ft of the Cow Creek Limestone consists of a coral-dominated bafflestone with most corals found in life position. This thick bafflestone is overlain by 5.5 ft of alternating foot-scale beds of coral-dominated floatstone and bafflestone that also contain gastropod, bivalve, and rudist (Caprinid) shells and shell fragments. These beds are horizontal, and some thin carbonate mudstone beds are present. These beds are overlain by a laminated carbonate mudstone bed that contains some shell fragments. The top of the Cow Creek Limestone is characterized by 4 ft of crossbedded wackestone-packstone with beds that dip up to 12 degrees. These are interpreted to be talus slopes or large ripples associated with a strandplain (fig. 11).

Figure 11. Outcropping of strandplain at the top of the Cow Creek Limestone at the Narrows along the Blanco River, western Hays County, Texas. Note dipping ripple marked beds of talus. Photograph taken on July 13, 2015, by Robert Morris.

Hensell Sand

The Hensel Sand (fig. 3), which extends from 44.4–54 ft of the measured section but varies in thickness from 10–15 ft, is a thick, very fine to fine-grained sandstone with carbonate cement. These sandstones contain micas and some rhombic dolomite crystals in thin section. Sedimentary structures include some ripple and trough crossbedding. The basal contact is erosional with the underlying Cow Creek Limestone and contains brecciated limestone clasts (fig. 12). The brecciated limestones at the base of beds are likely caused by erosion of preexisting hardgrounds. Diagenetic features such as iron staining and dendrites are common in the Hensell Sand, which also contains clasts of whole and fragmented bivalves and gastropod shells in outcrop, along with molds of palm fronds.

Figure 12. Close-up of the conglomerate/breccia bed at the base of the Hensell Sand at the Narrows along the Blanco River, western Hays County, Texas. Note circular hole where rock plug was removed. Photograph taken on July 13, 2015, by Allan Clark.

Honey Creek Hydrostratigraphic Unit

The Honey Creek HSU (fig. 3) is a transmissive section that extends from 54–89 ft of the measured section. The Droser-Bottjer ichnofabric index (ii) (Droser and Bottjer, 1986) was used to quantify the degree of bioturbation where an ii1 shows no bioturbation up to an ii6 where more than 60 percent of the bed is bioturbated. The Honey Creek HSU consists of tidal-dominated, yard-scale successions of coarsening-upward, nodular and massive marly wackestone-packstone beds with an ii 4–5 and some identifiable *Thalassinoides* networks. These successions grade up-section into marly wackestone-packstone with an ii3–4, characterized by open and wackestone-packstone-filled *Thalassinoides* networks. Some beds of laminated calcareous mudstone with an ii1 are located at the base of successions and grade up-section into the more typical nodular wackestone with an ii4–5. The bottom 30 ft of the Honey Creek HSU consists of the typical successions described and in some cases contains *Thalassinoides* networks filled exclusively with *Orbitolina texana*. The top 10 ft of the unit has a lower ii and consists of interbedded laminated calcareous mudstone and nodular wackestone with an ii1–2 and containing *Palaeophycus* with some *Thalassinoides* networks. Although defined as a transmissive unit, most of the bioturbation-influenced porosity of the Honey Creek HSU appears to be restricted to the bottom 22 ft of the unit in beds with an ii3–4.

Rust Hydrostratigraphic Unit

The Rust HSU (fig. 3) extends from 89–123 ft of the measured section and is a semi-confining unit, containing more mud than the underlying Honey Creek HSU. This section consists of coarsening-upward successions similar to most transmissive units. Burrow infill in the Rust HSU ranges from wackestone-packstone, and the uppermost beds contain *Palaeophycus* and mud-filled *Planolites*. These mud-filled ichnofossils in the Rust HSU do not increase bioturbation-influenced porosity.

Doeppenschmidt Hydrostratigraphic Unit

The Doeppenschmidt HSU (fig. 3) extends from 123–193 ft of the measured section and is dominated by rudist patch reef facies. The Doeppenschmidt HSU is a transmissive unit and commonly consists of coarsening-upward successions similar to the lower units in the Glen Rose Limestone. Along the Blanco River in western Hays County, the Doeppenschmidt HSU grades into discontinuous patch reefs consisting of rudist-dominated floatstone and bafflestone having an ii1–ii2. Floatstone beds are 0.7–6 ft thick with randomly-oriented clasts consisting of whole and fragmentary rudist shells. Rudist populations are dominated by *Caprinid* sp. Other clasts consist of whole and fragmented bivalve and gastropod shells, many of which are preserved as molds. Floatstone beds commonly grade up-section into rudist-dominated bafflestone facies. Cretaceous rudist reefs are commonly compared to more modern coral reefs with respect to depositional environment but without the rigid framework seen in such coral reef systems. Rudists grew in muddy environments with packstones and floatstones; some *Planolites* are observed in the mudstone matrix of these floatstones as well.

Twin Sisters Hydrostratigraphic Unit

The Twin Sisters HSU (fig. 3) is found at the top of the measured section from 193–194 ft, which is the highest point in the immediate vicinity. This HSU is confining and consists of yard?-scale beds of nodular, marly wackestone with an ii5–6 that are thoroughly homogenized by pervasive cryptobioturbation with some identifiable *Thalassinoides*. Unlike transmissive HSUs, confining units, like the Twin Sisters HSU, generally do not display coarsening upward trends, contain more mud, and show less fracture porosity.

Field Trip Stop 6: Burnett Ranch Community Park (optional stop, presentation by Marcus Gary)—No description provided

Field Trip Stop 7: Canyon Lake Gorge

By Carter Keairns

Introduction

A short stop in the Canyon Lake Gorge will visit the lower portion of the mile-long gorge that cuts through the Cretaceous (lower Albian) Glen Rose Limestone. We will walk through the lower member of the Glen Rose Limestone up to the *Corbula* bed that delineates the contact between the upper and lower members of the Glen Rose Limestone. The gorge was formed during a flooding event in 2002 and has been a wonderful classroom for geology and biology since then. One of the reasons the gorge is such a compelling stop is that we are presented with not only the typical cross section (or road cut) view, but also extensive lateral surfaces that provide unique views of carbonates in the subsurface. Karst-related features as well as structural geology, paleontology, sedimentology, and hydrology can be discussed at our stop and placed within the south Texas geologic framework. A brief summary of the

dam and flooding event follows to provide some background information, and photos of the gorge of features we will be able to visit.

2002 Flooding Event

The Canyon Lake Gorge is located just south of the Canyon Lake Dam. Its main purpose is to provide flood protection for the 157,250 acres of land downstream from the dam. The Canyon Lake Dam was begun in 1958 and completed in 1964; the lake was filled to capacity by 1968 (U.S. Army Corps of Engineers, http://www.swf-wc.usace.army.mil/canyon/Information/History.asp). It is an earthen dam 4,410 feet (ft) in length and at its maximum is 224 ft above the Guadalupe River, so it is a rather significant structure. None the less, if the lake levels were to rise enough to overtop the dam it would likely result in catastrophic flooding in downstream areas of the Guadalupe River. As a result, the Corps of Engineers have used rain and weather data to predict the worst flood that might reasonably occur in this region. This is called a "probable maximum flood." During such a flood, the reservoir would completely fill, and water would continue exiting through the dam. The existing concrete spillway was designed to pass all that water without allowing the dam to be overtopped. As evidenced during the flooding in the summer of 2002, the spillway was effective in performing its job.

During the 2002 event Canyon Lake received 8 in. of rain in 24 hours. While a significant amount, it was not a record; in flooding during 1998 there were 19 in. reported in a 24-hour period. What made the 2002 flooding so severe was not the short-term amount of precipitation, but the fact that it was a steady rainfall that continued for days. The average rainfall between June 29 and July 6 was around 22 in. (some areas received 40 in.). Not only did rainfall over the surface of the lake contribute to the pool level rising, but also the rainfall in the 1,432 square miles of drainage basin above the dam. A short calculation reveals that approximately 700,000 acre-feet of water entered Canyon Lake that week.

The conservation pool level of Canyon Lake is listed by the Corps as 908.62 ft. This number represents the elevation of the water surface in the lake above mean sea level, and the level that the Corps maintains by regulating the outflow from the lake. The top of the Canyon Lake Dam is 973 ft and the spillway is at an elevation of 943 ft, roughly 34 ft above the conservation level of the lake and 30 ft below the top of the dam. The previous record pool level was 942.67 ft on June 19, 1987; the 2002 event on July 6 had a flooding maximum of 950.32 ft or 7 ft 4 inches (in.) above the spillway. Several numbers have been listed as the maximum flow rate; most common is 66,800 cubic feet per second (ft^3/s) and the highest is 73,000 ft^3/s. In New Braunfels peak flow reached about 70,000 ft^3/s. Had the Canyon Lake Dam not been constructed, it is estimated that the flow would have been greater than 126,000 ft^3/s (Comal County Engineer's Office, http://www.cceo.org/flood/flood2002.asp). Farther downstream recorded peak flows at Cuero reached 64,700 ft^3/s and at Victoria reached 72,600 ft^3/s. Without Canyon Dam, flows at Cuero would have been about 103,000 ft^3/s and about 113,000 ft^3/s at Victoria.

All of this water created the spectacular Canyon Lake Gorge in a short period of time. Prior to 2002, the valley below the spillway had a small intermittent stream and some small springs, and it was thickly wooded with gently sloping topography. If you look at the sides of the gorge, observe the soil horizons on either side and imagine a more or less straight line connecting them, place similar vegetation that you see on either side across your imagined horizon and that is pretty much how the valley looked prior to the flood event. The entire gorge was formed during the 2002 event; the bulk of the erosion took place during the time around the maximum flow rate (July 6th), but water continued to flow over the spillway for weeks. At the end of July there was just under a foot of water still flowing over the spillway, or about 2,000 ft^3/s. This reduced flow was not strong enough to move any boulders

or cause significant erosion, but would have been effective at moving sand size and smaller sediments. The Southwest Texas State University Geography Department has mapped the new eroded surface of the gorge, and based on a comparison with old data from topographic maps and digital orthoquads has estimated that the volume of material (rock) removed during the flooding was approximately 500,000 cubic yards. Imagine a football field stacked 300 ft high with limestone blocks and you will have a good idea of what happened 1 week in July 2002.

Photos for Stop 7

Figure 13. Dissolution-enhanced joints in the lower member of the Glen Rose Limestone (Keairns, 2009).

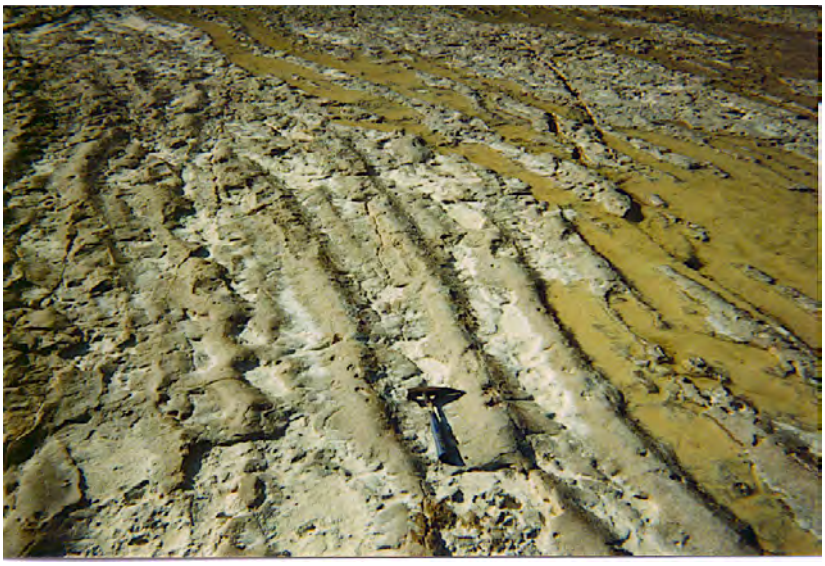

Figure 14. Carbonate ripples and Corbula bed marking the contact of the upper and lower members of the Glen Rose Limestone (Keairns, 2002).

Figure 15. Cross bedding and overlying bioturbated interval in the lower member of the Glen Rose Limestone (Keairns, 2012).

Field Trip Stop 8: Bracken Bat Cave

By George Veni and Ron Green

Introduction

Bracken Bat Cave (fig. 16) holds the world's largest colony of bats. Each spring, millions of pregnant Mexican freetail bats (also called Brazilian freetail bats), *Tadarida brasiliensis mexicana*, return from their winter migration to Mexico and give birth to an average one pup each, doubling the population by early summer. Population counts vary, but Bat Conservation International (BCI), which owns the cave, estimates the maximum summer population at about 15 million (Mylea Bayless, BCI, oral commun., June 2016). The cloud of bats that exits the cave nightly appears on the radar of the San Antonio International Airport and on Doppler weather radar.

The cave's entrance is impressive, about 20 m wide by 7 m high at the base of a 30-m diameter by 13-m deep collapse sinkhole (fig. 16). The cave's dimensions are less impressive. Although it maintains a large average size of 15–20 m wide by 10–15 m high, the cave descends steeply another 12 m down a bat guano-covered rubble slope, then continues south along a roughly level guano floor to where the ceiling abruptly lowers at a horizontal distance of about 130 m from the entrance, and the passage beyond is filled with guano to a depth of 31 m. Although figure 17 indicates a 36-m depth, that has since been revised by a high-precision survey for the in-cave geophysical surveys described below, although 36 m may have been accurate at the time and the 5-m difference may reflect the accumulation of guano. The cave is undoubtedly much longer and deeper, if only we could see north past the collapse of its entrance and the guano at its opposite end.

It is not known when the cave was discovered, but it was almost certainly located due to its impressive evening bat flights, as large clouds of bats emerge nightly during the spring through fall months. The cave was named for the nearby town of Bracken. Guano mining began in 1856, with most of the guano used as fertilizer. The cave yielded up to 70 metric tons of guano annually. Mining was usually done in the winter when the bats were absent. Shipments went by rail to the west and east coasts. During the Civil War the guano was leached for saltpeter used in Confederate gunpowder. Mining has continued sporadically to the present day.

Probably the most curious aspect of Bracken Bat Cave's history was when Dr. Lytle Adams used it in Project X-Ray. This formerly top secret World War II project proposed attaching incendiary bombs to bats, releasing them, and when the bats would roost in buildings the bombs would ignite to raze the cities. The project was abruptly abandoned when atomic bombs were used to end the war. Extensive ecological data were gathered during Adam's research, most of which became classified military information for some time.

Working in Bracken Bat Cave poses challenges not found in most. During the months when large numbers of bats are present, their body heat raises the cave's temperature to over 40 °C, and the guano and urine create hazardous atmospheric ammonia levels as high as 55 ppm. Meanwhile, the floor literally moves due to the probably millions of dermestid beetles feeding on guano and dead bats. The cave is rarely entered and usually only in the winter so as not to disturb the bats, but also when temperature and ammonia levels are at their lowest. Masks with filters are a necessity at all times, if only to prevent inhalation of the cave's fine guano dust that pervades the air.

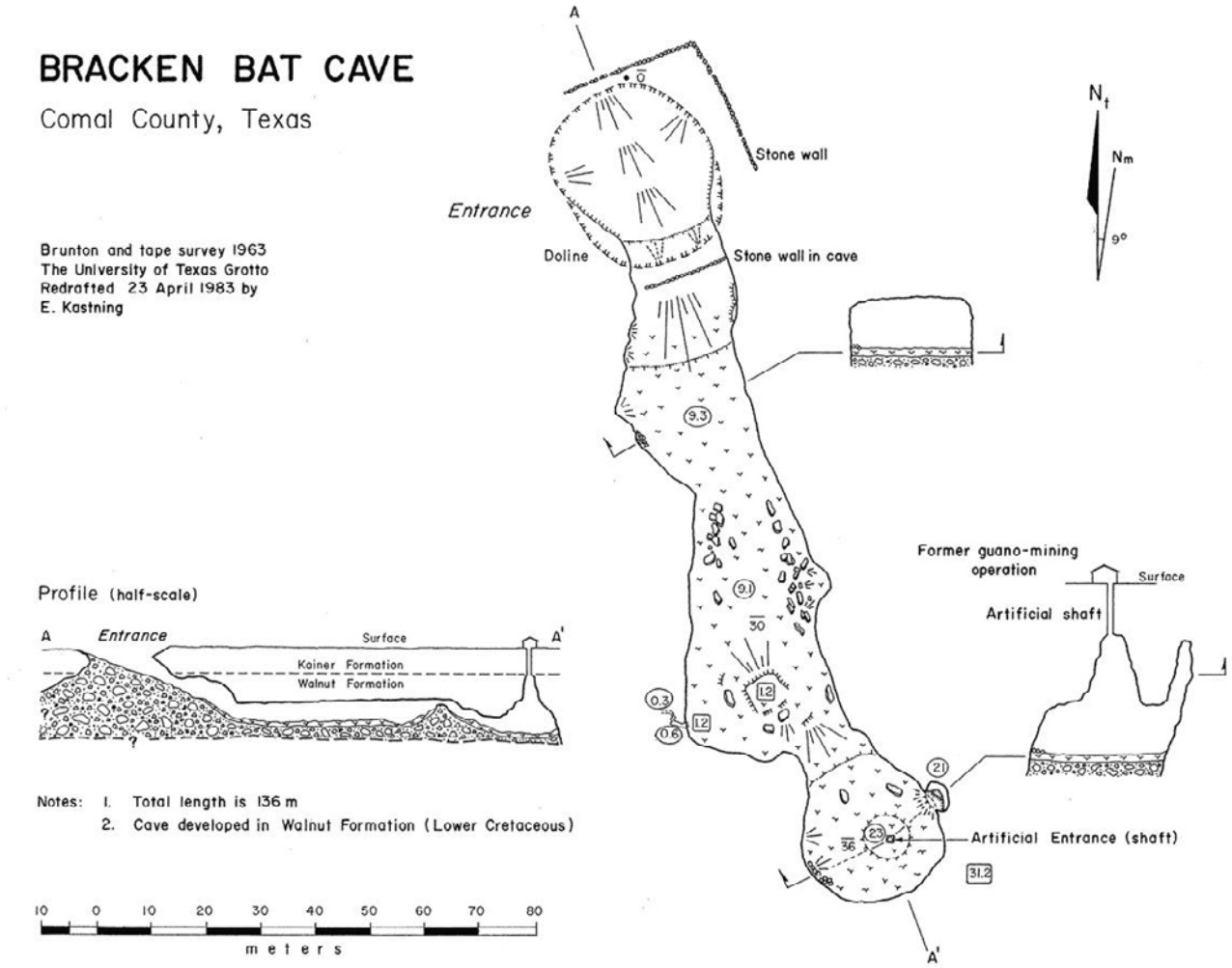

Figure 16. Map of Bracken Bat Cave, Comal County, Texas (Kastning, 1983).

In 1992, the cave was acquired by BCI to protect the bats, conduct research, and promote public education on bats. The initial purchase was for 0.3 km^2, which was expanded a few years later to 2.8 km^2. However, in the spring of 2013 the integrity of the preserve was threatened by a proposed housing development on an adjacent 6.2-km^2 property. Following an outcry from local citizens and a massive fundraising drive, $20.5 million were raised, with substantial portions coming from the City of San Antonio and The Nature Conservancy. On October 31, 2014, BCI bought the property and expanded the preserve to 9.0 km^2.

Elliott (1994) provides more general information on Bracken Bat Cave and Couffer (1992) offers a detailed and engaging account of Project X-Ray. For the most recent news on the cave, including a web cam to watch the evening flights live, visit BCI's website, http://www.batcon.org/.

Hydrogeology

Bracken Bat Cave is formed in the Cretaceous-age Kainer Formation of the Edwards Group and the underlying upper member of the Glen Rose Limestone of the Trinity Group (fig. 3). The dolomitic member of the Kainer Formation (fig. 3) extends from the surface down 9 m to the dripline of the cave's entrance (fig. 16). This thick-bedded, structurally competent unit forms the roof of many large cave chambers in the area, as well as the namesake bridge of Natural Bridge Caverns 1.1 km to the northeast.

The humanly accessible portion of Bracken Bat Cave is mostly within the 15-m thick basal nodular member of the Kainer Formation (fig. 16), previously designated as the Walnut Formation when figure 16 was drafted. Large solutionally formed chambers and passages are often present in the basal nodular member in Bexar County and southern Comal County, but the large passage of Bracken Bat Cave is not formed by solution (see Veni (2005) for a review of lithology as it affects cave morphologies in this area).

The deepest 7 m of Bracken Bat Cave are formed in the cavernous hydrostratigraphic unit (HSU) (fig. 3) of the upper member of the Glen Rose Limestone, described by Clark and others (2013). This unit is 37 m thick and contains most of the largest solutionally formed cave chambers and passages in Bexar and southern Comal Counties. Like the basal nodular member exposure in the cave, its humanly accessible section in the upper Glen Rose Limestone is not formed by solution. The entire known cave is formed by collapse.

Kastning (1983) was the first to conduct a detailed study of speleogenesis in the Bracken Bat Cave-Natural Bridge Caverns area. He found that the caves were likely formed by the same process, except that guano blocks access to most of the likely extent of Bracken Bat Cave and so the mechanism of its origin is best seen in Natural Bridge Caverns, which is much more extensive with a surveyed length of 3,354 m and vertical extent of 70 m, inclusive of sections physically separated by collapse (Fieseler and others, 1978). He attributed the origin of the caves to the development of early solutional porosity of the Glen Rose Limestone during late Cretaceous (post-Albian) time and later guidance of fractures on groundwater flow. Much of his sequence chronology of solutional enlargement, collapse, and speleothem development fits current thought. The jagged up-and-down profile of Natural Bridge Caverns shows the effect of multiple collapses along a large, deep solutionally formed passage, with its largest collapse breaching the surface to create the entrance. Similarly, the entrance and exposed portion of Bracken Bat Cave are at the top of a large collapse into a much deeper solutionally formed passage, which is currently inaccessible due to the thick deposits of bat guano.

For many years following its discovery, Natural Bridge Caverns posed a conundrum for local hydrogeologists. It was clearly formed in the upper Glen Rose, but conventional wisdom held that the Glen Rose was the impermeable basal confining unit for the Edwards (Balcones Fault Zone) aquifer (hereafter referred to as the "Edwards aquifer"). Veni (1995) first proposed hydrologic continuity between the Edwards aquifer and what was later described as the cavernous HSU of the upper Glen Rose Limestone (Clark and others, 2009) in Bexar County and portions of adjacent Comal and Medina Counties. This conclusion was based on caves that extend between the units, allowing recharge to enter the Glen Rose Limestone through the Edwards and with no likely discharge points for that water except transformational flow across faults back into the Edwards. This theory was demonstrated through dye-tracing studies (Johnson and others, 2010) and the hydrologic relationship is now generally accepted.

One problematic issue remains. Natural Bridge Caverns extends at least 18 m below the cavernous HSU into the upper Glen Rose Camp Bullis unit (Clark and others, 2013), which is otherwise a poor to minor cave-forming unit but has the most springs in neighboring Bexar County due to

groundwater-perching horizons (Clark and others, 2013). Part of this problem may be resolved by the U.S. Geological Survey's soon-to-be-published hydrostratigraphic mapping that includes the Bracken Bat-Natural Bridge study area, if it reveals more extensive zones for cave development in that part of the Glen Rose than in Bexar County.

Our report proposes that the two caves formed as tapoff passages. They are located across a meander of Cibolo Creek, which reverses its west-to-east flow by flowing south, then west 1.6 km north of the caves, then south 2.2 km west of Bracken Bat Cave. Where the seasonally active creek turns west, north of the caves, it forms a steep hydraulic gradient with the Edwards aquifer to the south; tapoff passages form along such gradients. They typical have no side passages, or few and under-fit side passages as seen in Natural Bridge Caverns. The cave's large size is consistent with the large volume of chemically aggressive water recharging Cibolo Creek to the north, which appears in the cave soon after the creek floods.

Surface Geophysics

Surface electrical resistivity surveys were conducted at the Bracken Bat Cave property during the past 10 years by staff from Southwest Research Institute and Raba-Kistner Environmental Services, with assistance by BCI, and the Bexar Grotto, the San Antonio chapter of the National Speleological Society. The objective of the surveys was to discern the possible presence of additional, yet undiscovered caves in the vicinity of Bracken Bat Cave. The electrical resistivity surveys were conducted using a 96-electrode, 10-channel Syscal Pro electrical resistivity system (IRIS Instruments, Orleans, France). Dipole spacing was 5 m in all surveys. The measured resistivity data were inverted to provide an interpretation of the subsurface using Advanced Geosciences, Inc. EarthImager™ software.

Electrical resistivity surveys were conducted along four two-dimensional transects and one three-dimensional array. The four two-dimensional transects were aligned approximately perpendicular to the line bisecting Bracken Bat Cave (fig. 17). All four transects were located on the collapsed side (north) of Bracken Bat Cave in the hope that any continuation of the cave that extends beyond the collapse would be detected. Locations of the northernmost two-dimensional transect and the three-dimensional survey are shown on figure 18. The remaining three two-dimensional transects were aligned between Bracken Bat Cave and the northernmost two-dimensional transect. Composite results from the four two-dimensional transects are overlain on an aerial photograph of the site of Bracken Bat Cave (fig. 17). Results from the three-dimensional survey are illustrated on figure 19.

The geoelectrical properties of the subsurface provided by the inverted data are illustrated on figures 17 and 19. More electrically resistive media are represented by warm colors (i.e., yellow, orange, red) and more electrically conductive media are represented by cooler colors (i.e., blue, green). In general, media with silts, clays, and possibly the presence of water are electrically conductive. On figures 17 and 19, the electrically conductive zones at depth are interpreted as the Glen Rose Limestone, which contains a greater content of clay than the electrically resistive Edwards Group. In addition, vertically oriented zones in the cross sections are interpreted as fault zones that contain water and possibly weathering products, both of which are less resistive than intact rock of the Edwards Group.

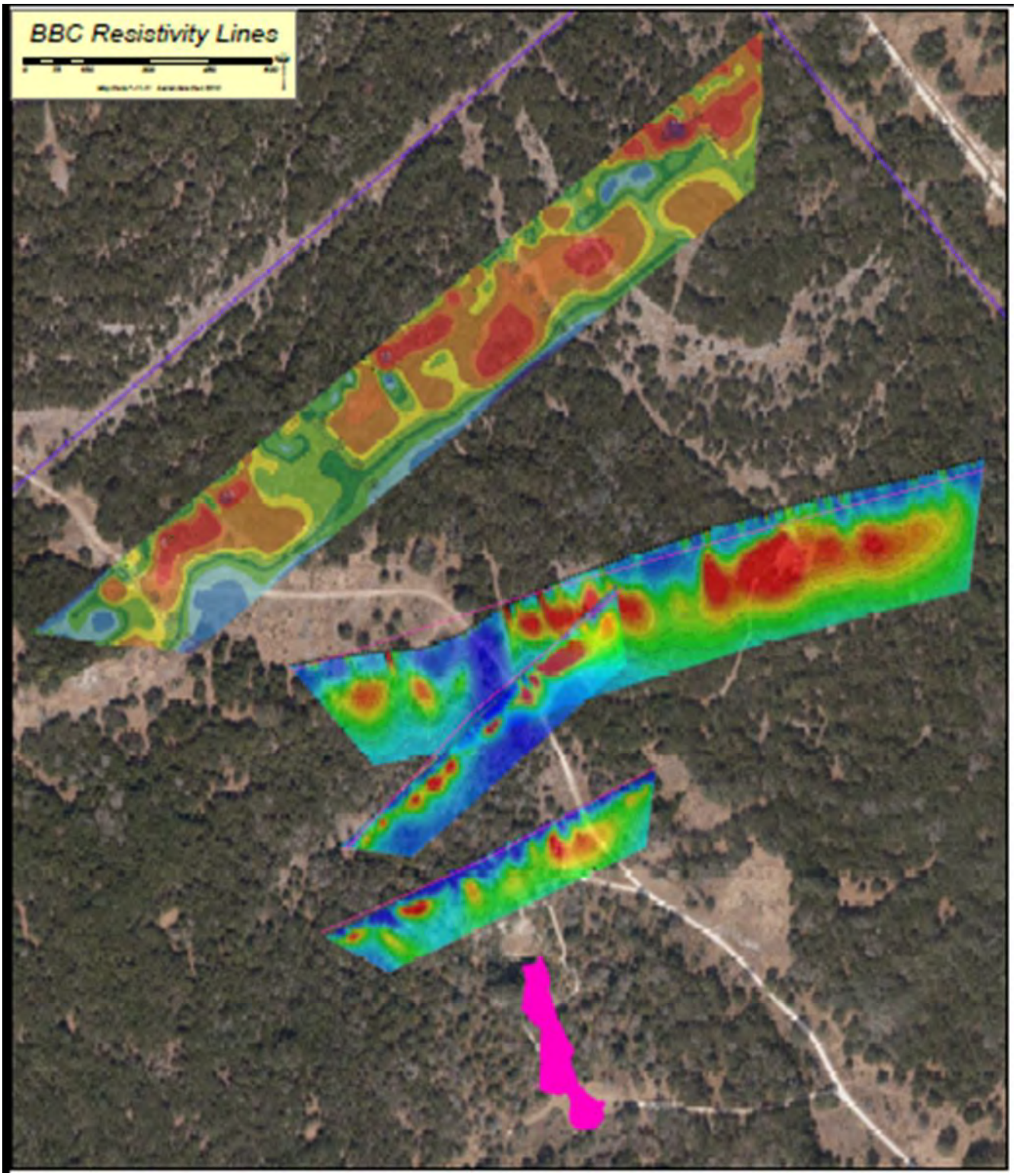

Figure 17. Composite results from four, two-dimensional electrical resistivity surveys. Bracken Bat Cave extent is shown in bright pink.

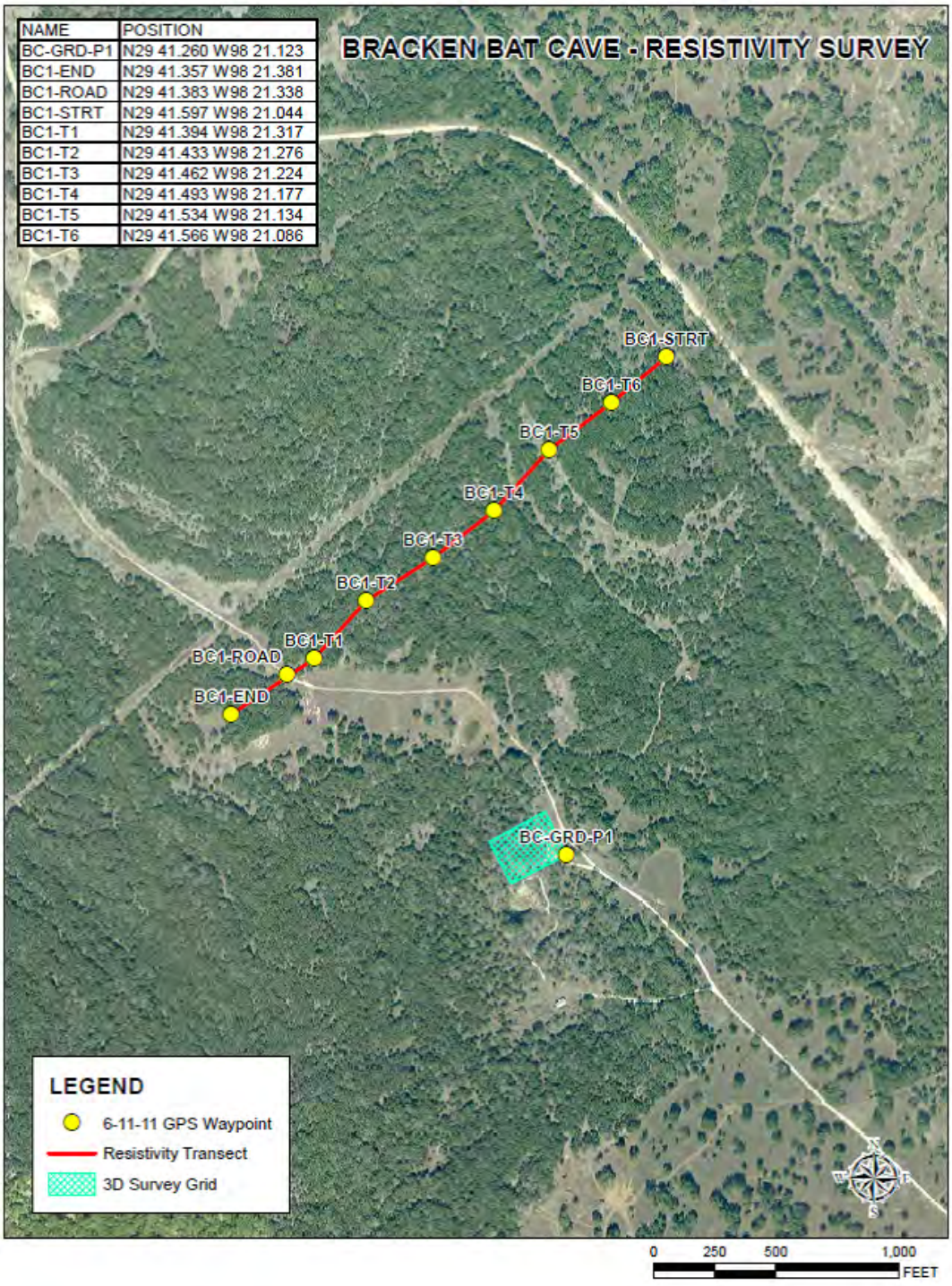

Figure 18. Map of Bracken Bat Cave area with locations of the 2011 two-dimensional transect and three-dimensional electrical resistivity surveys.

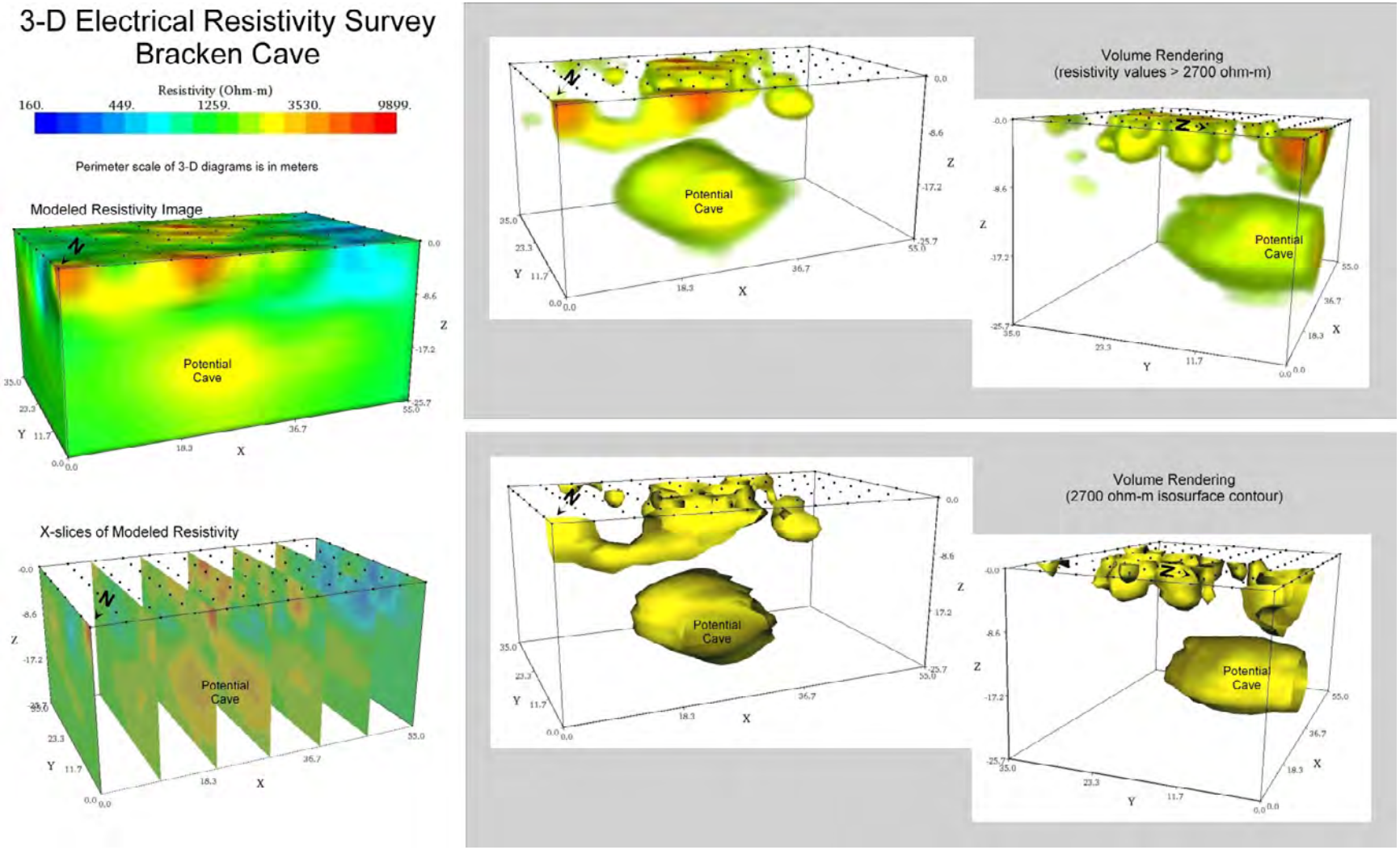

Figure 19. Results from the three-dimensional electrical resistivity survey conducted north of Bracken Bat Cave's entrance.

Electrically resistive zones in the cross sections are interpreted as intact rock. It is possible these resistive zones are indicative of open voids, such as a cave, because both intact rock and air-filled voids can have electrically resistive signatures. As illustrated on figure 17, there is substantial coverage of highly resistive zones in the cross sections. The highly resistivity zones are too pervasive to infer whether a particular highly resistive zone in one transect is aligned with a particular highly resistive zone in an adjoining transect, which could be an indication of a horizontal cave. Survey results would need to be corroborated with boreholes or trenches to be able to ascertain which high resistivity zone, if any, represents a cave feature.

Results from the three-dimensional resistivity survey conducted immediately north of the collapsed end of Bracken Bat Cave (fig. 18) are illustrated using different graphics on figure 19. By removing those media that are less resistive from the image, zones with higher resistivity are exhibited. This survey result indicates that a continuation of the cave may be present to the north of the collapsed entrance. Similar to the results of the two-dimensional surveys, this interpretation would need to be corroborated with boreholes or trenches to ascertain whether a cave is actually present to the north of the collapse.

Cave Geophysics

In 2013, a drilling company offered its services to BCI. Upon consideration, BCI contacted the National Cave and Karst Research Institute (NCKRI) to use the drilling services to core the guano in Bracken Bat Cave and analyze it for paleoenvironmental and paleoecological data. NCKRI organized a team of specialists to work on the study. Staff at Southwest Research Institute in San Antonio had previously worked at the cave conducting the surface geophysics described in the previous section. Dr. Bogdan Onac, of the University of South Florida, brought practical experience from his published research on coring guano in other caves and also had access to his university's lab facilities for additional analyses. Dr. Rick Toomey, of the Mammoth Cave International Center for Science and Learning at Mammoth Cave National Park, Kentucky, is a vertebrate paleontologist who is highly knowledgeable about both bat and Texas cave faunal remains. He would identify the bones recovered to determine what changes in species, if any, occurred over time. But the first step was to determine where to drill inside the cave.

BCI organized a team of volunteers to assist NCKRI in conducting four electrical resistivity surveys in the cave in January 2014. The wintertime study period coincided with the time when most of the bats would be in Mexico, resulting in minimal disturbance but also better working conditions. NCKRI used its SuperSting R8/IP electrical resistivity equipment, manufactured by Advanced Geosciences, Inc., to collect the resistivity data. The data were later processed using EarthImager™ software.

Three two-dimensional surveys were conducted. Resistivity Line 1 began about 40 m from the cave's entrance and ran south, close to the cave's west wall, 56 m to a corner at the widest part of the entrance. Line 2 began approximately 25 m south of the entrance and ran south down the middle of the passage 56 m to a large breakdown pile. Lines 1 and 2 used 56 electrodes spaced at 1-m intervals. Line 3 followed the cave's east wall, beginning 45 m from the entrance and extending 80 m southeast to the end of the cave. Its 84 electrodes were placed at 0.95-m intervals (fig. 20).

One three-dimensional survey was conducted at the back of the cave below the mine shaft. The electrodes were placed at 2-m intervals in a 14- by 12-m grid; a larger grid with 1-m spacing was initially planned but abandoned due to damage to some of the resistivity cables.

The powdery nature of the guano cast some concern on the feasibility of conducting an effective resistivity survey. The contact resistance could have been too high to yield meaningful results. To maximize electrical transmission into the guano, the 46-cm long electrodes were pushed as deep into the guano as possible, some of them to their full lengths. Saline water was poured onto electrodes showing high contact resistance during testing prior to starting the survey, which reduced contact resistance for most but not all such electrodes. In the end, the results proved acceptable and better than expected.

The purpose of the close electrode spacing was to maximize the resolution of the survey to detect breakdown hidden in the guano that could interfere with coring. The expected stratigraphic sequence was guano, interlaced with breakdown, underlain by a thick section of breakdown. Although the thickness of the breakdown could be estimated, using Natural Bridge Caverns as an analogue, there was no model to estimate the depth of the guano.

Line 2 was imaged to a depth of about 15 m and was interpreted to show a considerable mix of breakdown and guano. Lines 1 and 3 were imaged to depths of about 18 m and showed areas with less breakdown, more conducive to coring. Figure 20 shows the results of the Line 3 survey. (The results of the other surveys are not shown in this report because the research is ongoing.) The warmer colors correlate to buried breakdown; the cooler colors indicate guano. As guano decomposes, it develops a clay-like composition with lower resistivity. The lowest resistivity values occur under the mine shaft where water drips regularly, lowering the resistivity even further. While this location seems optimal for coring, it is also the area excavated by guano miners to an estimated depth of 9–18 m, so most or all of the guano in that area is recent and probably of little paleoenvironmental value. The abrupt transitions in resistivity at that location likely reflect the excavated pit. The area about 48 m from the start of the Line 3 survey was identified as a better coring location.

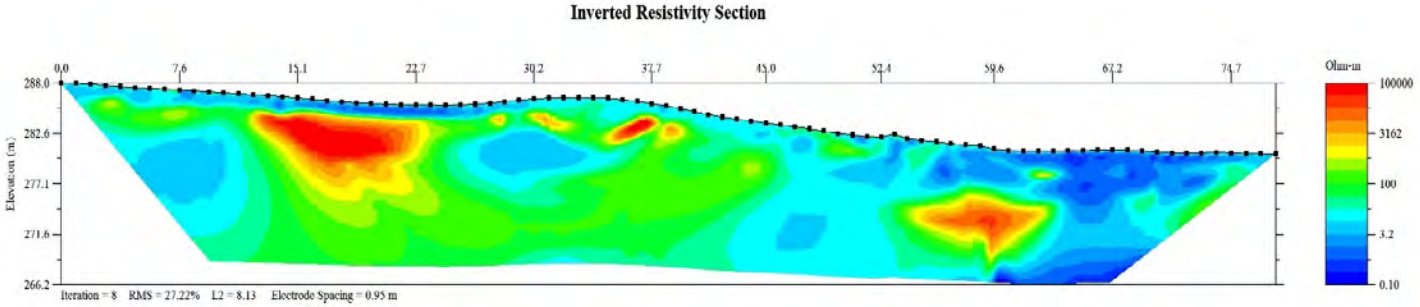

Figure 20. Resistivity profile of Line 3 along the east side of Bracken Bat Cave.

The results that the guano was at least 18 m deep left the main question unanswered—how deep is the guano? NCKRI returned to the cave 2 years later, in January 2016, and conducted two additional surveys. The 2014 surveys were focused on trying to find buried breakdown to avoid, as well as establishing the guano's depth. The 2016 survey focused on depth. The goal was to see through the guano and breakdown, and continue deeper through the sediment that probably underlies the breakdown to the floor of the original solutionally formed cave passage. Natural Bridge Caverns again served as a model to estimate target depths, except that the elevation and stratigraphic position of its solutionally formed bedrock floor are unknown. The deepest levels of that cave are covered in thick mud of unknown depth.

The 2016 surveys consisted of two lines. Both used 112 electrodes at 2-m spacing. Both lines were surveyed twice, once in a dipole-dipole configuration and then again in a pole-dipole configuration with the infinity electrode placed about 700 m to the north along BCI's property line to increase the

depth of penetration. The results were merged for a more complete and detailed image and interpretation. The first 56 m of Line 5 used the even-numbered electrode positions of Line 1 and then continued out of the east side of the cave's entrance and onto the surface. Line 6 could not overlap Line 3, due to the curvature of the cave wall, but ran subparallel to that line from the back of the cave and out of the west side of the entrance.

These surveys indicated the guano reaches a maximum depth of about 35 m to breakdown, which continues at least 20 m deeper. The original cave floor was not apparent, but this is based on a morphologic interpretation of the resistivity values. Presumably due to rainfall only a few days before the 2016 surveys, the resistivity values were similar for areas of known bedrock and breakdown and the two could not be distinguished. A return trip is planned when conditions are drier to provide more contrasts in the data, and with the resistivity array deployed to "see" deeper into the cave floor.

Guano Sampling

A guano sampling project currently underway at Southwest Research Institute aims to collect and examine bat guano cores from Bracken Bat Cave, and test the guano for chemical and other constituents that could be used to indicate the frequency, duration, and intensity of historical drought periods. Sampling campaigns into Bracken Bat Cave using hand-coring methods yielded over 2.7 vertical meters of guano sample material. Guano sample tubes are currently being sub-sampled and analyzed in the laboratory. Analysis of data collected will be correlated to established climatic variations to assess frequency, duration, and intensity of drought in south-central Texas. If determination of the regional paleoclimate is successful, historical groundwater recharge could be estimated using empirical relationships between precipitation and recharge. Future precipitation and drought cycles would then be predicted using historical climate frequency, duration, and intensity estimates, and future recharge estimates could be calculated using the predicted climatic conditions and the newly developed precipitation/recharge relationships.

References Cited

Adkins, W.S., 1932, The Mesozoic systems in Texas, *in* Sellards, E.H., Adkins, W.S., and Plummer, F.B., eds., The geology of Texas, vol. 1—Stratigraphy: The University of Texas Bulletin No. 3232, The University of Texas at Austin, p. 239–518.

Arthur, M.A., Jenkyns, H.C., Brumsack, H.J., and Schlanger, S.O., 1990, Stratigraphy, geochemistry and paleoceanography of organic carbon-rich Cretaceous sequences, *in* Ginsburg, R.N., and Beaudoin, B., eds., Cretaceous resources, events and rhythms: Boston, Dorbrecht, Kluwer Academic, p. 75–110.

Barnes, V.E., 1982, Geologic atlas of Texas, San Antonio sheet (revision of 1974 ed.): Bureau of Economic Geology, University of Texas at Austin, 1 sheet, 9 p. (revised 1983), scale 1:250,000, [Robert Hamilton Cuyler memorial edition].

Barron, E.J., Fawcett, P.J., Peterson, W.H., Pollard, D., and Thompson, S.L., 1995, A "simulation" of mid-Cretaceous climate: Paleoceanography, v. 10, no. 5, p. 953–962.

Bendik, N.F., Meik, J.M., Gluesenkamp, A.G., Roelke, C.E., and Chippindale, P.T., 2013, Biogeography, phylogeny, and morphological evolution in central Texas cave and spring salamanders: BMC Evolutionary Biology, v. 13, no. 201, accessed May 30, 2016, at http://www.biomedcentral.com/1471-2148/13/201.

Blakey, R., 2015, Western Interior Seaway paleogeographic maps and cross sections: Deep Time Maps, Albian (115 Ma), http://deeptimemaps.com/western-interior-seaway-map-list/.

Buffler, R.T., and Sawyer, D.S., 1985, Distribution of crust and early history, Gulf of Mexico basin: Transactions of the Gulf Coast Association of Geological Societies, v. 35, p. 333–344.

Clark, A.R., Blome, C.D., and Faith, J.R., 2009, Map showing the geology and hydrostratigraphy of the Edwards aquifer catchment area, northern Bexar County, south-central Texas: U.S. Geological Survey Open-File Report 2009-1008, 24 p., 1 pl.

Clark, A.K, Pedraza, D.E., Morris, R.R., and Garcia, T.J., 2013, Geodatabase and characteristics of springs within and surrounding the Trinity aquifer outcrops in northern Bexar County, Texas, 2010–11: U.S. Geological Survey Data Series 750, 20 p.

Couffer, J., 1992, Bat bomb, World War II's other secret weapon: University of Texas Press, 252 p.

Cuyler, R.H., 1939, Travis Peak Formation of central Texas: Bulletin of the American Association of Petroleum Geologists, v. 23, no. 5, p. 625–642.

Droser, M.L., and Bottjer, D.J., 1986, A semiquantitative field classification of ichnofabric: Journal of Sedimentary Research, **56** (4): 558–559, doi:10.1306/212f89c2-2b24-11d7-8648000102c1865d.

Dumble, E.T., 1892, Notes on the geology of the valley of the middle Rio Grande: Bulletin of the Geological Society of America, v. 3, no. 1, p. 219–230.

Dunham, R.J., 1962, Classification of carbonate rocks according to depositional texture, *in* Ham, W.E., Classification of carbonate rocks: American Association of Petroleum Geologists Memoir 1, p. 108–121.

Dyman, T.S., and Condon, S.M., 2006, Assessment of undiscovered oil and gas resources of the Upper Jurassic–Lower Cretaceous Cotton Valley Group, Jurassic Smackover Interior Salt Basins Total Petroleum System, in the East Texas Basin and Louisiana-Mississippi Salt Basins Provinces: U.S. Geological Survey Digital Data Series 069-E, chap. 1, 52 p.

Elliott, W.R, 1994, Bracken Bat Cave, *in* The caves and karst of Texas: National Speleological Society, p. 173–175.

Embry, A.F., III, and Klovan, J.S. 1971, A Late Devonian reef tract on northeastern Banks Island, N.W.T.: Bulletin of Canadian Petroleum Geology, v. 4, p. 730–781.

Erba, E., 2004, Calcareous nannofossils and Mesozoic oceanic anoxic events: Marine Micropaleontology, v. 52, no. 1–4, p. 85–106.

Erbacher, J., Huber, B.T., Norris, R.D., and Markey, M., 2001, Increased thermohaline stratification as a possible cause for an ocean anoxic event in the Cretaceous Period: Nature, v. 409, no. 18, January 2001, p. 325–327.

Erbacher, J., and Thurow, J., 1997, Influence of oceanic anoxic events on the evolution of mid-Cretaceous radiolaria in the North Atlantic and western Tethys: Marine Micropaleontology, v. 30, no. 1–3, p. 139–158.

Ewing, T.E., 2010, Pre-Pearsall geology and exploration plays in south Texas: Transactions of the Gulf Coast Association of Geological Societies, v. 60, p. 241–260.

Fieseler, R.G., Jasek, J., and Jasek, M., 1978, An introduction to the caves of Texas: Texas Speleological Survey, NSS Convention Guidebook 19, 116 p.

Föllmi, K.B., 2012, Early Cretaceous life, climate and anoxia: Cretaceous Research, v. 35, p. 230–257.

Föllmi, K.B., Godet, A., Bodin, S., and Linder, P., 2006, Interactions between environmental change and shallow-water carbonate build-up along the northern Tethyan margin and their impact on the early Cretaceous carbon-isotope record: Paleoceanography, v. 21, PA4211, 16 p.

Föllmi, K.B., Weissert, H., Bisping, M., and Funk, H., 1994, Phosphogenesis, carbon-isotope stratigraphy, and carbonate-platform evolution along the Lower Cretaceous northern Tethyan margin: Geological Society of America Bulletin, v. 106, no. 2, p. 729–746.

Forgotson, J.M.J., 1957, Stratigraphy of Comanchean Cretaceous Trinity Group: Bulletin of the American Association of Petroleum Geologists, v. 41, no. 10, p. 2328–2363.

Fullmer, S., and Lucia, F.J., 2005, Burial history of central Texas Cretaceous carbonates: Gulf Coast Association of Geological Societies Transactions, v. 55, p. 225–232.

Galloway, W.E., Henry, C.D., and Smith, G.E., 1982, Depositional framework, hydrostratigraphy, and uranium mineralization of the Oakville Sandstone (Miocene), Texas Coastal Plain: Bureau of Economic Geology, The University of Texas at Austin, Report of Investigations, no. 113, 51 p.

Gradstein, F.M., Ogg, J.G., Schmitz, M.D., and Ogg, G., 2012, eds., The geologic time scale 2012: Elsevier, 1,176 p.

Haq, B.U., 2014, Cretaceous eustasy revisited: Global and Planetary Change, v. 113, p. 44–58.

Haq, B.U., Hardenbol, J., and Vail, P.R., 1987, The chronology of fluctuating sea level since the Triassic: Science, v. 235, p. 1156–1167.

Hawthorne, J.M., 1990, Dinosaur track-bearing strata of the Lampasas Cut Plain and Edwards Plateau, Texas: Baylor Geological Studies Bulletin, v. 49, p. 1–45.

Hay, W.W., 2008, Evolving ideas about the Cretaceous climate and ocean circulation: Cretaceous Research, v. 29, p. 725–753.

Hazzard, R.T., 1939, Notes on the Comanche and Pre-Comanche Mesozoic formations for the Ark-La-Tex area and a suggested correlation with northern Mexico: Shreveport Geological Society, Fourteenth annual field trip guidebook, Upper and Lower Cretaceous of southwest Arkansas, p. 155–165.

Hill, R.T., 1887, The Texas section of the American Cretaceous: American Journal of Science, v. 34, p. 287–309.

Hill, R.T., 1891, The Comanche Series of the Texas-Arkansas region (with discussion by C.A. White and others): Geological Society of America Bulletin, v. 2, p. 503–528.

Hill, R.T., 1892, Geologic evolution of the non-mountainous topography of the Texas region—An introduction to the study of the Great Plains: The American Geologist, v. 10, no. 2, p. 105–115.

Hill, R.T., 1901, Geography and geology of the Black and Grand prairies, Texas with detailed descriptions of the Cretaceous formations and special reference to artesian waters: Twenty-first annual report of the United States Geological Survey to the Secretary of the Interior, 1899–1900, Part VII-Texas, 666 p.

Hill, R.T., and Vaughan, T.W., 1898, Nueces folio, Texas: U.S. Geological Survey Geologic Atlas of the United States Folio, v. GF-42, 4 p., scale 1:125,000.

Hull, D.C., 2011, Stratigraphic architecture, depositional systems, and reservoir characteristics of the Pearsall Shale-Gas system, Lower Cretaceous, south Texas: The University of Texas at Austin, M.S. thesis, 208 p.

Imlay, R.W., 1940, Lower Cretaceous and Jurassic formations of southern Arkansas and their oil and gas possibilities: Arkansas Geological Survey Information Circular, v. 12, 64 p.

Imlay, R.W., 1944, Cretaceous formations of central America and Mexico: Bulletin of the American Association of Petroleum Geologists, v. 28, no. 8, p. 1077–1135.

Jenkyns, H.C., 1980, Cretaceous anoxic events—From continents to oceans: Journal of the Geological Society, London, v. 137, p. 171–188.

Kauffman, E.G., 1977, Upper Cretaceous cyclothems, biotas and environments, Rock Canyon Anticline, Pueblo, Colorado, *in* Kauffman, E.G., ed., Cretaceous facies, faunas and paleoenvironments across the Western Interior Basin: The Mountain Geologist, v. 14, nos. 3, 4, p. 129–152.

Johnson, S., Schindel, G., and Veni, G., 2010, Tracing groundwater flowpaths in the Edwards aquifer recharge zone, Panther Springs Creek Basin, northern Bexar County, Texas: Edwards Aquifer Authority Report No. 10-01, 112 p.

Kastning, E.H., Jr., 1983, Geomorphology and hydrogeology of the Edwards Plateau karst, central Texas: The University of Texas at Austin, Ph.D. dissertation, 656 p.

Keller, G., Berner, Z., Adatte, T., and Stueben, D., 2004, Cenomanian-Turonian and $\delta^{13}C$, and $\delta^{18}O$, sea level and salinity variations at Pueblo, Colorado: Palaeogeography, Palaeoclimatology, Palaeoecology, v. 211, no. 1–2, p. 19–43.

Larson, R.L., 1991, Geological consequences of superplumes: Geology, v. 19, p. 963–966.

Leckie, M.R., Bralower, T.J., and Cashman, R., 2002, Oceanic anoxic events and plankton evolution— Biotic response to tectonic forcing during the mid-Cretaceous: Paleoceanography, v. 17, no. 3, p. 13-1–13-29.

Loeblich, A.R.J., and Tappan, H., 1949, Foraminifera from the Walnut Formation (Lower Cretaceous) of northern Texas and southern Oklahoma: Journal of Paleontology, v. 23, p. 245–266.

Lozo, F.E., and Stricklin, F.L.J., 1956, Stratigraphic notes on the outcrop basal Cretaceous, central Texas: Transactions of the Gulf Coast Association of Geological Societies, v. 6, p. 67–78.

Luttrell, P.E., 1977, Carbonate facies distribution and diagenesis associated with volcanic Cones-Anacacho Limestones (Upper Cretaceous), Elaine Field, Dimmit County, Texas: Gulf Coast Association of Geological Societies Transactions, v. 27, p. 441–442.

Mann, C.J., and Thomas, W.A., 1964, Cotton Valley Group (Jurassic) nomenclature, Louisiana and Arkansas: Gulf Coast Association of Geological Societies Transactions, v. 14, p. 143–152.

Millán, M.I., Weissert, H.J., and López-Horgue, M.A., 2014, Expression of the late Aptian cold snaps and the OAE1b in a highly subsiding carbonate platform (Aralar, northern Spain): Palaeogeography Palaeoclimatology Palaeoecology, v. 411, p. 167–179.

Montgomery, S.L., 1990, Horizontal drilling in the Austin Chalk—Part 1, Geology, drilling history and field rules: Petroleum Frontiers, v. 7, no. 3, 44 p.

Mort, H.P., Adatte, T., Föllmi, K.B., Keller, G., Steinmann, P., Matera, V., Berner, Z., and Stüben, D., 2007, Phosphorus and the roles of productivity and nutrient recycling during oceanic anoxic event 2: Geology, v. 35, no. 6, p. 483–486.

Murray, G., 1961, Geology of the Atlantic and Gulf Coastal Province of North America: New York, Harper, 692 p.

Phelps, R.M., Kerans, C., Loucks, R.G., Da Gama, R.O.B.P., Jeremiah, J., and Hull, D., 2014, Oceanographic and eustatic control of carbonate platform evolution and sequence stratigraphy on the Cretaceous (Valanginian-Campanian) passive margin, northern Gulf of Mexico: Sedimentology, v. 61, no. 2, p. 461–496.

Philip, J., 2003, Peri-Tethyan neritic carbonate areas—Distribution through time and driving factors: Palaeogeography, Palaeoclimatology, Palaeoecology, v. 196, no. 1–2, p. 19–37.

Reaser, D.F., and Dawson, W.C., 1995, Geologic study of Upper Cretaceous (Cenomanian) Buda Limestone in northeast Texas with analysis of some regional implications: Gulf Coast Association of Geological Societies Transactions, v. 45, p. 495–502.

Robison, C.R., 1997, Hydrocarbon source rock variability within the Austin Chalk and Eagle Ford Shale (Upper Cretaceous), east Texas, U.S.A.: International Journal of Coal Geology, v. 34, p. 287–308.

Rose, P.R., 1972, Edwards Group, surface and subsurface, central Texas: Bureau of Economic Geology, The University of Texas at Austin, Report of Investigations, no. 74, 198 p.

Ruppel, S.C., Loucks, R.G., and Frebourg, G., 2012, Guide to field exposures of the Eagle Ford-equivalent Boquillas Formation and related Upper Cretaceous units in southwest Texas: The University of Texas at Austin, Bureau of Economic Geology, Mudrock Systems Research Laboratory field trip guidebook, 151 p.

Salvador, A., 1991, Origin and development of the Gulf of Mexico, *in* Salvador, A., ed., The geology of North America: Boulder, Colorado, Geological Society of America, p. 389–444.

Schlanger, S.O., and Jenkyns, H.C., 1976, Cretaceous oceanic anoxic events—Causes and consequences: Geologie en Mijnbouw, v. 55, no. 3–4, p. 179–184.

Schröder-Adams, C., 2014, The Cretaceous polar and western interior seas—Paleoenvironmental history and paleoceanographic linkage: Sedimentary Geology, v. 301, p. 26–40.

Scotese, C.R., Gahagan, L.M., and Larson, R.L., 1988, Plate tectonic reconstructions of the Cretaceous and Cenozoic ocean basins: Tectonophysics, v. 155, no. 1–4, p. 27–48.

Scott, R.J., 1977, The Austin Chalk-Buda Trend of south Texas: Gulf Coast Association of Geological Societies Transactions, v. 27, p. 164–168.

Scott, R.W., Molineux, A.M., Löser, H., and Mancini, E.A., 2007, Lower Albian sequence stratigraphy and coral buildups—Glen Rose Formation, Texas, U.S.A., *in* Scott, R.W., ed., Cretaceous rudists and carbonate platforms—Environmental feedback: SEPM Society for Sedimentary Geology Special Publication 87, p. 181–191.

Sellards, E.H., Adkins, W.S., and Plummer, F.B., 1932, eds., The geology of Texas, vol. 1—Stratigraphy: The University of Texas Bulletin No. 3232, The University of Texas at Austin, 1,007 p.

Shearer, H.K., 1938, Developments in south Arkansas and north Louisiana in 1937: American Association of Petroleum Geologists Bulletin, v. 22, no. 6, p. 719–727.

Shumard, B.F., 1860, Observations upon the Cretaceous strata of Texas: Transactions of the Academie of Science of St. Louis, v. 1, p. 582–590.

Shumard, B.F., 1862, Descriptions of new Cretaceous fossils from Texas: Proceedings of the Boston Society of Natural History, v. 8, p. 188–205.

Snyder, R.H., and Craft, M., 1977, Evaluation of Austin and Buda Formations from core and fracture analysis: Gulf Coast Association of Geological Societies Transactions, no. 27, p. 376–385.

Stapp, W.L., 1977, The geology of the fractured Austin and Buda Formations in the subsurface of south Texas: Gulf Coast Association of Geological Societies Transactions, v. 27, p. 208–229.

Stephenson, L.W., 1927, Notes on the stratigraphy of the Upper Cretaceous formations of Texas and Arkansas: American Association of Petroleum Geologists Bulletin, v. 11, no. 1, p. 1–17.

Stricklin, F.L., Smith, C.I., and Lozo, F.E., 1971, Stratigraphy of Lower Cretaceous Trinity deposits of central Texas: Bureau of Economic Geology, The University of Texas at Austin, Report of Investigations, no. 71, 63 p.

Stein, W.G., and Ozuna, G.B., 1995, Geologic framework and hydrogeologic characteristics of the Edwards aquifer recharge zone, Bexar County, Texas: U.S. Geological Survey Water-Resources Investigations Report 95-4030, 8 p., 1 pl.

Swain, F.M., 1944, Stratigraphy of Cotton Valley beds of northern Gulf Coastal Plain: American Association of Petroleum Geologists Bulletin, v. 28, no. 5, p. 577–614.

Sweet, S.S., 1978, The evolutionary development of the Texas *Eurycea* (Amphibia: Plethodontidae): University of California, Berkeley, Ph.D. dissertation, 450 p.

Texas Speleological Survey, 2016, Texas deep caves, accessed May 30, 2016, at http://www.texasspeleologicalsurvey.org/deeplong/deepcaves.php.

Trabucho A.J., Tuenter, E., Henstra, G.A., van der Zwan, K.J., van de Wal, R.S.W., Dijkstra, H.A., and de Boer, P.L., 2010, The mid-Cretaceous North Atlantic nutrient trap—Black shales and OAEs: Paleoceanography, v. 25, PA4201, 14 p.

U.S. Fish and Wildlife Service, 2011, Bexar County karst invertebrate distribution: U.S. Fish and Wildlife Service, Austin Ecological Services Field Office, 13 p.

Vaughan, T.W., 1900, Reconnaissance in the Rio Grande coal fields of Texas: U.S. Geological Survey Bulletin, v. 164, p. 1–88.

Veni, G., 1988, The caves of Bexar County (2nd ed.): Texas Memorial Museum, Speleological Monographs 2, 300 p.

Veni, G., 1995, Redefining the boundaries of the Edwards (Balcones Fault Zone) aquifer recharge zone, *in* Water for Texas conference, 1995, Proceedings: Texas Water Resources Institute, p. 99–107.

Veni, G., 2005, Lithology as a predictive tool of conduit morphology and hydrology in environmental impact assessments, *in* Sinkholes and the engineering and environmental impacts of karst: American Society of Civil Engineers, Geotechnical Special Publication No. 144, p. 46–56.

Ward, W.C., and Ward, W.B., 2007, Stratigraphy of middle part of Glen Rose Formation (lower Albian), Canyon Lake Gorge, central Texas, U.S.A., *in* Scott, R.W., ed., Cretaceous rudists and carbonate platforms—Environmental feedback: SEPM Society for Sedimentary Geology Special Publication 87, p. 193–210.

Warner, A.J., and Moody, J.S., 1992, West Raymond Field (Mississippi): Mississippi Geology, v. 13, no. 2, p. 13–22.

Weeks, W.B., 1938, South Arkansas stratigraphy with emphasis on the older coastal plain beds: Bulletin of the American Association of Petroleum Geologists, v. 22, no. 8, p. 953–983.

Weissert, H., and Erba, E., 2004, Volcanism, CO_2 and palaeoclimate—A Late Jurassic-Early Cretaceous carbon and oxygen isotope record: Journal of the Geological Society, London, v. 161, p. 695–702.

Wentworth, C.K., 1922, A scale of grade and class terms for clastic sediments: The Journal of Geology, v. 30, no. 5, p. 377–392.

Whitney, M.I., 1952, Some zone marker fossils of the Glen Rose Formation of central Texas: Journal of Paleontology, v. 26, no. 1, p. 65–73.

Wilmarth, M.G., 1938, Lexicon of geological names of the United States: U.S. Geological Survey Bulletin, v. 896 (2 volumes), 2,396 p.

Wilson, P.A., Jenkyns, H.C., Elderfield, H., and Larson, R.L., 1998, The paradox of drowned carbonate platforms and the origin of Cretaceous Pacific guyots: Nature, v. 392, p. 889–894.

Winker, C.D., and Buffler, R.T., 1988, Paleogeographic evolution of early deep-water Gulf of Mexico and margins, Jurassic to middle Cretaceous (Comanchean): American Association of Petroleum Geologists Bulletin, v. 72, p. 318–346.

Young, K., 1965, A revision of Taylor nomenclature, Upper Cretaceous, central Texas: Bureau of Economic Geology, University of Texas at Austin Geological Circular, v. 65-3, 28 p.

ISSN 2328-0328 (online)
http://doi.org/10.3133/sir20175023